Theses and Dissertations   1. Thesis and Dissertation Collection, all items

1982

Asymmetric reinforcements of a quasi-isotropic graphite epoxy plate containing a circular hole.

O'Neill, Gary Sean.

Monterey, California. Naval Postgraduate School

http://hdl.handle.net/10945/20081

NAVAL POSTGRADUATE SCHOOL
Monterey, California

THESIS

ASYMMETRIC REINFORCEMENTS
OF A QUASI-ISOTROPIC GRAPHITE EPOXY PLATE
CONTAINING A CIRCULAR HOLE

by

Gary Sean O'Neill

June 1982

Thesis Advisor: M. H. Bank

Approved for Public Release; Distribution Unlimited

REPORT DOCUMENTATION PAGE		READ INSTRUCTIONS BEFORE COMPLETING FORM
1. REPORT NUMBER	2. GOVT ACCESSION NO.	3. RECIPIENT'S CATALOG NUMBER
4. TITLE (and Subtitle) Asymmetric Reinforcements of a Quasi-Isotropic Graphite Epoxy Plate Containing a Circular Hole		5. TYPE OF REPORT & PERIOD COVERED Master's Thesis; June 1982
		6. PERFORMING ORG. REPORT NUMBER
7. AUTHOR(s) Gary Sean O'Neill		8. CONTRACT OR GRANT NUMBER(s)
9. PERFORMING ORGANIZATION NAME AND ADDRESS Naval Postgraduate School Monterey, California 93940		10. PROGRAM ELEMENT, PROJECT, TASK AREA & WORK UNIT NUMBERS
11. CONTROLLING OFFICE NAME AND ADDRESS Naval Postgraduate School Monterey, California		12. REPORT DATE June 1982
		13. NUMBER OF PAGES 206
14. MONITORING AGENCY NAME & ADDRESS(II different from Controlling Office)		15. SECURITY CLASS. (of this report)
		15a. DECLASSIFICATION/DOWNGRADING SCHEDULE Unclassified

16. DISTRIBUTION STATEMENT (of this Report)

Approved for Public Release; Distribution Unlimited.

17. DISTRIBUTION STATEMENT (of the abstract entered in Block 20, II different from Report)

18. SUPPLEMENTARY NOTES

19. KEY WORDS (Continue on reverse side II necessary and identify by block number)

Composite
Asymmetric Reinforcement
Circular Hole
Graphite Epoxy Panel

20. ABSTRACT (Continue on reverse side II necessary and identify by block number)

The response to uniaxial loading of a graphite epoxy panel containing a one-inch diameter hole was analyzed by finite element analysis and tested experimentally. The analysis modeled the basic unreinforced panel and six different asymmetric reinforcements consisting of additional layers of the same material of circular shape on one side of the panel laminate. The reinforcement configurations varied the volume

of the reinforcement from 94% to 162% of the volume of the material removed by the hole, the number of reinforcing layers (1 to 4) and the outer radius of the reinforcement layers from 0.75 inches to 1.5 inches. The orientation of the reinforcing layers was either 45° or 0° to the load direction. Results of the computational analysis indicated that the reduction of maximum strain (in the direction of the load at a point at the edge of the hole 90° from the load direction) by the reinforcements was at most 12%, with apparent dependence on the number of layers used and the volume of the reinforcement. Experimental testing of three of the configurations confirmed the accuracy of the finite element analysis and demonstrated that the reinforced panels recovered 5 to 10% of the basic laminate strength above that of the reinforced panel. In addition to the computational analysis, two isotropic empirical predictions for stress (strain) concentration at the edge of a circular hole were examined to determine their applicability to asymmetric reinforcement of a quasi-isotropic panel, with mixed results.

Asymmetric Reinforcements of a Quasi-Isotropic
Graphite Epoxy Plate Containing a Circular Hole

by
Gary Sean O'Neill
Lieutenant, U.S. Navy
B.A.E., Georgia Institute of Technology, 1975

Submitted in partial fulfillment of the
requirements of the degrees of

MASTER OF SCIENCE IN AERONAUTICAL ENGINEERING
and
AERONAUTICAL ENGINEER

from the

NAVAL POSTGRADUATE SCHOOL

June 1982

ABSTRACT

The response to uniaxial loading of a graphite epoxy
panel containing a one-inch diameter hole was analyzed by
finite element analysis and tested experimentally. The
analysis modeled the basic unreinforced panel and six dif-
ferent asymmetric reinforcements consisting of additional
layers of the same material of circular shape on one side
of the panel laminate. The reinforcement configurations
varied the volume of the reinforcement from 94% to 162% of
the volume of the material removed by the hole, the number
of reinforcing layers (1 to 4) and the outer radius of the
reinforcement layers from 0.75 inches to 1.5 inches. The
orientation of the reinforcing layers was either 45° or 0°
to the load direction. Results of the computational analysis
indicated that the reduction of maximum strain (in the direc-
tion of the load at a point at the edge of the hole 90° from
the load direction) by the reinforcements was at most 12%,
with apparent dependence on the number of layers used and
the volume of the reinforcement. Experimental testing of
three of the configurations confirmed the accuracy of the
finite element analysis and demonstrated that the reinforced
panels recovered 5 to 10% of the basic laminate strength
above that of the reinforced panel. In addition to the
computational analysis, two isotropic empirical predictions
for stress (strain) concentration at the edge of a circular
hole were examined to determine their applicability to
asymmetric reinforcement of a quasi-isotropic panel, with
mixed results.

TABLE OF CONTENTS

LIST OF TABLES

LIST OF FIGURES

8

11

LIST OF SYMBOLS

A	cross sectional area of the reinforcement
a	semi-major axis length of an elliptical hole
b	semi-minor axis length of an elliptical hole
E	Young's Modulus
h	thickness of both reinforcement and panel
K	curvature
M	stress moment
N	stress resultant
R	radius of hole, 0.5 inches
t	thickness of panel
V	volume
X	coordinate axis, horizontal through plane of panel
Y	coordinate axis, through thickness of panel
Z	coordinate axis, vertical through plane of panel
ε	strain
μ_s	microstrain
o	midplane
x,z,xz	components in plane of panel
0	0° to load axis
90	90^9 to load axis

ACKNOWLEDGEMENTS

I. INTRODUCTION

The steady increase in the use of composite materials in aircraft design has been made possible by years of basic research concerning the qualities of composites. Examination of the behavior of composites in basic design configurations has provided the answers required to use composites in those configurations with a high degree of confidence, leading to the incorporation of those configurations in evolving designs. Present applications of composites in design are quite naturally dominated by configurations that have been understood for the longest time, and have avoided where possible the use of configurations which have not been as deeply researched. Because the researchers in composite materials must pay careful attention to the effects resulting from the inherent orthotropicity of the material, such as stacking sequence of layers, laminate direction and composition, the time required to understand the behavior of composites as fully as we understand that of isotropic materials such as steel alloys is much greater. There are many areas in which basic research in composites is still in progress.

One such area of research and possible application is that of a composite panel under tensile loading which contains an intentionally placed stress concentration such as a circular hole. A wing panel with an access hole or a tank having a hole in its wall to permit the attachment of a feed line

would be examples of such an application. The interlaminar shear present near the hole edge, coupled with the stress concentrations created by the existence of the hole, pose complications which seem to be avoided whenever possible by design engineers, causing the components to be potentially lacking in flexibility of design.

The response of composite panels containing stress concentrations to uniaxial tensile loading has been the subject of past research. Rowlands, Daniel and Whiteside [Reference 1] determined that the material properties of the laminate specify the strain behavior in the vicinity of the hole (see Analysis, page 49). Also, there was evidence that interlaminar stress did influence the response of the panel. The same work also demonstrated that a well constructed finite element model could be used to compute the behavior of the plate with a high degree of agreement with experimental results.

The same research team [Ref. 2] also pursued the influence of laminate orientation and stacking sequence on the stress and strain behavior of a plate containing a hole. Their findings show that the orientation of the plies in relation to the load axis (specifically the number of $\pm$ 45° plies) has a significant effect on the reduction of tangential strain around the edge of the hole. They also showed that the reduction of the total strength of the panel, compared with an identical panel without a hole, can be mitigated by the predominant use of $\pm$ 45° plies. In addition, the mode

of failure of the panel was shown to be dependent upon the stacking orientation and sequence.

While the reinforcement of holes in composite panels would seem to be a logical extension of this line of research, little information concerning reinforcements exists in the published literature. McKenzie [Ref. 3] demonstrated some success with hoop wound graphite epoxy rings attached asymmetrically to both aluminum and graphite epoxy panels. The effect of varying the outer radius and thickness of the reinforcements was investigated, and the potential difficulty of reinforcing only one side of the panel was mentioned. The method used in the investigation had the disadvantages of separate production of the reinforcement and panel, attachment processing, and post attachment adjustment if dimensional consistency was required.

The investigation reported here studied the effectiveness of asymmetric reinforcement of a quasi-isotropic graphite-epoxy plate containing a circular hole. Asymmetric reinforcements were chosen because of their greater potential ease of manufacture and their applicability in some instances, i.e., where mating of two panels would be adversely affected by small raised areas of reinforcement. The reinforcement proposed for study consisting of additional laminate added asymmetrically, i.e. to only one surface of the panel, and covering only a portion of the panel in the region of the hole. The reinforcements were arbitrarily chosen to be of

18

circular shape arranged symmetrically about the hole and varying in radius to gradually build up thickness near the hole. This choice was based on the historical use of such reinforcements in isotropic materials. In being laid up with additional layers of the same material, the reinforcements have the advantage of co-curing with the panel, with no thermal property variations and no complication on the underside tooling (which would be necessary if the reinforcement were symmetric).

This investigation selected six different reinforcement configurations based on volume of the reinforcement, number of layers of reinforcement and outer ring radius. These six configurations were then modelled for finite element analysis to compute stresses, strains and displacements. In addition, because of the quasi-isotropic nature of the panels, the parameters of the reinforcement configurations were used in two isotropic empirical analyses for comparison to the finite element results. Experiments were conducted on the quasi-isotropic nonreinforced panels with and without holes (to establish a baseline for comparison) and on panels having several of the reinforcement configurations. The experimental results were then compared with the finite element results to verify the models and to the alternate analysis to determine the accuracy of the more simplified approaches. The attention of the computations and comparisons concentrated on the maximum strain of the panel, located at the edge of the hole 90° from

the direction of the load, based on previous studies of composite panels which indicated that the strain in this area was the primary cause of failure. Finally, the experimental and computational results were compared in order to draw final conclusions about the effectiveness of the reinforcements studied.

II. COMPUTATIONAL ANALYSIS

A. MODEL FORMULATION

The analysis of the basic panel and all reinforcement configurations was completed through the use of a finite element computer code known as DIAL [Ref. 4], developed by Lockheed Missiles and Space Co. This code is a series of programs which compile files in a data base, develop the mesh, loading and boundary conditions of the model, and finally compute the nodal deflections and forces. All files created in the running of the several interrelated programs are then used in the post-processing portion of the code, which creates the output data in terms of strain and stress resultants. The actual solution to the matrix equation is computed using a modified Newton-Rapson technique and strictly linear analysis.

Since the computational analysis was to predict the behavior of panels which was to be experimentally verified, the physical dimensions of the computer model were determined by the design requirements for the test panels. For the discussion concerning the choice of the panel size, see the section on Panel Selection and Construction. The model created to duplicate the actual panels used in the experiment took advantage of the symmetry of the problem to reduce the number of elements and degrees of freedom. One quarter of the plate was used, corresponding to the upper right hand

21

corner of the actual plate as normally viewed. The mesh
was generated by a standard mapping from the k-j plane to the
x-z (actual) plane. Because of the strains and stresses were
expected to vary more rapidly near the hole edge and in
anticipation of the circular nature of the proposed reinforce-
ment configurations, several closely spaced rings were placed
near the hole at radii of 0.625, 0.75, 0.875, 1.00, and 1.25
inches. These dimensions were chosen to produce a sufficient
number of elements near the hole for accuracy while keeping
the total number of elements low enough to prevent excessive
computational run time. The mesh generated by the computer
is shown in Figure 1. For the basic panel, the mesh uses a
total of 262 elements and 853 node points, of which 45
elements are contained within the 1.25 inch radius.

The elements selected to occupy the mesh for the panel
were standard isoparametric quadrilateral elements having
eight side nodes and one interior node. The elements utilize
two Gauss quadrature integration points per side and include
two points through the direction of thickness, giving them
the properties of a modified thick shell element. The mate-
rial property definition of the code permitted the layering
of individual laminae within the element by defining the
material properties and orientation of the laminae, so that
in effect, each element of the basic panel has the identical
properties of the laminate it is to model. The code also
made provision for the buildup of laminae over a portion of
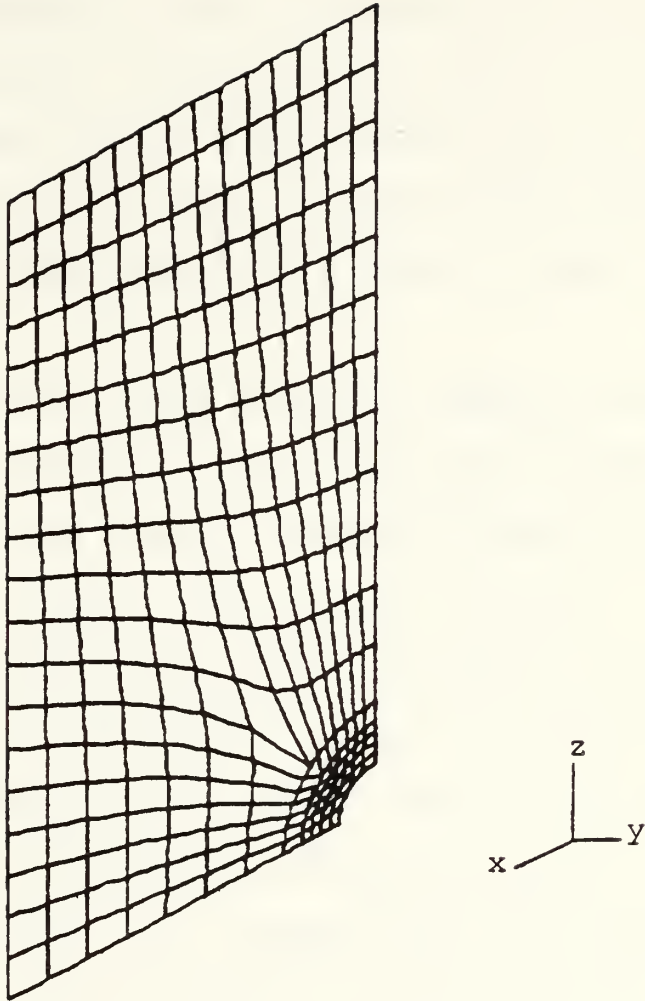
Figure 1.   Mesh Generated To Model Panel
             (Perspective View).

the panel to represent the areas of reinforcement, with the same ability to define the material properties of the partial laminae. This in effect adds additional elements to the panel by placing additional elements over the basic panel, but does not add any degrees of freedom. This provision restricts the placement of the reinforcement layers to the radii previously described above, but allows for one reinforcement layer to lay upon a layer below it. An example of the way the panel and reinforcements were built up by this process is shown in Figure 2.

The quarter panel mesh was constrained by symmetry boundary conditions along the lower edge and the right hand vertical edge as seen in Figure 1, two lines of symmetry passing through the center of the circular hole. In addition, to model tensile loading the upper edge was permitted to move in the plane (x and z deflections) and no rotations were permitted along that edge, which corresponds to the portion of the panel just at the edge of the load bearing fiberglass tabbing. All other nodal degrees of freedom were automatically made consistent by the code. By the application of these boundary conditions, the problem was reduced to one having a total of 4824 degrees of freedom in the solution.

The loading of the panel was modeled as a uniformly distributed load of 1000 pounds per inch across the top edge of the panel, in the positive Z direction. This corresponds to a total tensile loading of 10,000 pounds. The distributed loading was appropriately factored into concentrated loads at
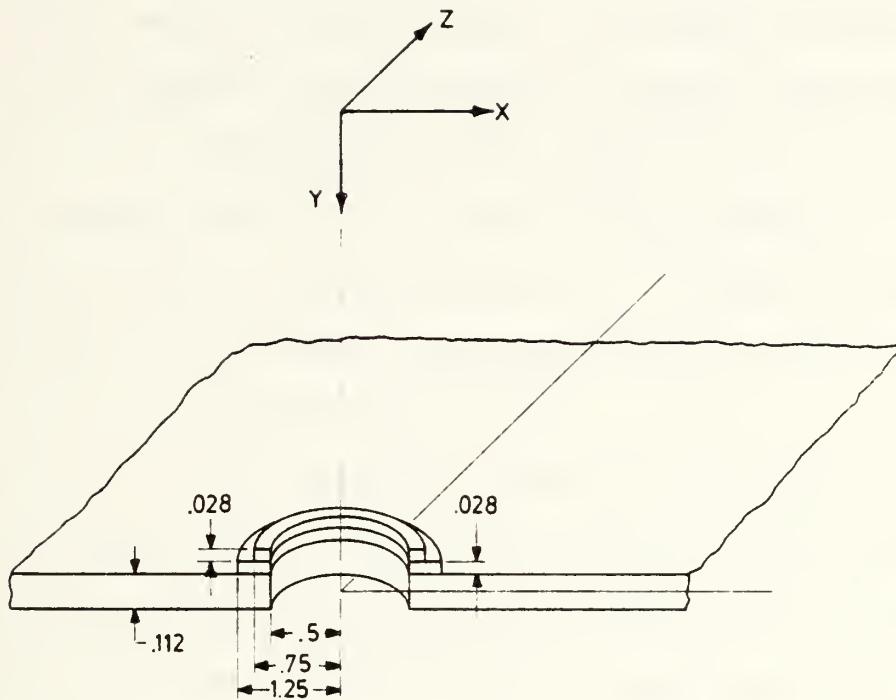
Figure 2. Cross Section of a Typical Reinforcement.

each of the 29 nodes along the top edge. Because of the linear solution technique, results of this one loading can be adjusted to show the effects of any similar concentrated loading by simply multiplying the results by the ratio of the other load to 10,000 pounds.

As previously discussed, the reinforcements chosen for study were circular in nature and approximately equal in volume to the material removed from the panel by the hole. The six reinforcement configurations discussed were also divided into two subconfigurations, representing: a) all laminae oriented $\pm 45°$; or, b) one or two laminae closest to the panel having an orientation of $0°$. Table I shows the different reinforcement configurations and the labels by which they will hereafter be referred.

The choice of 0.75 inches for the minimum outer ring radius was based on the concern that smaller reinforcements would be less effective due to the relative size of the region near the free edge affected by interlaminar stresses. Since the interlaminar stresses create a three dimensional stress state in a region about one thickness from the hole edge (a total radius of approximately 0.6 inches for these panels) [Ref. 5], the minimum outer radius should exceed that distance by a reasonable amount in order to be effective. (The variation of ring radii in 0.25 inch increments was partially dictated by the mesh generation and also because it created an effective ramp between the layers of approximately $3°$ for single layered rings and $6°$ for double layered

26

TABLE I

COMPUTATIONAL MODEL CONFIGURATIONS

CONFIGURATION % VOL	RING RADIUS, IN	THICKNESS IN	ORIENTATION DEG
1A 162%	0.75 1.25	Q.028 0.Q28	+45 -45
1B 162%	0.75 1.25	0.Q28 0.028	+45 0
2A 1Q3%	1.00 1.25	0.028 0.028	+45 -45
2B 1Q3%	1.00 1.25	Q.028 0.028	+45 0
3A 118%	Q.75 1.00 1.25	0.014 0.014 0.014	+45 -45 +45
3B 118%	0.75 1.00 1.25	0.014 Q.014 0.014	+45 -45 0
4A 96.9%	0.75 1.25	0.028 0.014	+45 -45
4B 96.9%	0.75 1.25	0.028 0.014	+45 Q
5A 106.2	0.75 1.0	0.028 Q.028	+45 -45
5B 106.2	0.75 1.00	0.028 0.028	+45 0
6A 100.0	1.5Q	0.014	+45
6B 100.Q	1.50	Q.014	0

rings.) These small ramp angles from one ring to the next were intended to provide an easy load path for the stresses in the panel, thus reducing stress concentrations in the transition region from one ring to the next.

The choices of the number of layers and radii were directed by two considerations: a) keeping the total volume of the reinforcements close to that of the material removed by the hole, to reduce the weight added to the structure and also to permit comparison to other investigations; and, b) avoiding configurations which are unusually thick in the vicinity of the hole, resulting in extremely high bending loads and potential problems in mating with adjacent surfaces.

For most of the twelve subconfigurations and the basic panel without reinforcement, the following results were obtained:

1. Contour Plots of the Stress Resultants

   a. N_z

   b. N_x

   c. N_{xz}

   d. Out of plane deflections (not available for all configurations)

2. Element strains and curvature for elements on the two lines of symmetry.

3. Element Stress Resultants and Stress Moments (N's and M's) for the same elements as above.

For convenience, all of the figures for the basic panel
and for each reinforcement configuration are separated into
individual sections found in Appendices A-G. The results
contained in the Appendices are discussed below.

B. COMPUTATIONAL RESULTS

1. Computed Surface Strains

Because the experimental portion of this investiga-
tion used strain measurements to determine the response of
the tested panels, the numerical output from the DIAL program
for all of the configurations was used to compute the value
of surface strains on the front (reinforced side) and back
of the panel. The values of the panel midplane strains and
curvatures were used to compute the surface strains using the
classical laminate theory strain equation

$$\begin{Bmatrix} \varepsilon_x \\ \varepsilon_z \\ \varepsilon_{xz} \end{Bmatrix} = \begin{Bmatrix} \varepsilon_x \\ \varepsilon_z \\ \varepsilon_{xz} \end{Bmatrix}_o + y \begin{Bmatrix} k_x \\ k_z \\ k_{xz} \end{Bmatrix} \qquad (1)$$

The values of the surface strains were computed by employing
the output of midplane strains and curvatures of one integra-
tion point per element to reduce the amount of data reduction.
The integration point selected was the point closest to the
edge of the hole and axis of symmetry. For consistency, the
same integration point was used for all other elements. In
this way, a total of 11 points was used for calculations
along the X axis (across the direction of the tensile stress)

and 16 along the Z axis (parallel to the stress). The results of these calculations are found in the first six figures of each Appendix, with both subconfigurations shown on the same plot for comparison.

The results for the basic (unreinforced) panel, shown in Figures 21 to 26 of Appendix A, demonstrate that the curvatures of the panel, which are of the order 10^{-10}, do not have any effect on surface strains; both sides of the panel have identical values. In addition, all six figures show that the behavior is generally smooth and continuous, except near the very edges of the hole for ε_x vs Z/R and ε_{xz} vs Z/R. All of the figures also show that the strains have virtually achieved their farfield values by 2-4 radii from the edge of the hole, which again is similar to isotropic plate behavior.

The computed results for the other configurations (shown in Appendices A-G) have several aspects in common which are important to understand before discussing those aspects which differentiate them. First, because of the asymmetry of the reinforcements, the values of Y, distance from the reference plane, for the front and back surfaces are different. The value of y for the back of the panel is constant at 0.056 inches (for all configurations) and the value of y for the front of the panel varies from .112 to 0.56 inches, depending on the configuration and distance from the center of the hole. The large separation of the two

30

surfaces coupled with the large curvatures in the areas of greatest reinforcement thickness create a large difference in the strain results for the two surfaces. These curvatures are created by the reinforcement being pulled toward the midplane of the panel as the load is applied, a phenomenon well documented to isotropic and orthotropic materials [Ref. 3]. For example, this curvature of the panel causes the unreinforced side of the panel (back) to be in tension, and the reinforced side to be in compression, so that the surface strains of the back of the panel will always be higher than the reinforced side. Additionally, the values of ε_z plotted against X/R on the back side for the reinforced configurations are typically higher at the edge than for the unreinforced panel, and the reinforced side strains are typically two thirds of the unreinforced panel values. The strain values for both sides decrease with increasing distance from the hole and approach the values for the unreinforced panel from above and below at distances far from the hole. Nearly all of the configurations (except 6 and 6A) show a marked dip in the distribution of ε_z vs X/R in the vicinity of the outer radius of the largest reinforcement layer, similar to the decrease in stress found just inside a reinforcement in an isotropic plate [Ref. 6] at a reentrant corner. In fact, in nearly every case, the lower portion of the curve is at Z/R = 2.0, a point in between the inner and outermost radii for most of the configurations.

There are some common features of the results for
all the configurations which are somewhat unexpected. For
example, the curves ε_x vs X/R and ε_x, ε_z and ε_{xz} vs Z/R
for nearly all the configurations show consistency in general
character and also in the numerical values close to the edge
of the hole, in spite of the wide variation of reinforcement
configuration geometry. The differences in the values plotted
against Z/R are so slight that they could be ignored to a good
approximation. Another example is the rather close agreement
among configurations of the numerical value of the strain
at the point closest to the hole on the unreinforced (back)
surface of the panel (in that location). Every configuration
has a maximum strain of between 3100 and 330 μ strain, values
in excess of the corresponding value for the unreinforced
panel.

Perhaps the most important common feature of all the
results is the fact that the B subconfigurations (those with
a 0° layer/layers closest to the basic panel) consistently
produce significantly lower values of ε_z and ε_x on the
front surface near the edge of the hole than that for the
corresponding A subconfigurations. The amount of reduction
varies among the configurations, with the greatest reductions
produced by the configurations with larger thicknesses of the
0° portion of the reinforcement. The DIAL output for the A
and B subconfigurations consistently shows differences in
corresponding values of strains and curvatures. The difference

in curvature varies with the distance of the elements away from the hole edge, with the greatest differences (at the hole edge) being up to 20% for values k_z and up to 50% for k_x and k_{xz}. In addition, it often happens that corresponding values of k_x or k_{xz} for the two subconfigurations have differing signs which can significantly alter the corresponding surface strain values. The midplane strains for corresponding locations of the subconfigurations are consistently lower for the B configuration than those configuration A for areas within the reinforcement, and this effect often extends out beyond the reinforced region. The values of ε_z seem to be most affected, with the variation being as much as 20-25% depending upon the configuration.

In contrast to the common aspects of the results, each configuration has some individual results which warrant detailed examination. The DIAL output for the first configuration, shown in Figures 33 to 38 of Appendix B, show several interesting features. First, in Figure 33, the difference between front and back surface strains (ε_z) is quite large, with the corresponding values near the hole edge differing by almost 1800 μ_s. The maximum front surface strain is about 1400-1700 μ_s, depending on subconfiguration, and the minimum strain is about 5-700 μ_s, or only 20% of the maximum value of the back side. There is little difference in the strains for the back surface between the two subconfigurations, showing that changes in orientation of the reinforcement material has little effect on strains of the unreinforced side. Figure 34,

33

showing ε_x vs X/R, also shows significant difference between
the subconfigurations and the two surfaces of the panel.
Figure 35 shows that there is less difference between the
configurations for ε_{xz}, but there is still a large difference
between the front and back surfaces, on the order of 200 μ_s
(30% of the maximum value). When ε_z is plotted vs Z/R
(Figure 36), there is a large difference in ε_z between the
two surfaces and the strain is rapidly changing in the vicinity
of the hole; however, there is little difference between the
subconfigurations. Figure 37 and 38 show similar results for
ε_x and ε_{xz} vs X/R, again showing little variation between
the subconfigurations.

The second configuration with a reinforcement, con-
sisting of one layer of 1.25 inch radius and one layer of 1.0
in radius, exhibits behavior which is essentially similar to
the first configuration, although it differs in degree. In
Appendix C, Figure 51 plots ε_z vs X/R and shows surface
strains at the edge of the hole differing by about 1000 μ_s.
The maximum strain on the front side is about 21-2300 μ_s
and the minimum is approximately 750 μ_s. There is far less
variation between the subconfigurations than for configuration
1.

The third configuration results found in Appendix D
have some slight differences from the two configurations
above. First, in Figure 61, the maximum front surface strain
(ε_z) is slightly lower, being between 1800-2000 μ_s, with the
minimum about the same as for #2 at 7-800 μ_s. The dip in ε_z

34

is more severe as in the previous cases, and there are smaller variations between the subconfigurations. In Figure 62, the maximum difference in ε_x near the hole edge is about 600 μ_s. There is only a slight difference between the front and back surface strains for the B subconfigurations (about 20 μ_s near the hole edge) while there is a large difference between the surface strains for the A subconfiguration.

The fourth configuration results shown in Appendix E are similar to the results for the third configuration. Figure 81 shows the maximum front surface value of ε_z to be about 1800-2000 μ_s , with the minimum around 800 μ_s. The dip in ε_z is shallower and has more gently sloping sides than in the previous results. Figure 82, showing ε_x vs X/R shows the same relative difference between front and back as the third configuration and a similar difference between configurations. Figure 83, showing ε_{xz} vs X/R shows the characteristic large difference between surfaces for the A and B subconfigurations.

The fifth configuration results are found in Appendix F show some similarity to the first configuration. Figure 95, showing ε_z vs X/R, shows the maximum front surface strain to be about 14-1800 μ_s with the minimum between 500-700 μ_s. The dip in ε_z is not as deep as the first configuration, and it is slightly offset to X/R = 1.5 due to the smaller outer radius. In Figure 96, the variation of ε_x is seen to be about the same as in the other configurations.

35

The sixth configuration, reinforced by only one layer, has some major differences from the other configurations. In Appendix G, Figure 109 shows the maximum front surface value of ε_z to be in the range of 24-2600 μ_s, with essentially no dip to values much below the farfield results. This plot also shows the smallest variation between A and B of all the configurations, although B still has lower values than A. Figure 110 shows that the difference between subconfigurations for ε_x is not as large as with the other configurations.

To further illustrate the different features of the results of the several configurations, the variation of ε_z vs X/R for the front surface of the plain panel and the B subconfigurations of the six reinforcements are plotted together in Figure 3. This plot clearly shows the range of values for the strain at the edge of the holes, the dip at X/R = 2.0, and the similarity of values for X/R greater than 6. To highlight the similarities discussed above for all the results, the variation of front surface strains, ε_x vs Z/R are plotted in Figure 4. This plot shows vividly the remarkable consistency between configurations and seems to indicate that there is little reduction in strain for any of the configurations modeled, despite the variations in height, diameter or ply orientation.

2. Contour Plots

The output of the analysis computed by DIAL also included contour plots of the Stress Resultants, N_z, N_x, N_{xz}
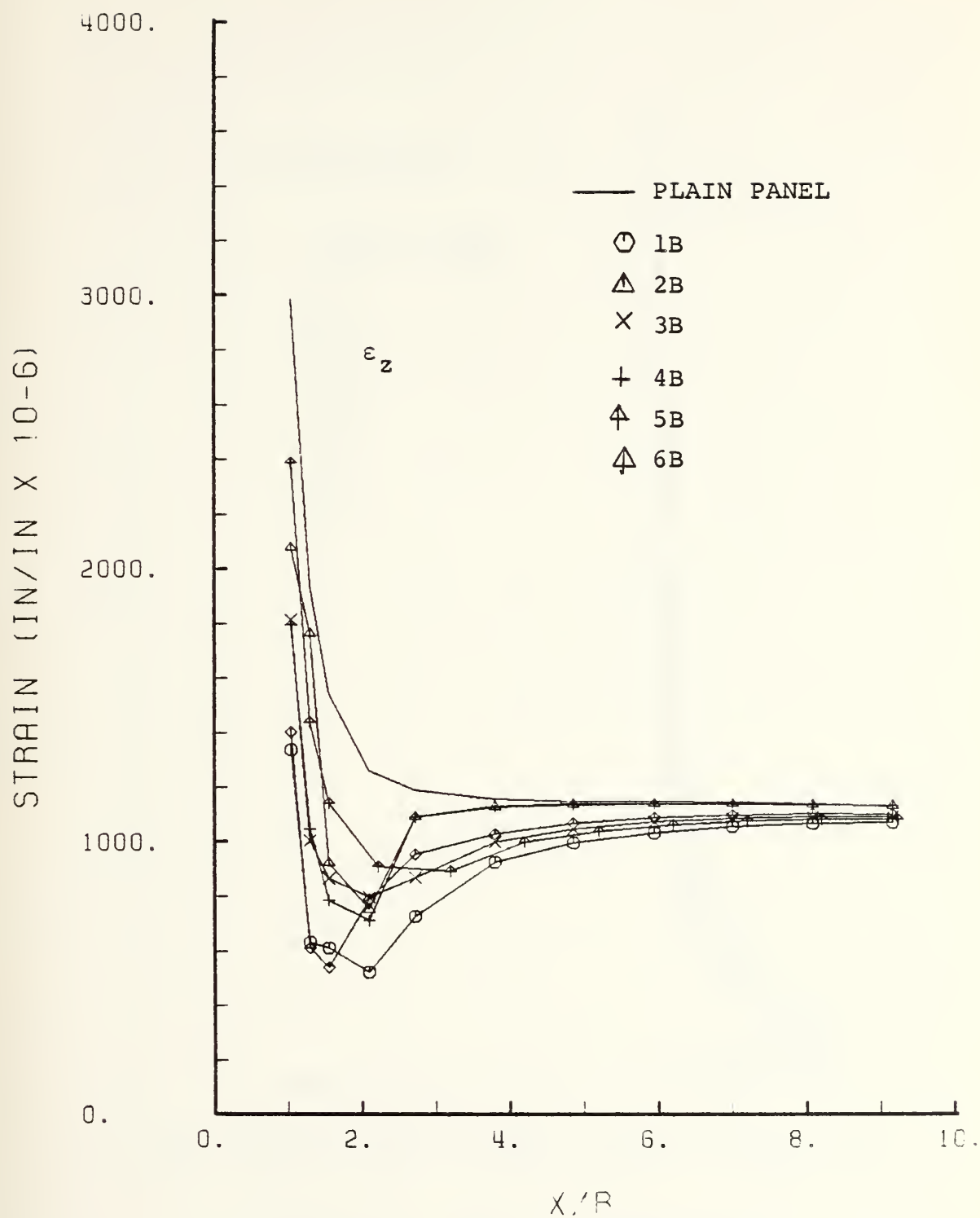
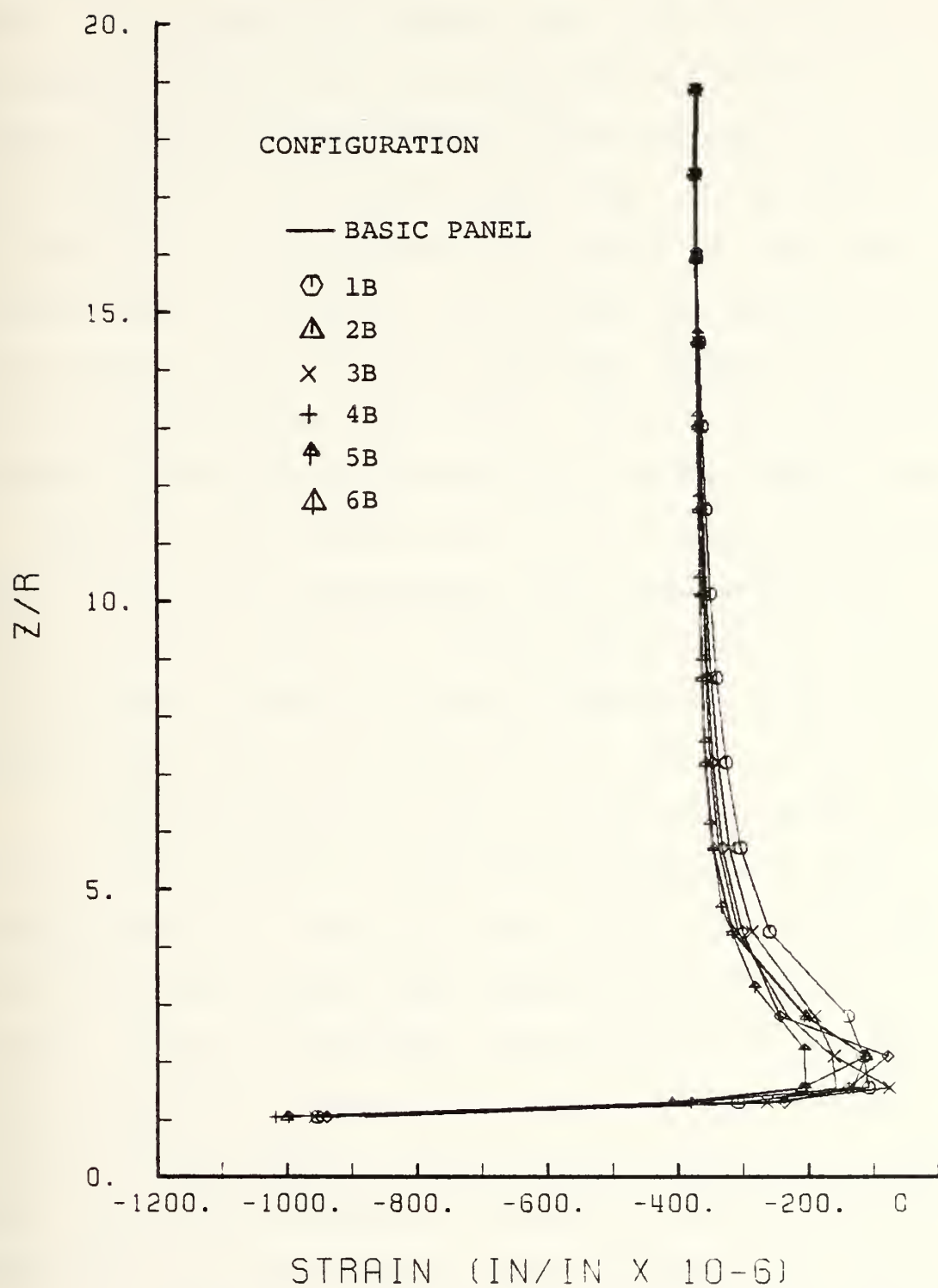Figure 3.   Comparison of Front Surface Strains
(ε_z)

37

Figure 4. Comparison of Front Surface Strains (ε_x).

38

and the out of plane deflections (y direction). The plots for the basic (unreinforced) panel shown in Figures 27 to 30 of Appendix A show that the panel behaves in an isotropic manner. The contours all exhibit very localized behavior in the vicinity of the hole and comparison of the plots of N_x, N_z and N_{xz} show only one nonzero stress resultant, N_z, exists at an appreciable distance from the hole. At the edge of the hole 90° from the applied load (Figure 27), the value of N_z approaches 3000 lb/in, or three times the applied stress. At the edge of the hole at the load axis (Figure 28), the value of N_x approaches -1000 lb/in. Both of the values are identical to the values predicted by isotropic theory [Ref. 7]. Figure 30, the contour plot of out of plane deflections, shows that the panel experiences very slight deflections along its entire width in a smooth gradual manner. There is also a roughly triangular region of deflection which occurs above the hole due to the compressive strains in this area.

Contour plots of N_x, N_x, N_{xz} and out of plane deflections are also included in the other Appendices for most subconfigurations. Like the strain results discussed above, these plots also contain some similarities that are of interest. First, as expected, the contours of N_z roughly follow the circular shape of the reinforcements near the edge of the hole because of the changing thickness in this area. The spacing between the contours in the reinforced region varies by configuration, being farthest apart where

39

the reinforcements are thickest. Second, the contour plots
of N_x and N_{xz} show great similarity among all the subconfigu-
rations, just as the results for ε_x and ε_{xz}.

The contour plots of out of plane deflections (for
those cases where plots are available for both subconfigura-
tions) indicate one important difference between the subcon-
figurations. With the exception of Configuration 5, all
other plots show that the B subconfigurations experience
greater out of plane deflections and that these deflections
have slightly higher gradients in the vicinity of the hole.
In addition, the deflections for the B subconfigurations
seem to extend across the entire panel, while the A subcon-
figurations show contours of roughly elliptical shape centered
about the hole. Since all other factors between the subcon-
figurations are identical, this difference in the nature of
the deflections must be attributed to the orientation of the
fibers of the innermost ring.

3.   Computed Strain Concentration Factors

To reiterate, the results discussed above and shown
in Appendices are for values at the surfaces of the panels
above the chosen integration points of the finite elements.
Because of the established behavior of plates containing
holes, the quantities of most interest are the values of
strain at the hole edge at two positions: 90° and 0° to the
axis of the uniaxial load. There are empirical and theoreti-
cal results for the strains at these locations in the litera-
ture, so it is useful to compare the results of these finite

40

element analyses to those found in the literature. Because the empirical results do not specify the precise position at which the strain or stress concentration applies, this investigation assumed that the point of comparison is the midplane of the basic panel. To this end, the output results of the finite element program for the elements of the basic panel were used as a basis for determining the strains at the hole edge. To accomplish this comparison, some means of extending the results from the closest point computed (X/R, Z/R = 1.05) must be used. The technique that produced the most useful results was a simple power curve fit of the three values of midplane strain for the panel elements closest to the hole edge (X/R, Z/R of 1.05, 1.302 and 1.552). The curve fit in all cases was excellent when only three points were used. When additional points were tried, the accuracy of the fit quickly deteriorated because of the generally wavy character of the curve near X/R = 2.0, the vicinity of the reinforcement edge. Values extrapolated to the hole edge using the power curve fit were then used as the numerators for the strain concentration factors, K_{90} and K_0.

Because the different reinforcement configurations caused the strain distributions to be different, a common reference strain, that for the panel without a hole, was used as the denominator in calculating the strain concentration factors. This permitted unambiguous comparisons between the configurations. A panel without a hole, identical in dimensions and physical properties but with fewer finite

41

elements, was analyzed by DIAL and the strain for the mid-plane of an element in a position corresponding to the hole location was obtained. This value of strain (ε_z) was then appropriately factored to represent the strain of a solid panel with the same cross sectional area as the panels containing the hole. The resulting net section strain was used as the denominator of the ratio to compute K_{90} and K_0. The strain concentration factors computed in this way are listed in Table II. Because finite element models tend to be stiffer than actual [Ref. 8], the strain concentration factors produced by this technique were expected to be lower than the actual factors by roughly the same order as the difference in stiffness.

The results of Table II can be used to gain an understanding of the effect of reinforcement on the strain response of the panel. For example, to show the effect of reinforcement height, the values of K_{90} and K_0 are plotted against the number of reinforcement layers in Figure 5 and 6. If configuration (1B) is not considered due to its much larger reinforcement volume, Figure 5 indicates that K_{90} has a minimum value in the range of two to three layers, suggesting that there is an optimum configuration. However, configuration 1 does exhibit the lowest overall values of K_{90}. Figure 6 also shows that the number of layers of reinforcement influences the compressive strain at the hole edge (0° to the load), but the dependence is less clearly defined. In this case, the reinforcements which are both tall and wide seem to

42

TABLE II

COMPUTED STRAIN CONCENTRATION FACTORS

CONFIGURATION	K_{90}	K_0
PLAIN	2.48	-.812
1A	2.30	-.755
1B	2.19	-.717
2A	2.34	-.785
2B	2.27	-.762
3A	2.32	-.774
3B	2.25	-.712
4A	2.33	-.783
4B	2.25	-.762
5A	2.32	-.796
5B	2.25	-.795
6A	2.38	-.788
6B	2.29	-.796

have the lowest value of K_0. Figure 5 also shows several
other items of interest. First, it is apparent that all
subconfiguration B results are lower than for A, and that 1B
offers the greatest potential reduction in strain, with the
reduction being approximately 12% of the plain panel value.
The close grouping of the values for configurations 1 and 5
suggests that increasing the outer reinforcement radius (all
other parameters being the same) has only a slight effect on
the reduction of strain. The results for configurations 3

43

and 4 suggest that the effect of the radii of the layers is not as great as the number of layers in the reduction of strain. As an additional perspective on the results, the value of strain concentration factor K_{90}, representing the maximum value of strain in the panel, is plotted versus the percentage of hole volume of the reinforcement. This result, shown in Figure 7, serves as an approximate measure of the efficiency of the reinforcement. This figure shows that all of the configurations near 100% of the hole volume have virtually the same strain, and that for significant increases in weight (configurations 1 and 3) there is only a small decrease in strain. The most significant feature of all of the above results is the magnitude of the strain reduction caused by the reinforcements. The reduction of strain, based on the linear computer analysis for a relatively light load condition is disappointingly small.
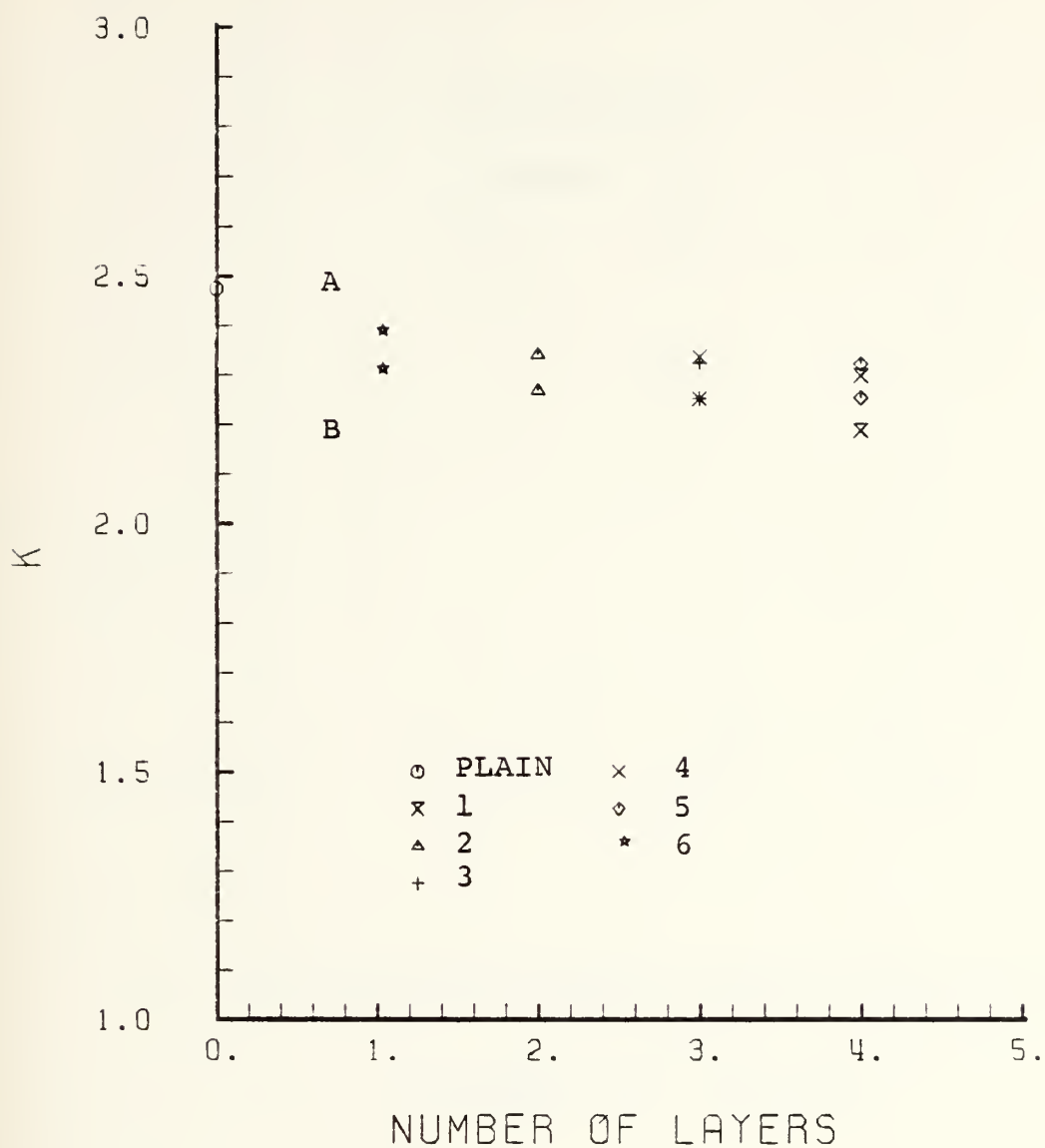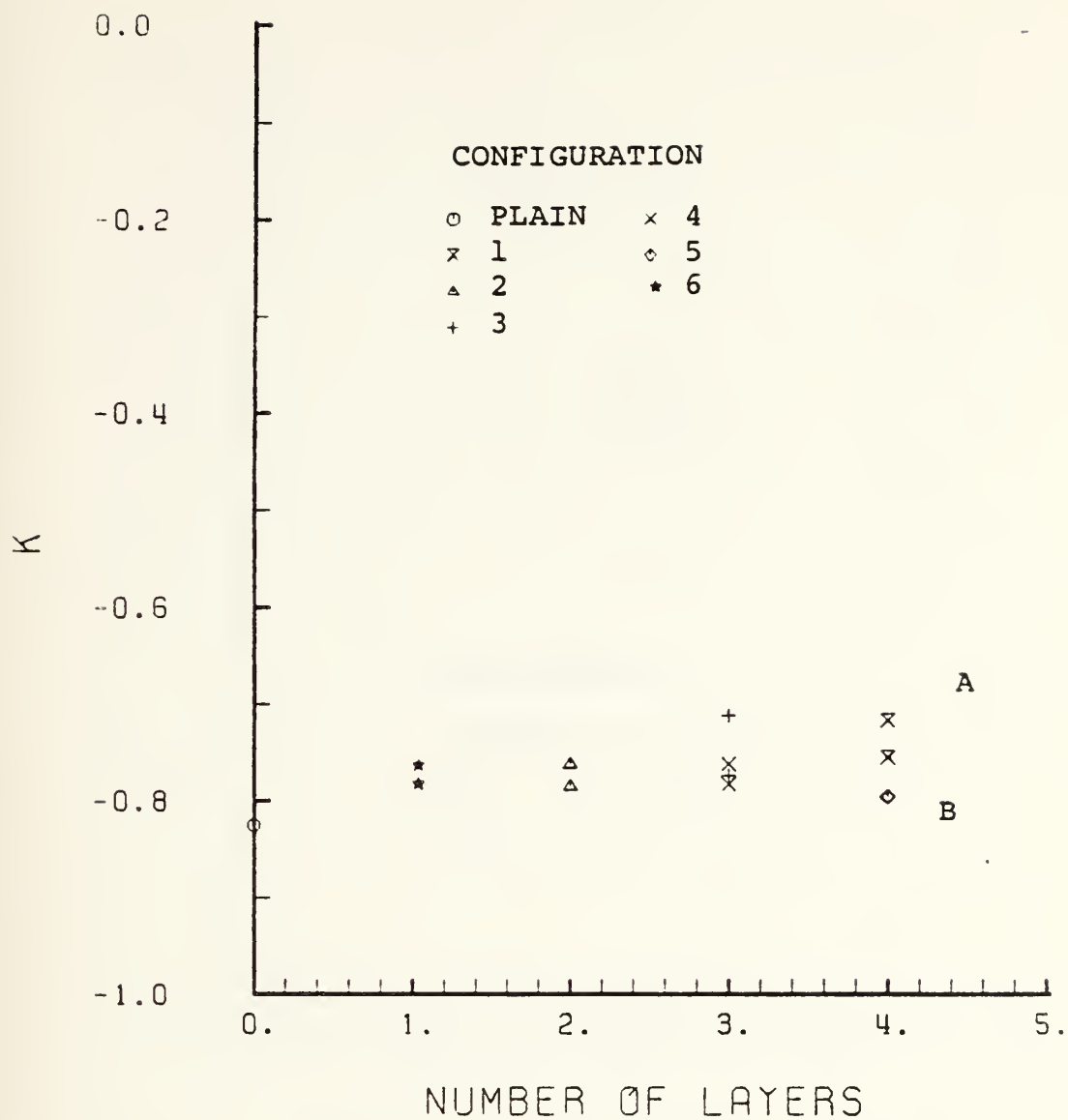
Figure 5. K_{90} vs Number of Reinforcement Layers.
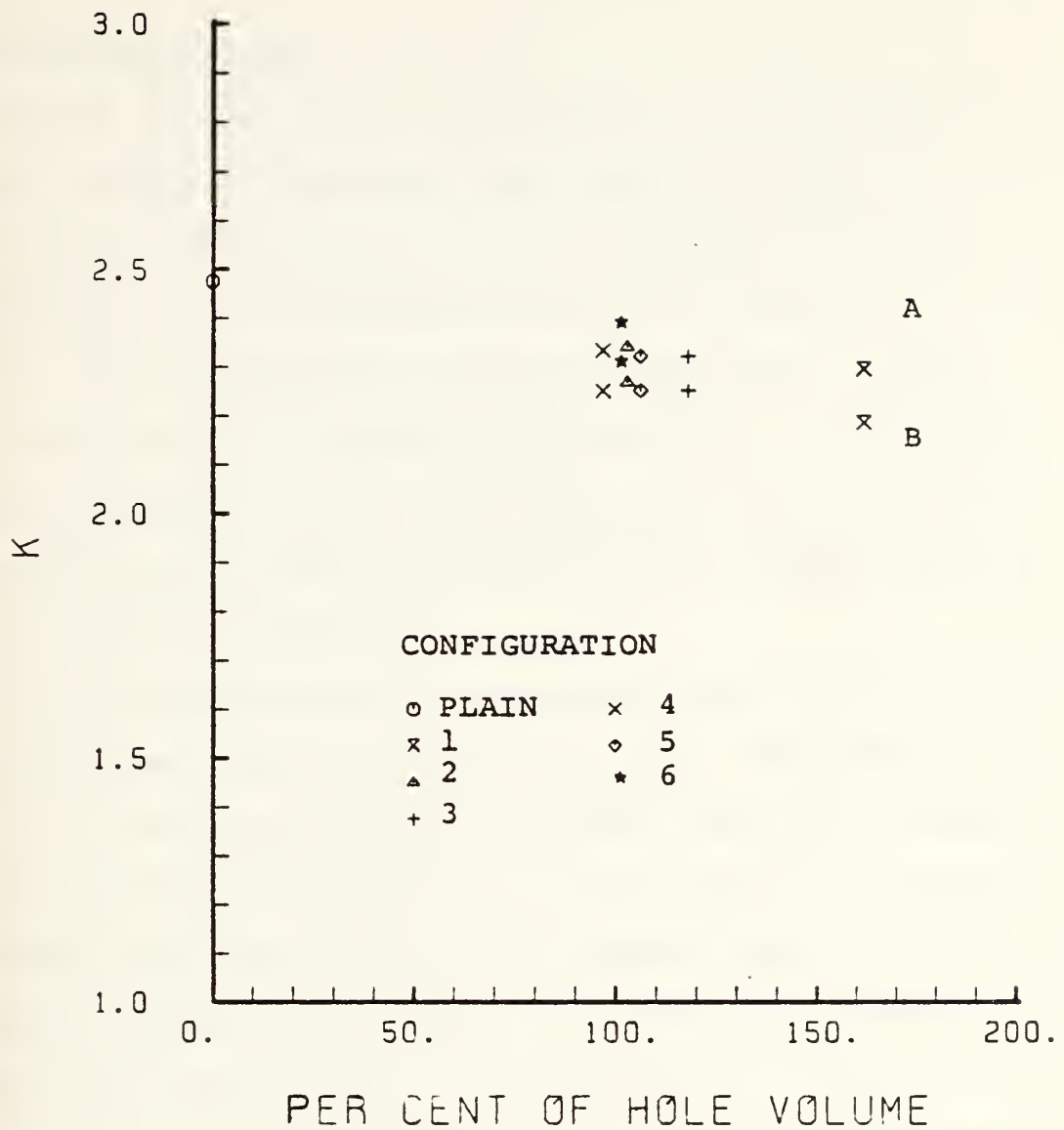
45

Figure 6. Number of Reinforcement Layers.

Figure 7. K_{90} Vs Reinforcement Volume.

47

III. ALTERNATE THEORETICAL ANALYSIS

A. UNREINFORCED PANEL

Because of the lengthy computation time for even as simple as model as described above (up to 1.5 hours of clock time on the mainframe used by the author for the computation of one subconfiguration) it is useful to examine other theoretical analyses to determine if they can produce similar results with less effort. Examination of the theoretical solutions for isotropic and orthotropic plates containing holes will also put the results obtained above in proper perspective.

Stress concentrations in isotropic plates containing holes have been understood for some time. Timoshenko [Ref. 9], extending the work of Kirsch, shows the maximum stress concentration factor, K, to be 3.0 at a location at the edge of the hole 90° from the applied load. The plot of K versus distance from the hole shows the rapid decrease of stress away from the hole. In addition, K is shown to be -1.0 at the edge of the hole at the axis of the load application. Rowlands, et.al. [Ref. 1], show that for a plate constructed of orthotropic laminae with the same dimensional criteria, the stress concentration factors are dependent on the material properties of the laminate. The dependence is of the form

$$K_{90} = 1 + 2\left(\frac{E_{11}}{E_{22}} - \nu_{12}\right) + \frac{E_{11}}{G_{12}} \qquad (2)$$

$$K_0 = -\frac{E_{22}}{E_{11}}$$

Using the material properties for the basic laminae and for the laminate (see Table V and Table VI), the equations above produce the following results

$$K_{90} = 4.106$$

$$K_0 = -.9845$$

Comparing these results to the theoretical isotropic results demonstrates the quasi-isotropic nature of the symmetric layup.

B. REINFORCED PANELS

    1. Empirical Isotropic Approaches

        There are few analytical results for asymmetrically reinforced isotropic panels, but some experimentally derived values of stress concentration factors can be found in the literature. Peterson [Ref. 10] shows results for an unsymmetric circular reinforcement with B/a (reinforcement diameter/hole diameter) and h/t (reinforcement panel thickness/panel thickness) as parameters. These results, for the case where reinforcement volume is 100% of the removed hole volume and the ratio a/t equal to .1883, show the value of K_{90} varying between 2 and 3.0.

Since the panel being modeled and tested is quasi-
isotropic, it is of interest to determine whether or not
these results can be extended to the panel under investiga-
tion, even though the panels do not precisely match all of
Peterson's parameters. If the results obtained by this
approach are sufficiently close to the results of the finite
analysis and are verified by testing, using these results as
a first estimate of the actual behavior of the panel would
seem to be not only attractive, but justified.

To adapt the panel reinforcement cross-sections to
the rectangular form used for the isotropic results, a
simplifying assumption must first be made. Since the actual
reinforcements are layered in steps, the volume of the actual
reinforcement is adjusted mathematically to an equivalent
rectangular cross-section with an averaged radius and identi-
cal volume. With the volume of the reinforcement given by

$$V = \sum \pi t (r_o^2 - r_i^2)$$

the averaged radius is

$$r = \frac{V}{\pi \sum t_i}$$

These equations are used on configurations 1-6 to determine
the parameters B/a and h/t to determine K_{90} from Figure 97
of reference 7. Using the three net section curves shown
to extrapolate a similar curve for a/w = 0.1, values of K_{90}
were taken from the graph and listed in Table III.

50

TABLE III

ISOTROPIC PREDICTION OF K_{90}

CONFIGURATION	VOL	r	B/a	h/t	K_{90}
1	.1429	1.030	2.06	1.5	2.48
2	.0907	1.132	2.26	1.25	2.50
3	.1044	1.020	2.04	1.375	2.48
4	.0852	.946	1.89	1.375	2.46
5	.0934	.979	1.96	1.5	2.47
6	.0880	1.50	3.00	1.125	2.58

There is another set of results for isotropic
material which has ability to account for the roughly
triangular cross sectional shape of the reinforcements
[Ref. 11]. These results, predictions of gross section
stress (strain) concentration at the hole edge, are for
elliptic holes in an isotropic plate for material with a
Poisson's Ratio of .33, quite close to the value computed
for the laminate. The results are for symmetric reinforce-
ments, but can be used for asymmetric reinforcements by
adjusting the cross sectional area by a factor dependent
upon its shape. The specified value of the correction
factor for the roughly triangular shape of most reinforce-
ments is 1/3. The cross sectional area is used along with

the values of major and minor axes of the elliptical hole
(for this case, a = b = 0.5 in) and the thickness of the
panel to form the parameter

$$\frac{A}{(a + b)t}$$

which is the required known value to find the value of K
from Figure 1 of Ref. 10. The cross sectional area A for
use in this approach is given by

$$A = \sum t_i (r_o - r_i)$$

for the configurations under study. Table IV shows the
values of the parameter A/(a+b)t calculated for the con-
figurations and the values of K obtained from the plot of
Ref. 10 and corrected to net section values by the appro-
priate factor, i.e., the ratio of gross and net panel cross
sectional areas. These values are generally lower than
those produced by the previous isotropic prediction.

TABLE IV

ALTERNATE ISOTROPIC PREDICTION OF K_{90}

CONFIGURATION	$\frac{A}{(a+b)t}$	K_{90}
1	0.0833	1.95
2	0.0521	2.37
3	0.0625	2.23
4	0.0521	2.37
5	0.0625	2.23
6	0.0313	2.60

IV.   EXPERIMENTAL METHOD

A.   PANEL SELECTION AND CONSTRUCTION

The particular layups for the basic panel and reinforce-
ment configurations analyzed above were dictated in part by
considerations involved in the experimental portion of this
investigation. In addition, as previously noted, quasi-
isotropic panels are the most frequent topics of other similar
investigations in the literature. The use of such panels in
this investigation permitted comparison of the results with
these other investigations. The use of a quasi-isotropic
layup also has the following advantages:

    1)   residual stress from curing are minimized, if not
eliminated.

    2)   the layup minimizes the out of plane deflections
under loading of the basic panel, which reduces the
chance of masking deflections produced by the assym-
metric reinforcements to be tested.

The particular choice of an eight layer $[0/+45/-45/90)]_s$
layup was the result of two considerations. First, this
is a universally employed and easily duplicated layup.
Second, using eight layers produces a laminate of significant
strength. This high strength permits high test loads, which
in turn reduce the magnitude of potential experimental errors,
such as small load fluctuations, in relation to the total
load. This reduction of the error fraction has obvious
benefits for the accuracy of the experiment.

Because of the limited scope and resources of this investigation, the number of panels selected for testing was restricted to five configurations. First, to establish a baseline for strain behavior and ultimate strength for the laminate, a basic panel without a hole was used. This configuration, tested twice for reliability, was also the means used to verify that the test apparatus applied an evenly distributed load across the panel. The second configuration was the basic panel with a hole, also tested twice for reliability. This configuration was the baseline for strain behavior in the vicinity of the hole for the unreinforced configuration.

The last three configurations, each single tests, were three of the reinforcement configurations analyzed in the Computational Analysis section above. Rather than concentrate only on those configurations which achieved the lowest strain concentration factors, the experimental investigation considered the full spectrum of the results of the analysis by testing configurations 1B, 3B and 6B. By examining the response range of these three configurations and comparing the experimental results to the corresponding finite element predictions, more information could be gained about the analysis and the potential effects of the reinforcement parameters on the computed results. These three configurations were chosen because they represented the widest spread of the number of reinforcement layers, outer radius of the

54

reinforcement and volume of the reinforcement. All of the test panels were tested to failure to reveal potential non-linear effects or degradation of performance caused by bending of the reinforcements at loads above the analysis load.

The physical dimensions of the panel (shown in Figure 8) were the result of two considerations: limitations placed on the panel size by the test apparatus, and requirements dictated by the choice of hole diameter. Because of the well known variation of strain concentration factor with hole size [Ref. 12], a diameter of 1 inch was used to avoid these effects. The chosen diameter is also representative of the potential applications mentioned previously. With this chosen diameter and the first estimates of reinforce-ment diameter, the 10-inch width of the panel provided more than the 5 to 1 panel width to hole diameter ratio suggested by Timoshenko [Ref. 8]. The twenty-inch untabbed length of the panel was intended to provide sufficient distance for uniform load distribution. The width of the tabbing provided sufficient distance for load diffusion into the panel.

The material properties of the HMF 330/34 graphite epoxy cloth used for the preliminary design calculations and the finite element analysis of the panels are listed in Table V. In addition to these values of laminae strength, carpet plot data for HMF 330/34 laminate properties are also available. Table VI shows the values for the basic quasi-isotropic

55

Figure 8. Test Panel Dimensions.

laminate. The ultimate strength predicted by similar
carpet plot data for uniaxial loading is approximately
60,000 psi, which for the basic panel corresponds to a
tensile load of approximately 67,000 pounds. All data
used in the tables below were furnished by Lockheed
Missiles and Space Co., which manufactured the panels
tested.

TABLE V

MATERIAL PROPERTIES OF HMF 330/34

ROOM TEMPERATURE DATA NOT COMPENSATED FOR MOISTURE DEGRADATION

TENSION

E^{11} 11.1 msi E^{22} 10.4 msi

COMPRESSION

E^{11} 9.5 msi E^{22} 8.9 msi

SHEAR

G^{12} 1.0 msi
interlaminar shear   150 ksi

ADDITIONAL PROPERTIES

α^{11} 1.6 $\mu in/in/^{O}F$
α^{22} 2.0 $\mu in/in^{O}F$
density   .056 lb/in^3

TABLE VI

QUASI-ISOTROPIC LAMINATE PROPERTIES

For 50% $\pm 45^\circ$ Plies

E^{11}	8.15×10^6 psi	12	0.31
E^{22}	7.9×10^6 psi		
G^{12}	2.7×10^6 psi		

B. TEST APPARATUS

A Riehle PS 300 Test Machine was used to apply the
uniaxial tensile loading to the experimental panels. The
concentrated applied load was diffused through the panel
by a whiffle tree, shown in Figure 9. Because of the large
load needed to test the panels to failure, it was necessary
to apply the load through the four bolts at the upper edge
of the plates and diffuse the load through the plates by
the eight lower bolts which pass through the tabbing of the
panel. The eight lower bolts were torqued to a moderate
value (90 in-lbs) and the faces of the plate which mate to
the fiberglass tabbing were checkered to insure that the load
diffused completely into the tabbing and the panel. The
whiffle tree was designed to withstand a load 1.5 times
greater than the anticipated failure load of approximately
67,000 pounds for the basic panel without hole or reinforce-
ment. All parts of the whiffle tree were constructed of 4130
steel and all bolts were close tolerance high strength bolts.
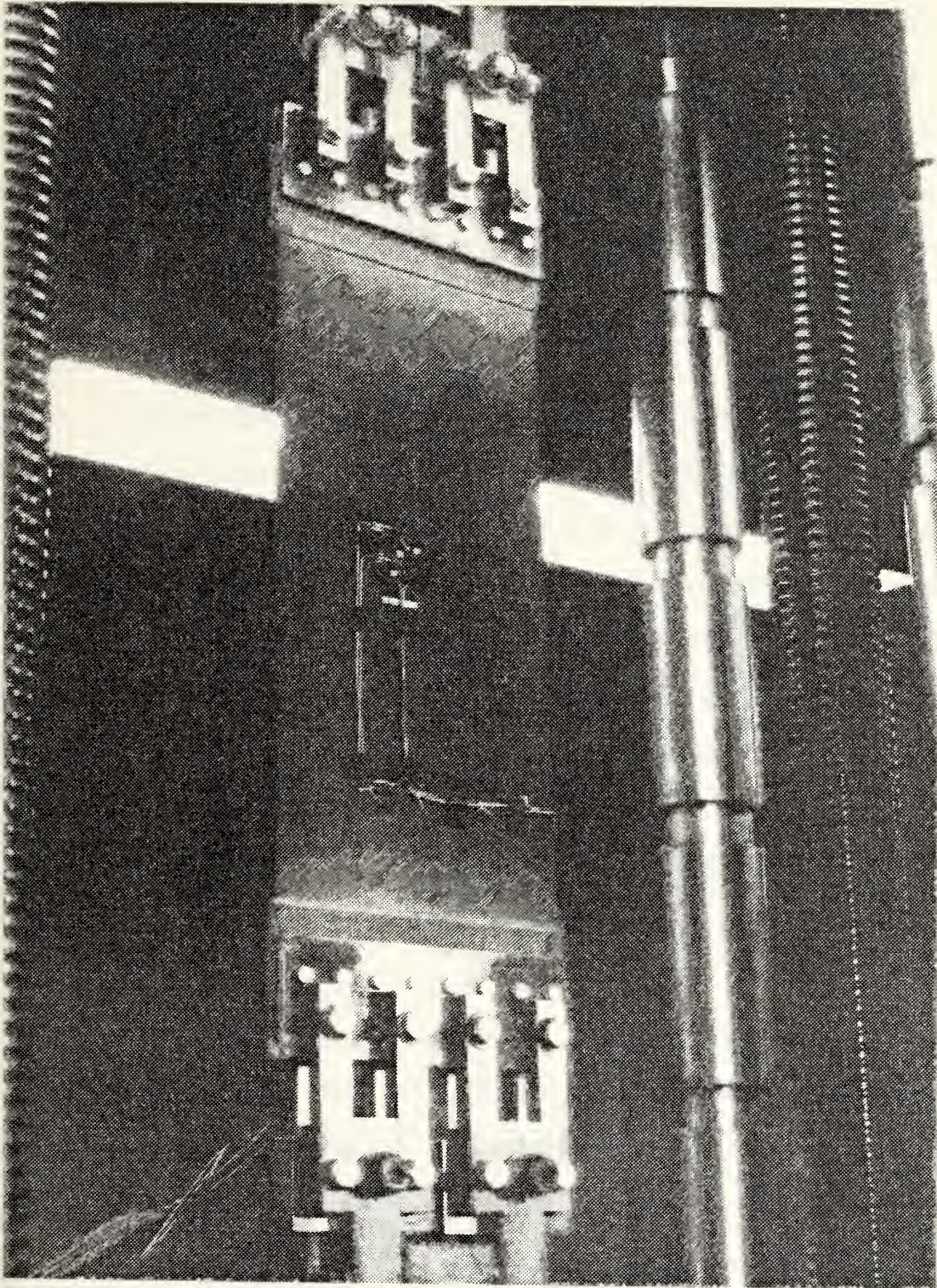
Figure 9. Experimental Apparatus.

Strain gauges were used to record the response of the panel to the loading. Other methods such as photoelastic coating techniques were not used because of the risk that the slight reinforcement from those materials could change the actual behavior of the asymmetric reinforcement from that which would occur in the absence of the coating. In addition, because of the nature of the panels to be tested, only the unreinforced side of the panel could have been coated. This would then have had to be considered in the analysis of the panels. This additional effort in the analysis was thought to be an unnecessary complication.

Because of the rapidly changing strain states near the edge of the hole, small single element gauges (120 ohm) were used to enable close grouping. A total of twenty-one gauges, including 3 gauges in one rectangular rosette, were arranged as shown in Figure 10. Because of the symmetrical nature of the loading of the panel, all gauges on the same side of the hole were oriented in the same direction and different sides of the hole had different gauge orientations. In addition, gauges were mounted tangentially to the hole edge at different orientations to the load axis to investigate the behavior of strains at those locations. Three gauges were placed on the back of the panel at the most likely locations of out of plane deflections, at orientations of 0°, 45° and 90^9 to the load axis (gauges 19, 20, 21).
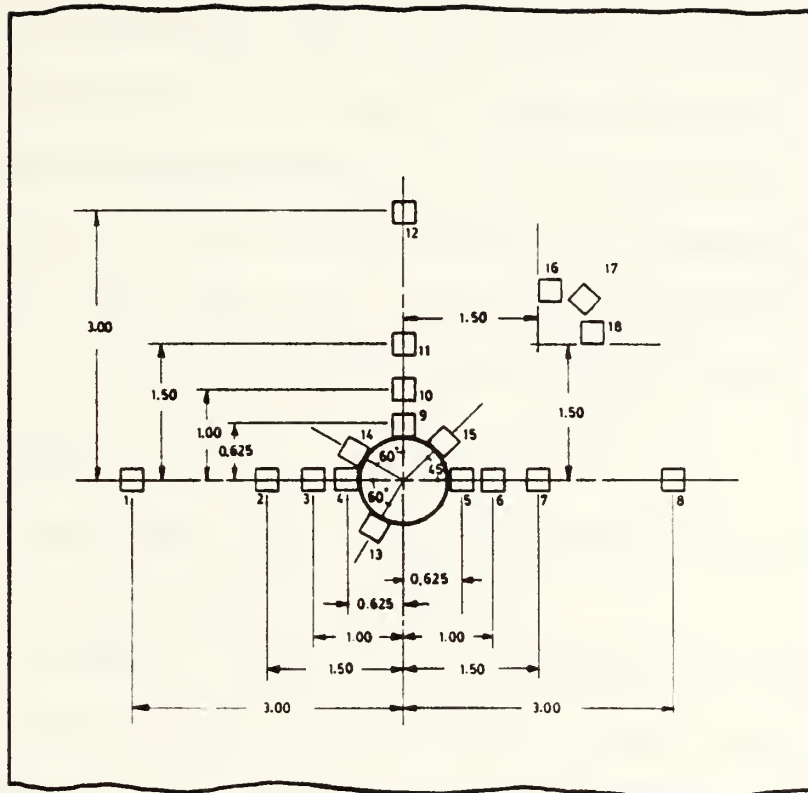
NOTE: Gages 19, 20, 21 directed behind gauges 5, 15, 9 on unreinforced surface.

Figure 10. Strain Gauge Placement On All Panels.

61

The strain gauge measurements were made using a Vishay Measurements Group System 4000. This system consists of a controller, 5 Measurements Group Model 4270 Strain Gauge Scanners mounted in parallel (100 channel capability), a Hewlett Packard 9825T desktop computer and software to operate the system. The software is capable of assigning a channel for automatic temperature compensation, configuring any channel for differing types of strain gauges or sensors, incorporating calibration data, gauge factor, transverse sensitivity coefficient, and material property definition. The system records and reduces all zero readings and all subsequent readings which can be manually or automatically initiated. For this experiment, only manually initiated load readings were used as discussed in the section below.

C. TEST PROCEDURE

To obtain the experimental data for each of the panels tested, the following steps were used:

1. With the panel attached to the whiffle tree and hanging in the Riehle machine, strain gauges connected to the scanners and system 4000 up and running, zero readings were taken.

2. The whiffle tree was then clamped into the lower set of jaws and the panel was subjected to small tensile loads (1000 lbs) for several cycles until the strain readings for two cycles were virtually the same.

62

3. The lower jaws were released and a new set of zero readings were taken and recorded.

4. The lower jaws of the Reihle were reclamped onto the test item.

5. The load was raised to and held at predetermined levels and strain readings were recorded for later reduction.

6. At several points, strain readings were printed out. Based on these results, the subsequent load increments could be changed to obtain more readings before the anticipated failure.

7. As the loading progressed, significant events such as fiber cracking and noticeable deflections were recorded in writing and photographically.

8. Testing proceeded until total failure of the panel was achieved.

9. All collected data were reduced and printed; additional photographs of the failed panel were obtained.

V. EXPERIMENTAL RESULTS

A. UNREINFORCED PANEL

The experimental results for the two panels without holes established the baseline behavior of the laminate without reinforcement. These results confirmed that the strain response of the panel is linear up to the point of failure, with an average failure load of 65,000 lbs. The strain (ε_z) for a 10,000 lb load was recorded and corresponds to 1515 μ_s for the net section of the panels with holes. This is approximately 18% higher than the value for panel strain based on the DIAL output.

The two basic panels with holes were tested to failure and produced consistent results. Their ultimate tensile loads varied slightly, with panel 1 failing at 35,000 lbs (34,700 psi based on net section) and panel 2 failing at 37,000 lbs (36,700 psi). Failure was preceded by audible fiber cracking beginning at approximately 18,000 lbs with increasing intensity and frequency up to total failure. Both panels failed very rapidly, with no visible deformation or damage prior to failure. The edge of the hole at the fracture showed signs of delamination just inside both surfaces of both panels. The panels failed at the edge of the hole 90° from the load through the horizontal axis of symmetry, with the fracture continuing in a nearly straight line to the side edge. The response of the strain gauges for

both panels was linear up to the point of failure, and corresponding gauge readings for the two panels showed insignificant variation. Figures 11, 12 and 13 show the experimental measurements and computational predictions for ε_z and ε_x vs X/R and Z/R for a 10,000 lb tensile load. The values shown are the actual strains plotted at the positions corresponding to the location of the middle of the gauge. In general, the experimental values show excellent agreement with the analysis, particularly close to the edge of the hole where the geometric size of the elements was smallest. To underscore the linearity of the strain response and the absence of significant warping of the panels, Figure 14 shows the strain readings for one pair of corresponding gauges (5 and 19) on the front and back surfaces of the panel 90° from the load axis. Similar gauge pairs at locations 45° and 0° from the load axis produced similar results (Appendix A, Figures 31 and 32).

B. REINFORCED PANELS

The reinforced panels which were tested (configurations 1B, 3B and 6B) had several aspects in common with the basic panel results. During the tests, none of the reinforced panels showed observable deformation or visible damage prior to failure. The reinforced panels also had the characteristic fiber cracking noises. The onset of audible fiber cracking appeared to be delayed slightly, beginning at loads approximately 21,000 to 23,000 lbs, depending on the configuration.

65
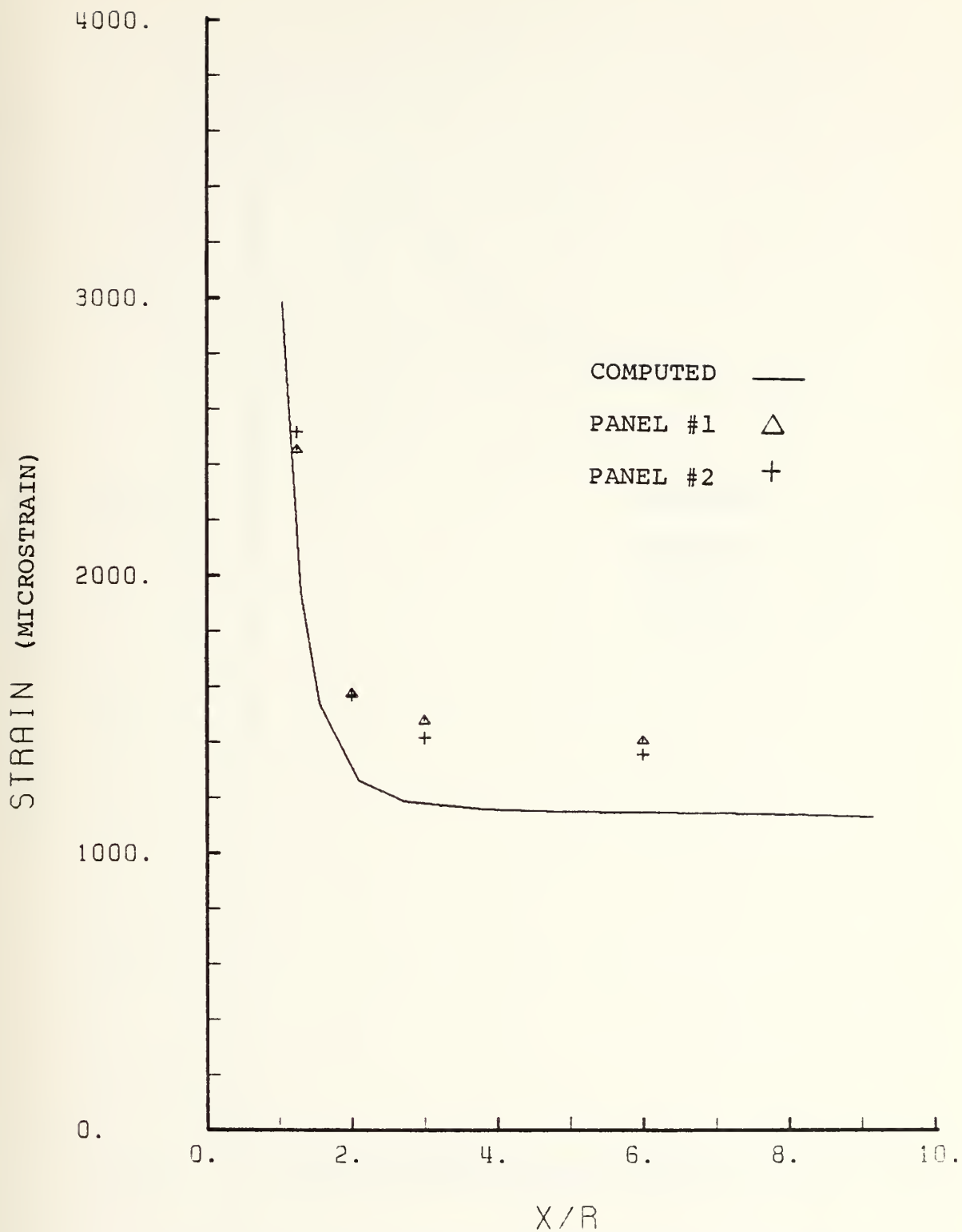
Figure 11. Comparison of Computed and Measured
Strains ε_z vs X/R Basic Panel.
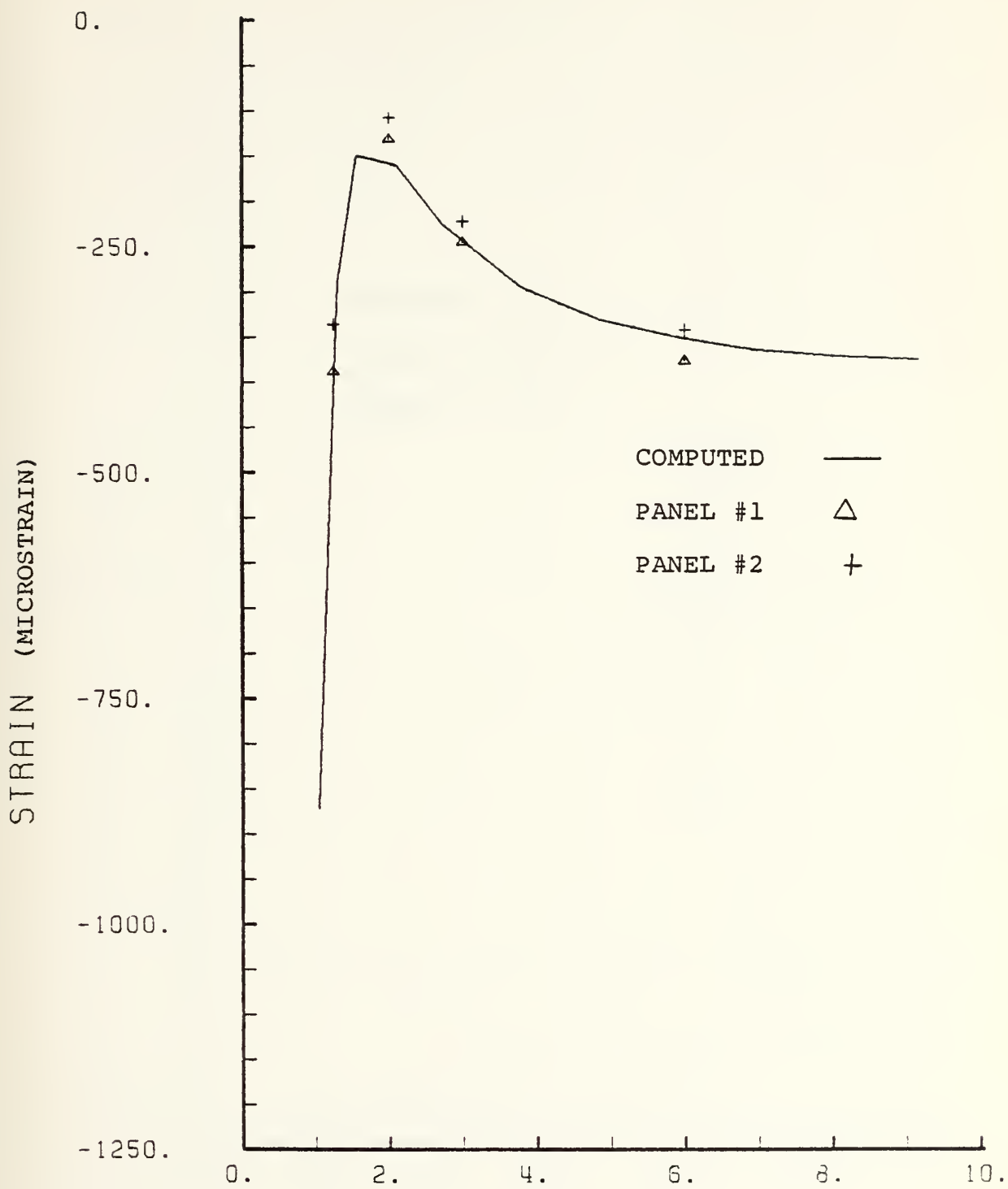
Figure 12.   Comparison of Computed & Measured
Strains ε_x vs X/R - Basic Panel.

67
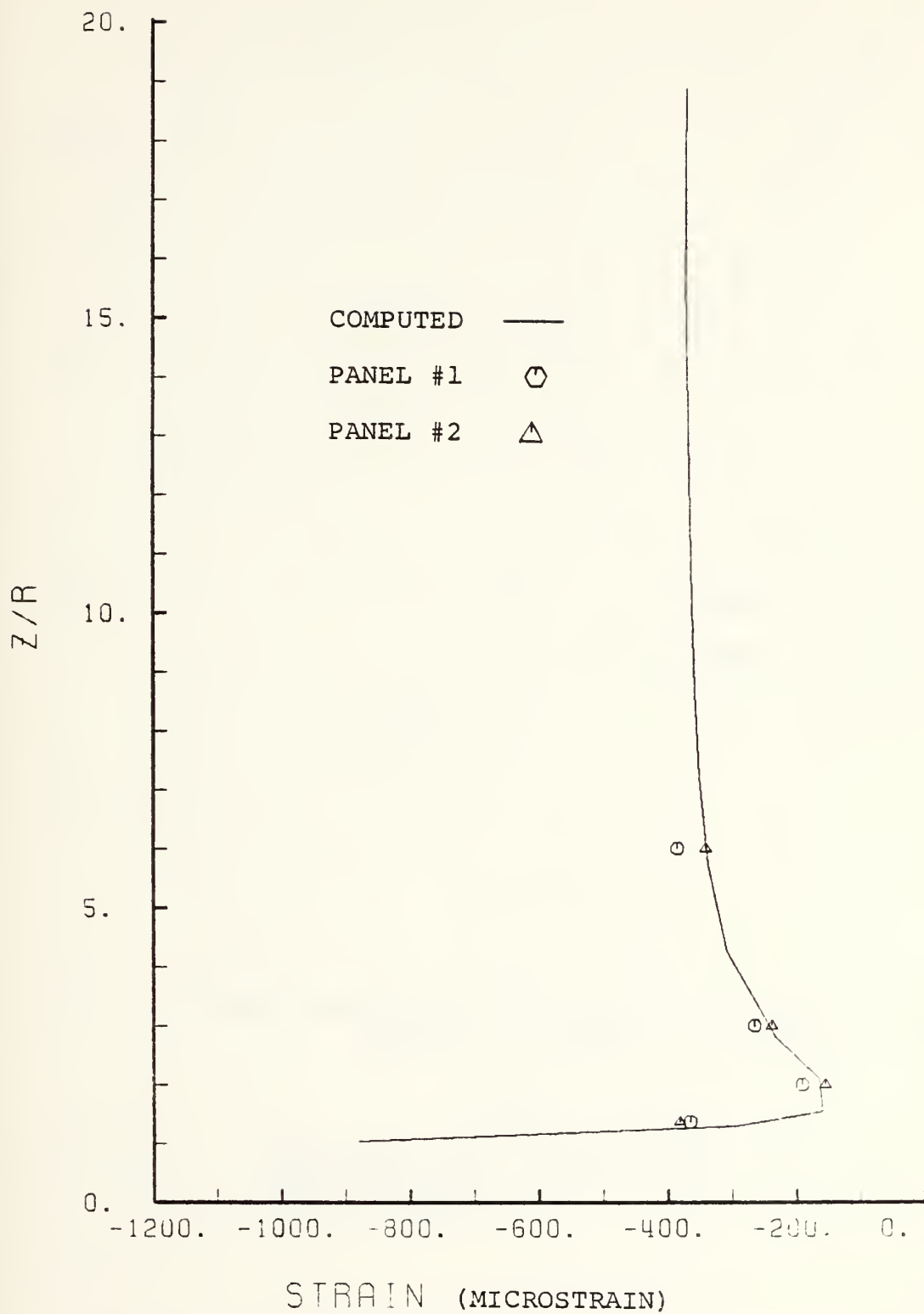
Figure 13. Comparison of Computed and Measured
Strains ε_x vs Z/R - Basic Panel.
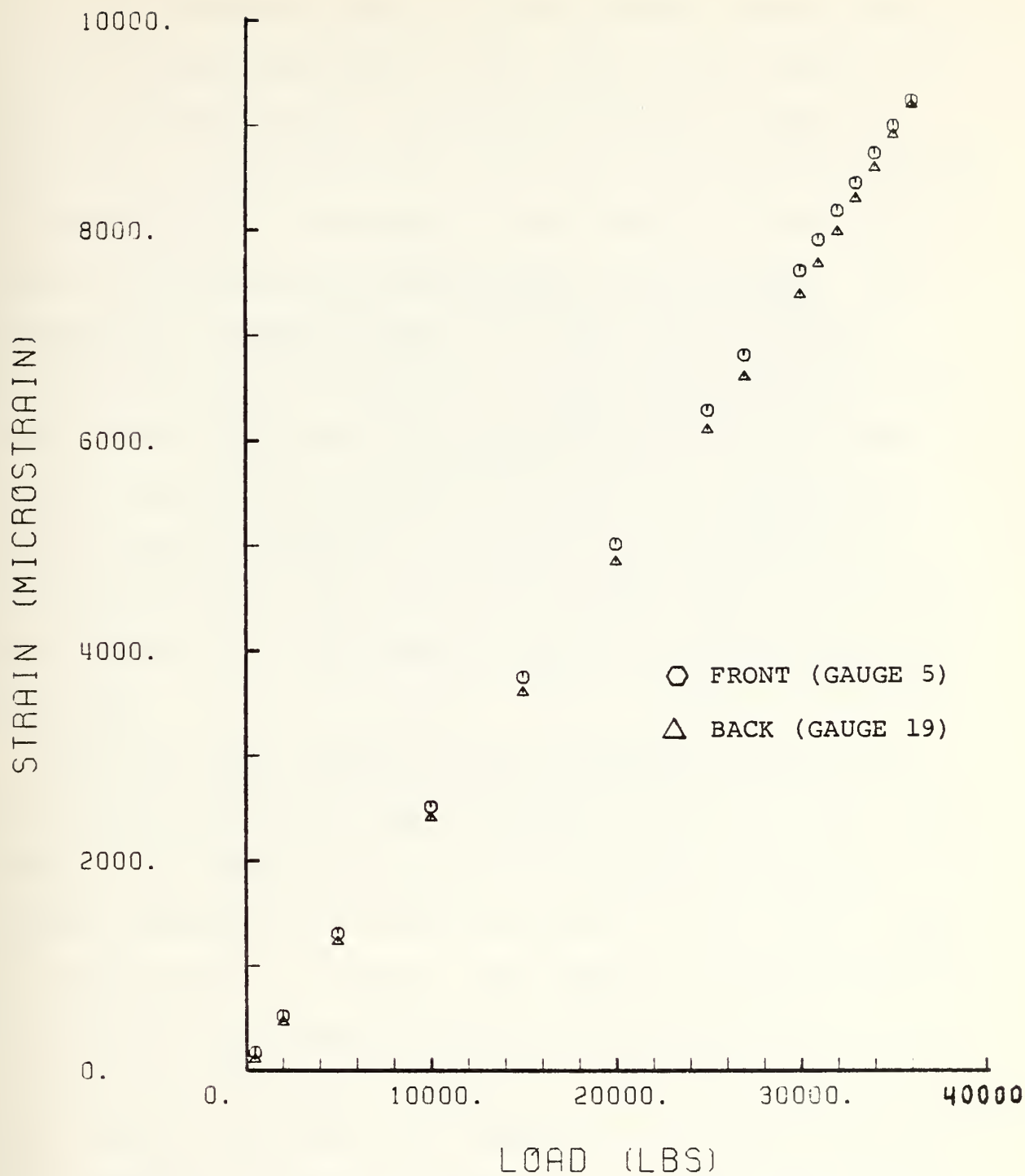
Figure 14. Comparison of Front and Back Strain 90°
From Load Axis - Basic Panel
Gauges 5 and 19.

All of the reinforced panels failed virtually instantaneously and the fracture appearance in all cases failed identical to that of the basic panel. A typical fracture is shown in Figure 15. In addition, all reinforced panels showed evidence of delamination in the region of the fracture, both at the edge of the hole and at the side edges of the panels. The delamination extended roughly 10° either side of the 90° position and was most severe in the two layers closest to the front and back surfaces. The comparisons of measured and computed strains for a 10,000 lb tensile load (Appendix B, Figure 48 to 50; Appendix D, Figures 75 to 77; Appendix G, Figures 123 to 125) show the same agreement seen in the basic panel results, with the closest agreement occurring near the hole edge.

There are some results for the reinforced panels which have both similarities to and differences from the basic panel results. One example of this is the behavior of strains measured tangentially at the hole edge 0°, 30°, 45°, 60° and 90° to the axis of the load. The tangential strains measured for the basic panel and reinforced configurations for a load of 30,000 lbs are shown in Figure 16. The basic panel strains show a smooth transition from compressive to tensile strains, very similar to results in section 2.5.1 of [Ref. 13]. The unreinforced panel has the highest value of tensile strength at the edge of the hole 90° from the load. This plot also shows that the strains for all configurations are very similar

70
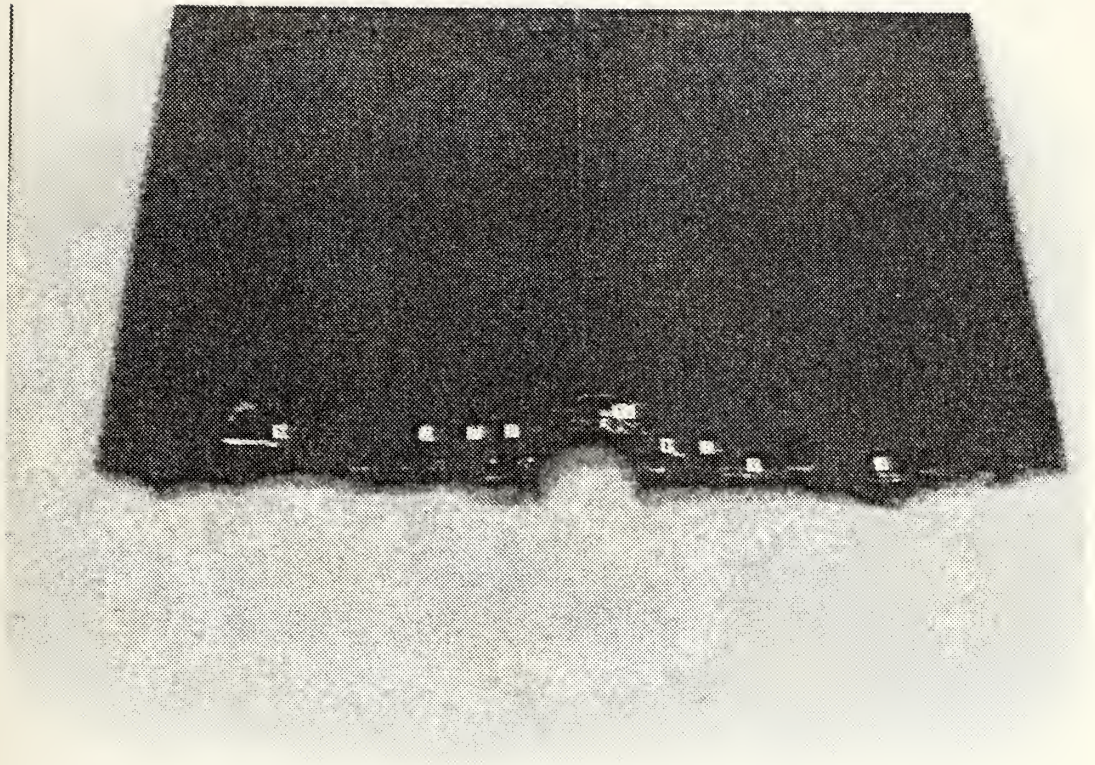
Figure 15. Typical Panel Fracture.
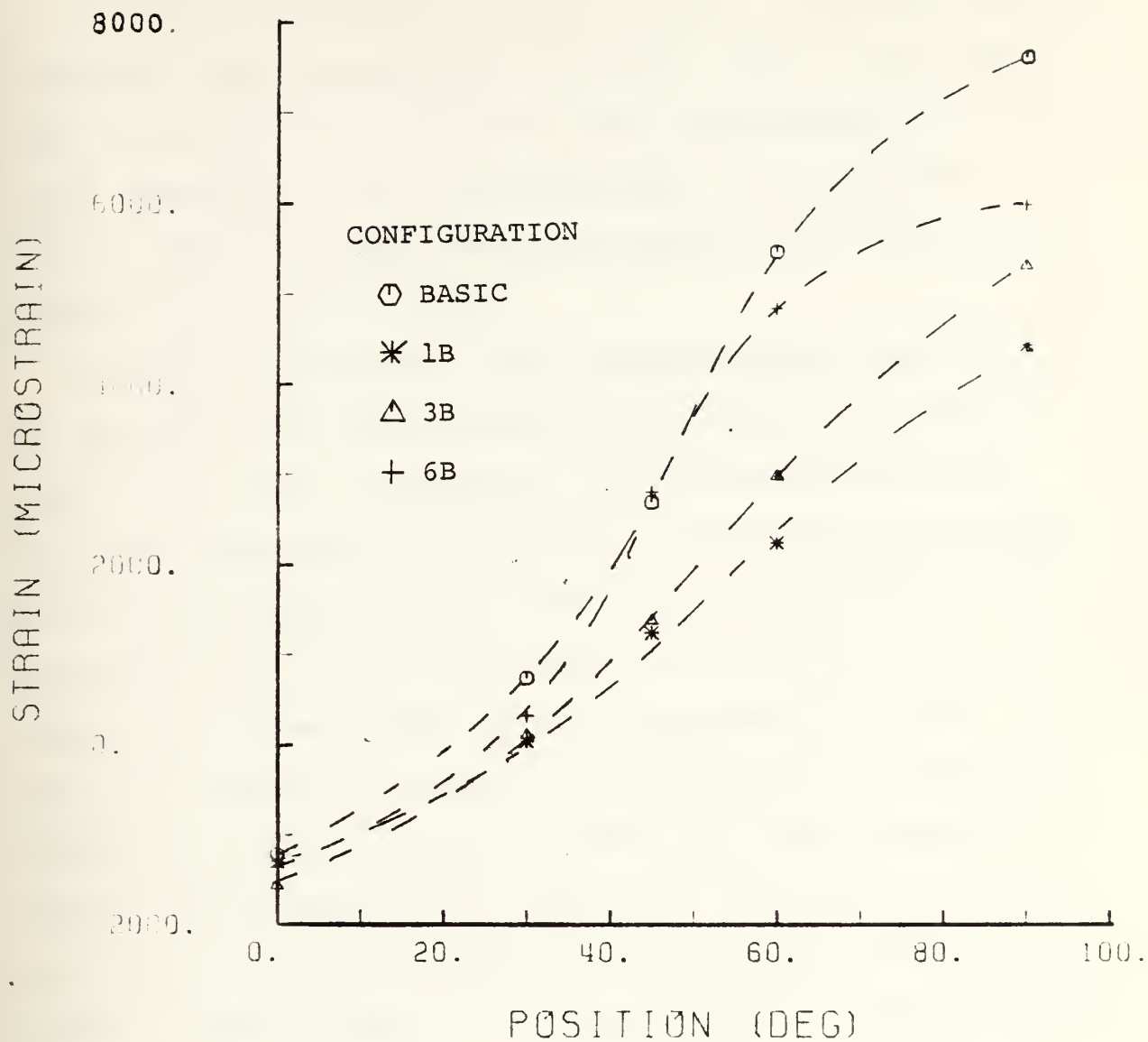
Figure 16. Measured Tangential Strains at
The Hole Edge For a Load of 30,000 lbs.

72

at the top of the hole (0° to 30°) but they begin to separate in the region of increasing tensile strain. In addition, the reinforced panel strains are reasonably close to the basic panel strains at the top of the hole, and then increase more slowly (depending on the configuration) than the basic strains, with the widest separation between all the results occurring at the 90° location.

The added thickness of the reinforced panels permitted the inclusion of a gauge mounted in the hole at the edge 90° from the load axis, to measure ε_z at the exact hole edge. The strain measured by this gauge was included in the comparisons to the computed strains (see plots of ε_z vs Z/R in the Appendices) and in all cases appears to be close to the average of the two surface strains (extended to Z/R=1). To study the behavior of strain at the hole edge, the measured strains for all three configurations are shown plotted against the applied load in Figure 17. The plot indicates that there is a slight difference in stiffness between the configurations and that all the panels behave nearly linearly. At loads above 27,000 lbs, Configurations 1B and 3B show a slight increase in slope of the data points, indicating that some stress relief was occurring around the hole. This stress relief, described in [Ref. 14], is caused by microfailures of fibers, usually in regions of maximum strain. In addition, both configurations show values of strain in excess of 10,000 μ_s (or 1% strain), which is the generally accepted limit of strain for this material.
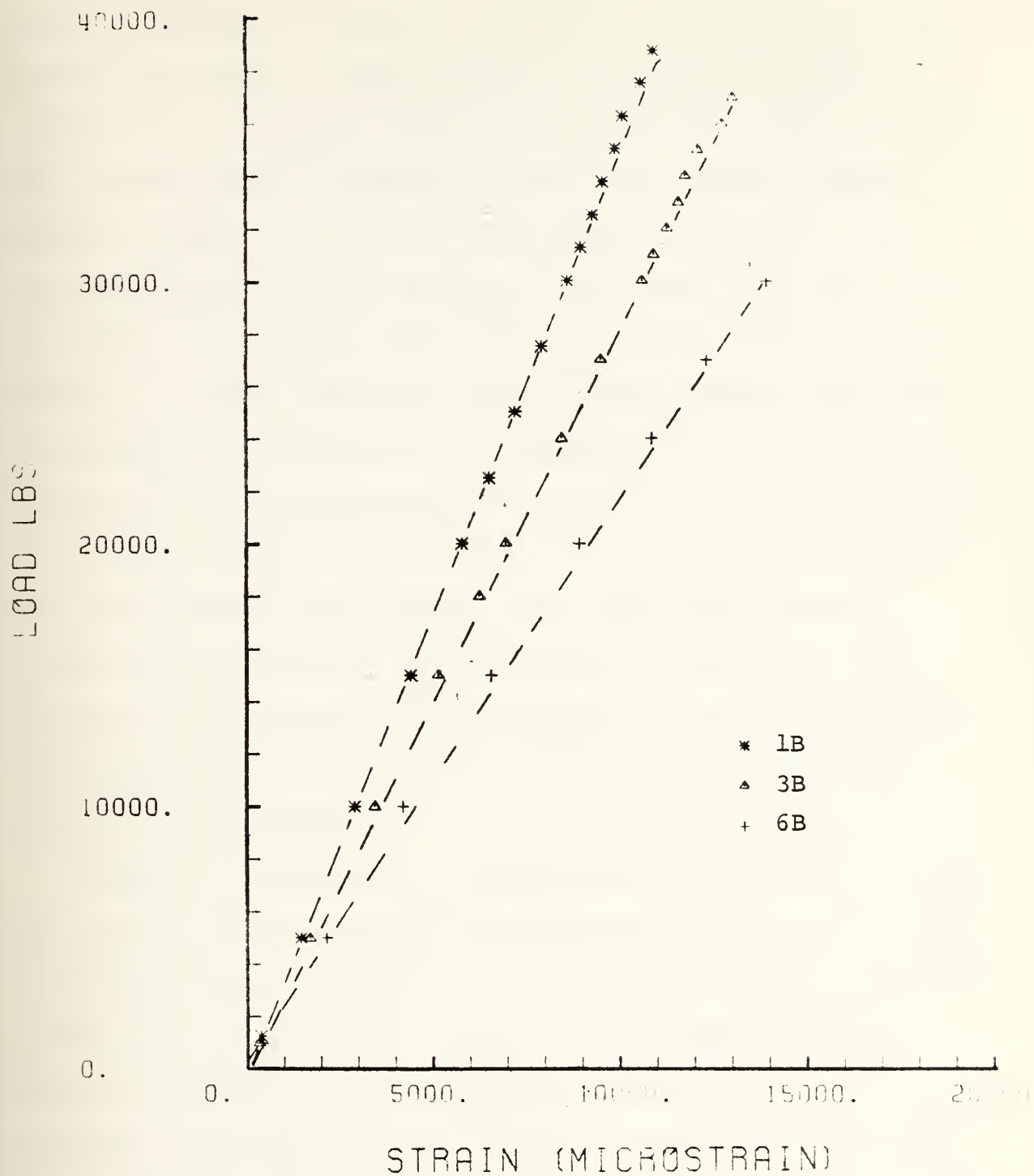
Figure 17. Strain ε_z vs Load at Hole Edge.

74

There are some results for the individual reinforced panel configurations which are unusual and important. The panel reinforced by Configuration 1B failed at a load of 39,500 lbs, an increase of 10% over the basic panel average. The surface strain recorded for the back surface (maximum) before failure was 6400 μ_s, significantly below 1%, while the strain measured in the hole at the edge was greater than 1%. This could signify that the strain is changing very rapidly away from the hole, more so than for the other configurations. Figures 45 to 47 (Appendix B) show the strains on the front and back surfaces at the hole edge 90°, 45° and 0° to the load axis. These plots show major variation with the corresponding basic panel plots, and show that the region most affected is the region 45° to the load. This plot has particularly large differences in values of points and the apparent slopes of the curves, compared with the other configurations.

The panel reinforced by Configuration 3B failed at 38,000 lbs, with a failure strain of approximately 10,000 μ_s (1%) on the back surface at the hole edge and over 13,000 μ_s recorded by the gauge in the hole. Figure 78 (Appendix D) shows a smaller variation in strain between the surfaces 90° to the load than Configuration 1B. Figure 79 (Appendix D) for the strains 45° to the load again shows a large difference in the values and slopes between the surfaces. In addition, there is a distinguishable nonlinear region close to the failure load.

The panel reinforced by Configuration 6B also failed at 38,000 lbs with the back surface strain measured in excess of 10,000 μ_s (the gauge in the hole failed well below the failure load). The front and back strain comparisons (Figures 126 to 128, Appendix G) show very little difference from the corresponding plots for the basic panel.

To summarize the experimental findings, the relevant results for all panels with holes are collected below in Table VII. The last column contains the ratio (P/P_0) of the panel failure load to the failure load for the same sized panel without a hole.

TABLE VII

EXPERIMENTAL FINDINGS

PANEL	FAILURE LOAD (LB)	EDGE FAILURE STRAIN (gauge 22) μ_s	SURFACE FAILURE STRAIN (gauge 19) μ_s	$\dfrac{P}{P_0}$
BASIC #1	35,000	10,000[1]	9300	.54
BASIC #2	37,000	10,000[1]	9400	.57
1B	39,500	10,000	6500	.61
3B	38,000	12,000	10,000	.58
6B	38,000	13,000	10,000	.58

NOTE [1]: Estimates based on extrapolation of experimental data.

C. EXPERIMENTAL DETERMINATION OF K_{90}

For comparison to the experimental results, the value of strain concentration factor, K_{90} was computed from the experimental results. The value of strain for the laminate without a hole was obtained from the plain laminate tests described above, with the value cited on page 64 for strain (ε_z) used as the constant reference strain. Because the basic (unreinforced) panels had no gauges mounted in the hole to measure ε_z at the edge, a curve fit analogous to the method used in the Computational Analysis section was employed. Using strain readings for the first three gauges for ε_z along the X axis (5-8), at a load of 10,000 lbs, the strain at X/R = 1 was computed and used to determine K_{90} for the basic panel. For the reinforced panels, the value of strain recorded by the gauge in the hole at the same load was taken to be the strain at X/R = 1 for the midplane of the panel. The strain concentration factors computed with these results are listed in Table VIII.

TABLE VIII

EXPERIMENTALLY COMPUTED VALUES OF K_{90}

Configuration	K_{90}
Basic	2.42
1B	1.96
3B	2.28
6B	2.78

VI. DISCUSSION OF RESULTS

A. COMPUTATIONAL RESULTS

The computer analysis for the basic panel and reinforced configurations indicated that the strains and curvatures near the hole edge had characteristics which were dependent on the configuration geometry and the layer orientation. The output from DIAL showed that the values of panel element midplane strain at the Gaussian quadrature point closest to the hole edge varied from 2987 μ_s (basic panel) to 2631 μ_s (panel 1B) for ε_z and -1032 μ_s (panel 1A) to -725 μ_s (panel 1B) for ε_x. The curvature k_z which contributes to ε_z at the surfaces of the panel was in all cases for the B subconfigurations greater near the hole edge, and decreased uniformly with distance from the hole. For the A configurations the value of k_z was typically 15-20% less than that for the B configurations at the hole edge. While the A configurations showed a roughly exponential decrease with distance from the hole, the B configurations had a local minimum of k_z around $X/R = 1.3$. The other curvatures, k_x and K_{xz} were larger in all cases for the A subconfigurations than for B, but often included changes in sign (sense of the curvature) with increasing distance from the hole and for corresponding locations of the subconfigurations.

The increased curvature (k_z) for the B subconfigurations would seem to dictate higher maximum surface strains for those cases. However, the higher surface strains which would be expected do not develop because the midplane strains for the B configuration are less than those for the A configurations. The lower strain computed for the B subconfigurations have a greater number of $0°$ fibers (the load direction) causing the panel to be stiffer with respect to the $0°$ unidirectional tension load applied. This result is consistent with the findings of [Ref. 2], which shows that the hole gets 'softer' with additional $45°$ plies. Therefore, even though the panel deflections and curvatures are greater for the B subconfigurations, the value of K_{90} is based on the strain of the midplane of the panel element.

Because the critical factor during panel testing appeared to be the maximum strain (ε_z) occurring on the back surface, the method of calculating the strain concentration factor was reconsidered. A second series of calculations were carried out which took the DIAL output and computed the strains at the midplane of the outer laminae of the back surface (.049 inch from the panel centerline) again using Equation 1. Using the same procedure as before, an identical curve fit was used to extend the computed results to the edge of the hole for comparison to the experimental results. The results for K_{90} are shown in Table IX. From these results, panel 1B would seems to have the highest strain at the back laminae and

presumably would fail first, followed by panels 3B and 6B. As described in the experimental findings, this is the reverse of what actually occurred.

TABLE IX

STRAIN CONCENTRATION FACTOR BASED ON MAXIMUM STRAIN

CONFIGURATION	K_{90}
1A	2.632
1B	2.626
2A	2.583
2B	2.569
3A	2.613
3B	2.601
4A	2.616
5B	2.617
5A	2.647
5B	2.626
6A	2.534
6B	2.522

To briefly explore the effect of reinforcement shape on the results, a computational analysis was completed for a one layer square reinforcement to be compared to Configuration 6. The square patch was sized to have a volume equal to that of the hole and had 2.625 inch sides. The patch was oriented so that the distance along the X and Z axes was 1.3125 inches and the sides of the square were perpendicular to the axes. Computations identical to those performed in

the Computational Analysis section were performed. The results indicated that the strains, curvatures and deflections for the square patch and circular patch were virtually identical. To verify these findings, a panel with the square patch reinforcement was tested. The failure load, strains at 10,000 lbs and the failure appearance were nearly identical to the circular patch results. These limited results seem to indicate that the planform shape of the reinforcement has limited effect on the strain response of the panel.

The effect of symmetry was also briefly explored by modelling two symmetric circular reinforcements similar to configuration 6 for analysis. The first model was identical in the material and outer ring radius to configuration 6 with a one layer reinforcement 1.5 inches in radius added to both sides of the panel, with a reinforcement volume of 200% that of the hole. The other model used one layer reinforcements on both sides with a radius of 1.125 inches to create a reinforcement with a volume equal to that of the hole. The same method of analysis was used and the same output generated by DIAL. As for the unreinforced panel, the curvatures were reduced to the order of 10^{-10}, with virtually no out of plane deflections. The value of ε_z at the edge of the hole (using the same curve fit) for the large symmetric reinforcement was computed to be 2691 μ_s, which gave this reinforcement a strain concentration factor of 2.09. This represents an improvement of 15% over the basic panel and 25% over the results for configuration 6B. The smaller reinforcement had

81

similar results, with a value of ε_z at the hole edge of
2752 μ_s and K_{90} of 2.15, representing improvements of 11%
and 20% over the basic panel and Configuration 6B,
respectively.

The results above concerning the variation of reinforce-
ment volume and planform shape indicate that there may be
other asymmetric reinforcement configurations which have
superior performance to the configurations covered by this
investigation. The results for Configuration 1B and the
large symmetric reinforcement clearly indicate that large
reinforcement volumes do produce greater maximum strain
reductions. The fact that the square planform reinforcement
did not have a lower strain concentration factor than the
comparable round reinforcement implies at the very least that
reinforcement planform shape does not produce harmful effects.
Confirmation of this planform shape independence could be
quite useful in applications, permitting the most easily
producible shapes to be used. However, because only one
non-circular planform was modelled, it is not possible to
assert with certainty that the shape of the planform is
unimportant.

B. EXPERIMENTAL RESULTS

The experimental results appear to agree with most of the
computational predictions regarding strain (ε_z) near the hole
edge 90° from the load axis. For the unreinforced panels,
the difference between the front and back surface strains was
minimal, as predicted by the computational analysis. The

82

measured strains, ε_z, averaged 2447 μ_s, which differs from the computed value of approximately 2200 μ_s by nearly the same amount (18%) as the difference in net section strains discussed above (page 64). Additionally, the value of ε_z from the extrapolated experimental data for the strain at the hole edge (3660 μ_s) is higher than the computationally extrapolated value (3176 μ_s) by about the same amount.

For the reinforced panels, experimentally measured surface strains (ε_z) at X/R = 1.25 (location of center of the gauge) for a 10,000 lb load are compared to the computed values of ε_z obtained from the plots of ε_z vs X/R at X/R = 1.25, in Table X. In addition, the measured strains from the gauge in the hole are compared with the values of ε_z extrapolated to the hole edge for the panel midplane in Table XI. From these results, Configurations 3B and 6B are in excellent agreement with the computed predictions for front and back strains, while 1B shows the experimental readings to be 25-30% higher than predicted. The difference in readings for 1B may be explained by the fact that the finite element model is stiffer than the actual panel (previously discussed) and that this particular model has three sets of elements layered on top of each other near the hole, causing that region to be more affected by the analytical approximation. The midplane strain comparisons show 1B and 3B to be in good agreement with the computational predictions, the error being less than the difference in net section values for ε_z discussed above.

83

The experimental results for the gauge in the hole of panel 6B are significantly higher than the computer values.

TABLE X

COMPARISON OF EXPERIMENTAL AND COMPUTED MICRO-STRAINS

CONFIGURATION	FRONT SURFACE	BACK SURFACE	MIDPLANE
1B			
Computed	900	2500	2800
Measured	1194	1821	2919
3B			
Computed	1500	3000	2884
Measured	1538	2710	3452
6B			
Computed	1800	2500	2950
Measured	1876	2700	4204

The experimental findings indicated that failure occurred at the load for which ε_z reaches approximately 10,000 μ_x (1% strain) somewhere through the thickness of the panel and re-inforcement, near the hole edge, and approximately 90° from the load axis. For the basic panels, the failure strain at the edge of the hole on the surfaces was assumed to be the same throughout the panel thickness because of the small cur-vatures indicated from the analysis. This assumption could not be verified experimentally, but there was no visible evidence to the contrary. The results for the reinforced panels 3B and 6B indicated that the back surfaces of both panels at the edge of the hole also reached the strain re-quired for failure, while at the same time, the strains

84

recorded by the gauges in the holes indicated strains far higher than required occurred before failure. This appears to indicate that either the hole is stretching by some mechanism, such as the stress relief caused by microfailures [Ref. 13] or that the gauges were not recording accurate information, or both. The presence of delamination in the failure region suggests the possibility that the hole is stretching and the gauges may be affected by the complex strain state in that vicinity. The findings for panel 1B are even less clear in that the maximum surface strains were well below 1% strain, but the gauge recording strain in the hole did achieve values in this range. Also, the recorded strains for the front and back surfaces (Figure 45, Appendix B) show far less variation than the analysis predicted (Figure 33, Appendix B), which suggests that some mechanism is creating an unusual strain distribution. This complicated distribution of strain through the thickness of panel 1B is not easily explained, but again the presence of delamination in the failure region suggests that interlaminar shear is both present and contributory to the strain state recorded.

In addition to the complicated strain behavior discussed above, the results of the front and back surface strain behavior confirmed that the panels behave in a nonlinear fashion near the hole edge when the panel were subjected to loads above that used in the computational analysis (10,000 lbs). Comparison of the ratios of front and back surface strains (ε_z) 90° from the load axis, show that the ratios

85

decrease when the load increases. This suggests that there may be some mechanism which is reducing the curvature of the panel and therefore the difference in strain readings as the load is increased. Because the experimental setup had no provision for measuring out of plane deflections or curvature, there was no way to determine whether the decrease in front to back surface strain ratio was accompanied by reductions in curvature. The nonlinear behavior of the panel is even more evident when ε_z is plotted vs X/R, as done for panel 1B in Figure 18. The most striking feature of this plot is the increasing ratio of the highest strain (X/R = 1.25) to the lowest (X/R = 2.0). For panel 1B, this ratio increases from 1.57 at 10,000 lbs to 1.73 just prior to failure, an increase of about 10%. Similar results for panel 3B (Appendix D, Figure 80) and 6B (Appendix G, Figure 129) show less severe increases in this ratio, but there is clearly nonlinear behavior at high loads across the entire panel. Because these effects are only slightly above variations that could be attributed to experimental error, there is no pressing require- ment to alter the computational model to perform nonlinear computations.

Before any firm conclusions can be drawn from the experi- mental results, some consideration should be given to the accuracy of the experiment. Since there are inevitably small variations in panel construction, gauge bonding, and load history, it is possible that results for repeated tests would

86
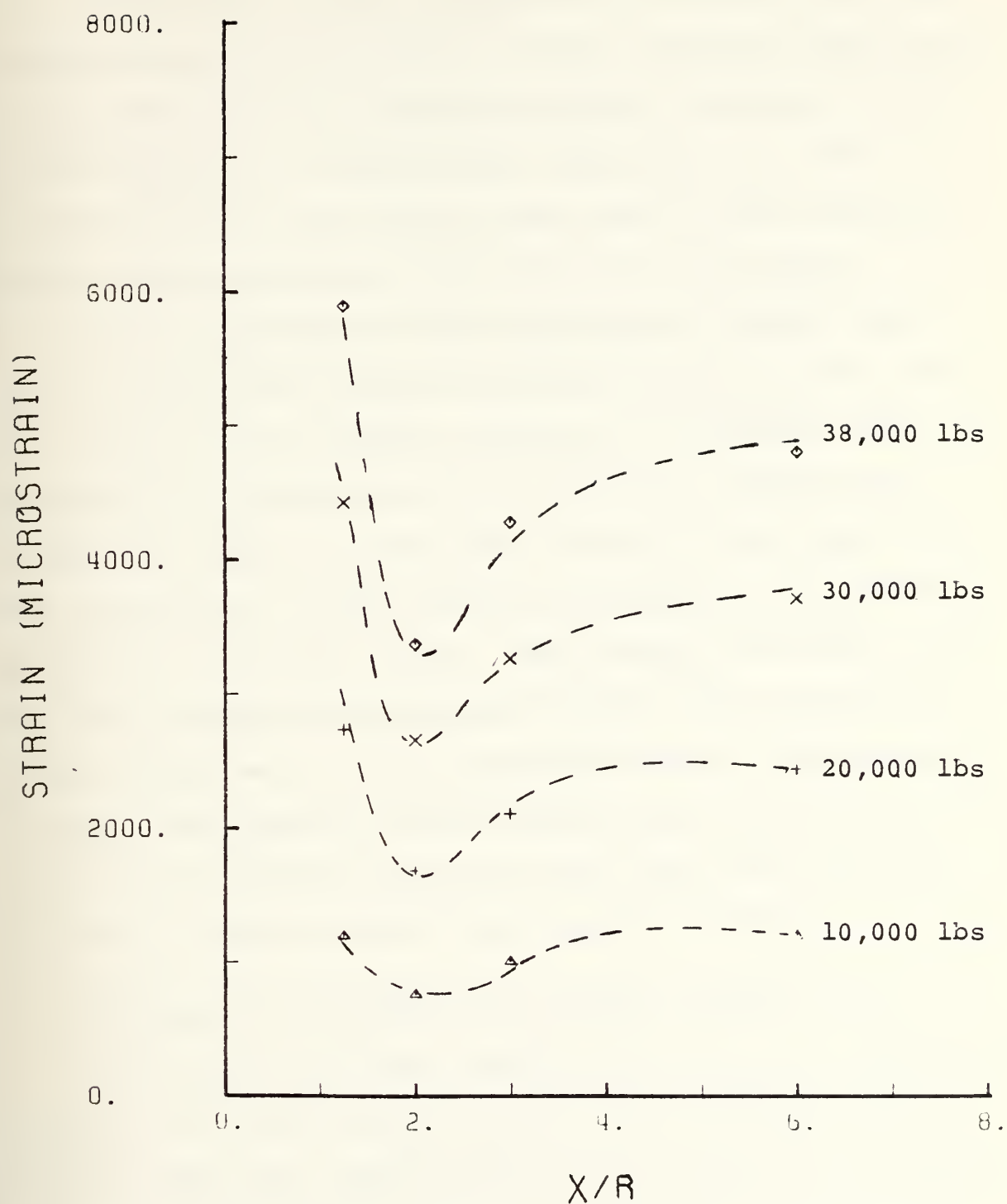
Figure 18. Nonlinear Behavior of Panel 1B
ε_z vs X/R at the Hole Edge.

87

average to higher or lower values for failure load and strain. Therefore, it is difficult to assert with certainty that panel 1B had the best results or that 6B had the worst. However, since none of the test results indicate improvements of more than 10% of the laminate ultimate strength, in spite of the variation of reinforcement configuration, there is justification for the assertion that none of the configurations produce significant strengthening of the panel.

From the discussion of the experimental results above, it is apparent that the most important measured results were the values of ε_z at various locations of the panel. The variation of ε_z with Z/R was also important, showing the compressive strains in the panel parallel to the load axis. The variation of ε_x with X/R and the results of the rosette proved to be of little value. The recorded variation of ε_z with X/R provided an added demonstration that the computational models were in close agreement with the experimental results. The rosette results verified that the principal strains were oriented parallel to the load axis away from the hole, a result expected for uniaxial loading.

C. COMPARISON OF PREDICTED AND MEASURED VALUES OF K_{90}

To evaluate the various predictions of K_{90} for suitability of use, all of the previous results for the basic (unreinforced) panels and Configurations 1B, 3B and 6B are assembled in Table XI. Table XI indicates that the results based on Figure 97 of Peterson [Ref. 9] are in question, being 25 to

30% high and low. The predictions based on this technique, shown with the experimental values in Figure 19, show no real consistency or trend. Because of this, the use of such predictions seem suspect, even with the results being conservative, i.e., larger than expected from the experimental results.

On the other hand, the alternate isotropic prediction method, based on Ref. 10, gives predictions which are in reasonable agreement with the experimental results. The results closely follow the correct trend as shown in Figure 20, with only the reinforced panel being far from the prediction. Because of the general accuracy, the use of a curve such as found in Ref. 11 seems to be justifiable in cases where estimates of behavior of quasi-isotropic plates are desired.

The predictions based on the computational analysis are in better agreement with the experimental results than the other predictions. The agreement points to the excellent modelling capability of the DIAL code, and to the suitability of the techniques used in the analysis, i.e., the method of extending the computed results to the edge of the hole. The slight variations noted for panels 1B and 6B can be partially accounted for by experimental errors and difficulties previously mentioned. In view of the results, the DIAL code has proven to be an accurate means to predict the true behavior of a laminate containing a hole. It seems reasonable to

assert that similar results can be expected for nearly any
isotropic balanced laminate to be modelled.

TABLE XI

COMPARISON OF MEASURED AND PREDICTED VALUES OF K_{90}

TYPE PREDICTION	BASIC PANEL	1B	3B	6B
MEASURED	2.42	1.96	2.28	2.77
COMPUTER	2.478	2.185	2.250	2.299
R.Ae.S	2.70	1.75	2.00	2.34
PETERSON	2.6	2.48	2.47	2.58
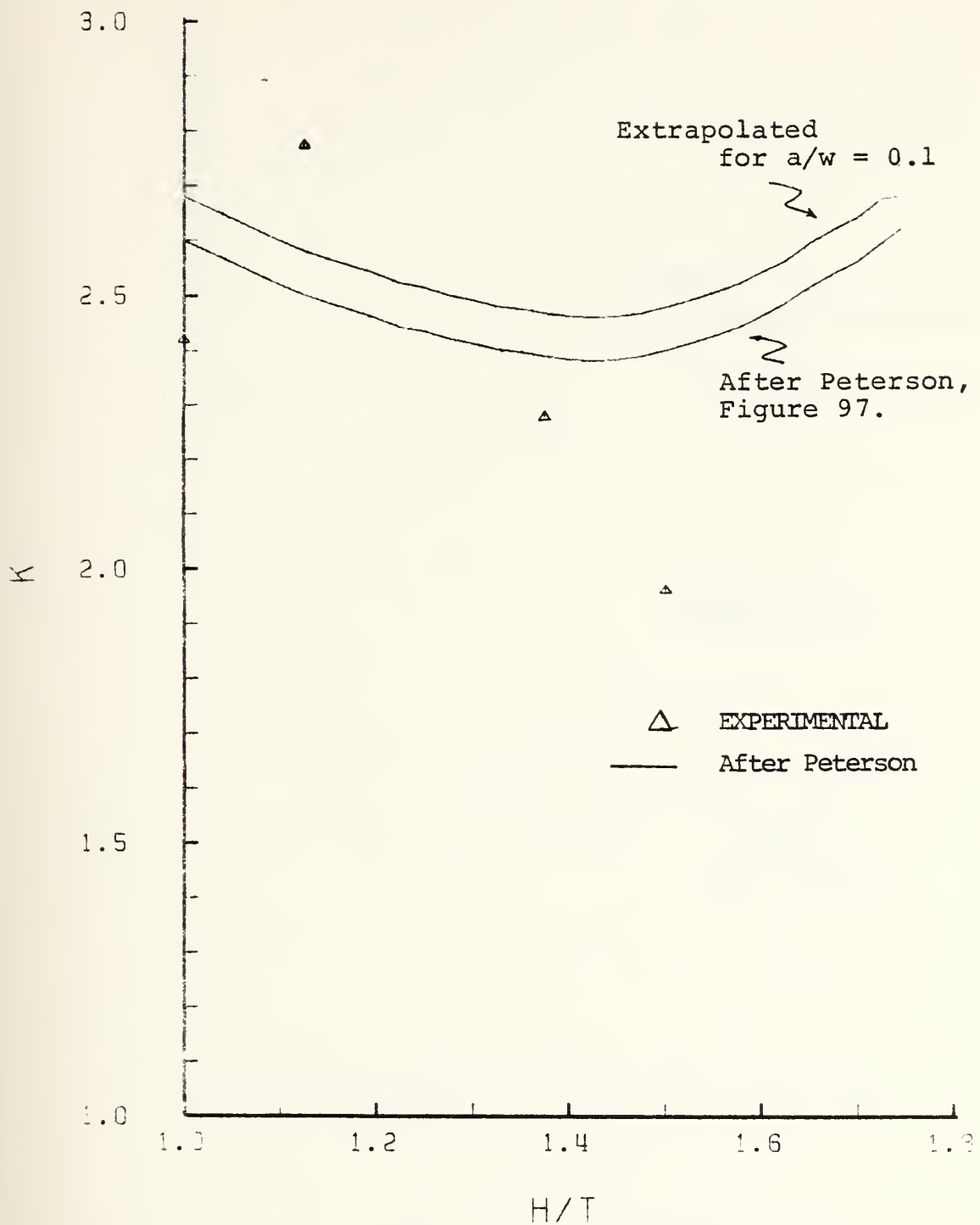
Figure 19. Comparison of Isotropic Prediction and Measured Values of K_{90}.
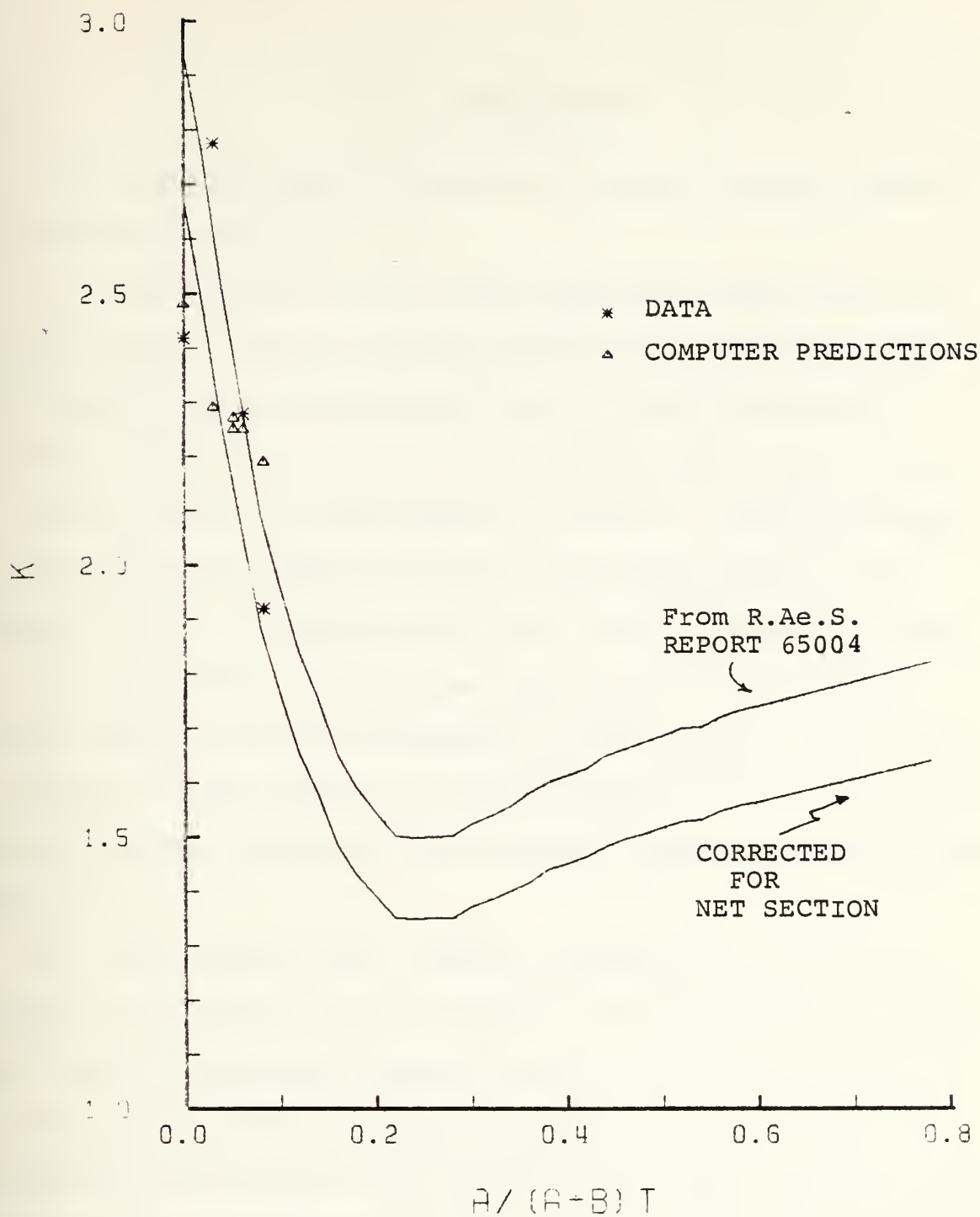
Figure 20. Comparison of Isotropic Prediction and Measured Values of K_{90}.

92

VII. CONCLUSIONS

The following conclusions can be drawn from the results of this investigation:

1. The results for the quasi-isotropic panel modelled in the finite element analysis indicate that reinforcements of circular shape consisting of two or three additional layers of material hold the best potential for the reduction of maximum strain at the edge of the hole. The improvement is not large, with the maximum strains approximately 10% lower than for an unreinforced panel with an identical hole.

2. From the analysis, the reduction of the maximum strain seems to be more dependent on the volume of the reinforcement and the number of layers used (height) than on any other parameter regarding the physical shape of the reinforcement.

3. The computational results indicate that there is a greater reduction in maximum strain for configurations which have the reinforcement layers closest to the panel oriented parallel to the load axis, even though the out of plane deflections and curvatures are greater for these configurations than for configurations with all reinforcement layers oriented 45° to the load axis.

4. The finite element analysis code employed in the investigation showed excellent general agreement with the experimental results. The observed nonlinear nature of

93

strains at some points on the panel under high loads is
small enough (approximately 10%) that it can be neglected
for the purposes of this investigation. However, the non-
linear behavior of ε_z at the point on the panel experiencing
the maximum strain is likely, to influence the failure
strength of the panel.

5.   The reductions in maximum strain predicted by the
analysis were corroborated by the experimental results for
the panels tested.

6.   The experimental results indicate that asymmetric
circular reinforcements will only increase the strength of
the panel by 5-10% of the total laminate strength. The
slight variation of failure loads for the different configu-
rations tested indicates that the small range of improvement
in maximum strain indicated in the analysis is true up to
failure of the panels, and that configuration geometry
apparently has little effect on the ultimate strength of the
panels.

7.   The analytical results for the two symmetric configu-
rations indicate that far greater reductions in strain are
possible for even very thick symmetric reinforcements.

8.   The use of the Royal Aeronautical Society plot of
stress (strain) concentration factors for isotropic materials
to predict strain concentrations for asymmetric reinforcements
of a quasi-isotropic laminate seems justified by the experi-
mental results.

VIII. RECOMMENDATIONS

From the experience gained during the course of this investigation the following recommendations are submitted:

1. Further investigations should be conducted to determine whether or not significant improvements in strength and strain reduction can be made by varying the following parameters of asymmetric reinforcements:

    a. Increasing the outer radius of the reinforcement beyond $X/R = 3.0$

    b. Significantly increasing the volume of the reinforcement.

    c. Changing the planform shape of the reinforcement.

    d. Submerging the reinforcement layers below one or two layers of the laminate.

2. In future experiments, strain gauges should be arranged to measure ε_z vs X/R and ε_x vs Z/R on both sides of the panel. The measurement of ε_x vs X/R is not of great importance.

3. In future experiments, strain gauges should be mounted tangentially to the hole at several orientations to the load axis on both sides of the panel. Also, gauges should be mounted in the hole at locations 0° and 90° to the load axis.

APPENDIX A
NONREINFORCED PANEL
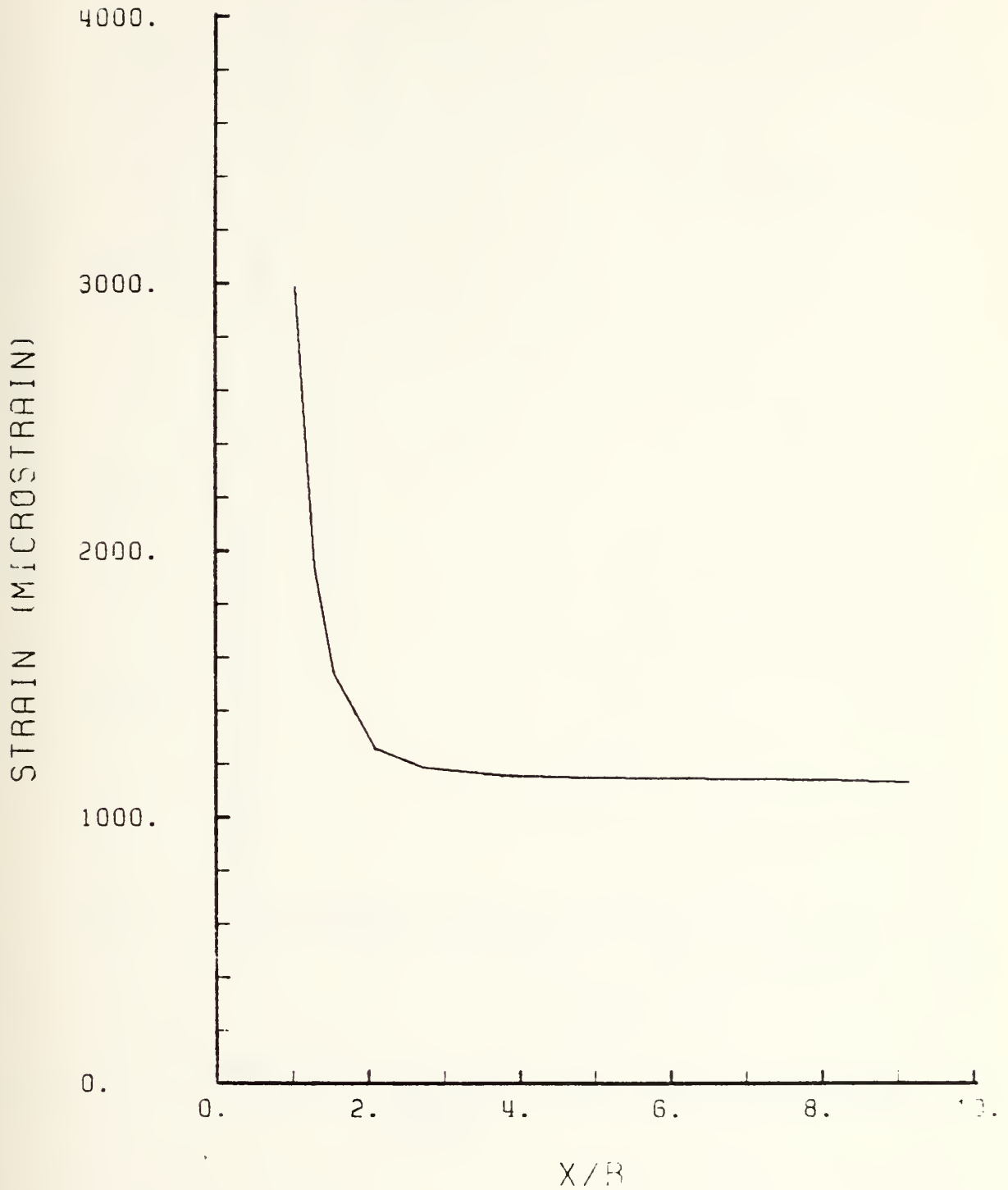
Figure 21.   Computed ε_z Vs X/R Unreinforced Panel.

Figure 22.   Computed ε_x Vs X/R Unreinforced
Panel.
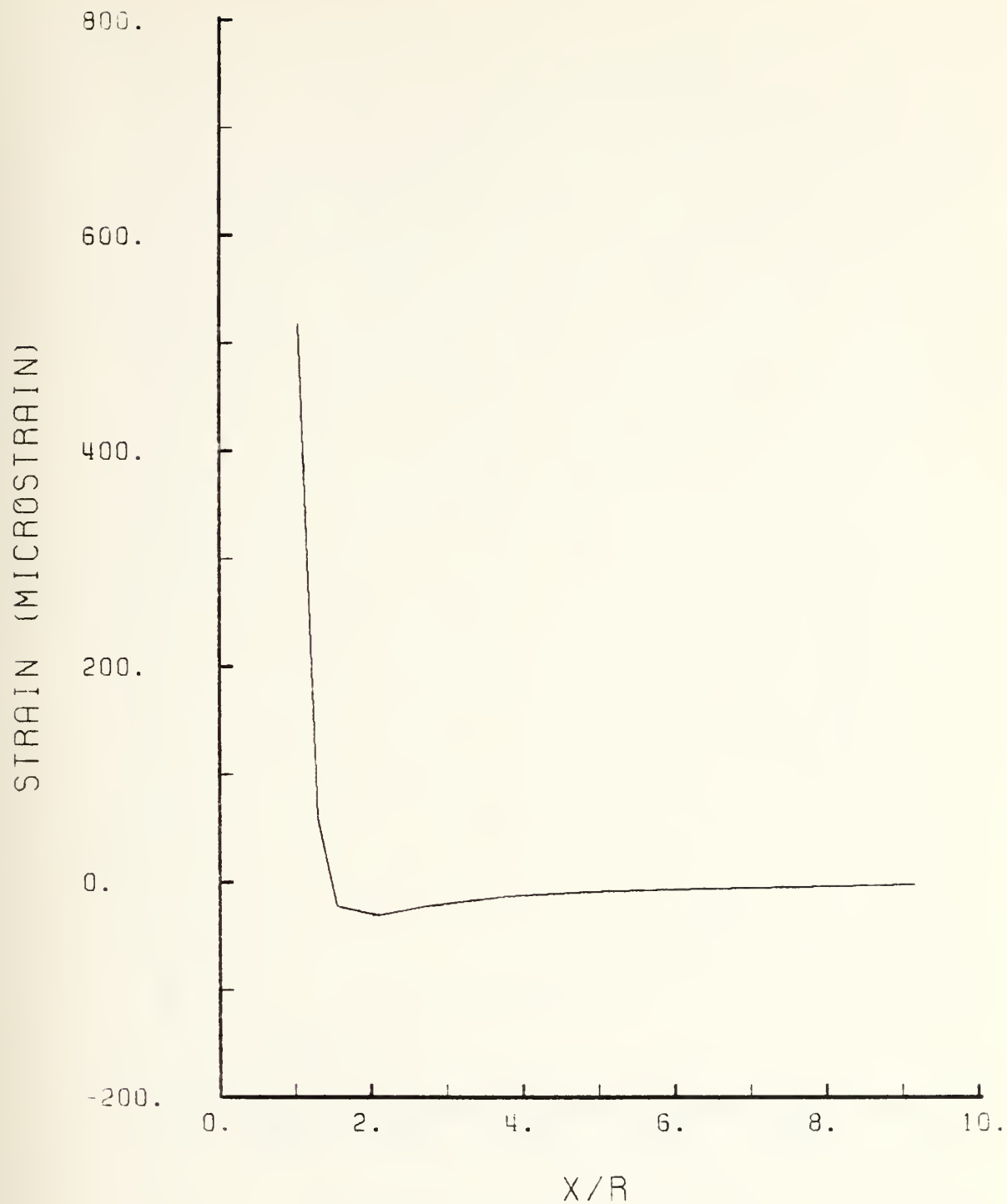
Figure 23.   Computed ε_{xz} Vs X/R Unreinforced
Panel.
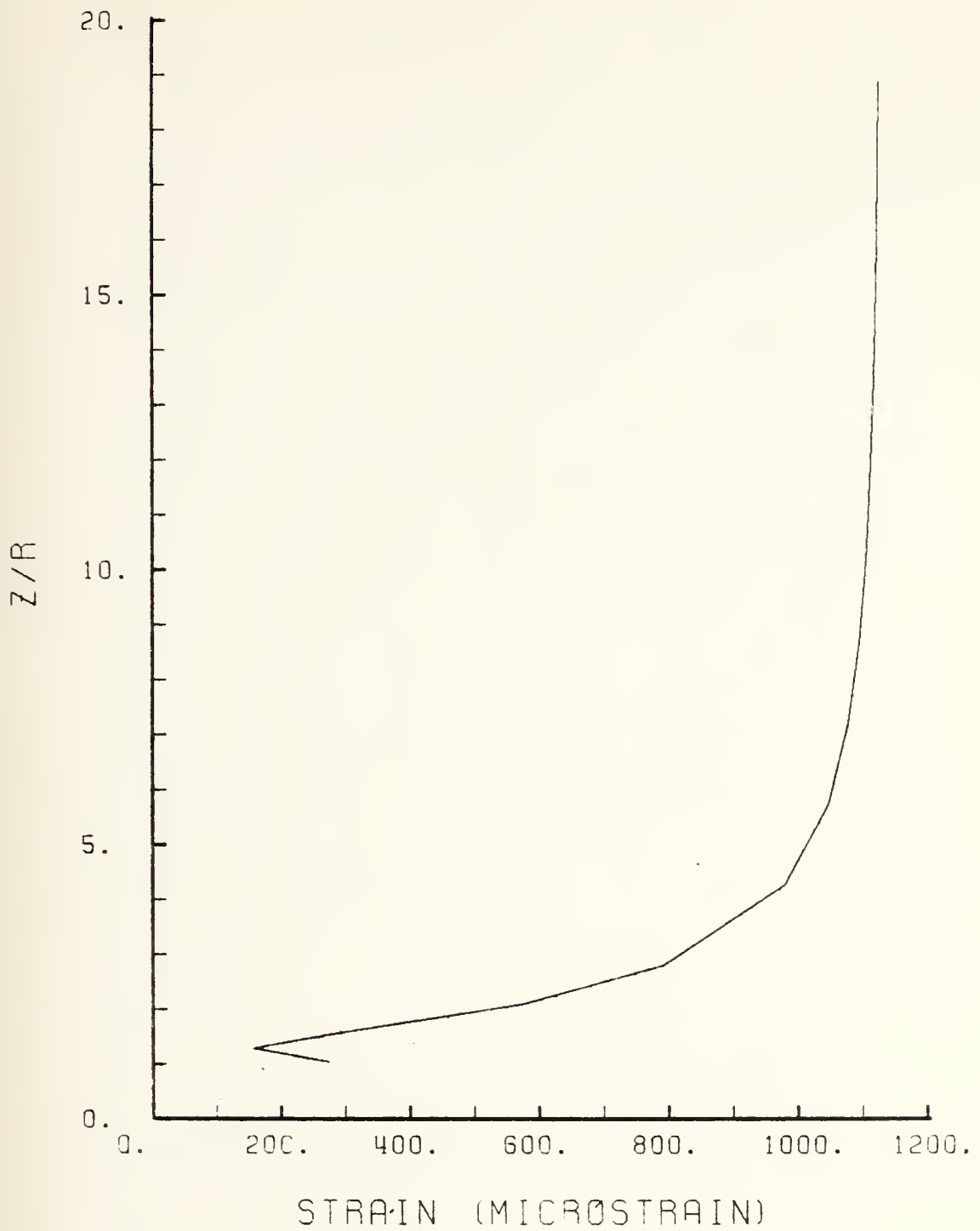
Figure 24. Computed ε_z Vs Z/R Unreinforced Panel.
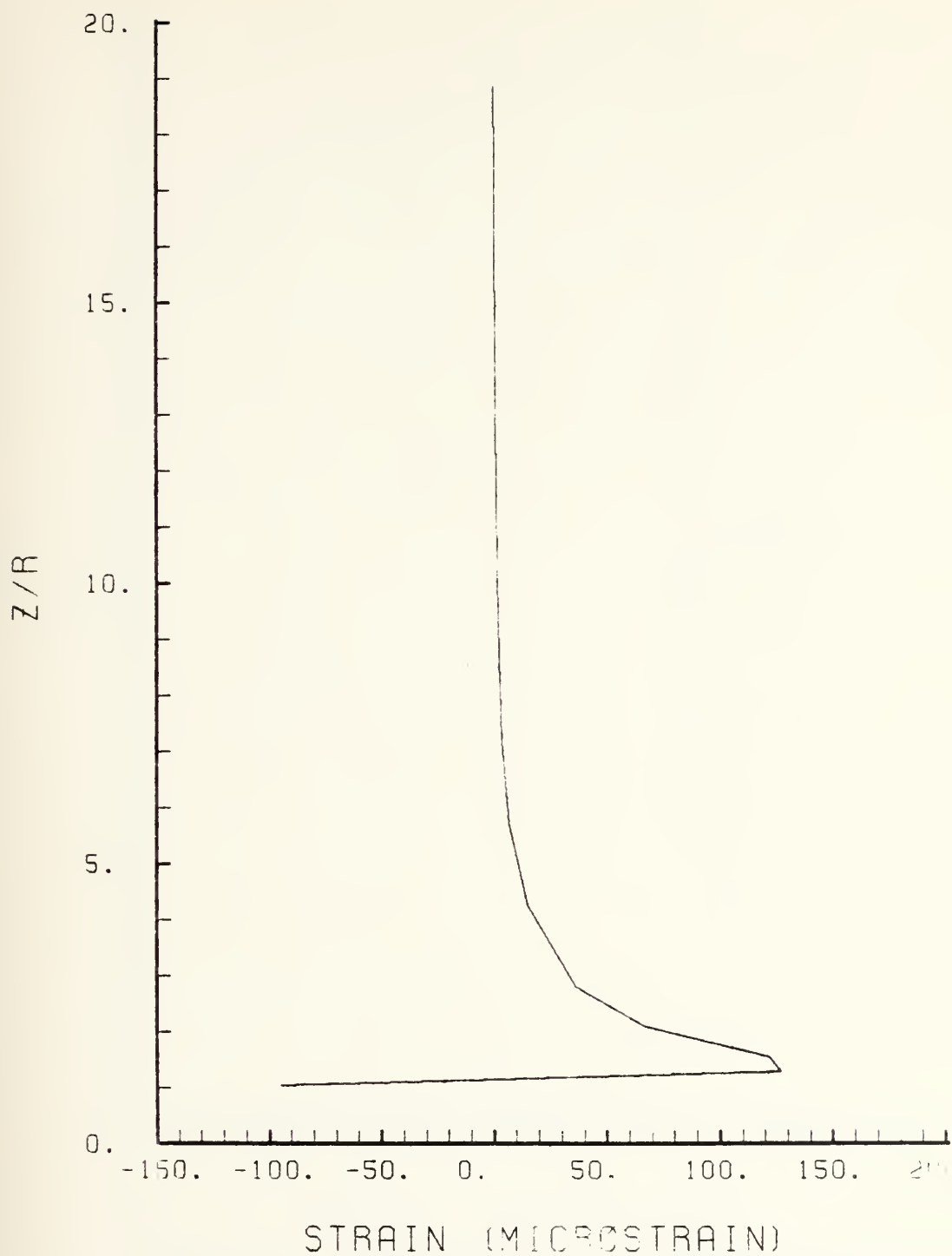
Figure 25. Computed ε_{xz} Vs Z/R Unreinforced Panel.
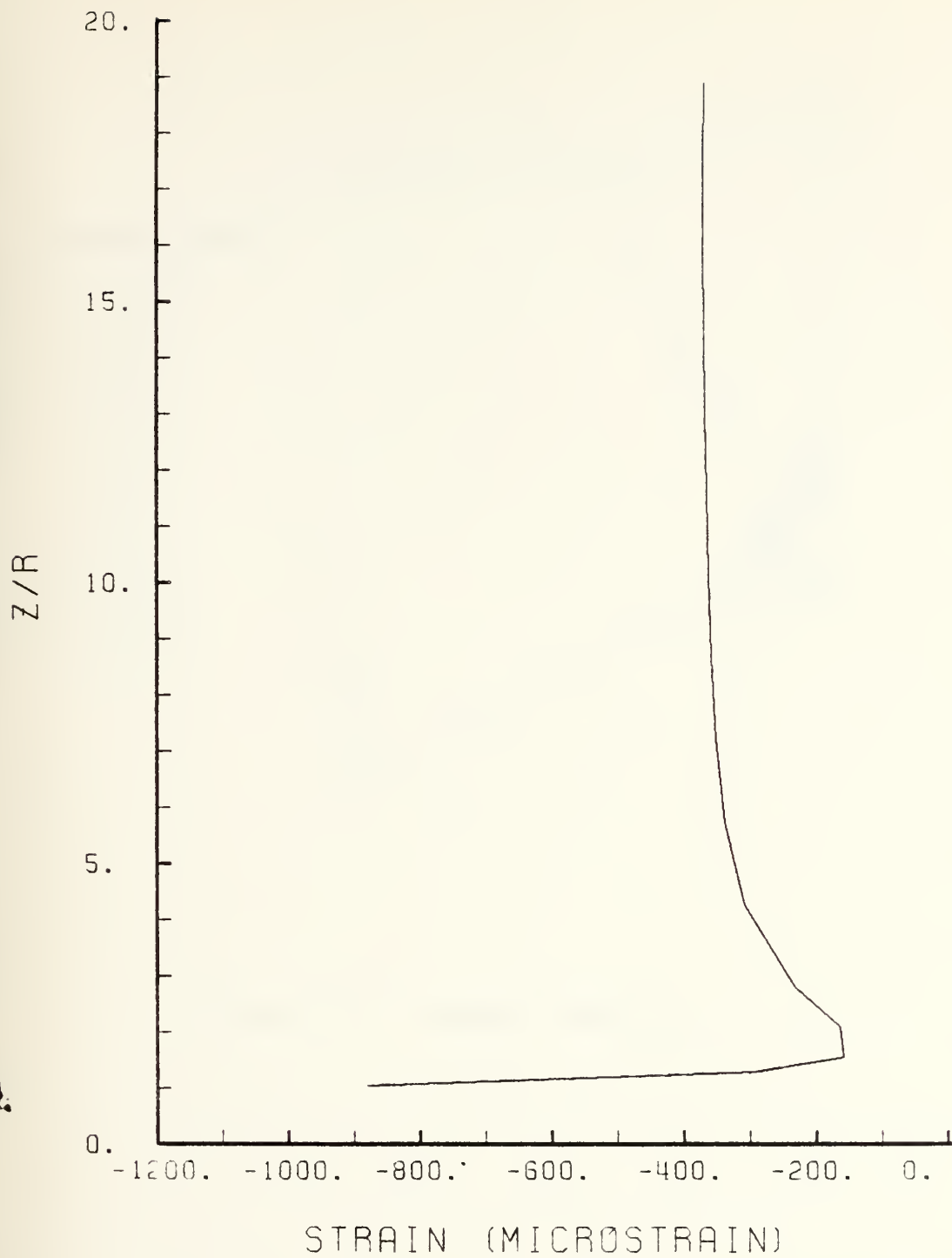
Figure 26. Computed ε_x Vs Z/R Unreinforced Panel.

CONTOUR INDEX

1 - 3.1×10^{-5}

2   5.0×10^{2}

3    $1.0^{x} 10^{3}$

4   1.5×10^{3}

5   2.0×10^{3}

6   2.5×10^{3}

7   3.0×10^{3}

Figure 27.   Contour Plot N_z.

CONTOUR INDEX

1	3.1×10^{-5}
2	5.0×10^{2}
3	1.0×10^{3}
4	1.5×10^{3}
5	2.0×10^{3}
6	2.5×10^{3}
7	3.0×10^{3}
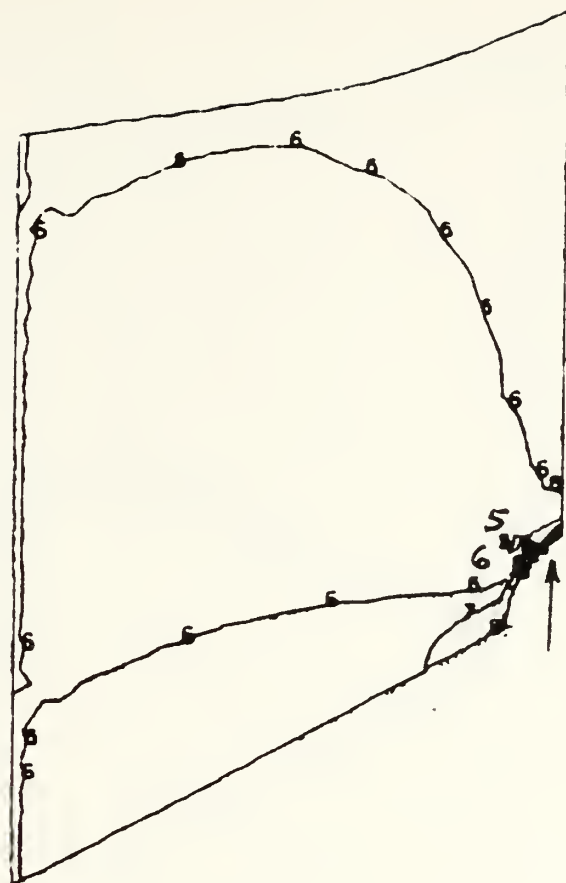
Figure 28. Contour Plot of N_x.

CONTOUR INDEX

1	2.0×10^2
2	0.0
3	2×10^2
4	4×10^2
5	6×10^2
6	8×10^2
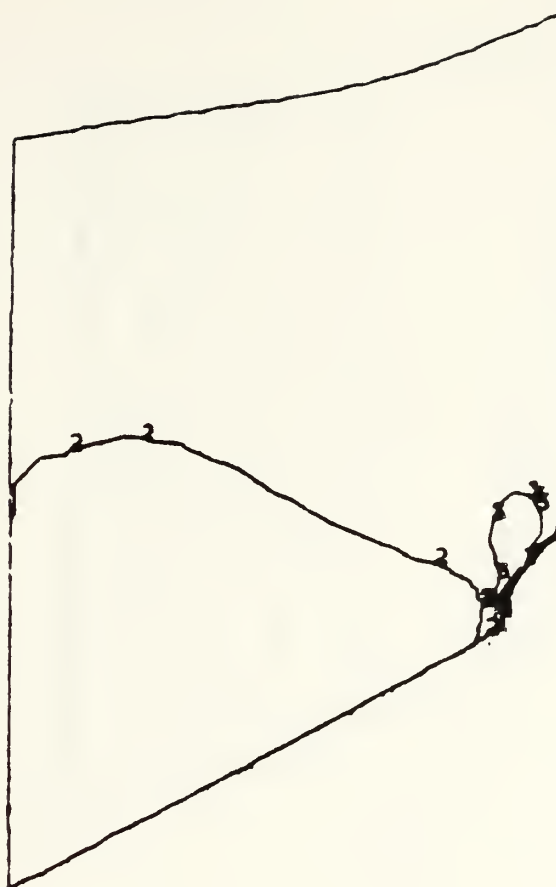
Figure 29. Contour of N_{xz}.

Figure 38. Contour of 3

CONTOUR INDEX

1	10×10^{-10}
2	-8×10^{-10}
3	-6×10^{-10}
4	-4×10^{-10}
5	-2×10^{-10}
6	0
7	2×10^{-10}
8	4×10^{-10}
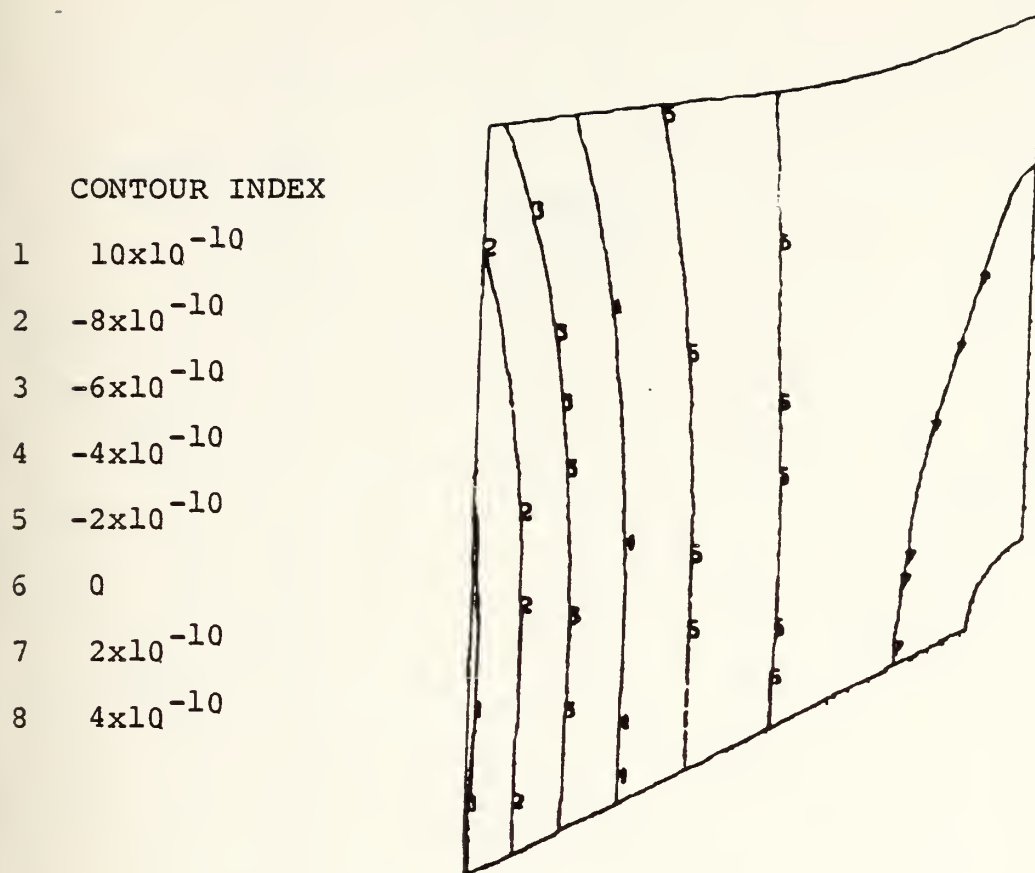
Figure 30. Contour of Out of Plane
Deflections.
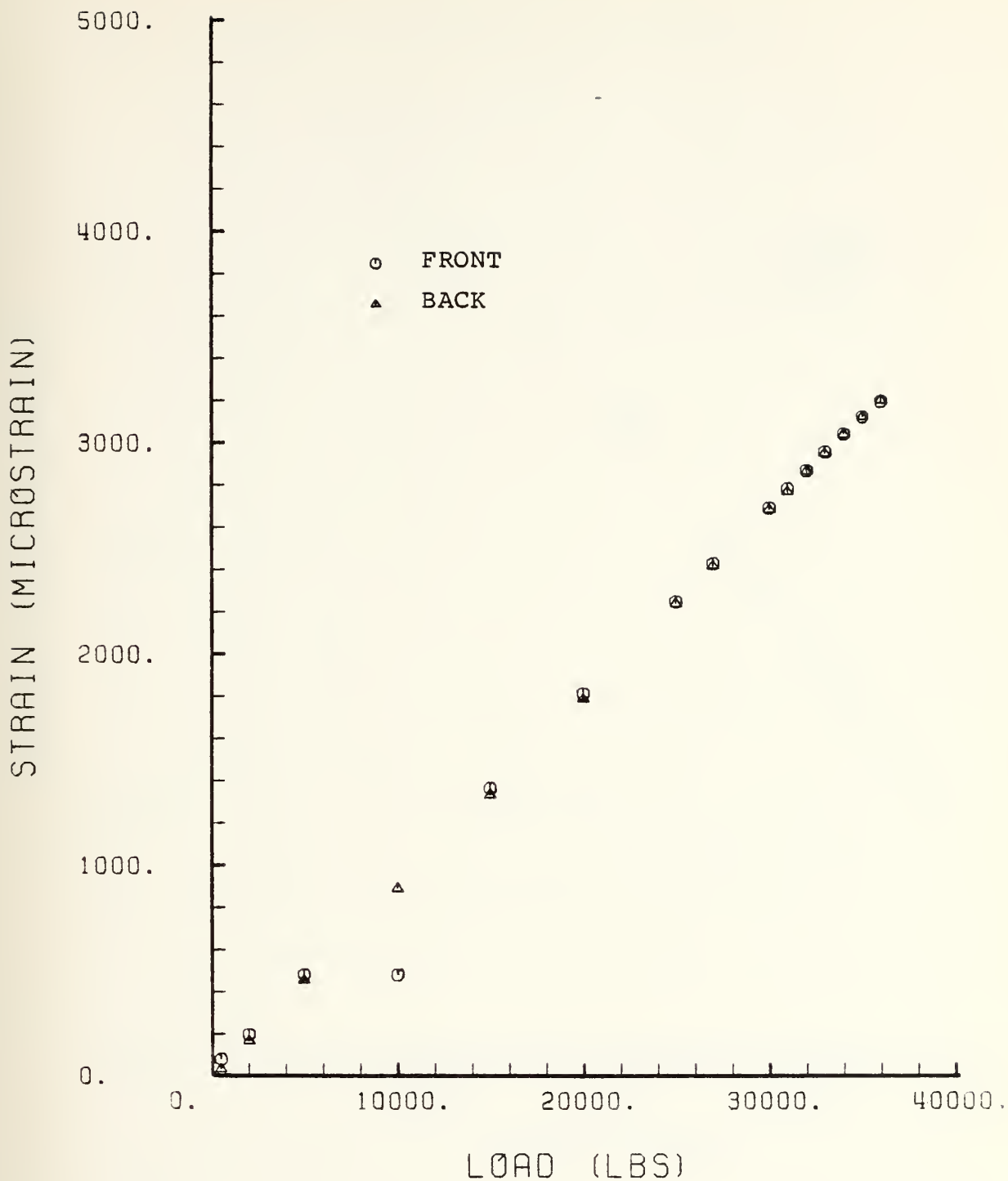
Figure 31.   Comparison of Measured Front and Back
            Strains at Gauges 15 and 20 - Basic Panel.
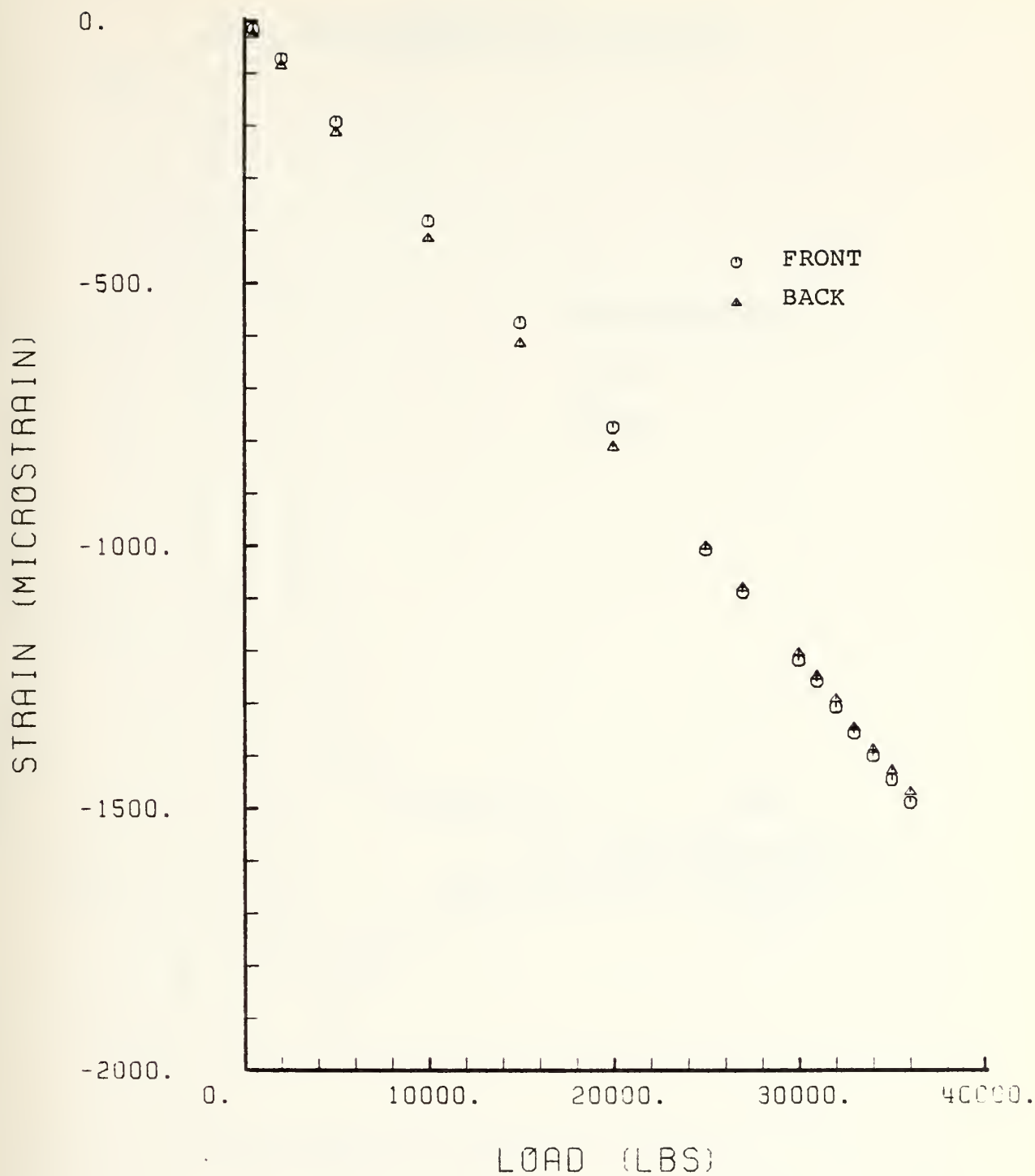
Figure 32.   Comparison of Measured Front and Back
             Strains at Gauges 9 and 21 - Basic Panel.
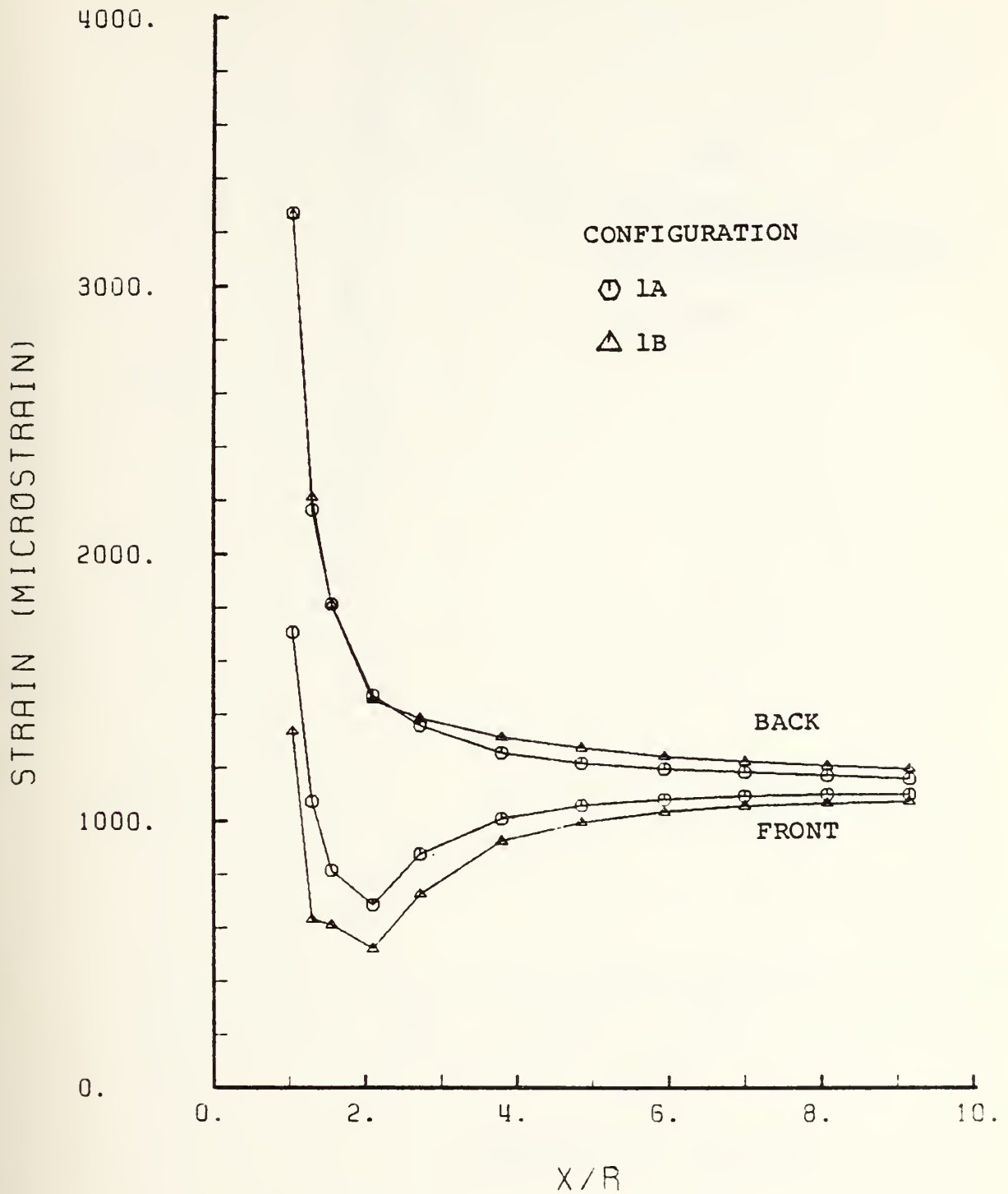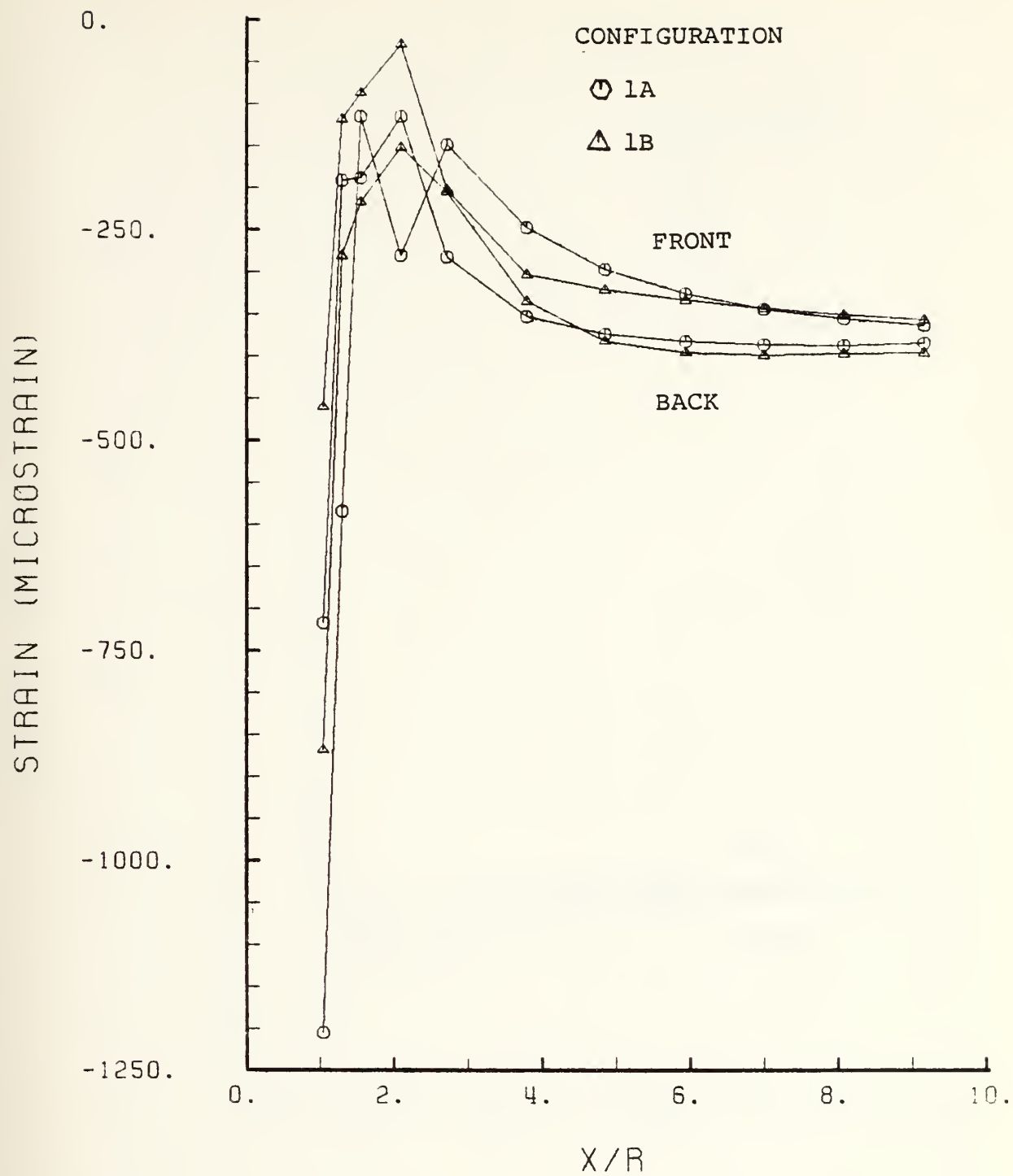
Figure 33. ε_z Vs X/R.

Figure 34. ε_x Vs X/R.

109

Figure 35. ε_{xz} Vs X/R.

110

Figure 36. ε_z Vs Z/R.

111

Figure 37. ε_x Vs Z/R.

112

Figure 38. ε_{xz} Vs Z/R.

113
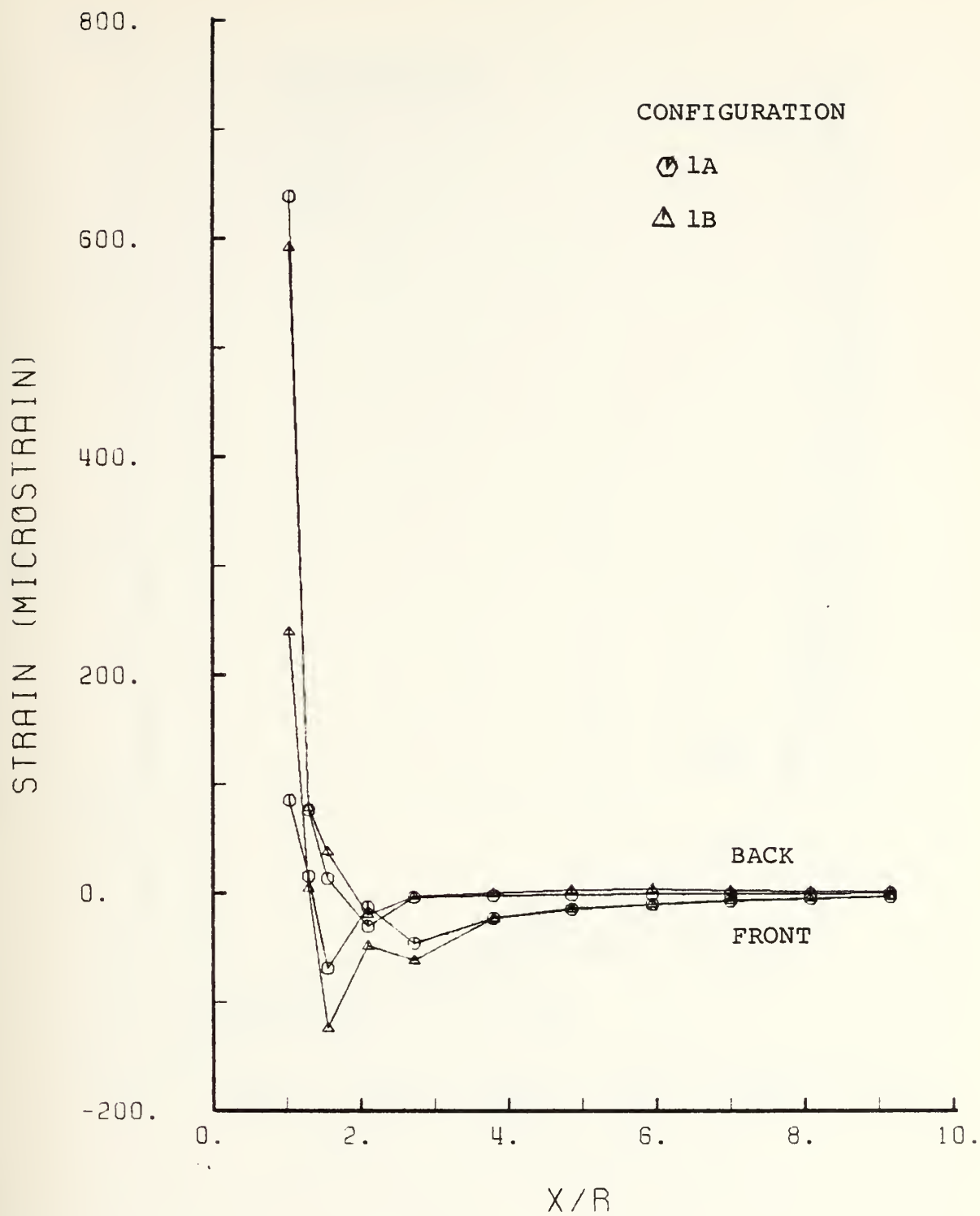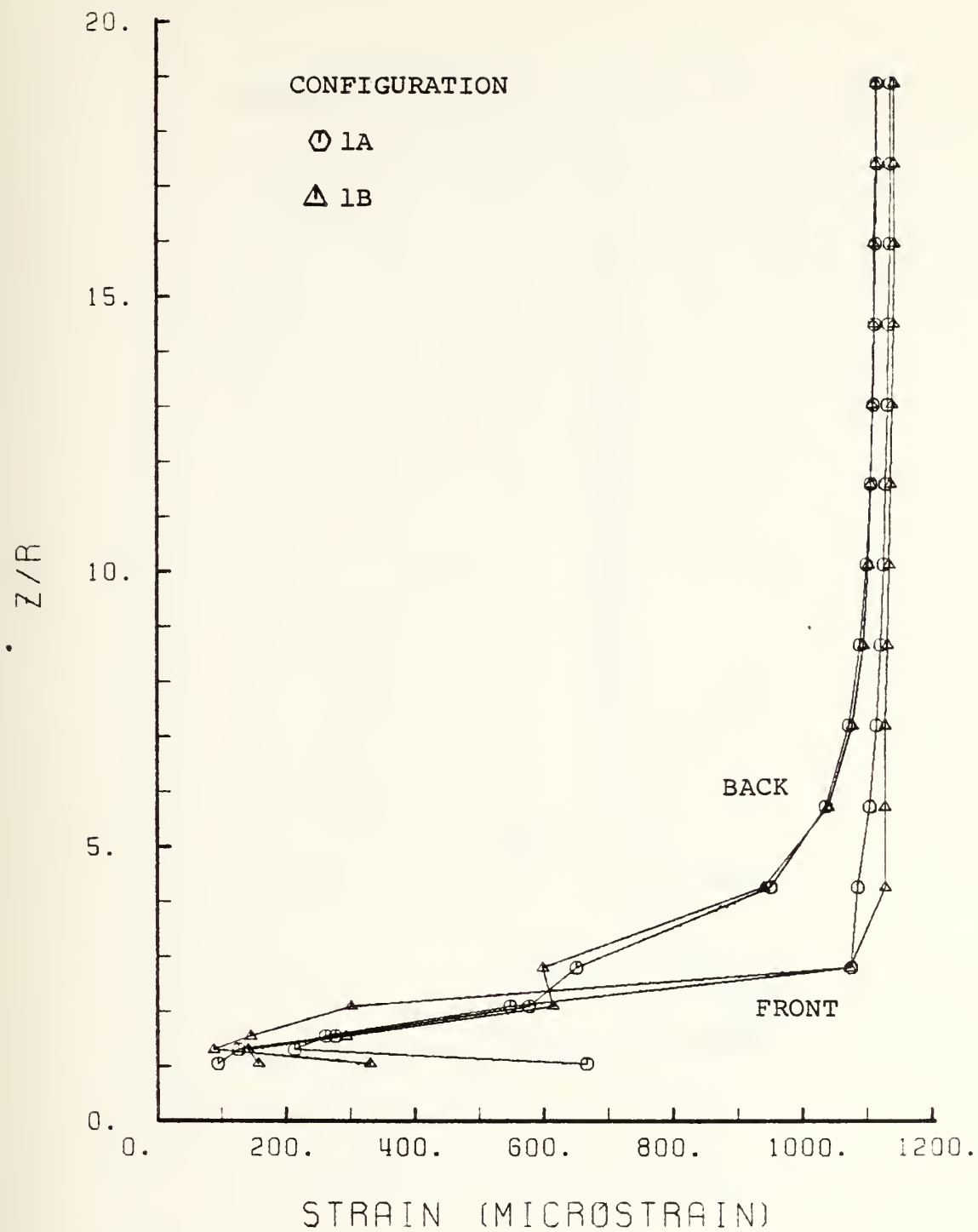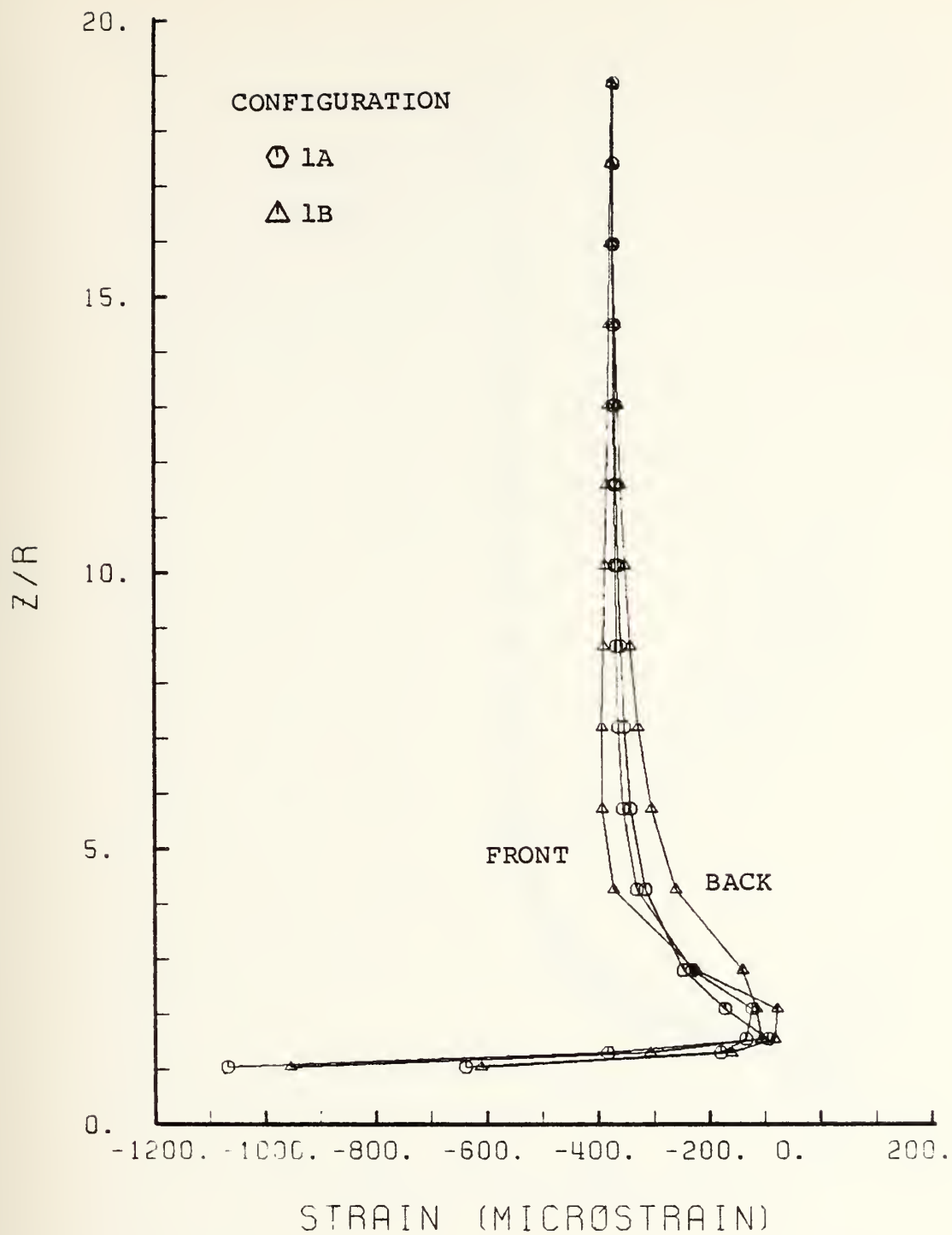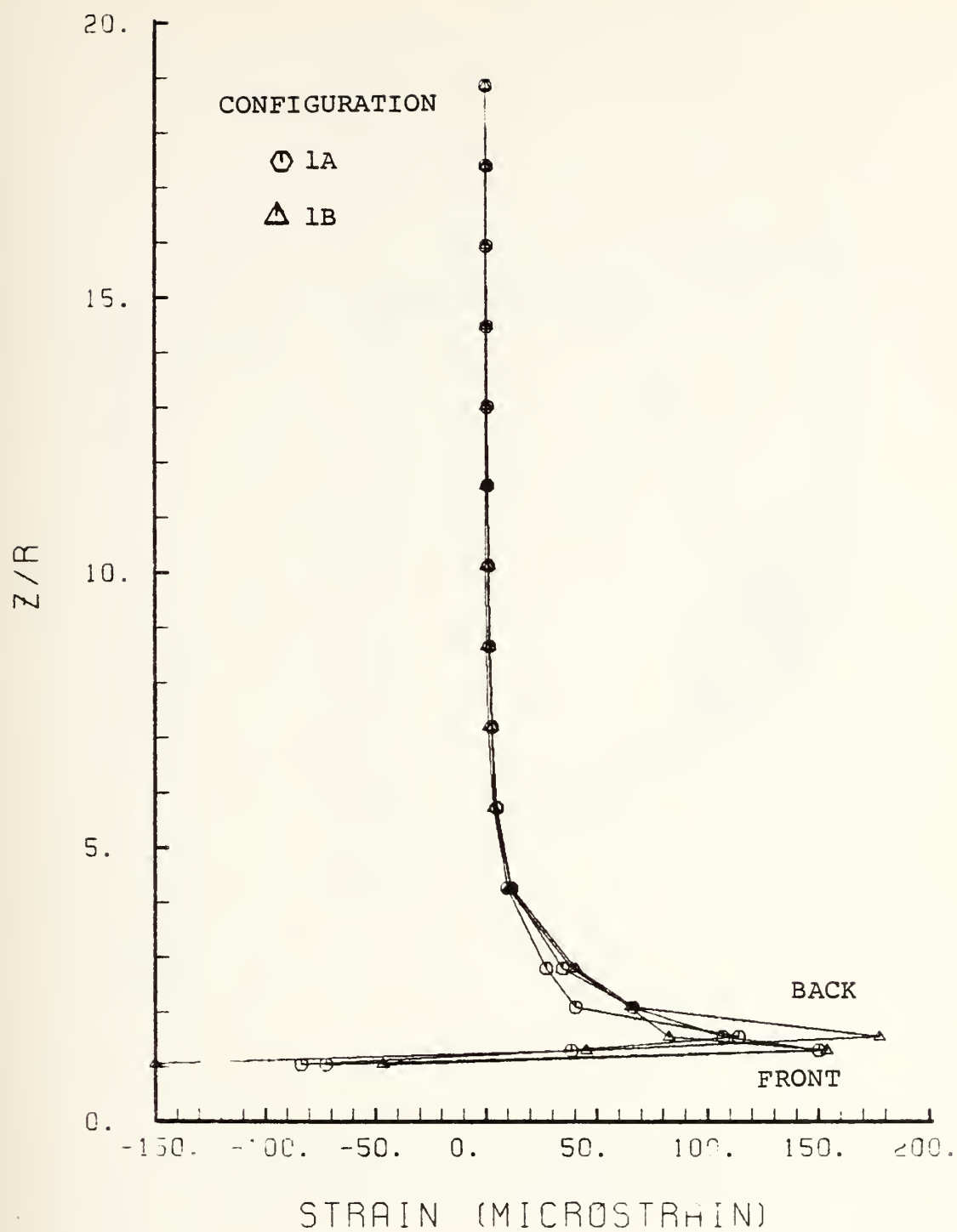
CONTOUR INDEX

1	-1.5×10^{-5}
2	2×10^{2}
3	4×10^{2}
4	6×10^{2}
5	8×10^{2}
6	1.0×10^{3}
7	1.2×10^{3}

Figure 39. Contour Plot of N_z Configuration 1A.

CONTOUR INDEX

1   -4×10^2

2   -3×10^2

3   -2×10^2

4   -1×10^2

5   0.0

6   1.0×10^2

7   2.0×10^2
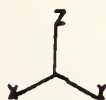
Figure 40.   Contour Plot of N_x
Configuration 1A.

CONTOUR INDEX

1   -1×10^3

2   0

3   1×10^3

4   2×10^3

5   3×10^3

6   4×10^3
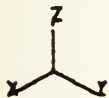
Figure 41.   Contour Plot of N_{xz} Configuration 1A.

116

CONTOUR INDEX

1	0.Q
2	2×10^2
3	4×10^2
4	6×10^2
5	8×10^2
6	1.0×10^3
7	1.2×10^3
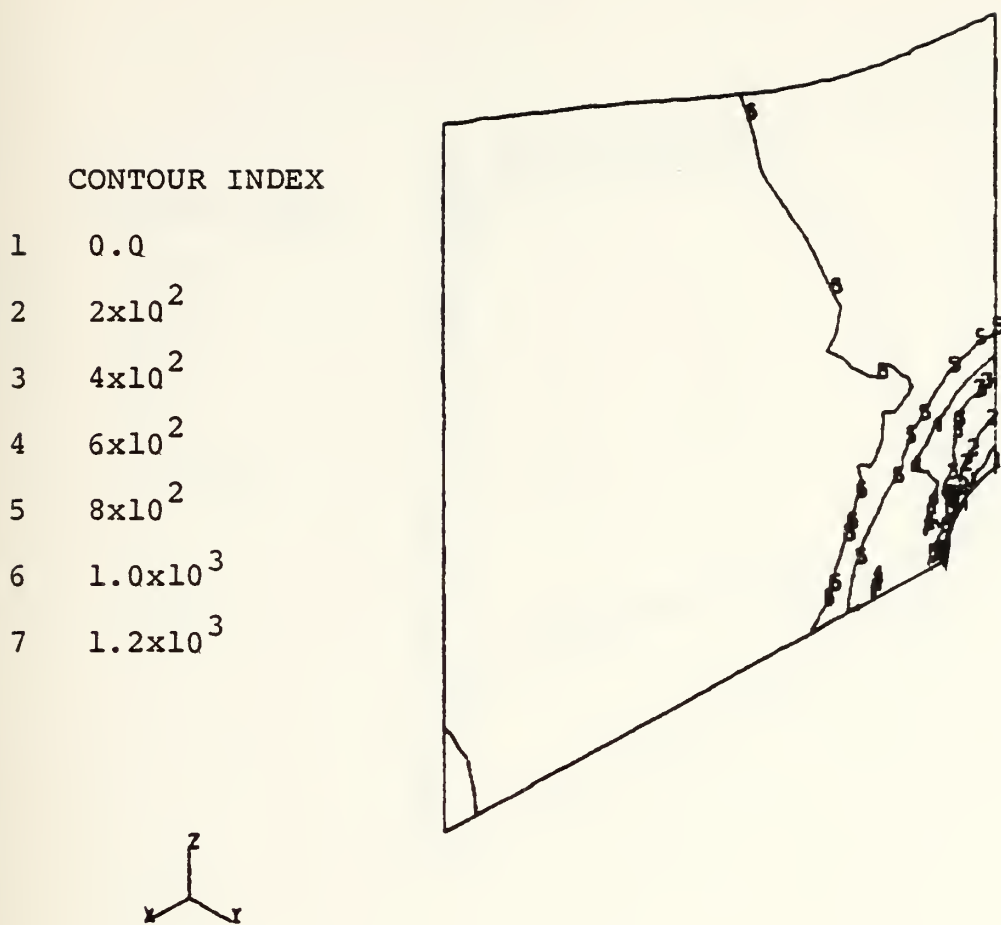
Figure 42. Contour Plot of N_z Configuration 1B.
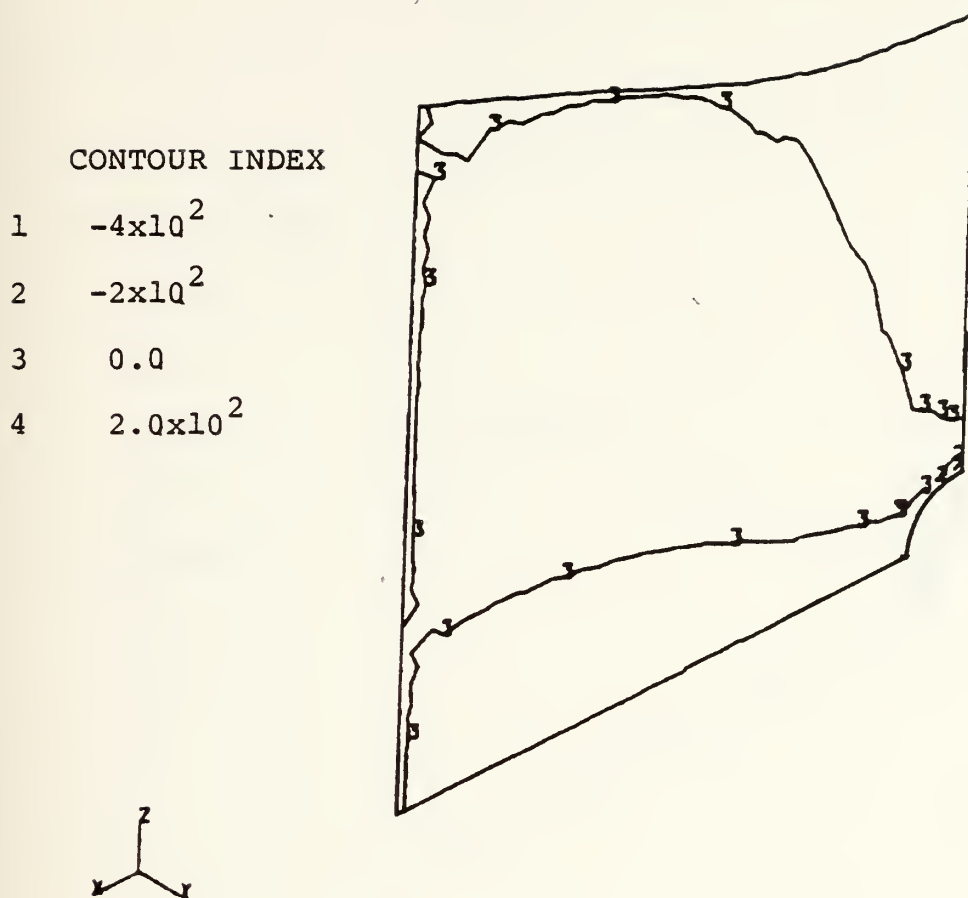
Figure 43. Contour Plot of N_x Configuration 1B.

Figure 63. Compound from

CONTOUR INDEX

1   -1×10^2

2   0.0

3   1.0×10^2

4   2×10^2

5   3.0×10^2
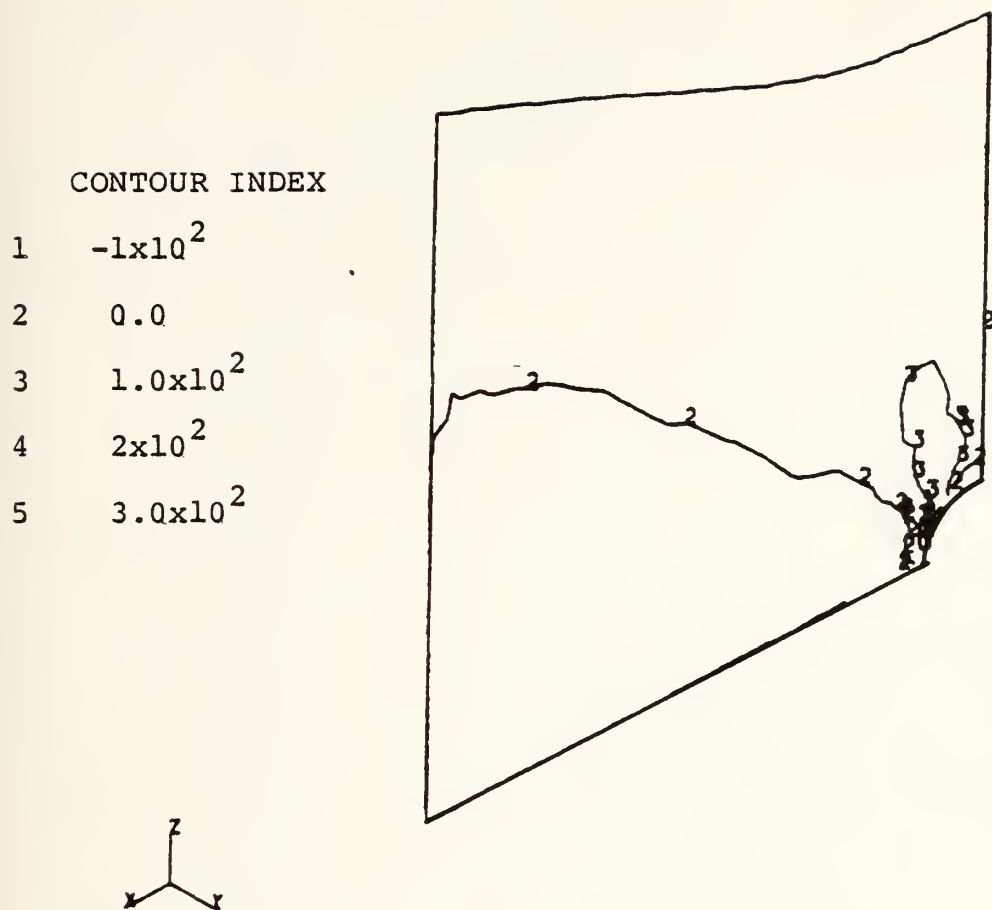
Figure 44.   Contour of N_{xz} Configuration 1B.
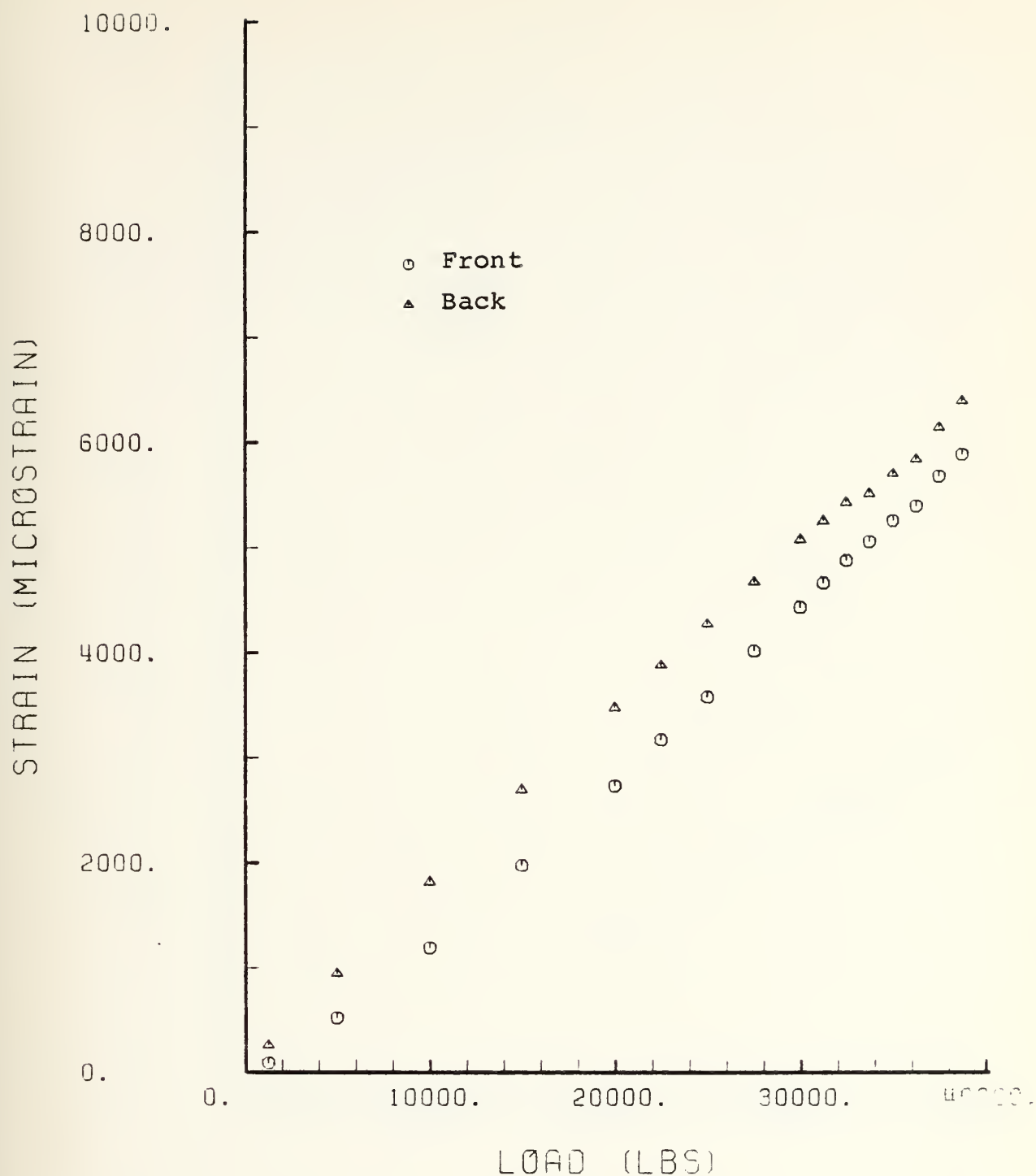
Figure 45. Comparison of Measured Front and Back
Strains at Gauges 5 and 19 –
Configuration 1B.

120
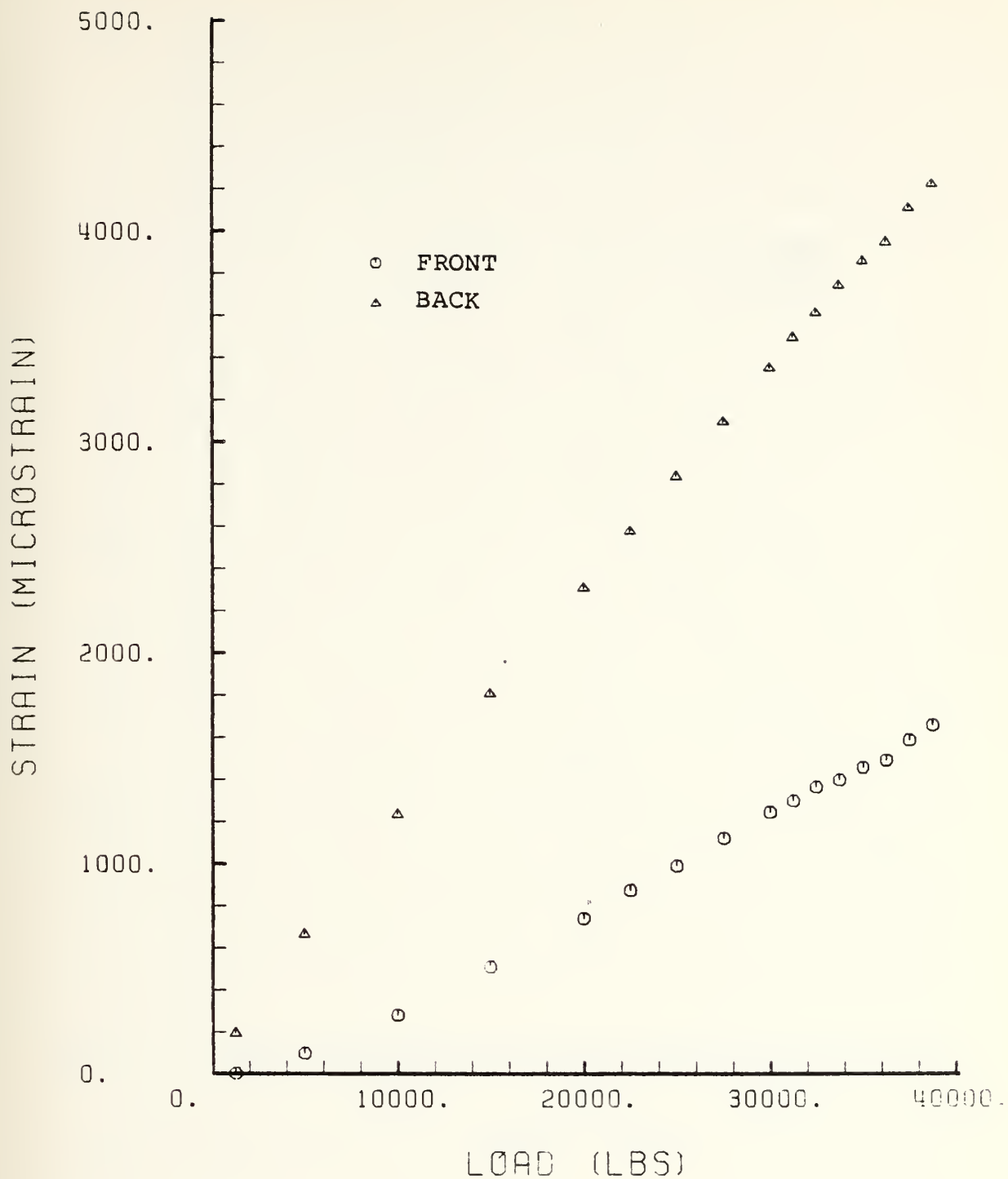
Figure 46.   Comparison of Measured Front and Back
   Strains at Gauges 15 and 20 –
             Configuration 1B.

121
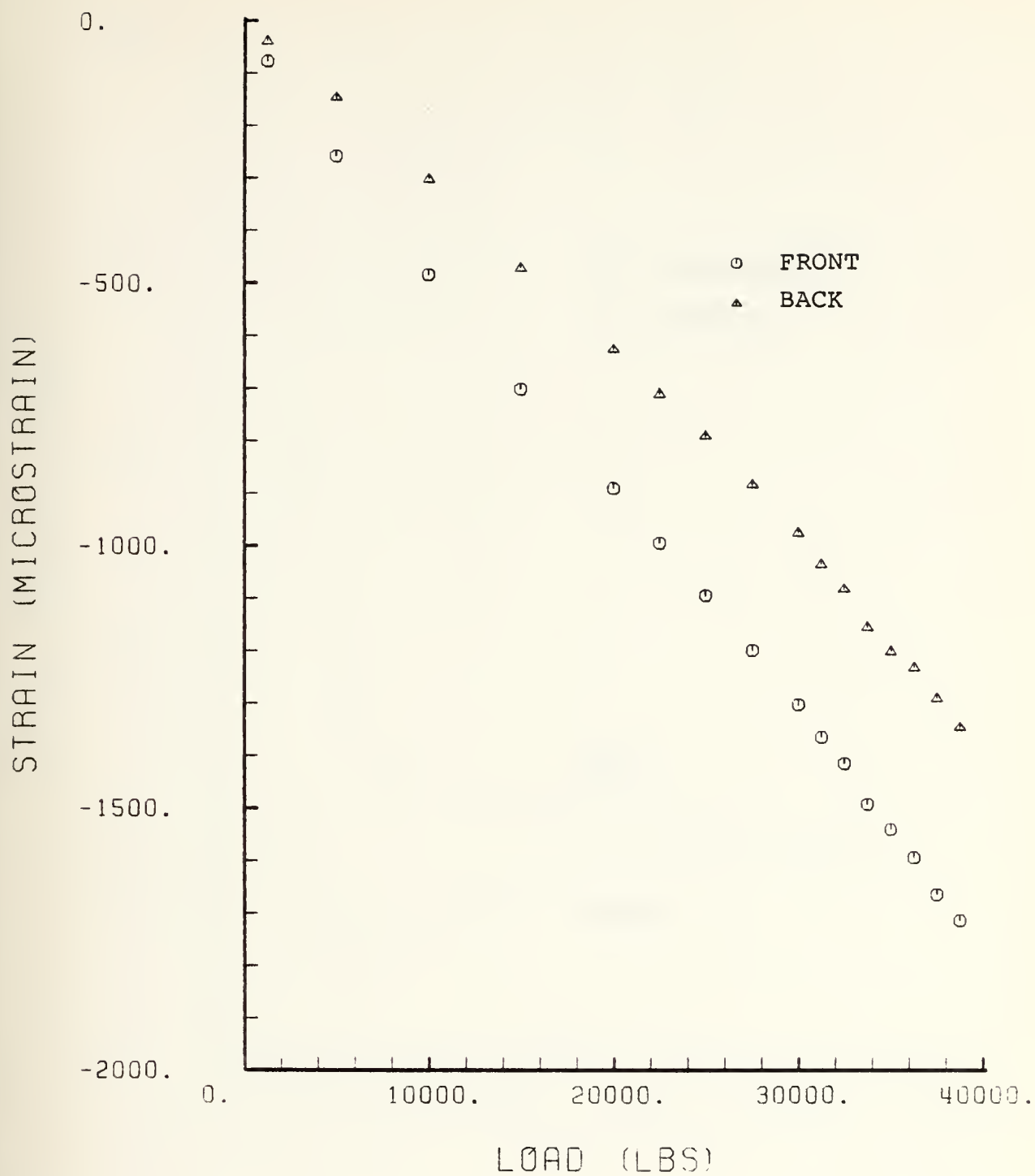
Figure 47. Comparison of Measured Front and Back Strains at Gauges 9 and 21 - Configuration 1B.

122
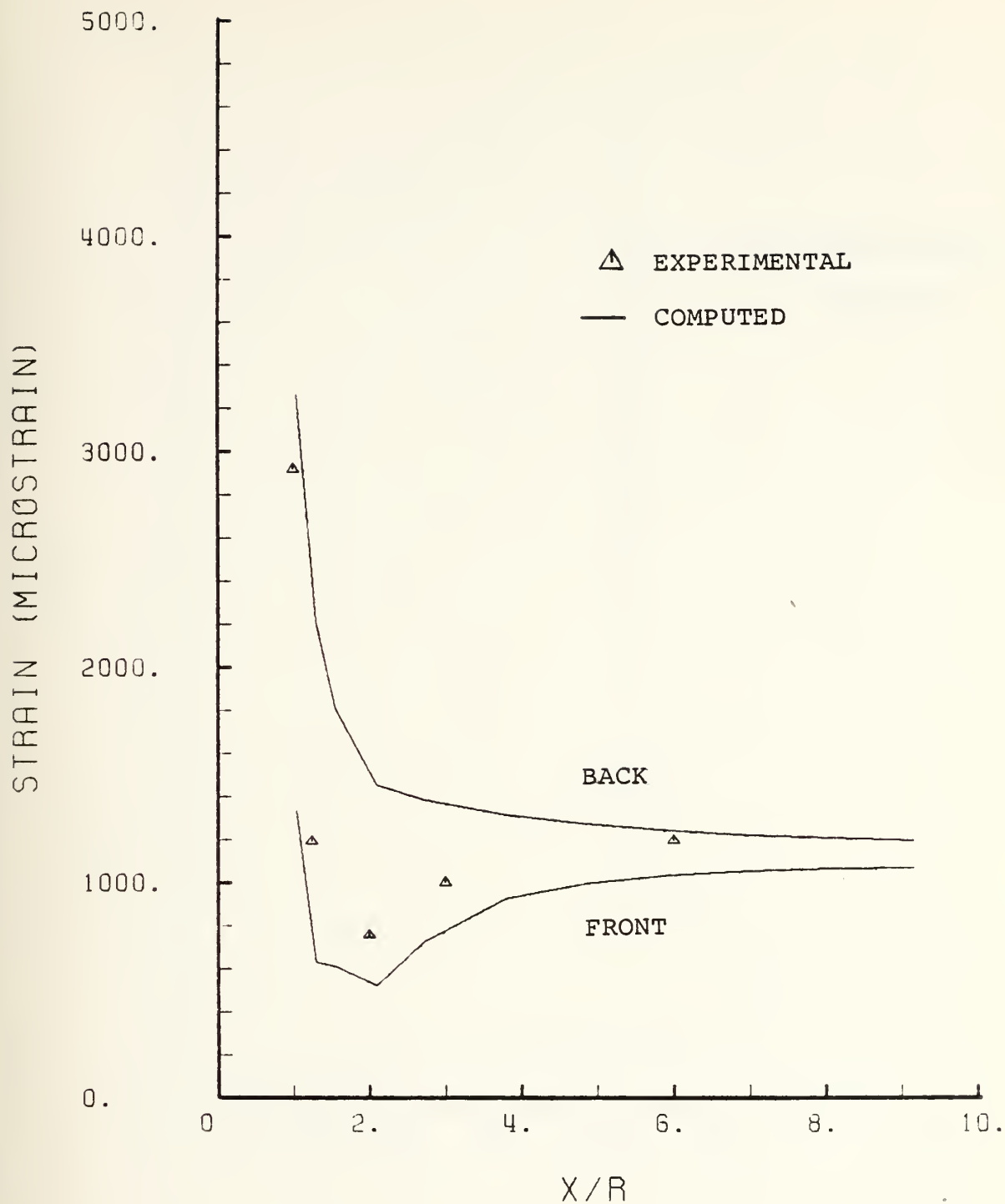
Figure 48.   Comparison of Computed and Measured ε_z vs X/R Configuration 1B.
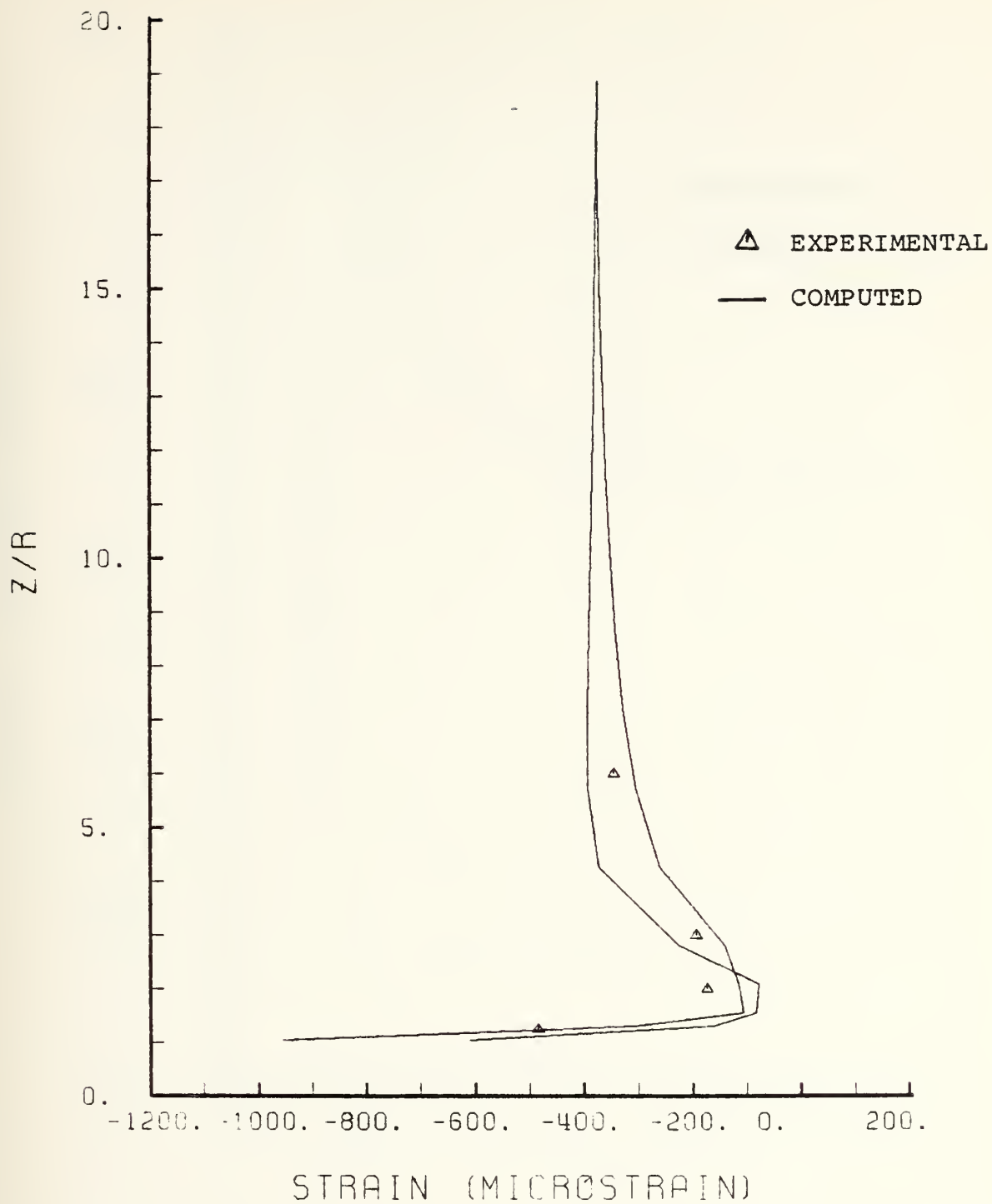
Figure 49. Comparison of Computed and Measured Strain ε_x Vs Z/R Configuration 1B.

124
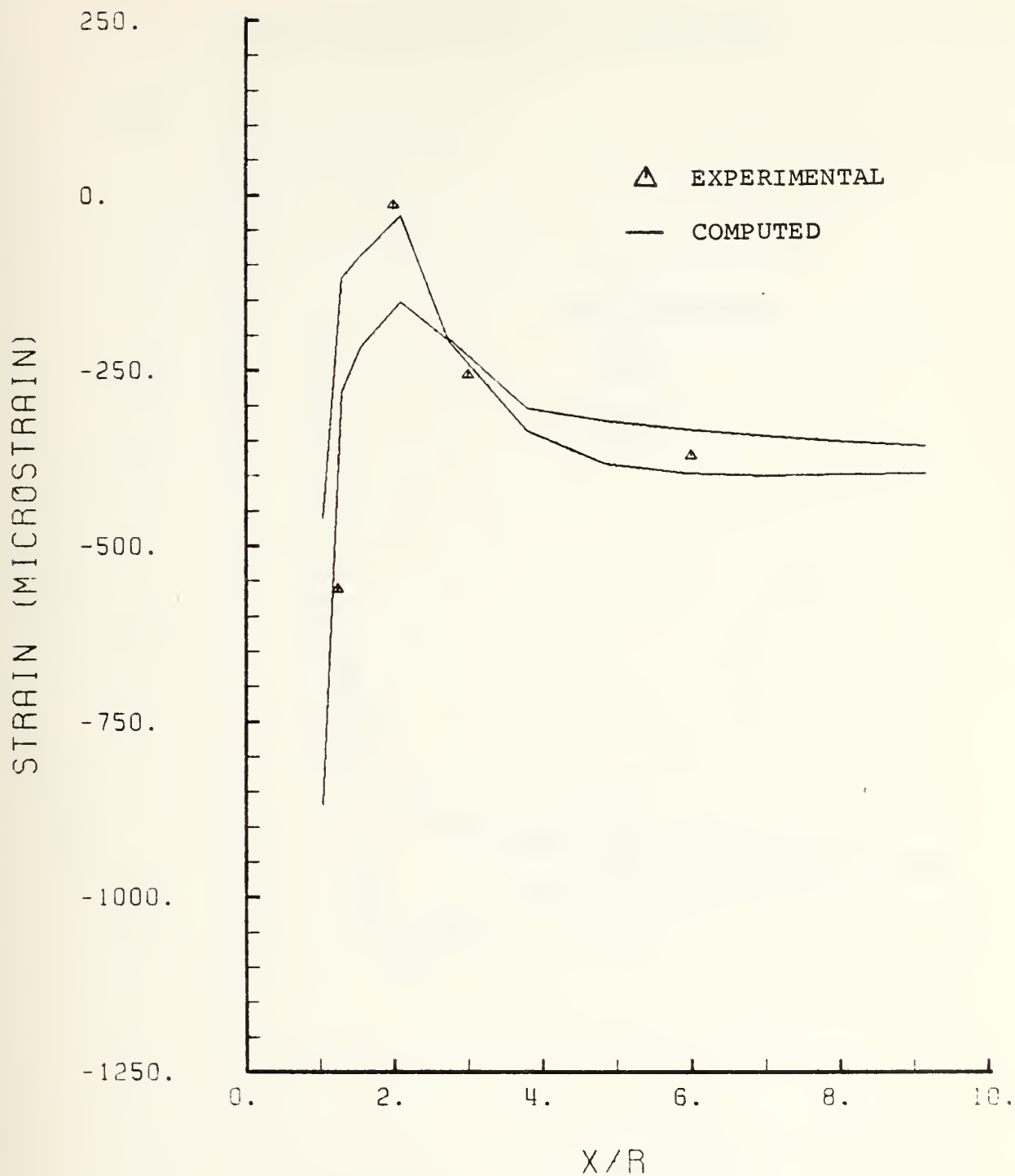
Figure 50.   Comparison of Measured and Computed Strains ε_x Vs X/R Configuration 1B.

APPENDIX C

SECOND REINFORCEMENT CONFIGURATION
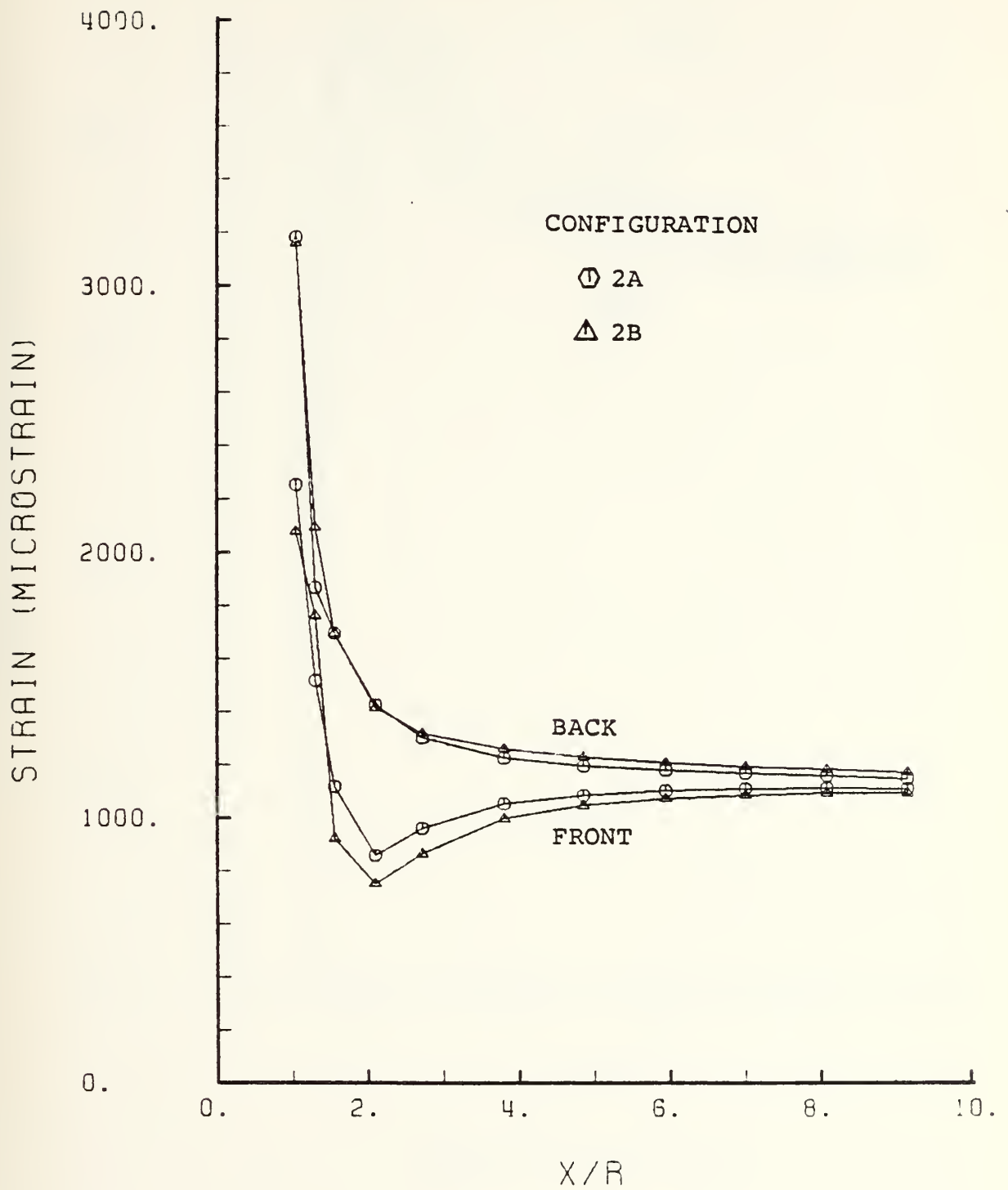
Figure 51. ε_z Vs X/R.
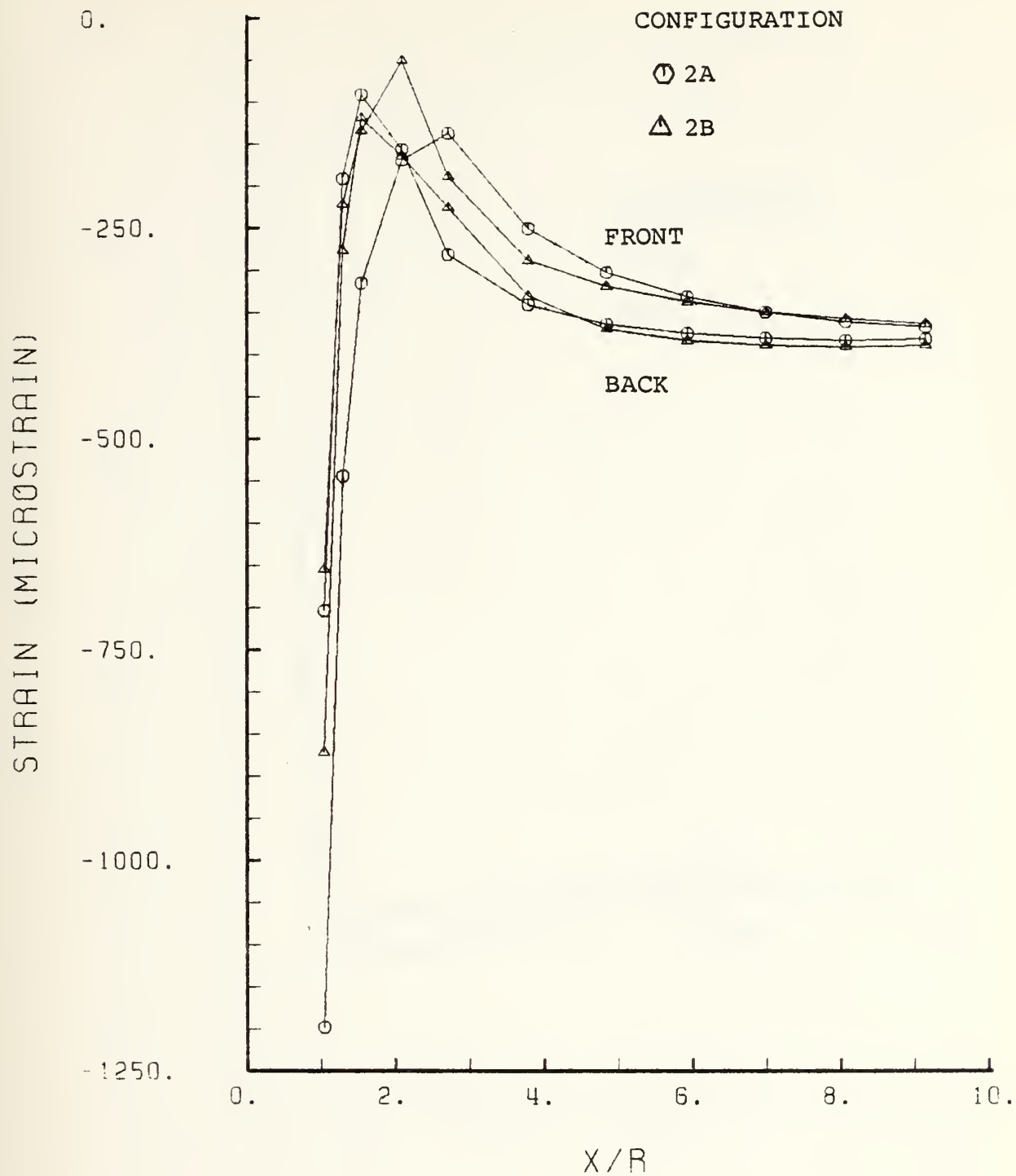
Figure 52. ε_x Vs X/R.

127

Figure 53. ε_{xz} Vs X/R.

Figure 54. ε_z Vs Z/R.

129

Figure 55. ε_x Vs Z/R.

130

Figure 56. ε_{xz} Vs Z/R.

131
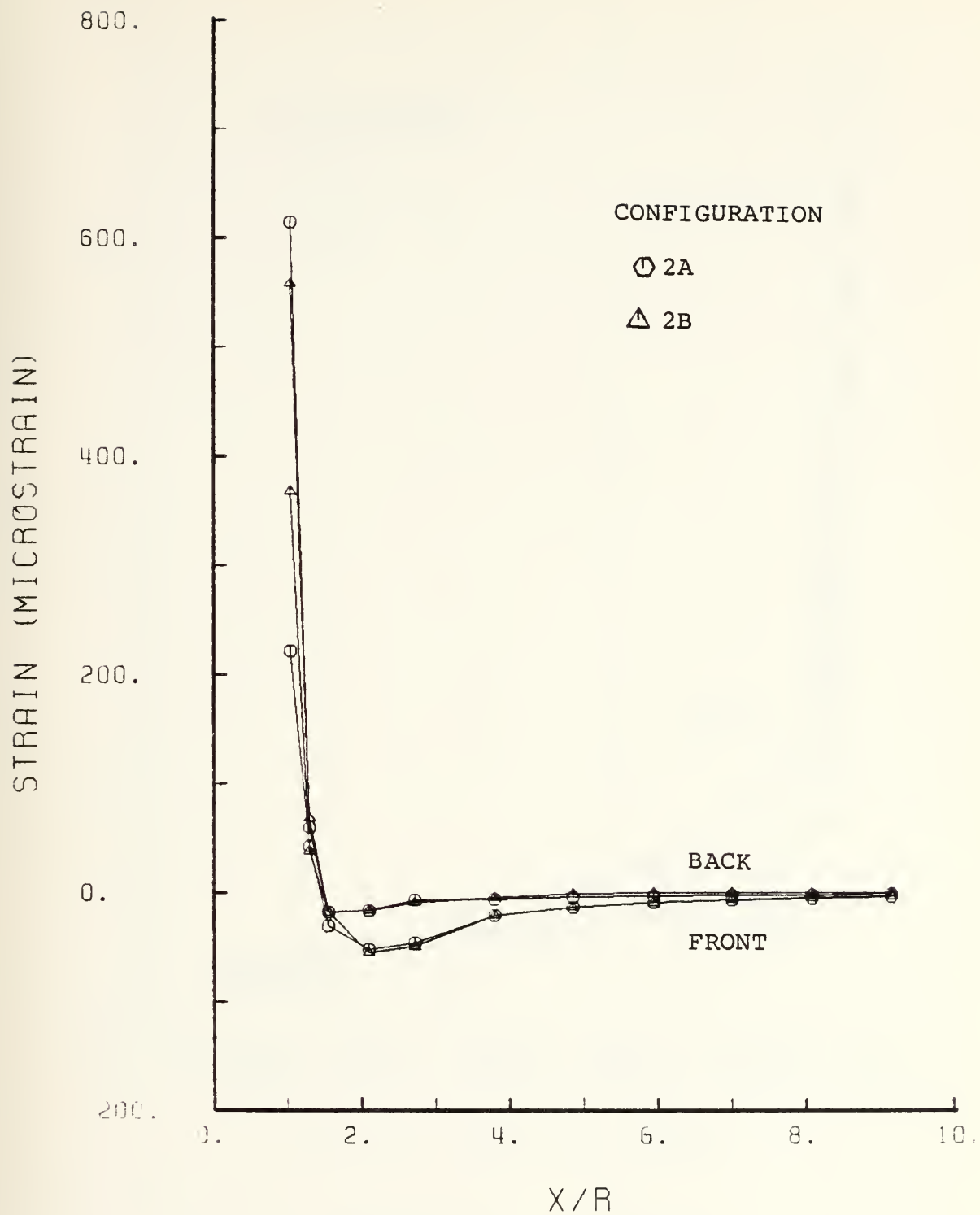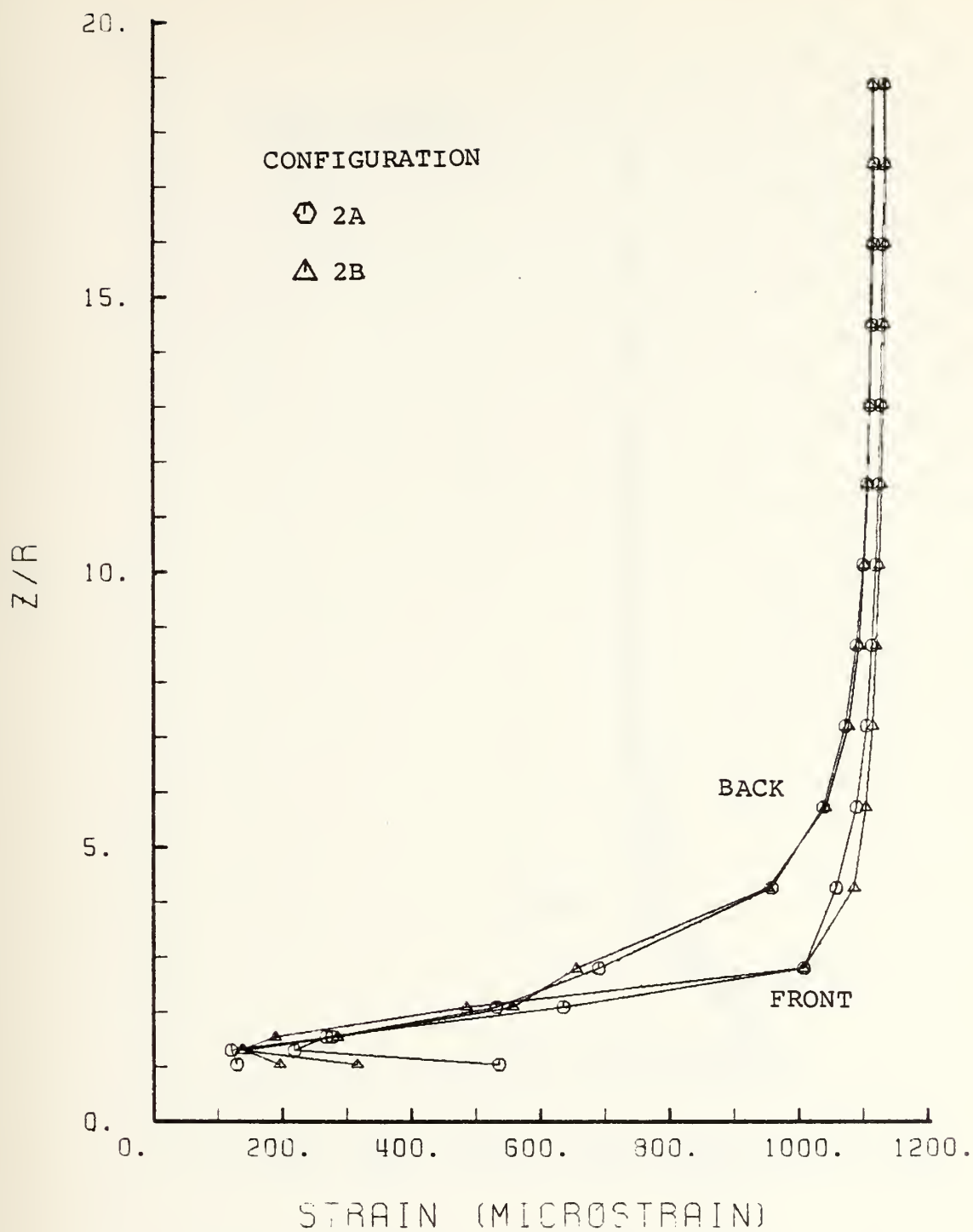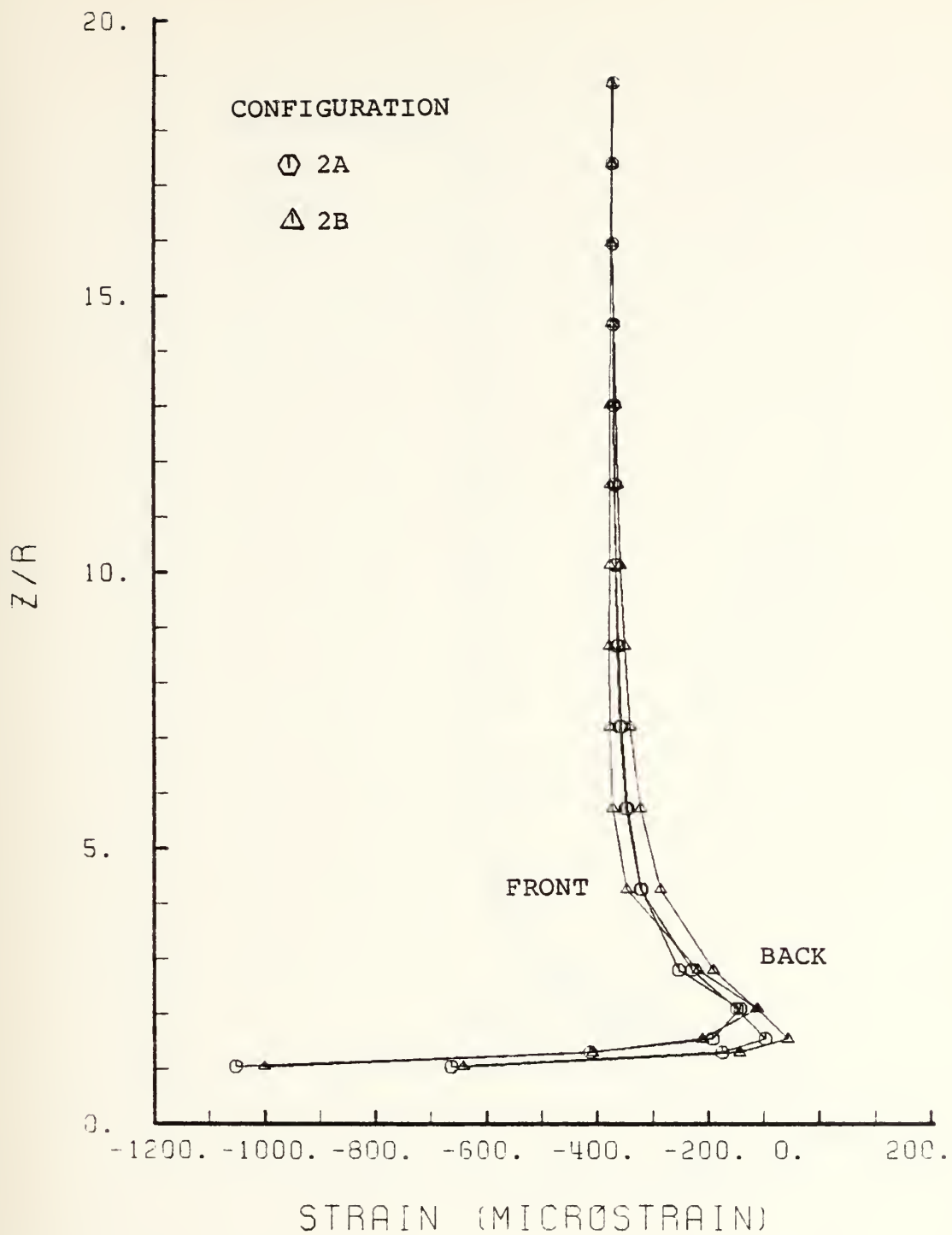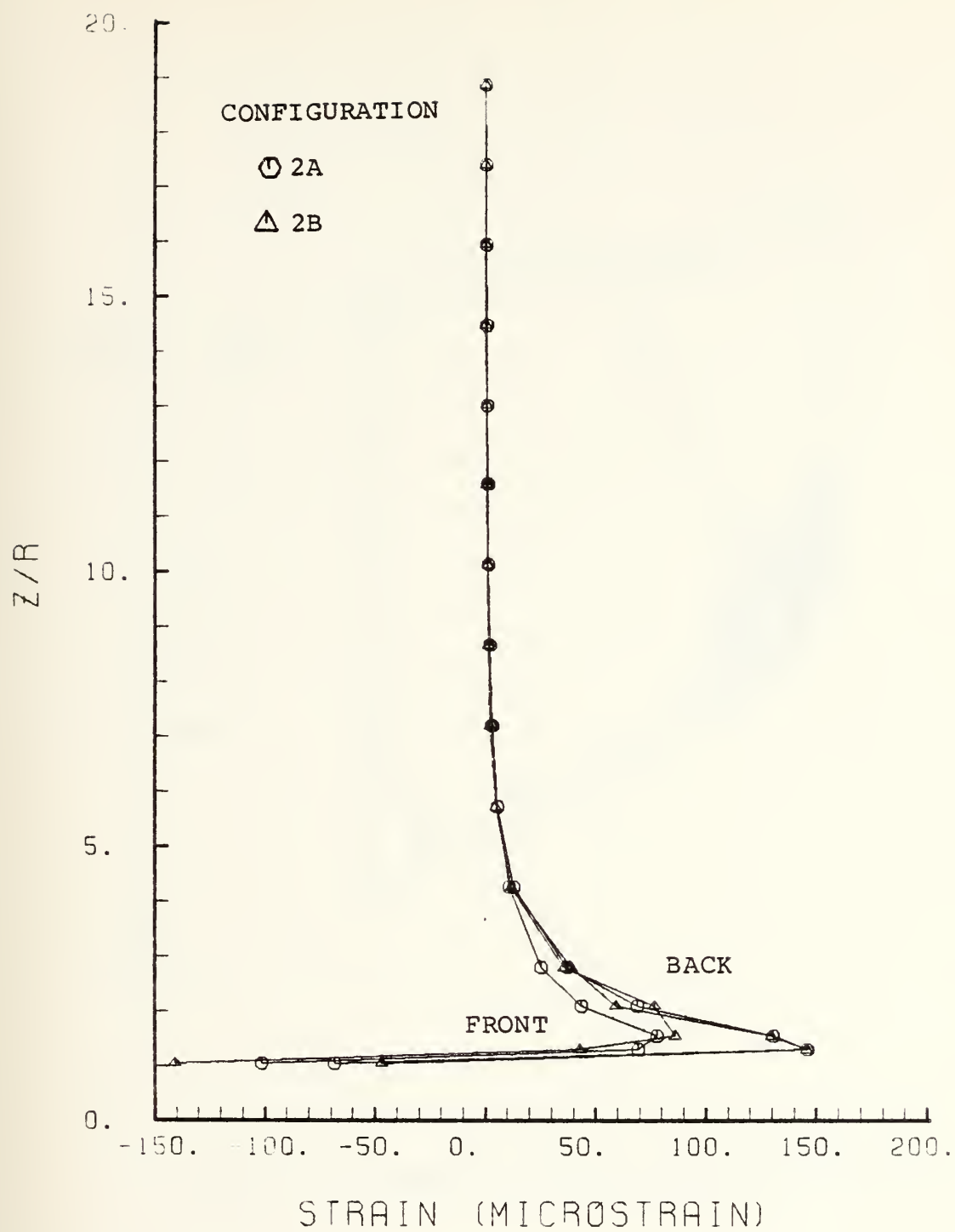
CONTOUR INDEX

1   -1.5×10^{-6}

2   2.0×10^{2}

3   4.0×10^{2}

4   6.0×10^{2}

5   8.0×10^{2}

6   1.0×10^{3}

7   1.2×10^{3}
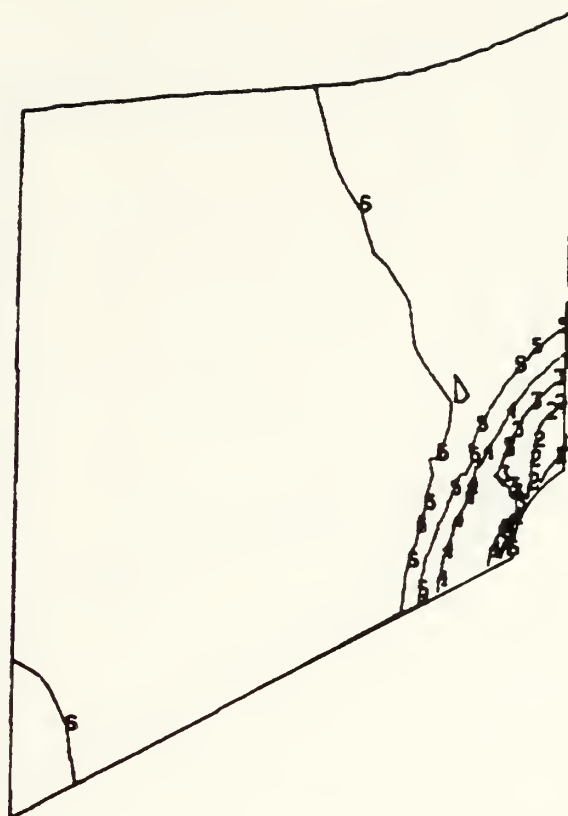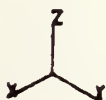
Figure 57.   Contour Plot of N_z Configuration 2A.

CONTOUR INDEX

1   -4×10^2

2   -3×10^2

3   -2×10^2

4   -1×10^2

5   0.0
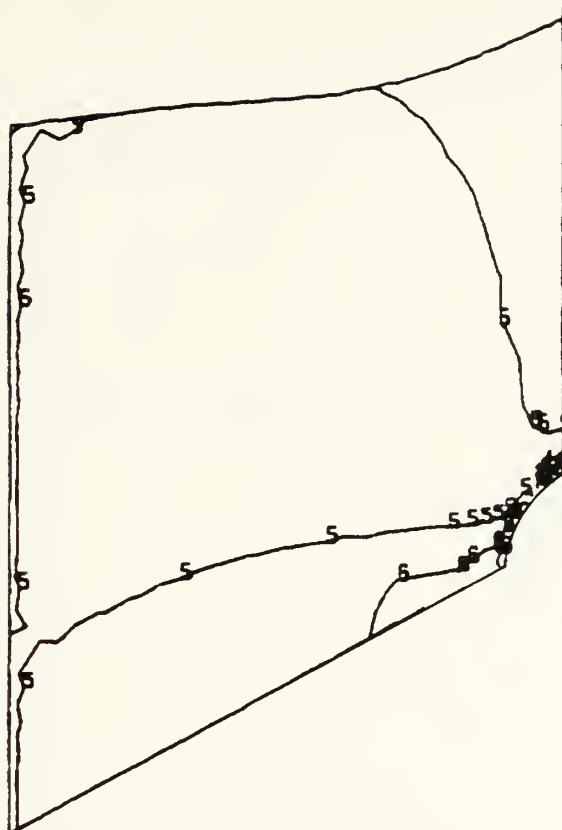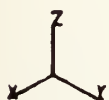
6   1.0×10^2

7   2.0×10^2

Figure 58.   Contour Plot of N_x Configuration 2A.

CONTOUR INDEX

1	-1×10^{2}
2	0.0
3	1.0×10^{2}
4	2.0×10^{2}
5	2.0×10^{2}
6	3.0×10^{2}
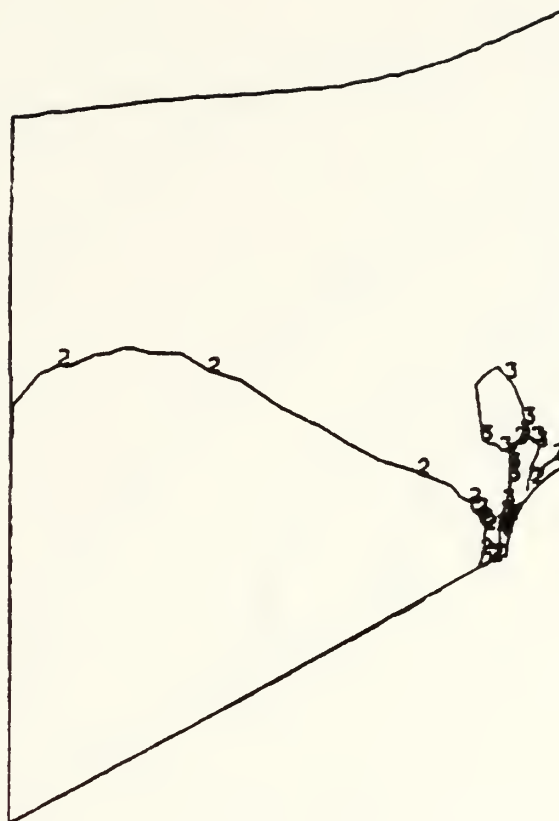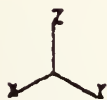
Figure 59.   Contour Plot of N_{xz} Configuration 2A.

CONTOUR INDEX

1   2×10^{-3}

2   4×10^{-3}

3   6×10^{-3}

4   8×10^{-3}

5   10×10^{-3}
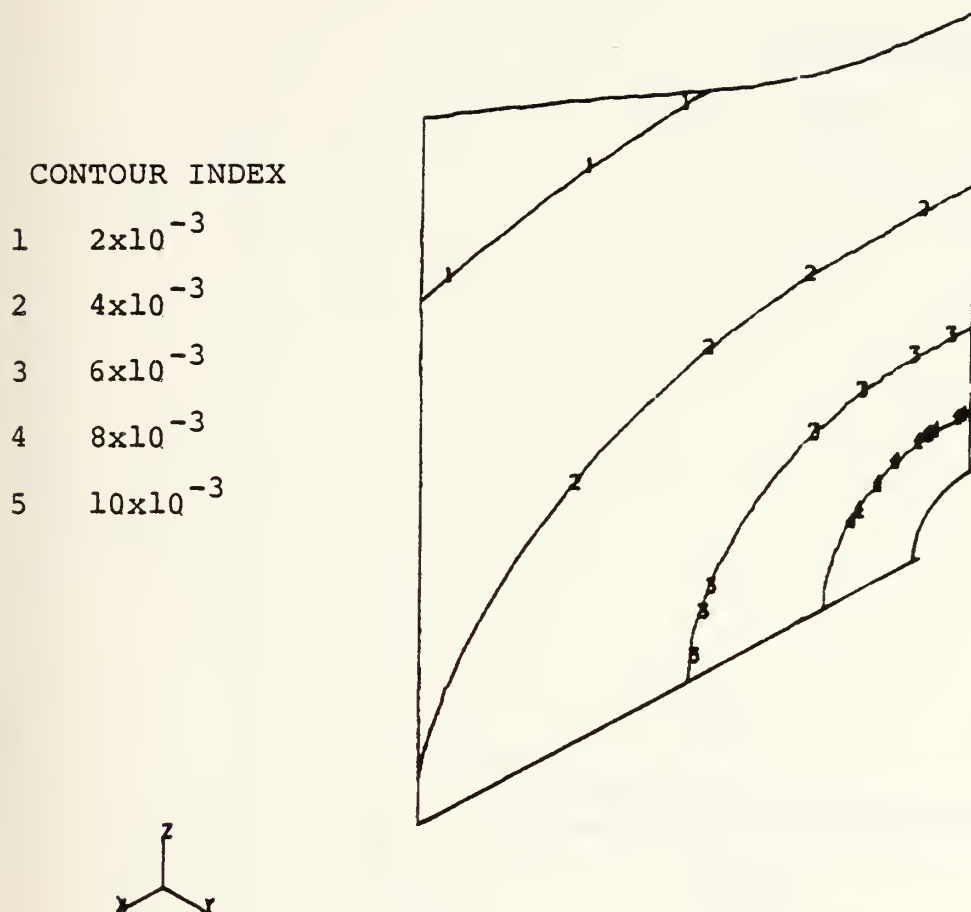
Figure 60.   Contour of Out of Plane Deflections
Configuration 2A.

135

APPENDIX D
THIRD REINFORCEMENT CONFIGURATION
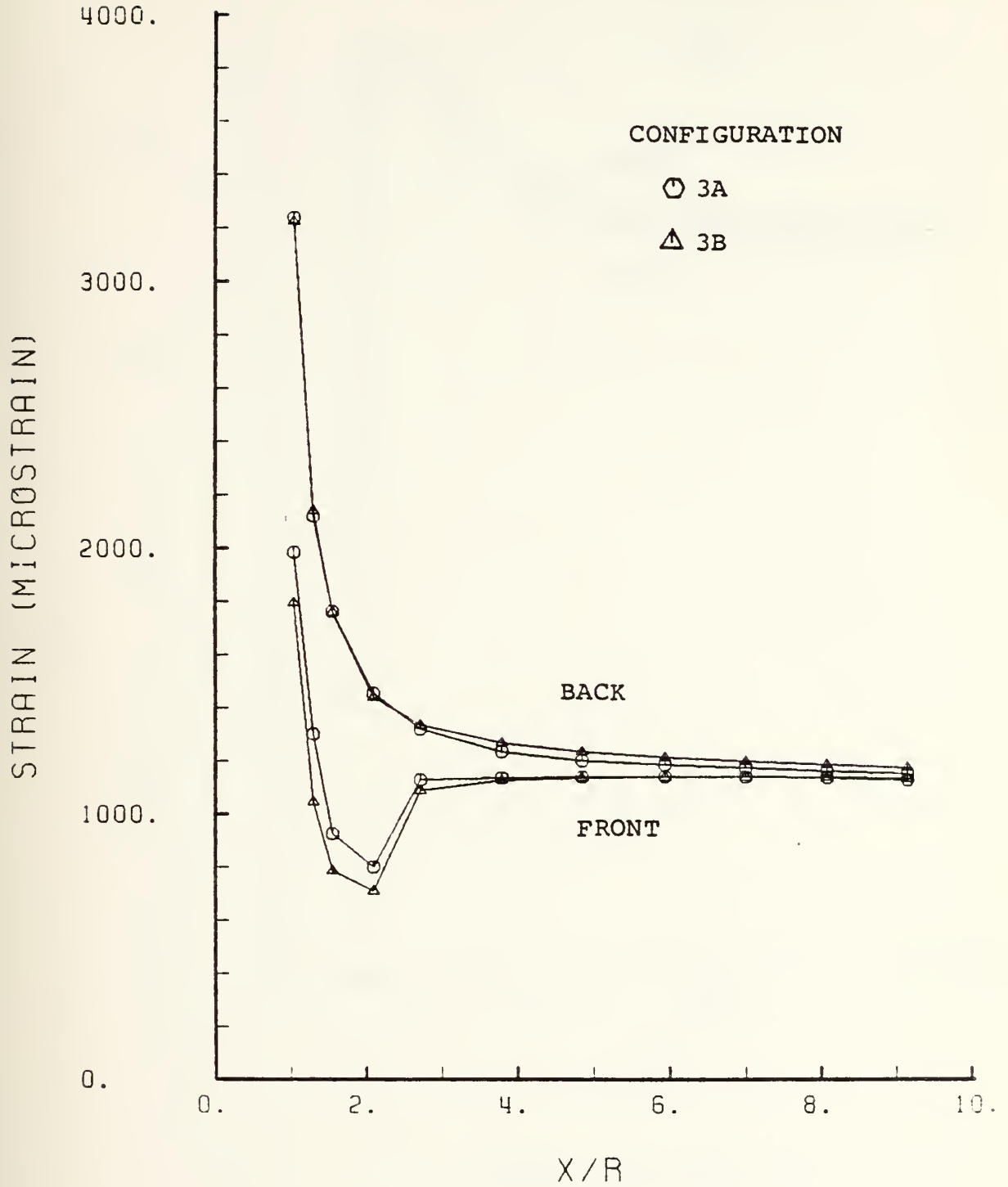
Figure 61. ε_z Vs X/R.
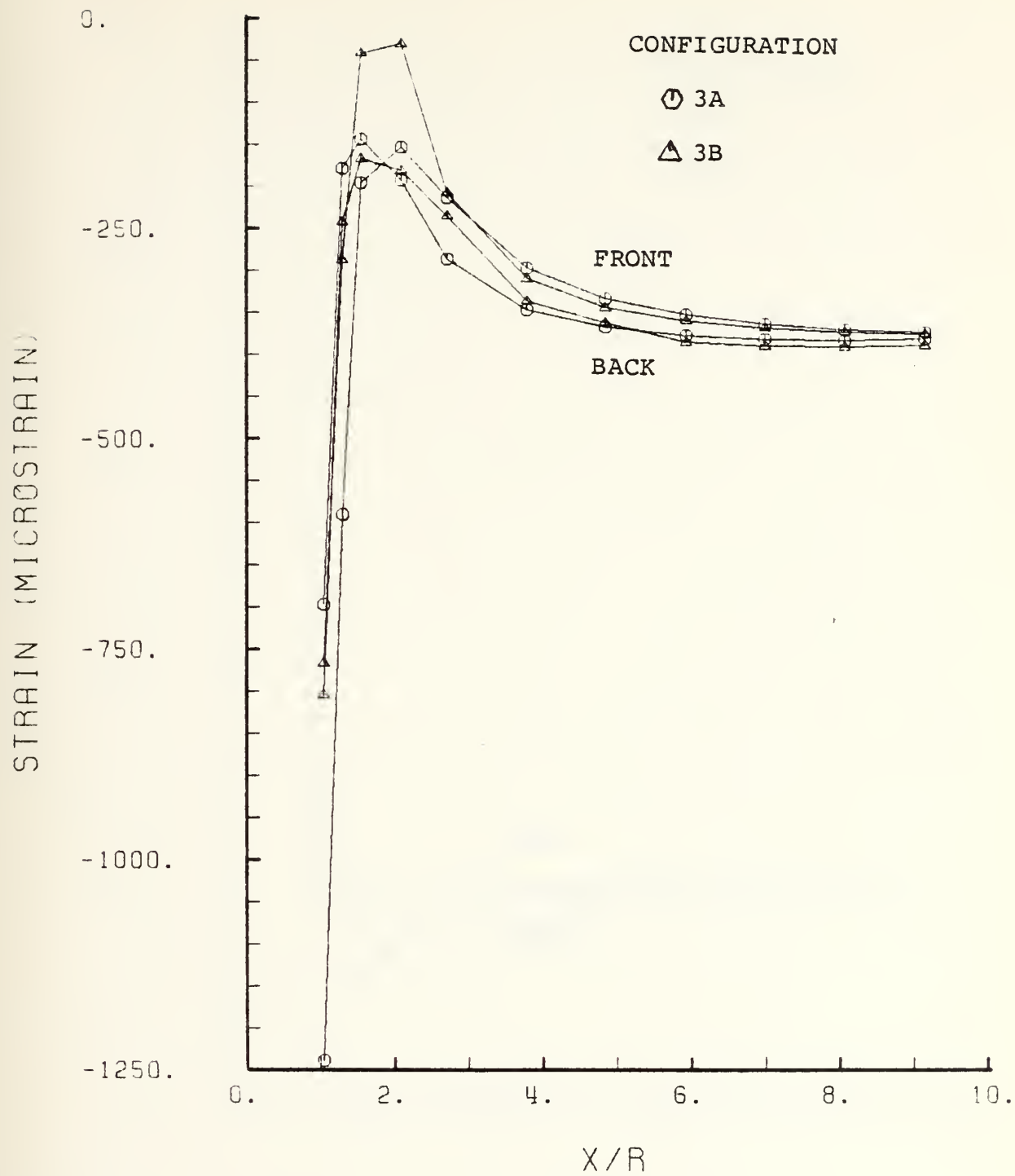
136

Figure 62. ε_x Vs X/R.

137

Figure 63. ε_{xz} Vs X/R.

138

Figure 64. ε_z Vs Z/R.

139

Figure 65. ε_x Vs Z/R.

140

Figure 66. ε_{xz} Vs Z/R.

141

CONTOUR INDEX

1	-1.5×10^{-5}
2	2×10^2
3	4×10^2
4	6×10^2
5	8×10^2
6	1.0×10^3
7	1.2×10^3
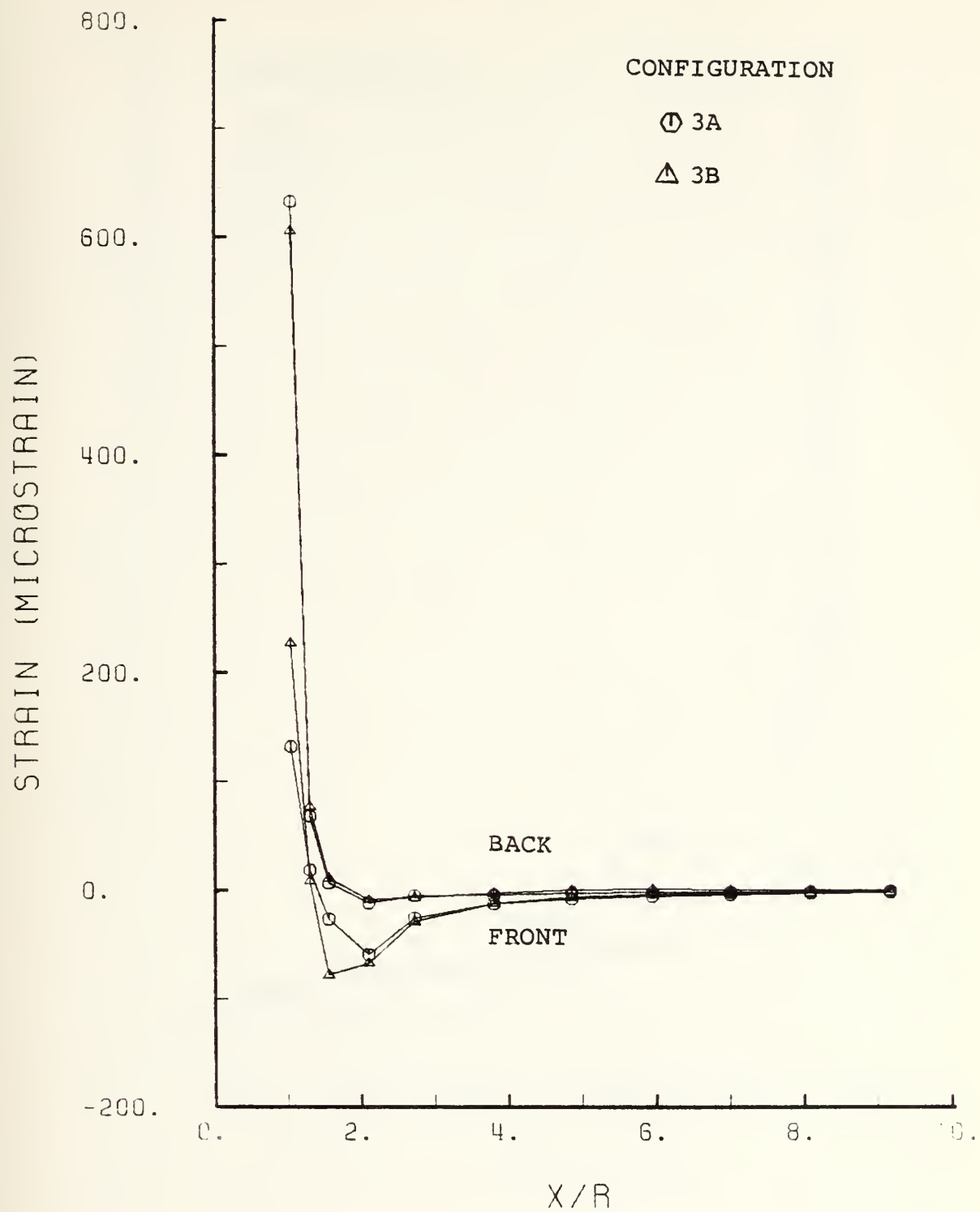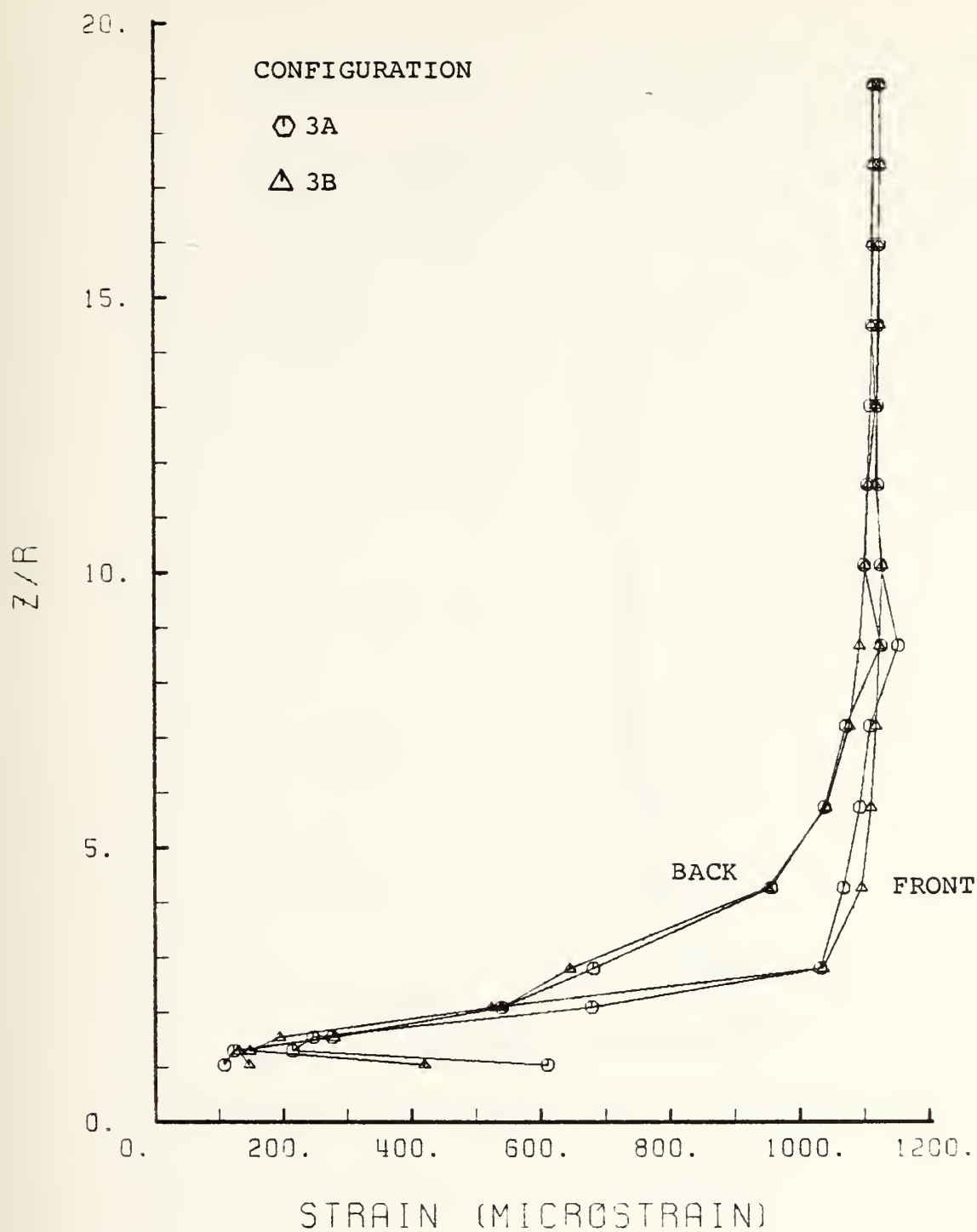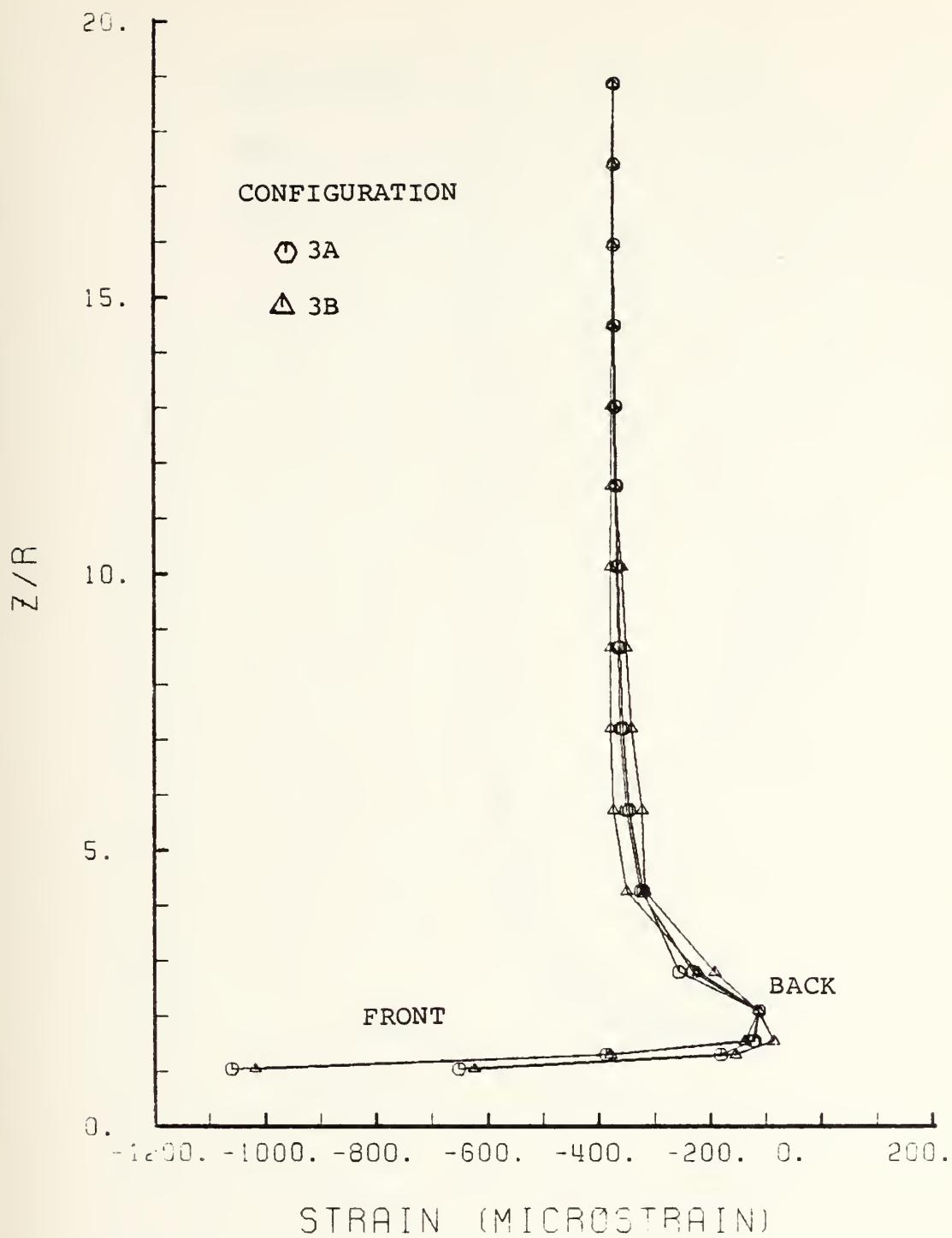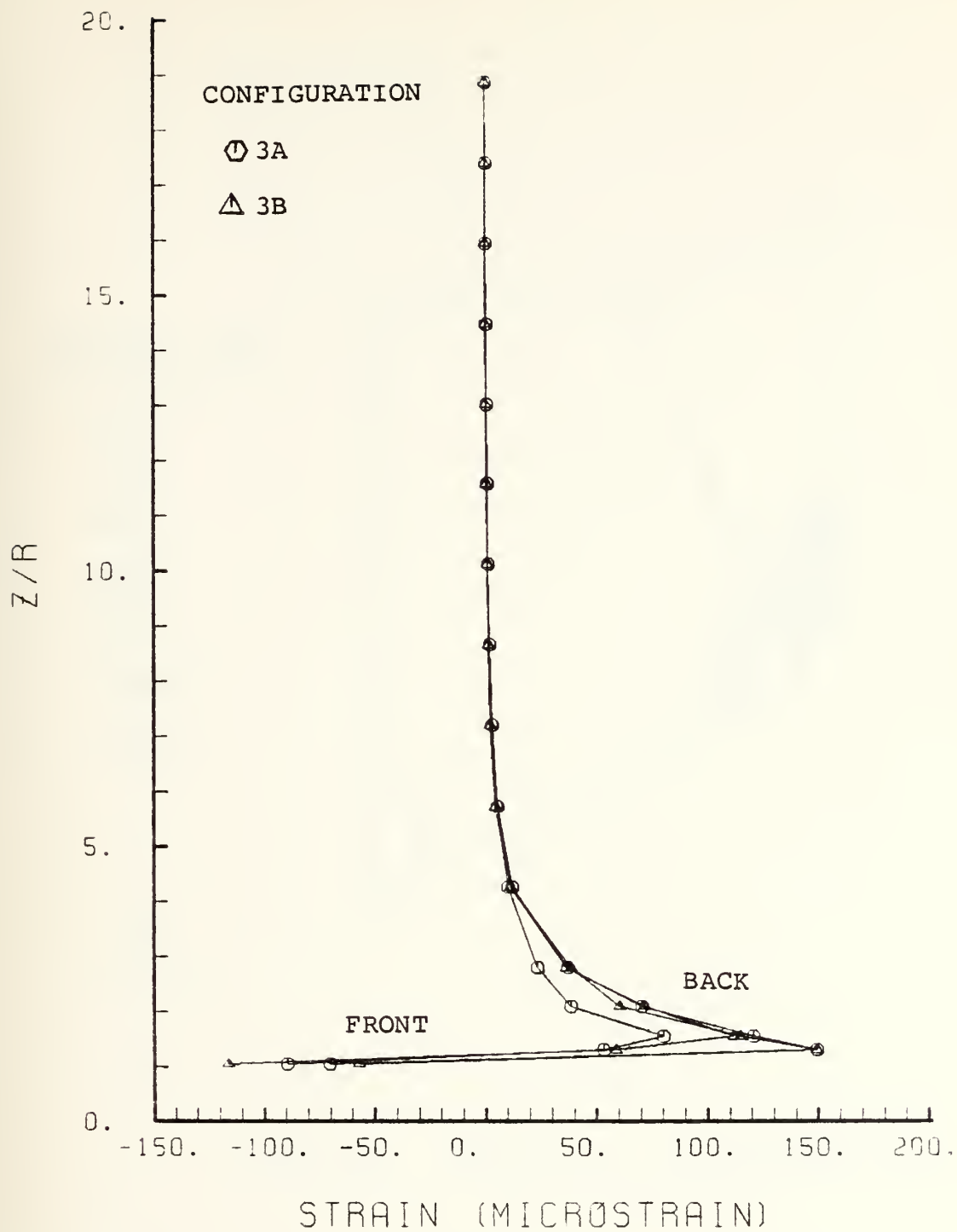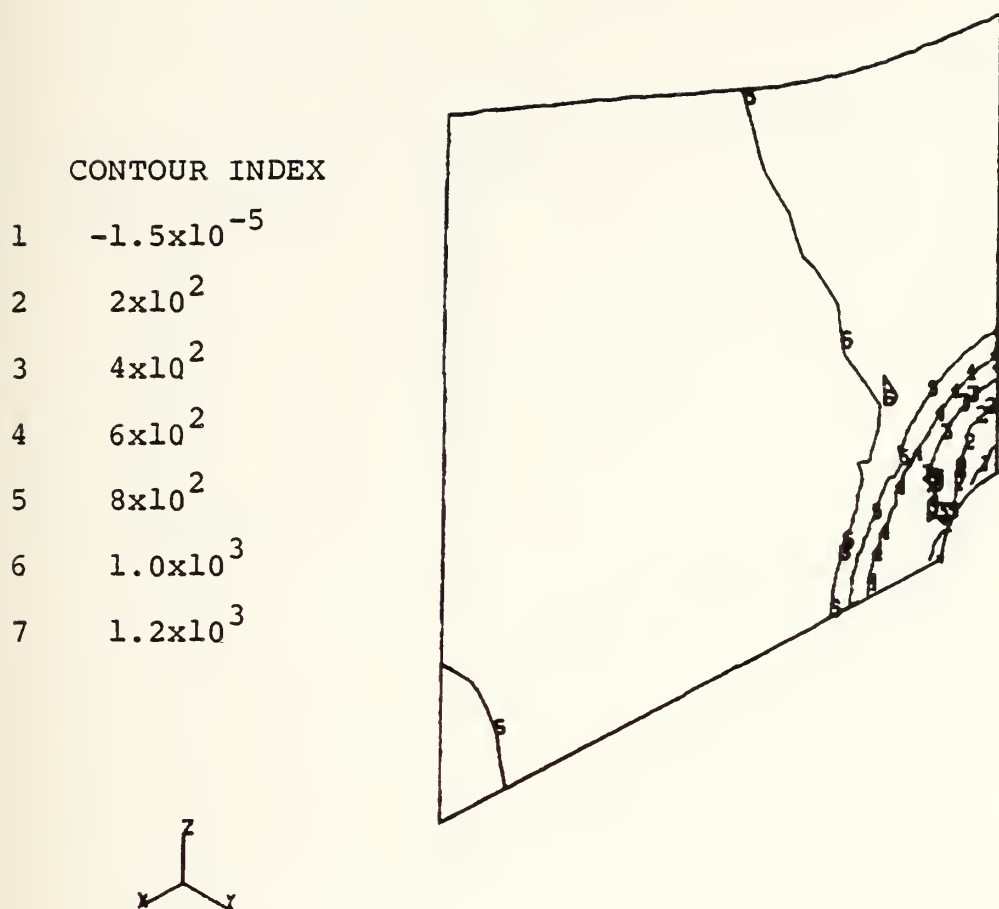
Figure 67. Contour of N_z Configuration 3A.

CONTOUR INDEX

1   -3×10^2

2   2×10^2

3   -1×10^2

4   0.0

5   1.0×10^2
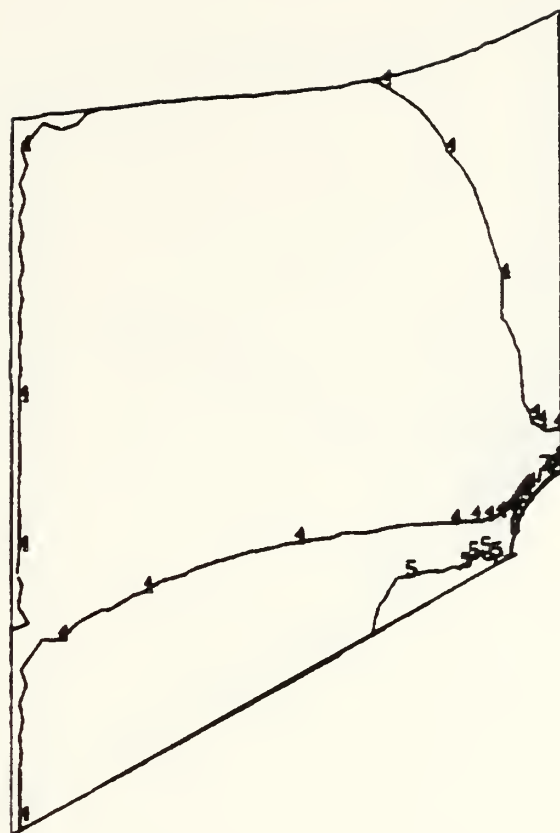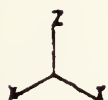
Figure 68.   Contour of N_x
             Configuration 3A.

143

CONTOUR INDEX

1	-5×10^{1}
2	0.0
3	5×10^{1}
4	1×10^{2}
5	1.5×10^{2}
6	$2.\times10^{2}$
7	2.5×10^{2}
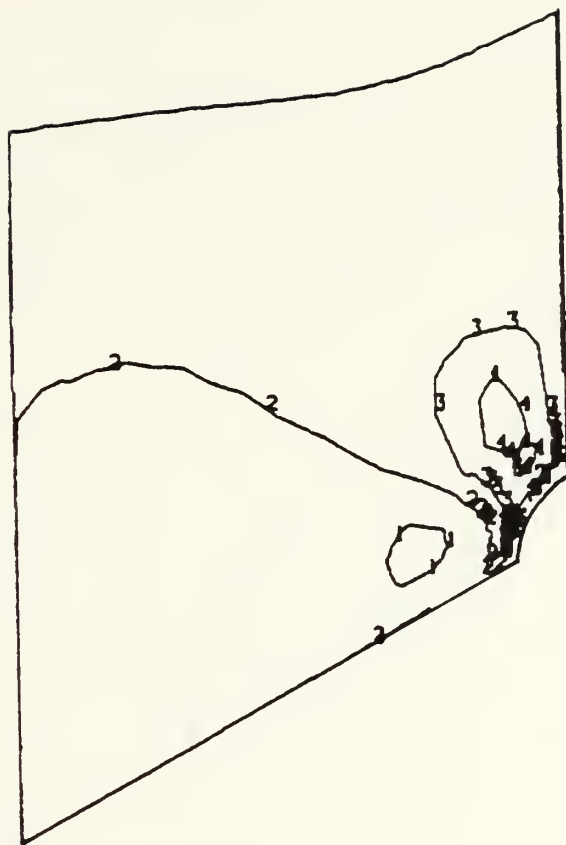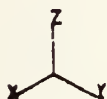
Figure 69. Contour of N_{xz} Configuration 3A.

CONTOUR INDEX

1   2×10^{-4}

2   4×10^{-3}

3   6×10^{-3}

4   8×10^{-3}

5   10×10^{-3}

6   1.2×10^{-2}
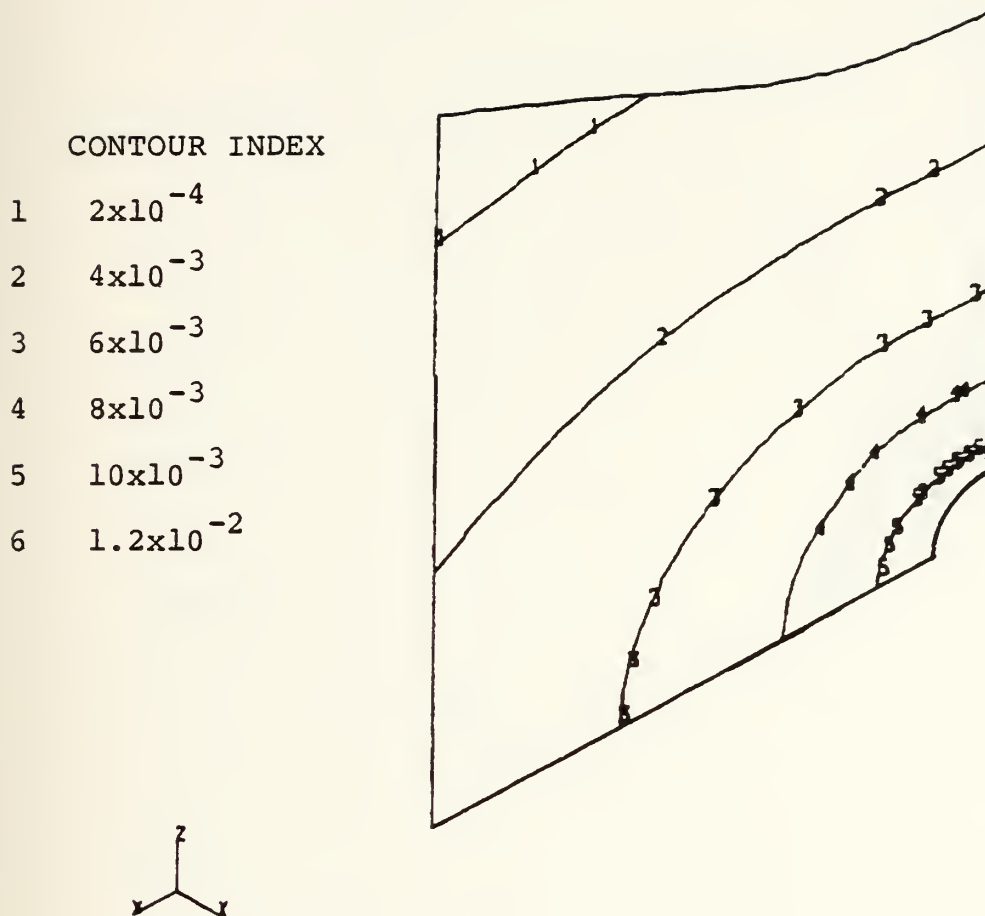
Figure 70.   Contour of Out of Plane Deflections
             Configuration 3A.

CONTOUR INDEX

1	0
2	2×10^2
3	4×10^2
4	6×10^2
5	8×10^2
6	1×10^3
7	1.2×10^3
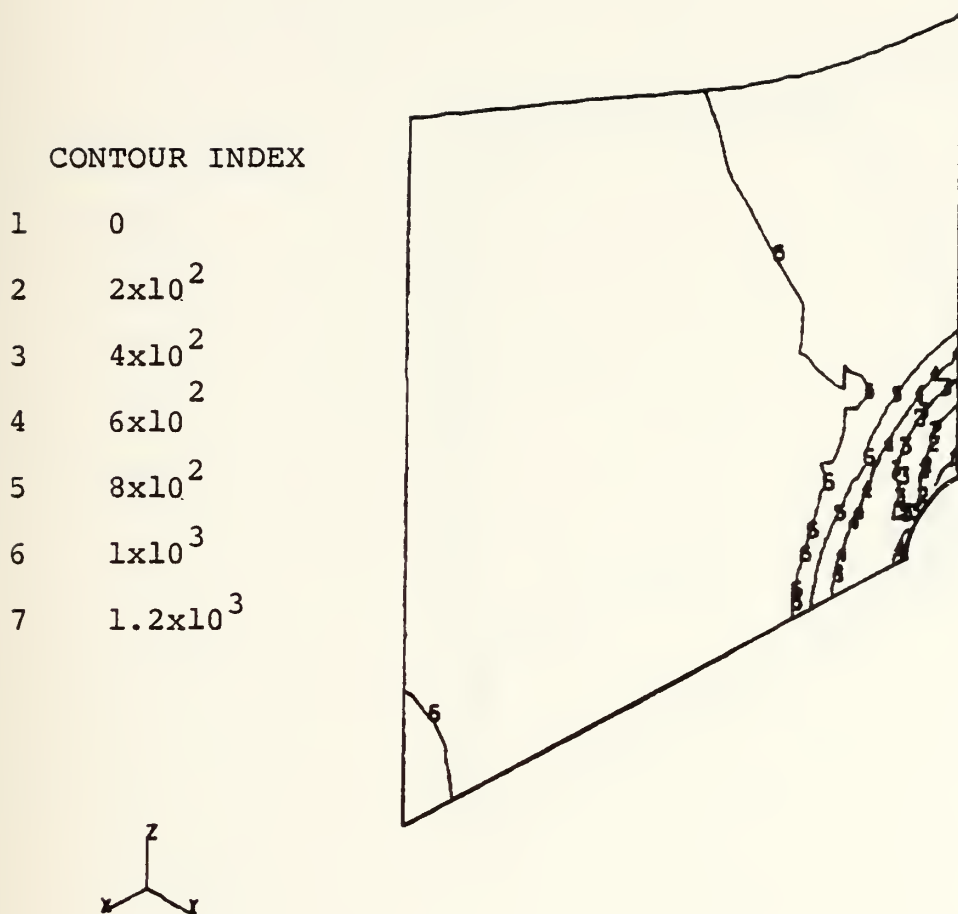
Figure 71. Contour of N_z Configuration 3B.

146

CONTOUR INDEX

1   -3×10^2

2   -2×10^2

3   -1×10^2

4   0.0

5   1×10^2
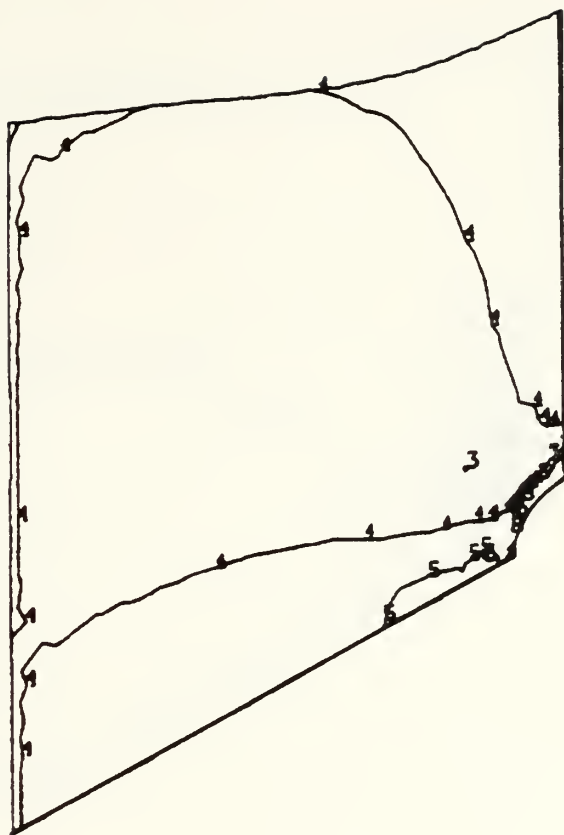
Figure 72.   Contour of N_x Configuration 3B.

CONTOUR INDEX

1	-1×10^2
2	-5×10^1
3	0
4	5×10^1
5	1×10^2
6	1.5×10^2
7	$2. \times 10^2$
8	2.5×10^2
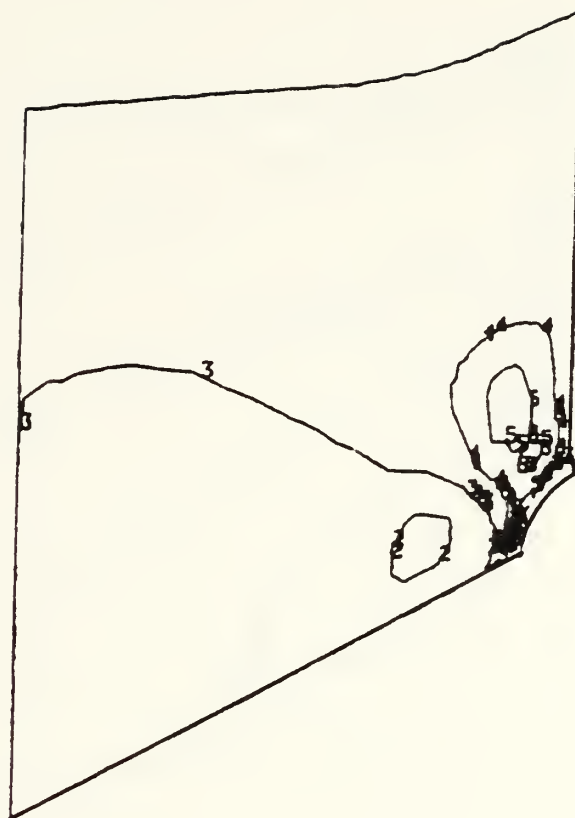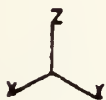
Figure 73.   Contour Plot of N_{xz} Configuration 3B.

CONTOUR INDEX

1	2×10^{-3}
2	4×10^{-3}
3	6×10^{-3}
4	8×10^{-3}
5	1×10^{-2}
6	1.2×10^{-2}
7	1.4×10^{-2}
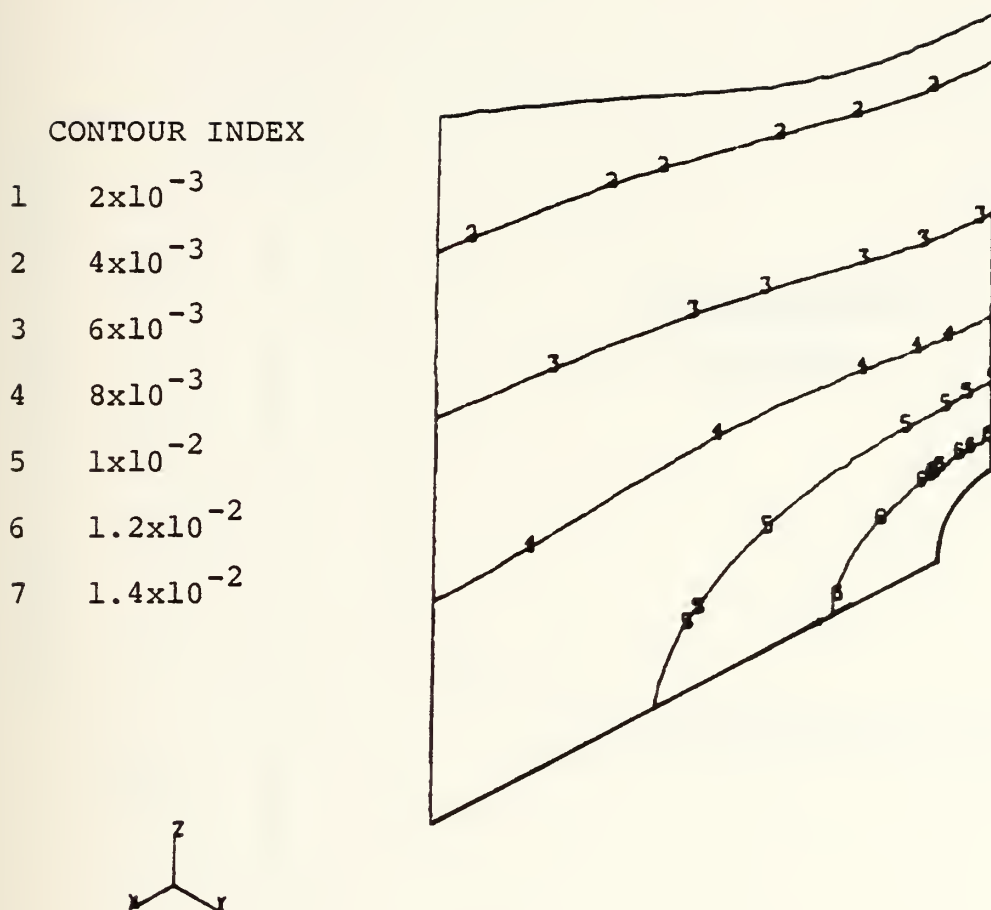
Figure 74.   Contour Plot of Out of Plane
Deflections - Configuration 3B.
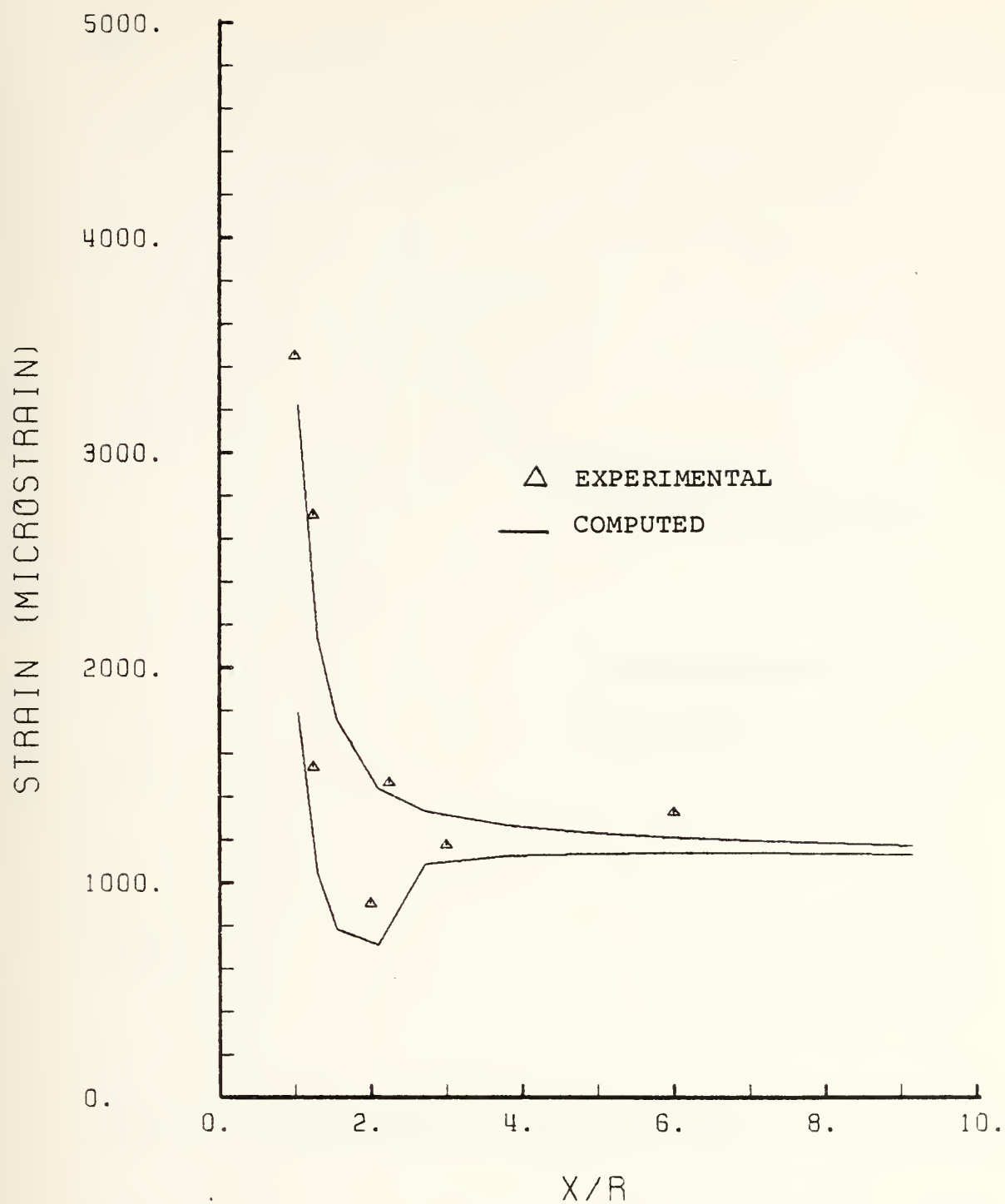
Figure 75. Comparison of Measured and Computed Strains ε_z Vs X/R - Configuration 3B.
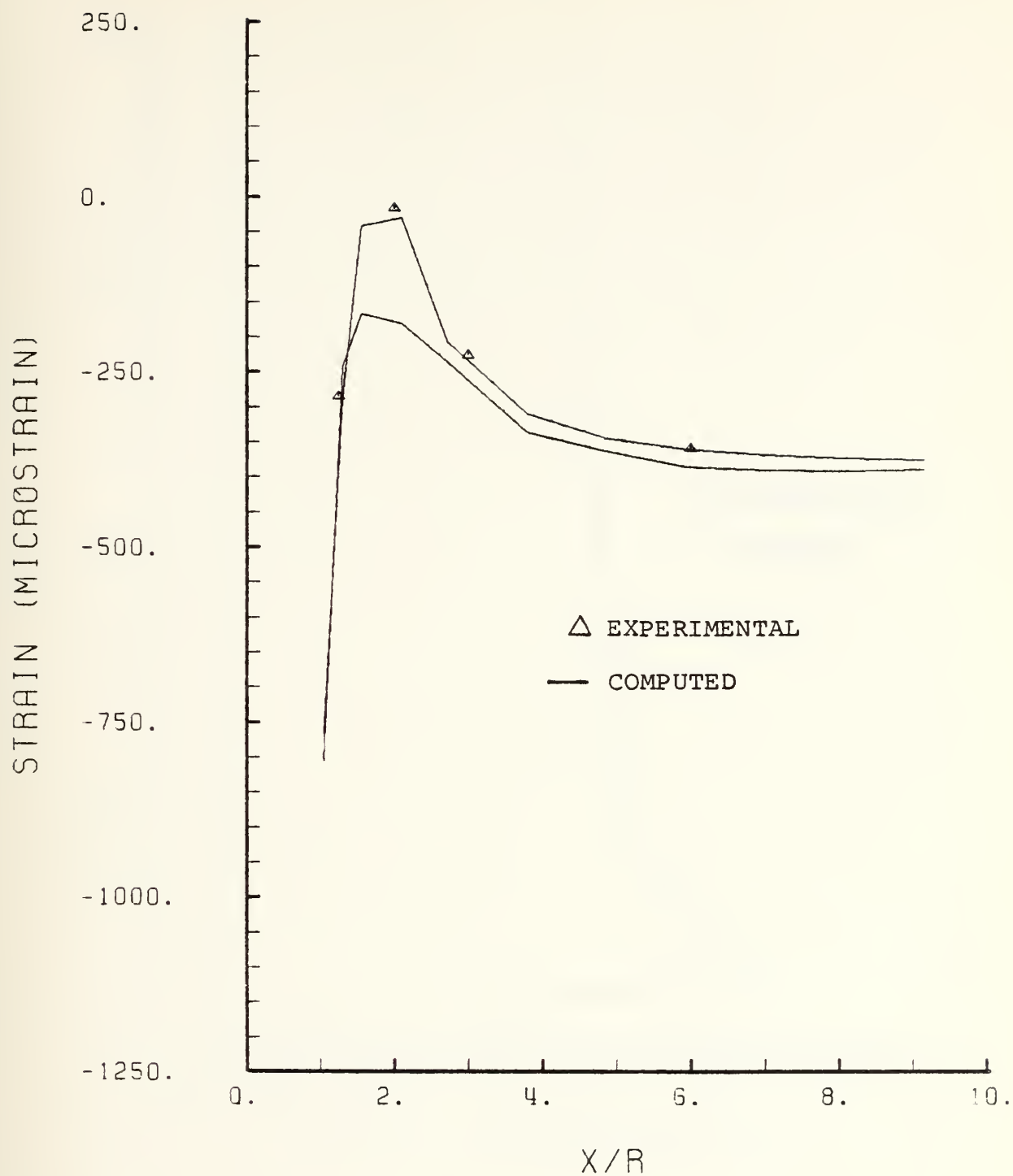
Figure 76.   Comparison of Measured and Computed Strains
ε_x Vs X/R Configuration 3B.

151
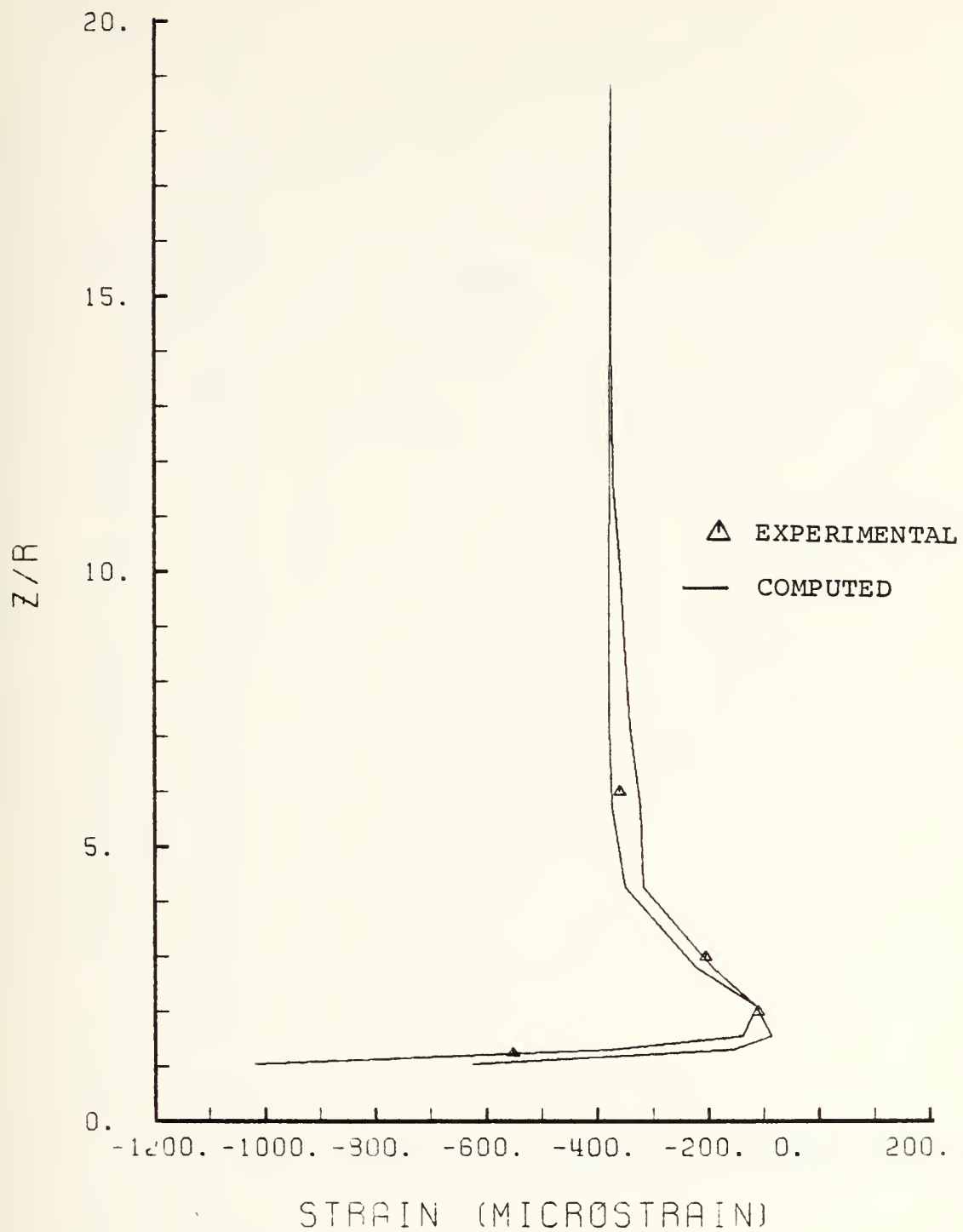
Figure 77.   Comparison of Measured and Computed
Strain ε_x Vs Z/R - Configuration 3B.

152
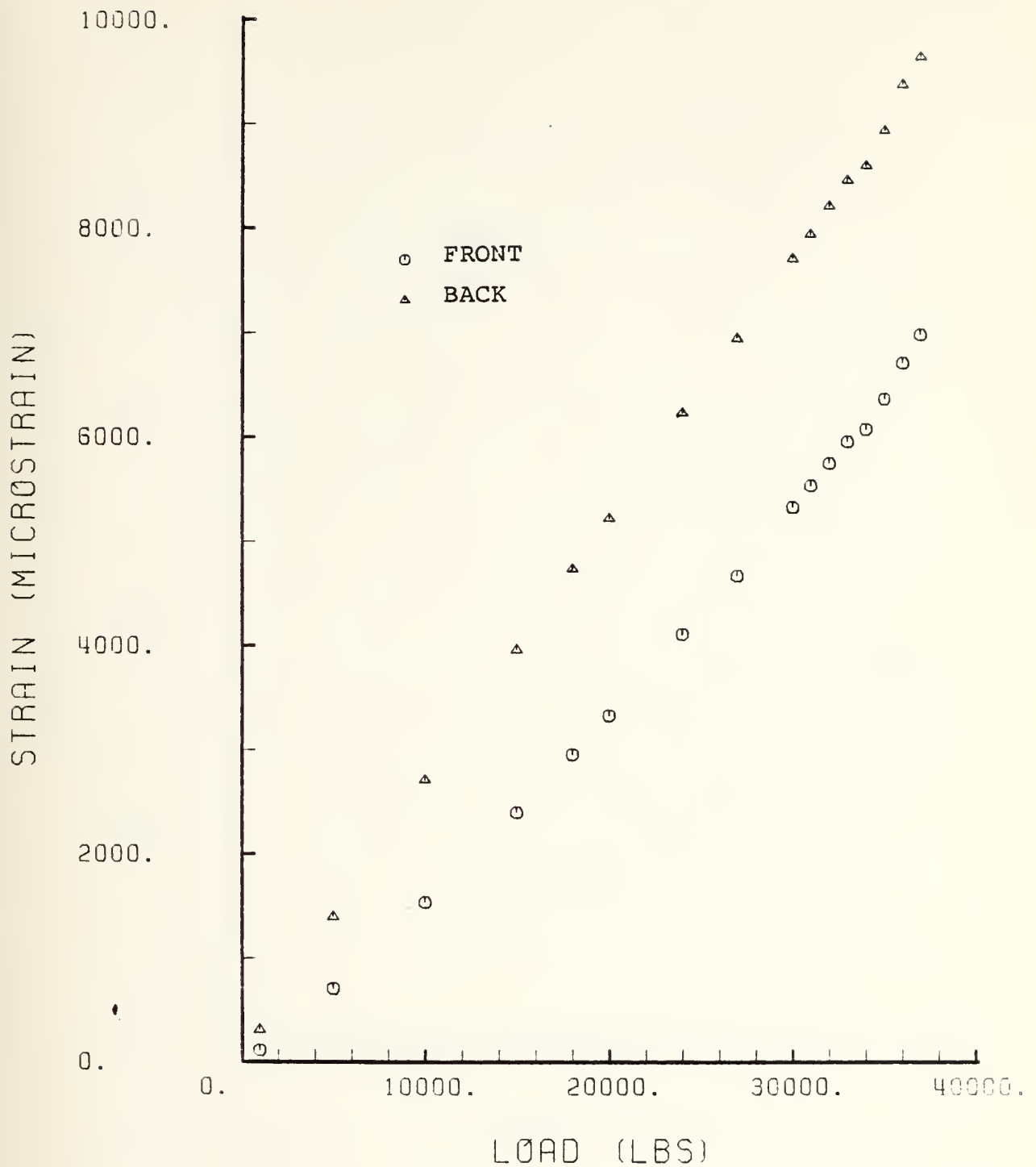
Figure 78. Comparison of Measured Front and Back
Strains at Gauges 5 and 19 –
Configuration 3B.
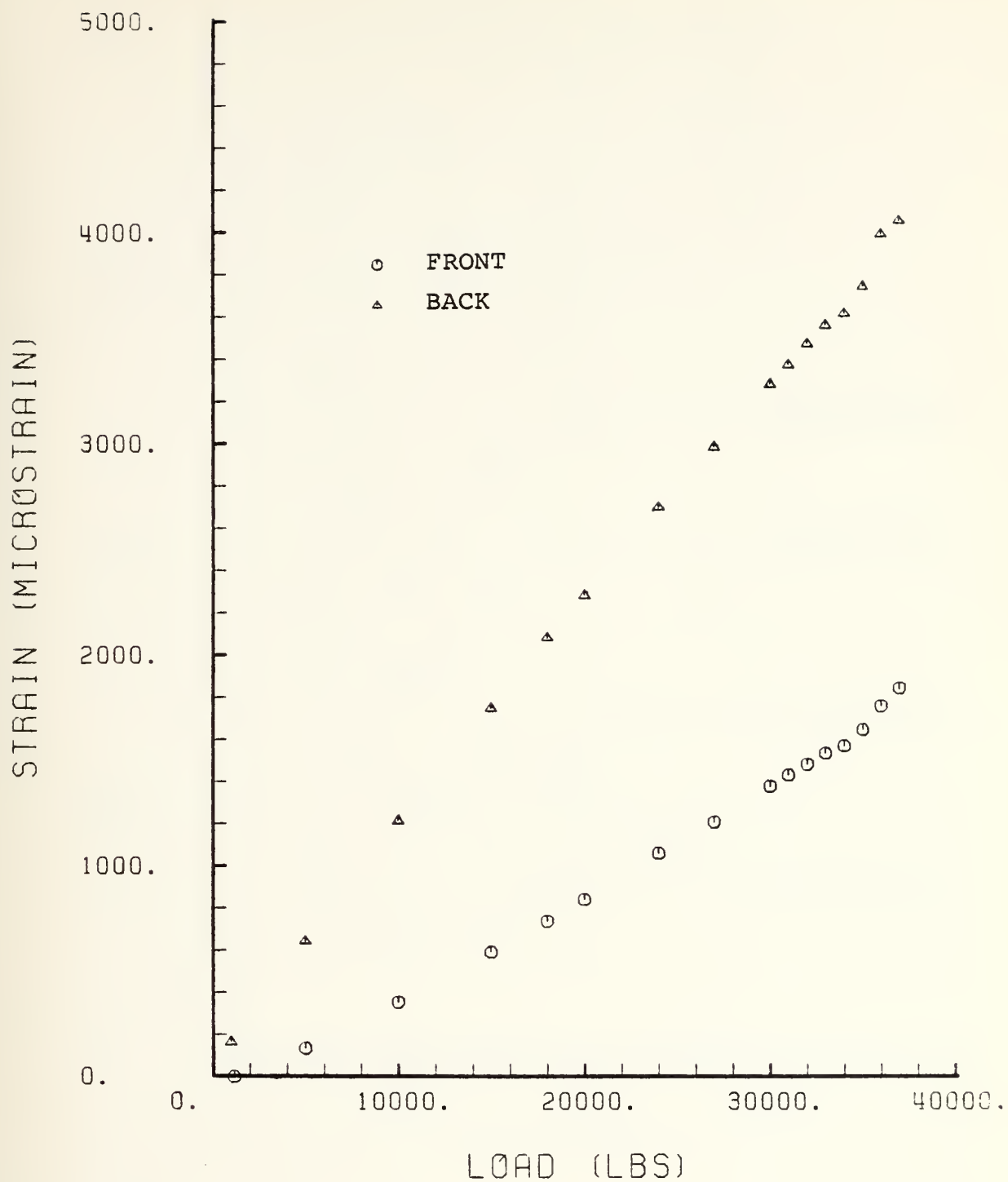
Figure 79. Comparison of Measured Front and Back
Strains at Gauges 15 and 19 –
Configuration 3B.

154
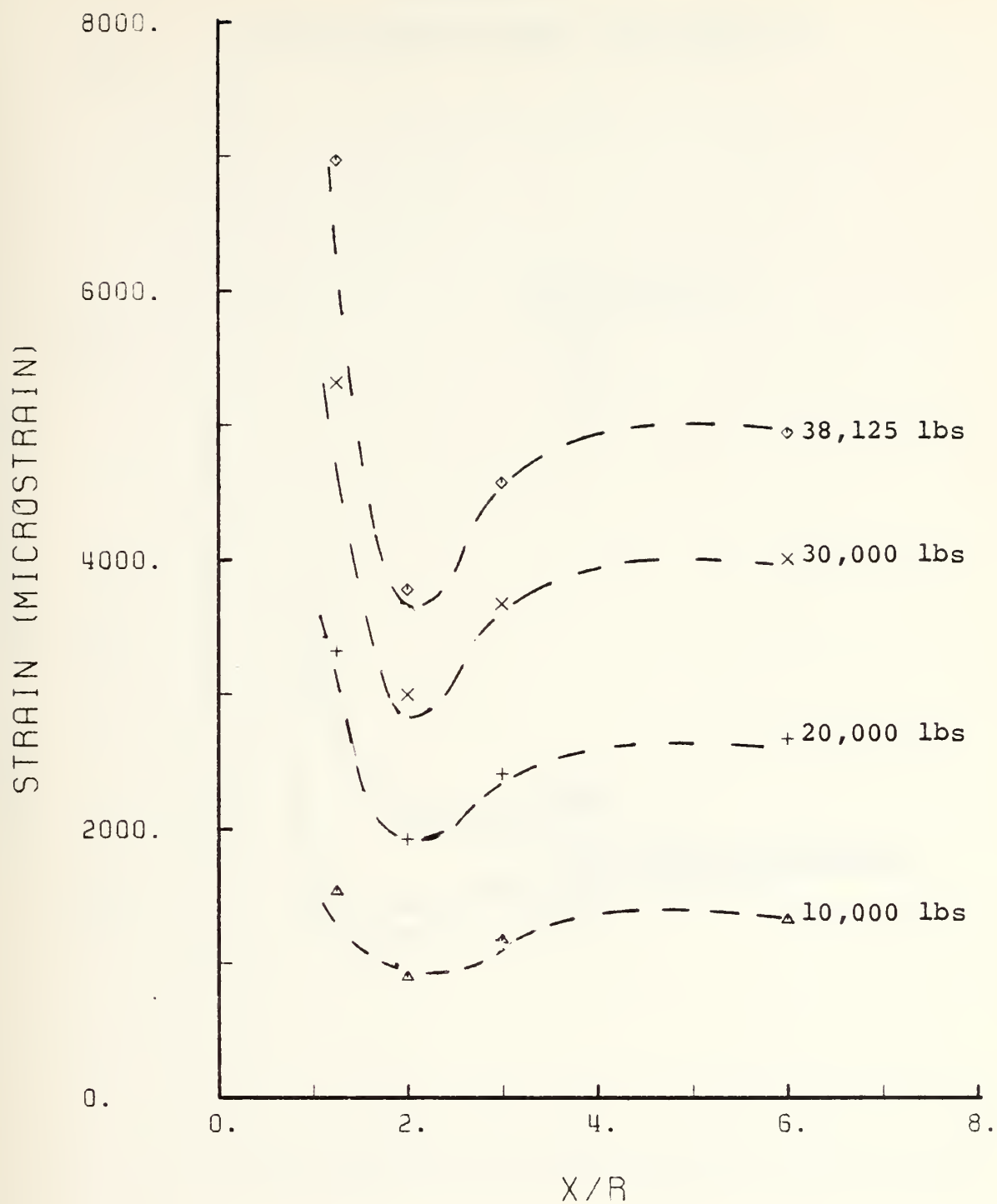
Figure 80. Nonlinear Behavior of Panel 3B
ε_z Vs X/R at the Hole Edge.

155

APPENDIX E
FOURTH REINFORCEMENT CONFIGURATION
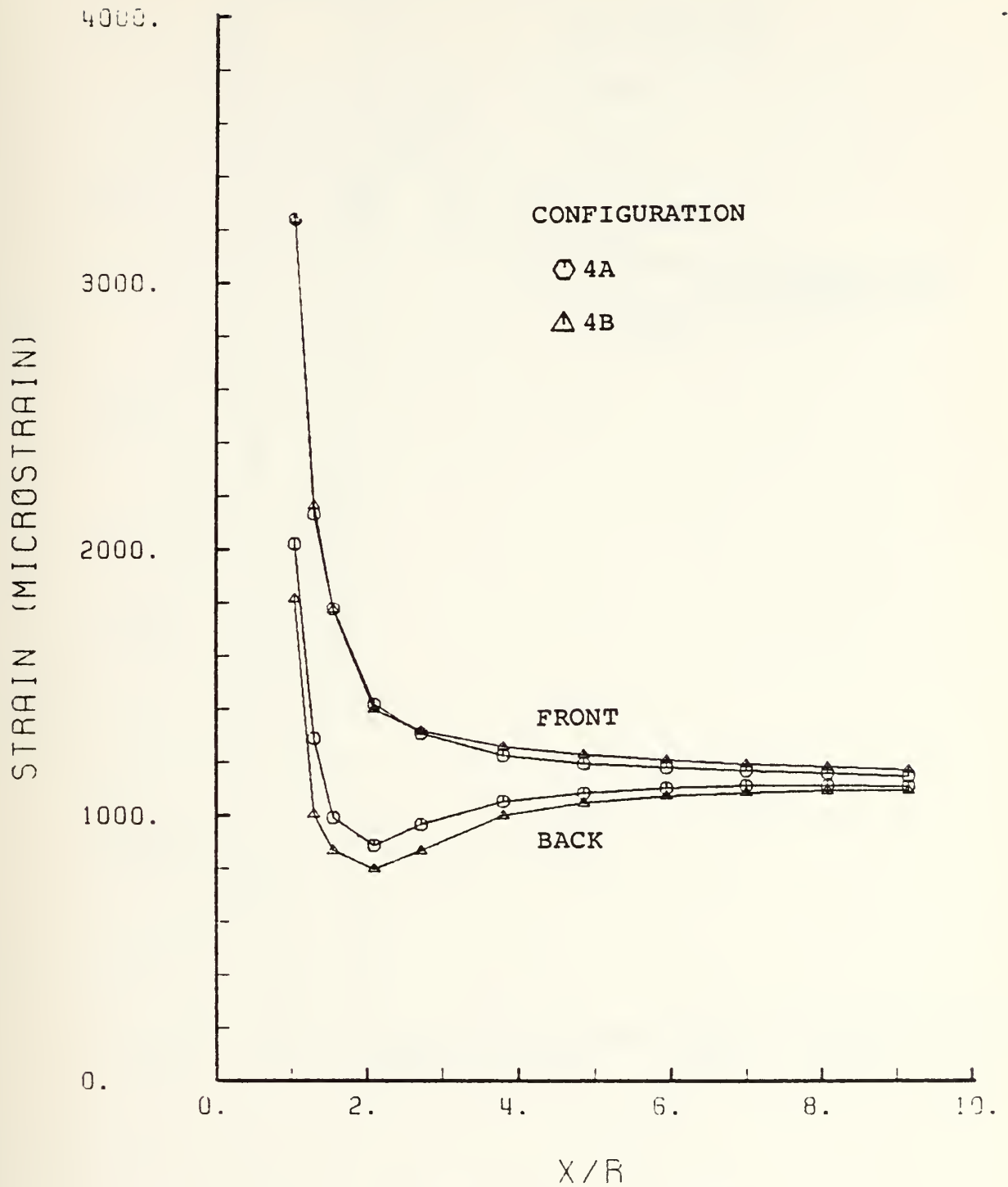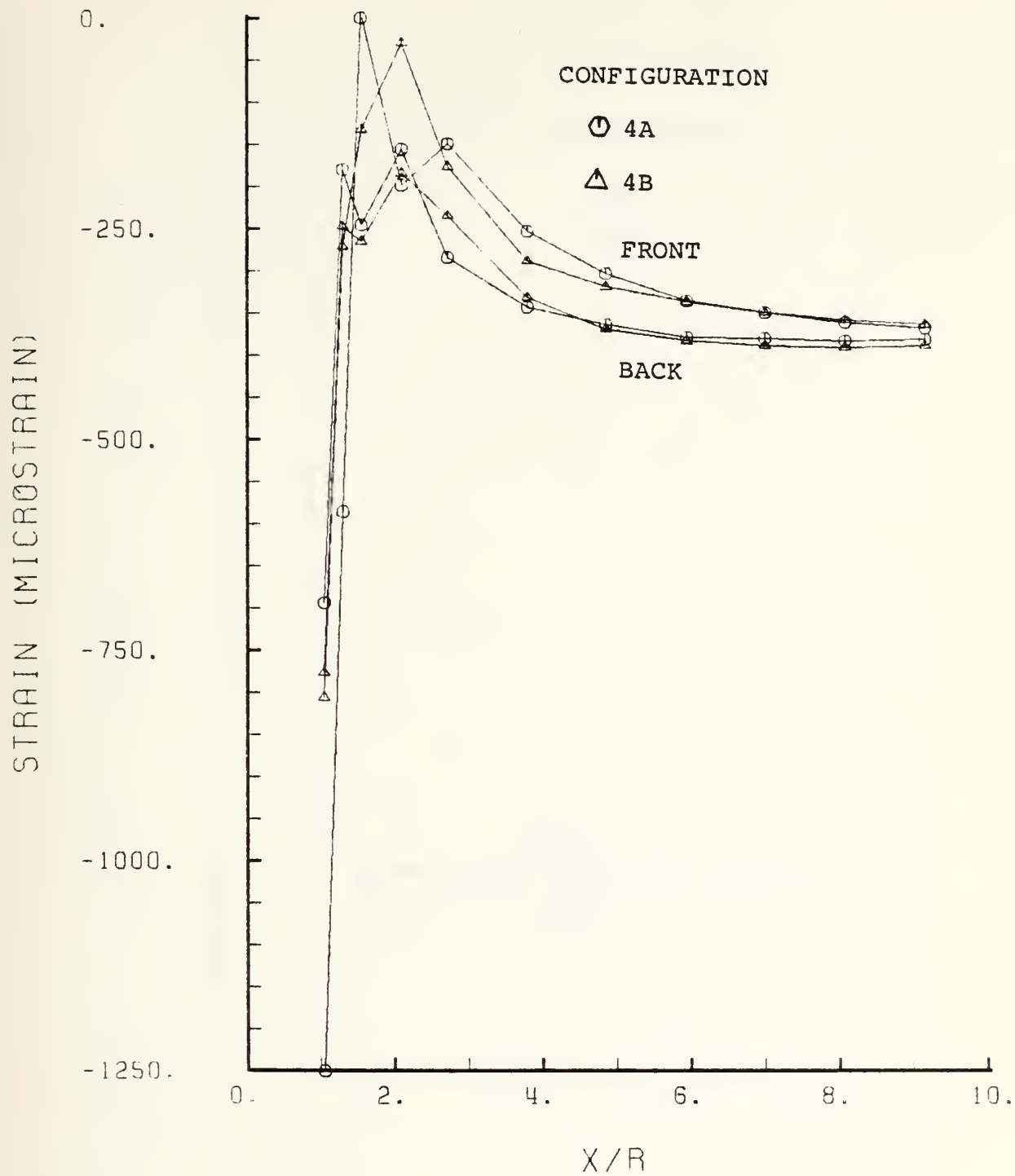
Figure 81. ε_z Vs X/R.

156

Figure 82. ε_x Vs X/R.

157

Figure 83. ε_{xz} Vs X/R.

158

Figure 84. ε_z Vs Z/R.

159

Figure 85. ε_x Vs Z/R.

160

Figure 86. ε_{xz} Vs Z/R.

CONTOUR INDEX

1   0.0

2   2×10^2

3   4×10^2

4   6×10^2

5   8×10^2

6   1.0×10^3

7   1.2×10^3
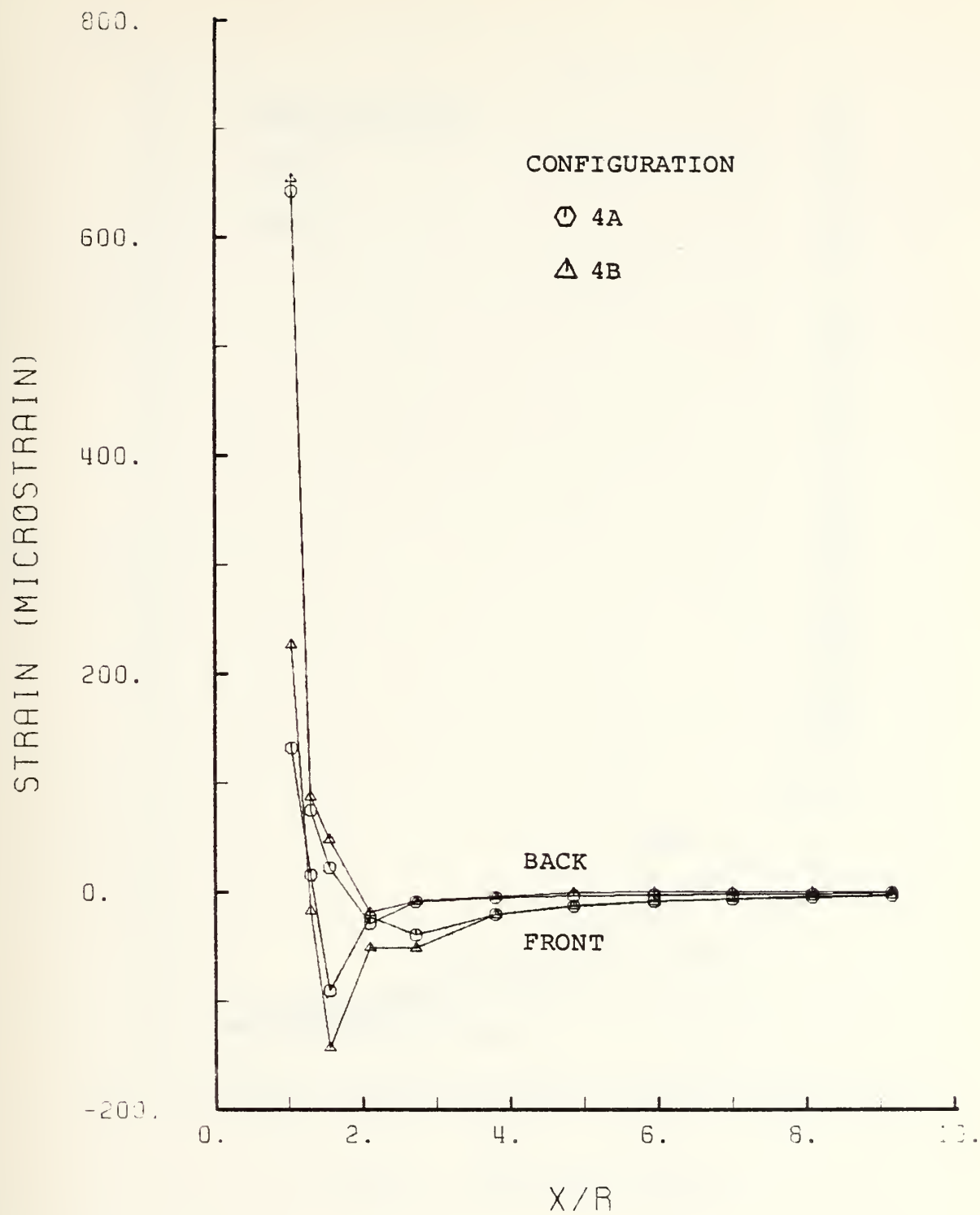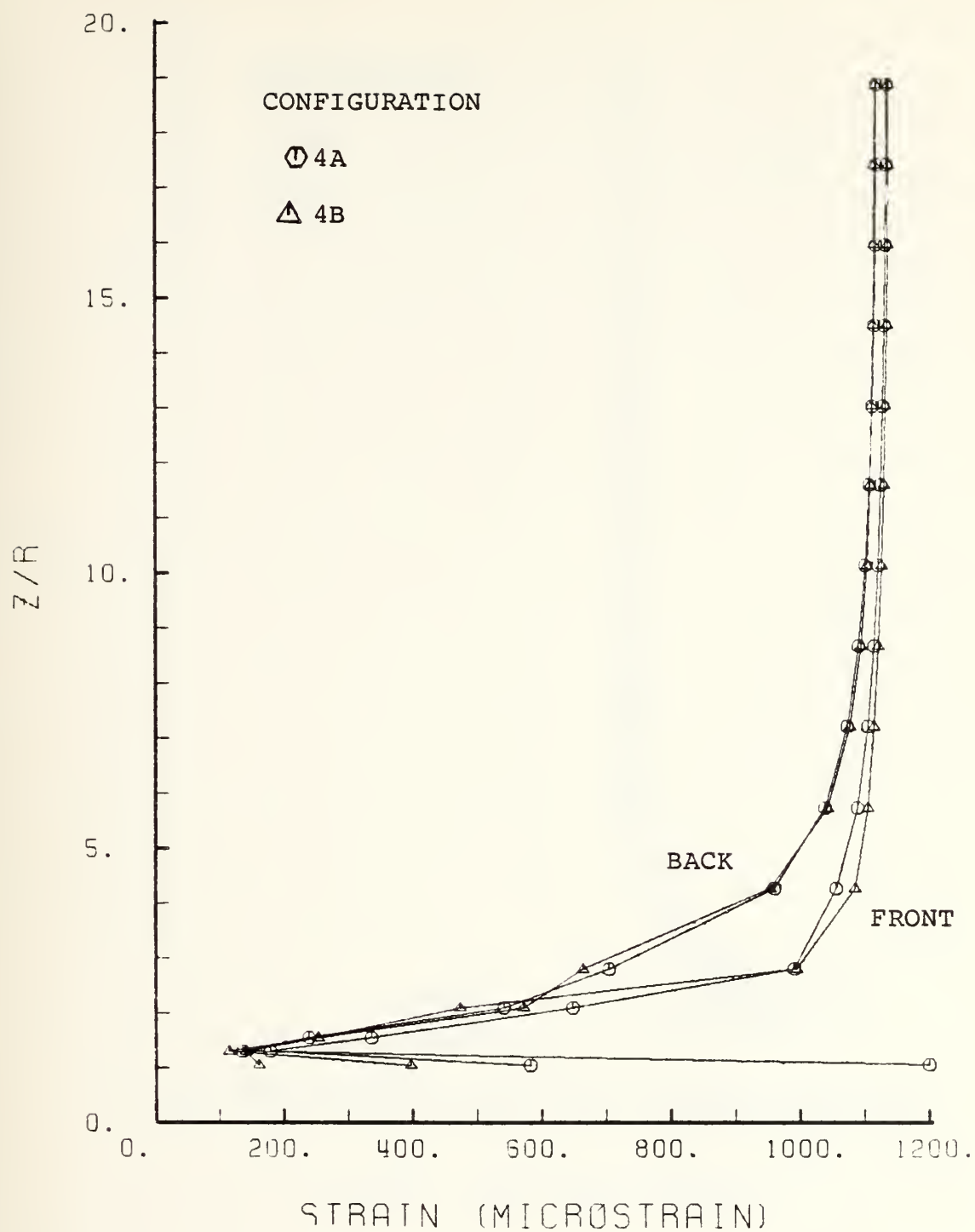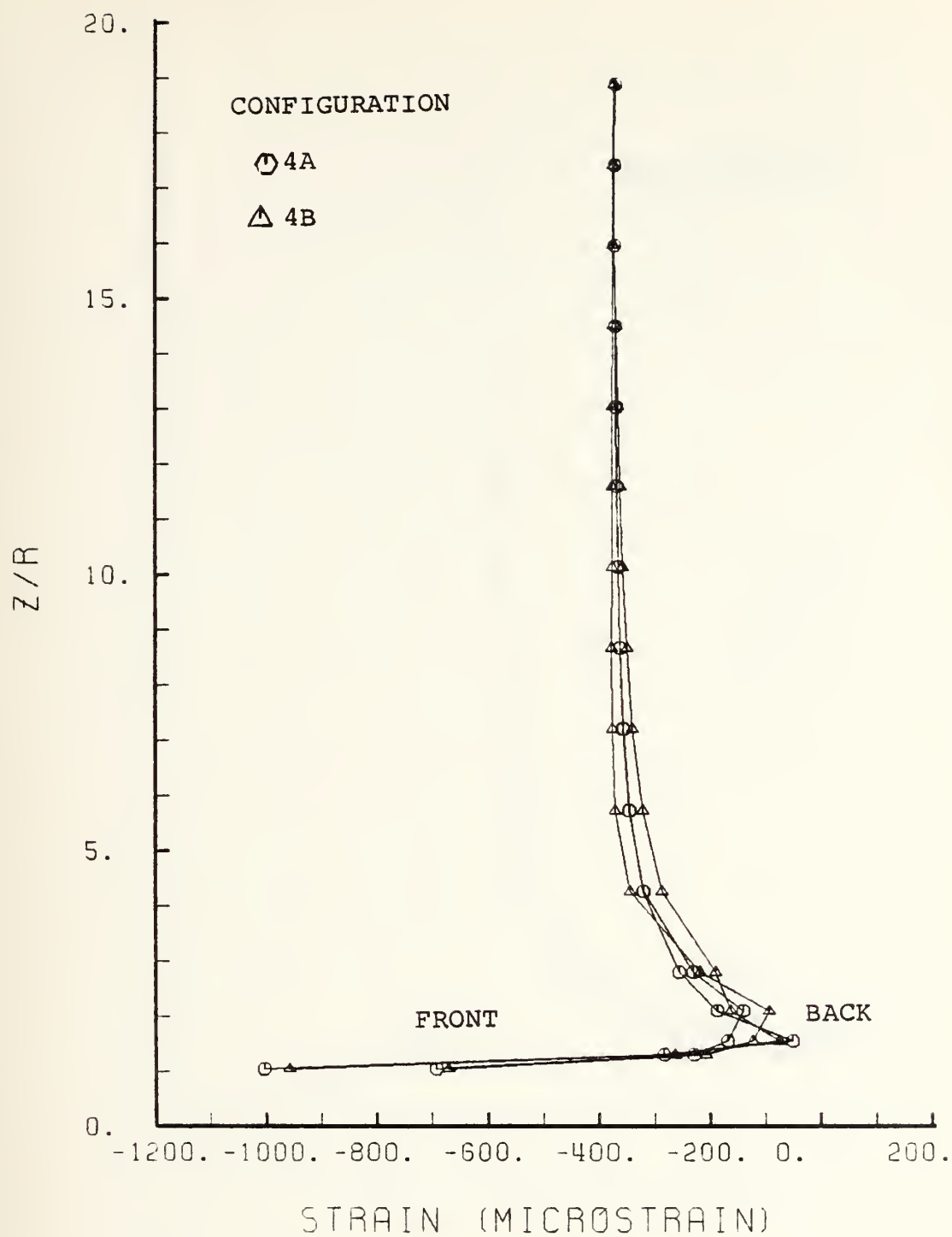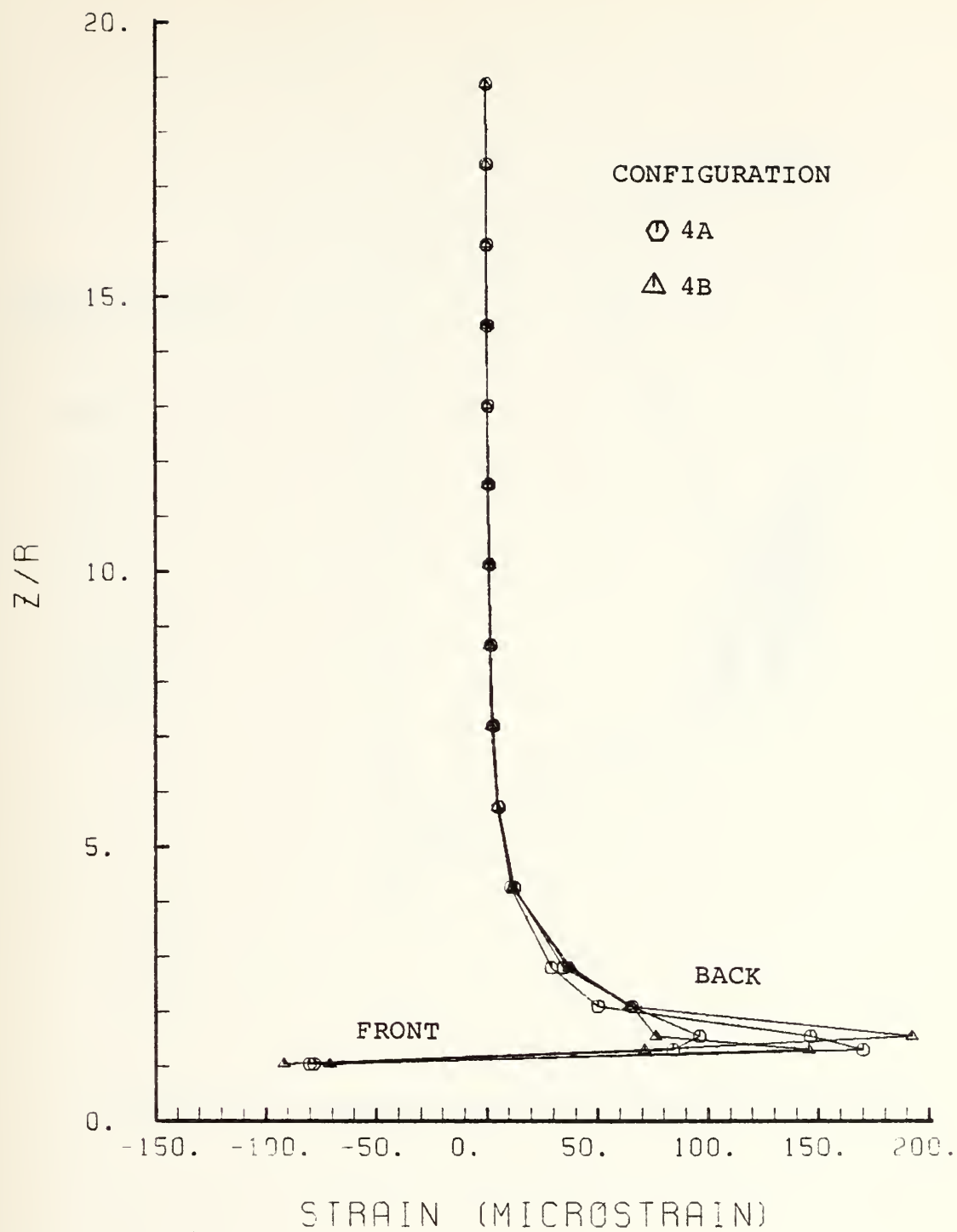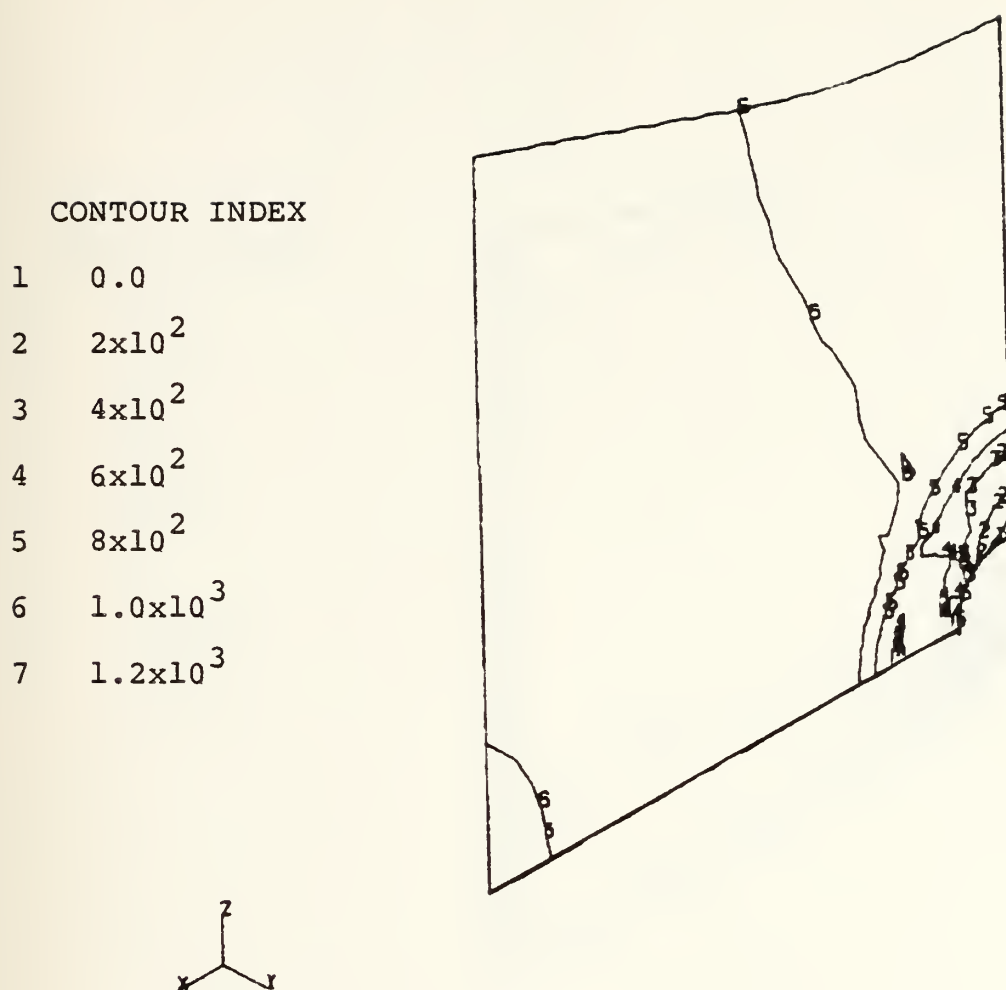
Figure 87.   Contour Plot of N_z Configuration 4A.

162

CONTOUR INDEX

1	-4×10^2
2	-3×10^2
3	-2×10^2
4	-1×10^2
5	0
6	1.0×10^2
7	2.0×10^2
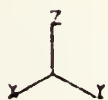
Figure 88. Contour Plot of N_x - Configuration 4A.

CONTOUR INDEX

1	-1×10^{-2}
2	0
3	1×10^2
4	2×10^2
5	3×10^2
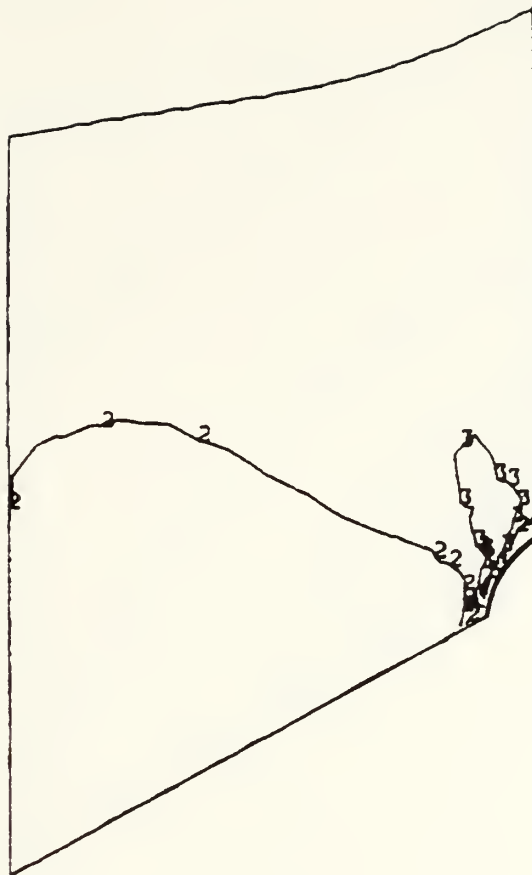
Figure 89.   Contour Plot of N_{xz} - Configuration 4A.

164

CONTOUR INDEX

1   -2.3×10^{-5}

2   2×10^{-3}

3   4×10^{-3}

4   6×10^{-3}

5   8×10^{-3}
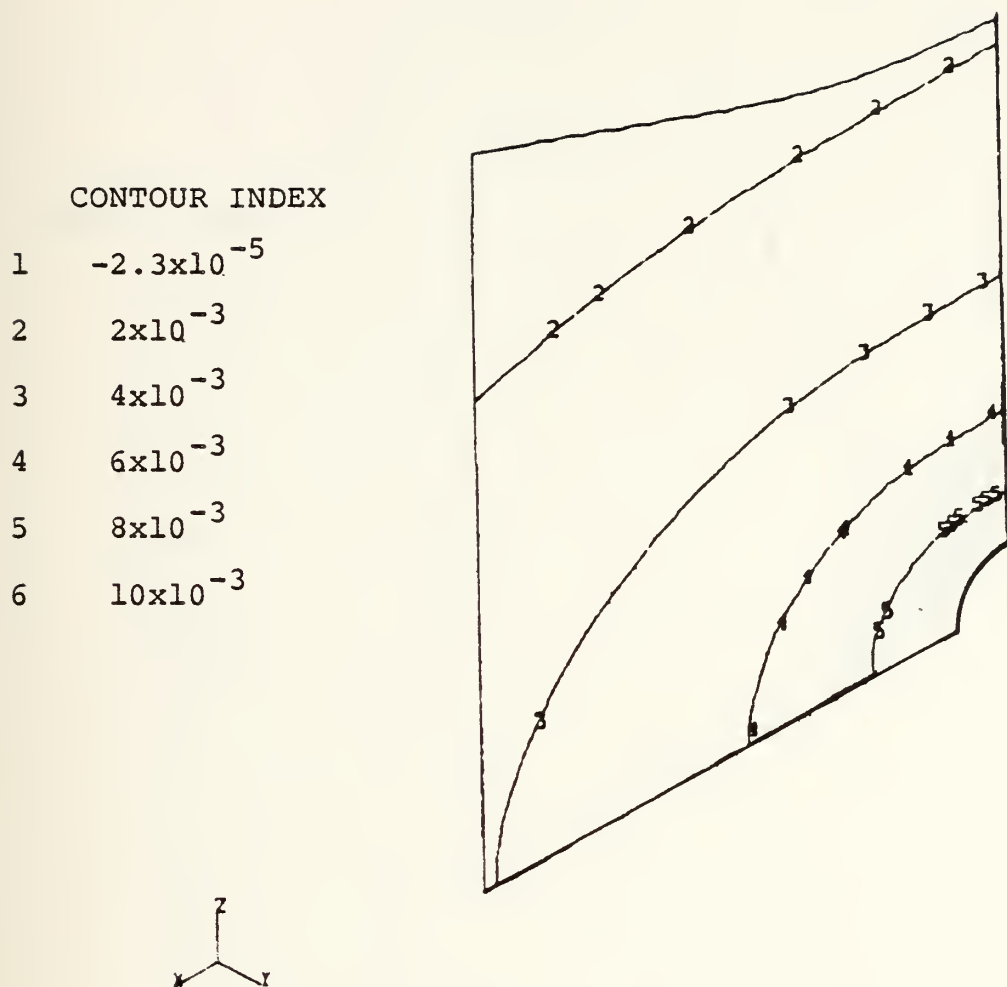
6   10×10^{-3}

Figure 90.   Contour Plot of Out of Plane Deflections Configuration 4A.

CONTOUR INDEX

1   -1.5×10^{-5}

2    $2. \times 10^2$

3    $4. \times 10^2$

4    $6. \times 10^2$

5   8×10^2

6   1.0×10^3

7   1.2×10^3
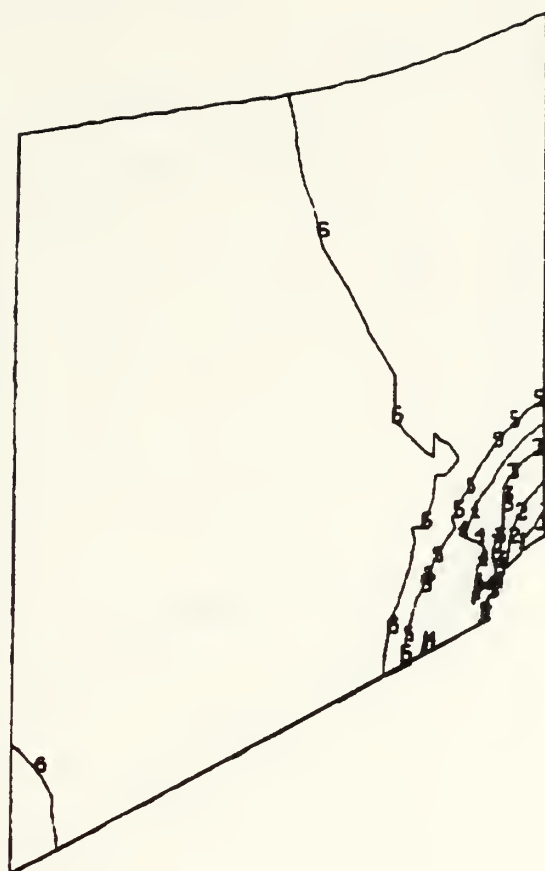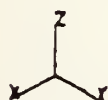
Figure 91.   Contour Plot of N_z - Configuration 4B.

CONTOUR INDEX

1	-1×10^2
2	0.0
3	$1. \times 10^2$
4	$2. \times 10^2$
5	$3. \times 10^2$
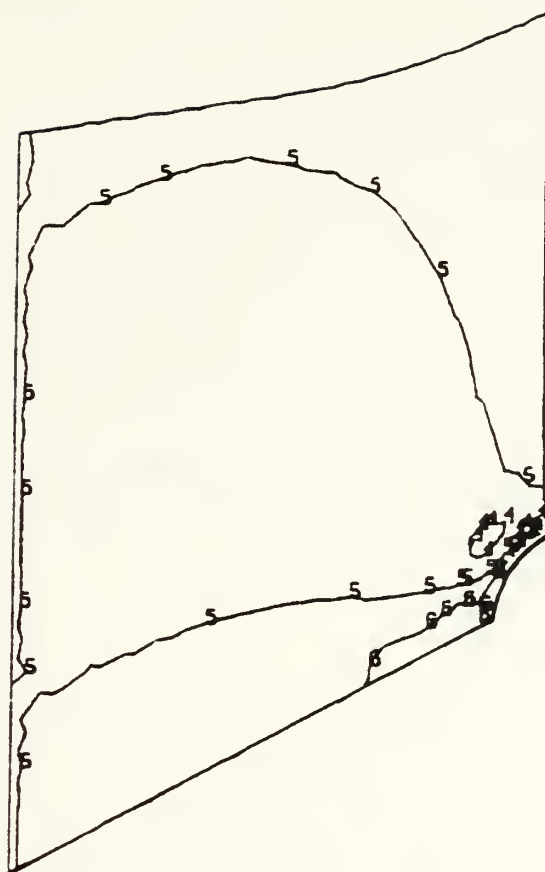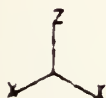
Figure 92.   Contour Plot of N_x - Configuration 4B.

167

CONTOUR INDEX

1	-1×10^2
2	0
3	1×10^2
4	2×10^2
5	3×10^2
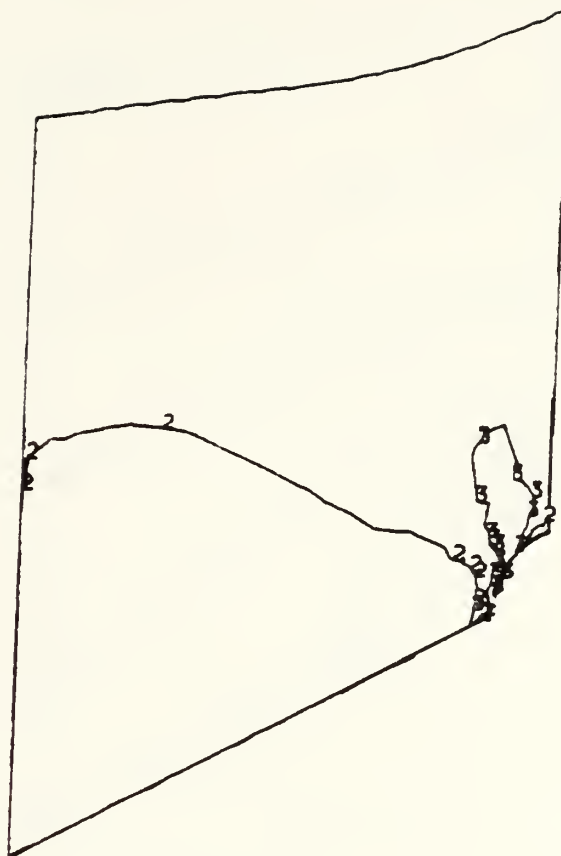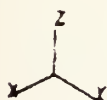
Figure 93.   Contour of N_{xz} - Configuration 4B.

CONTOUR INDEX

1   2.0×10^{-3}

2   4.0×10^{-3}

3   6.0×10^{-3}

4   8.0×10^{-3}

5   10.0×10^{-2}

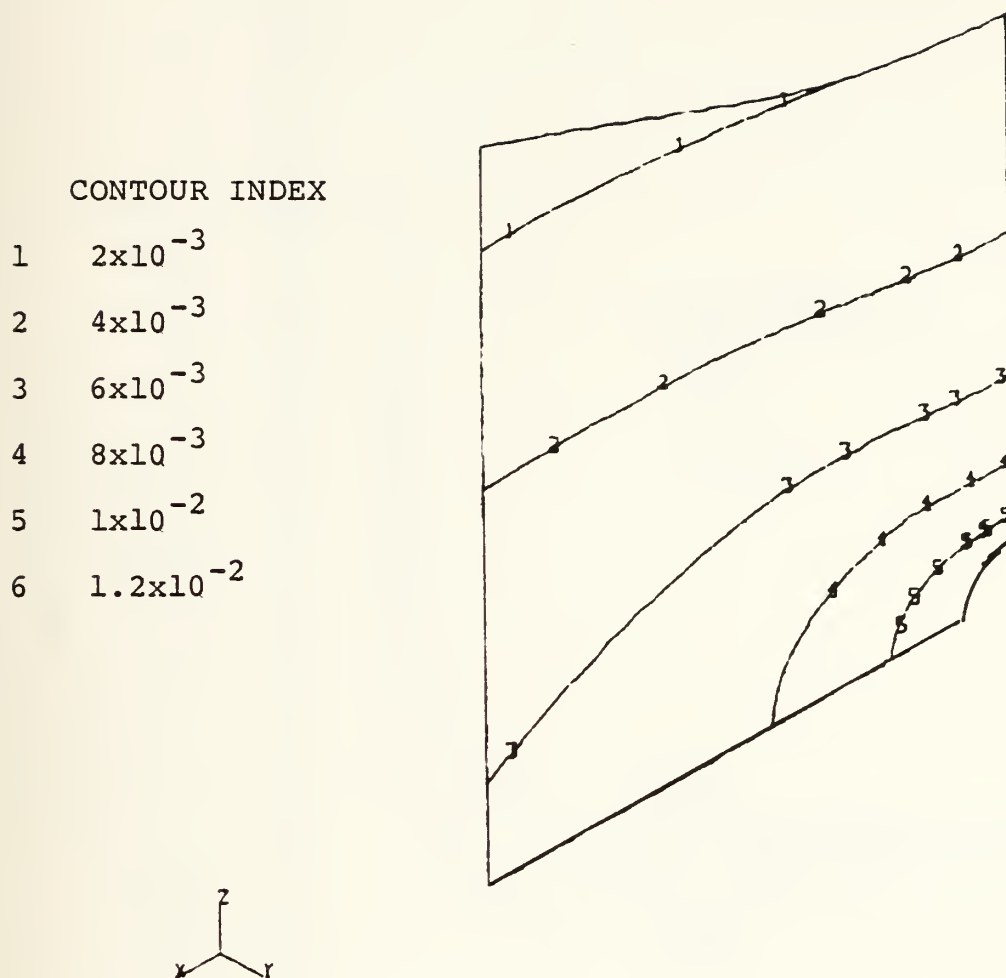6 1.2×10^{-2}
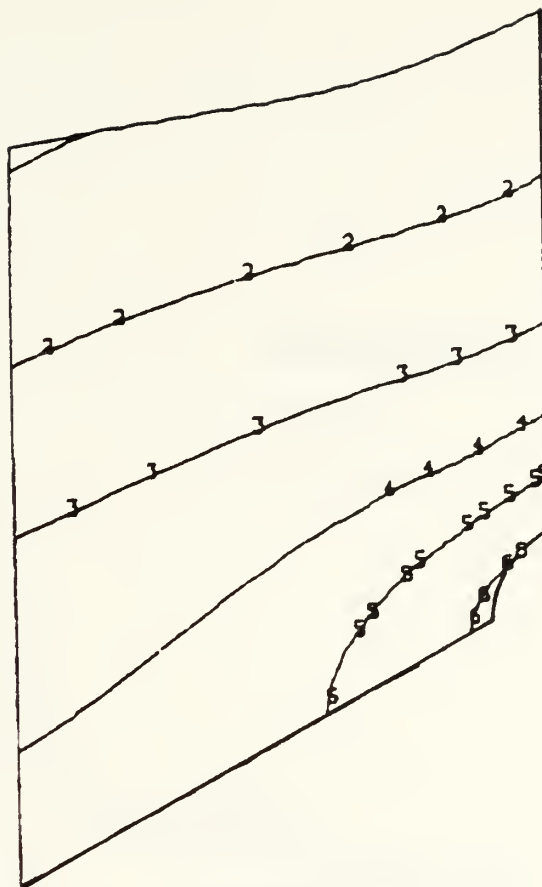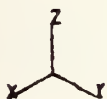
Figure 94.   Contour Plot of Out of Plane
Deflections - Configuration 4B.

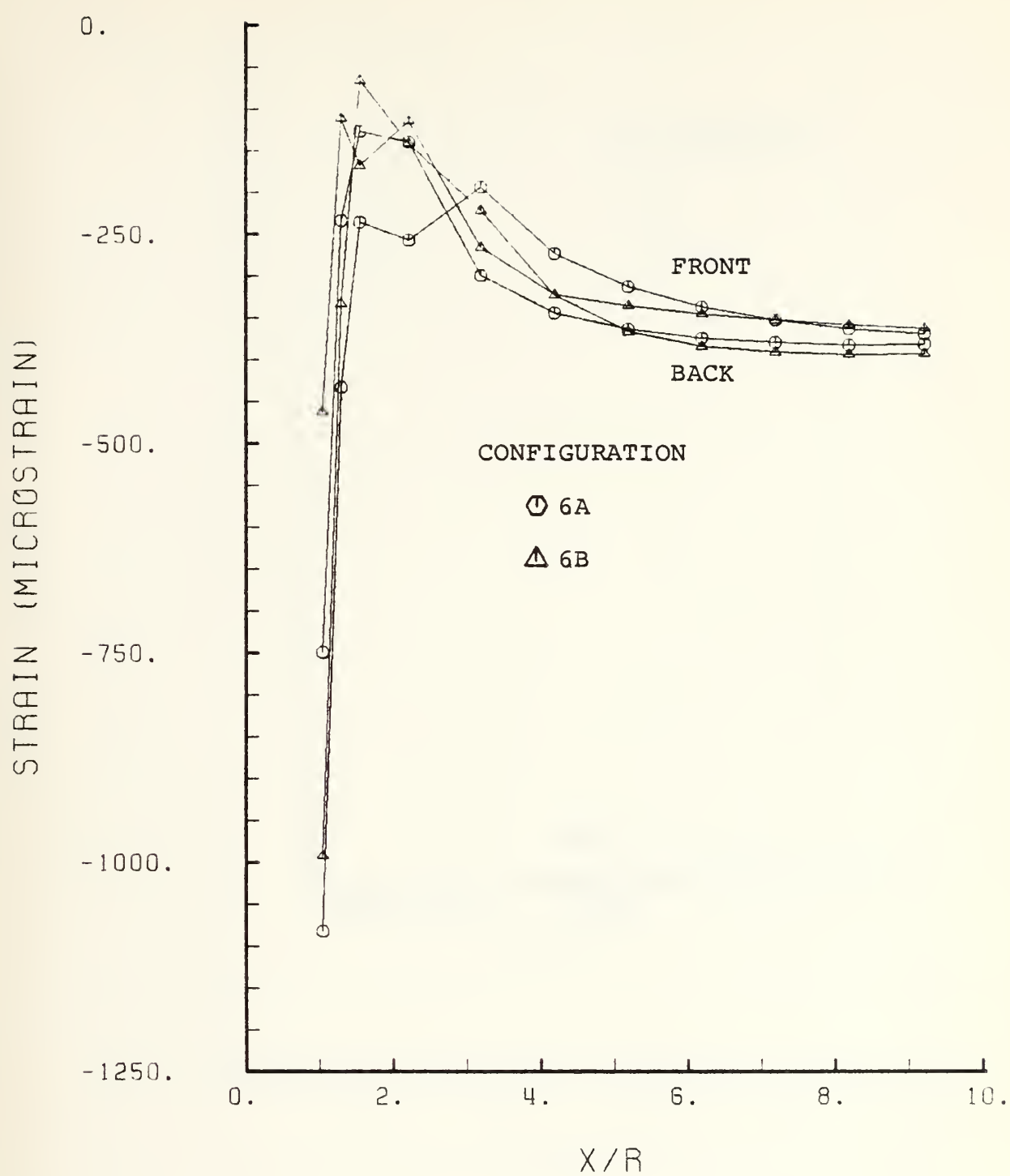APPENDIX F
FIFTH REINFORCEMENT CONFIGURATION
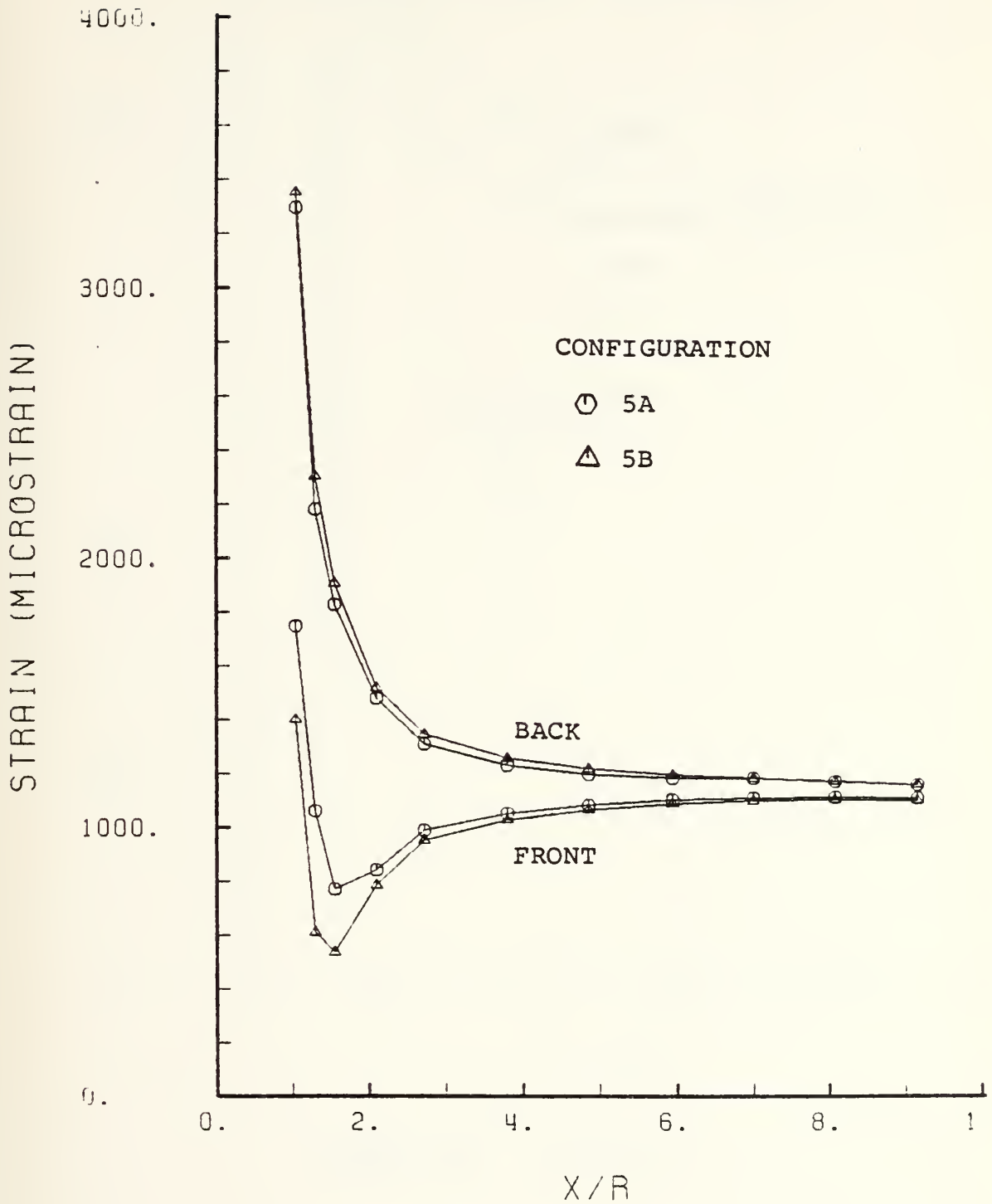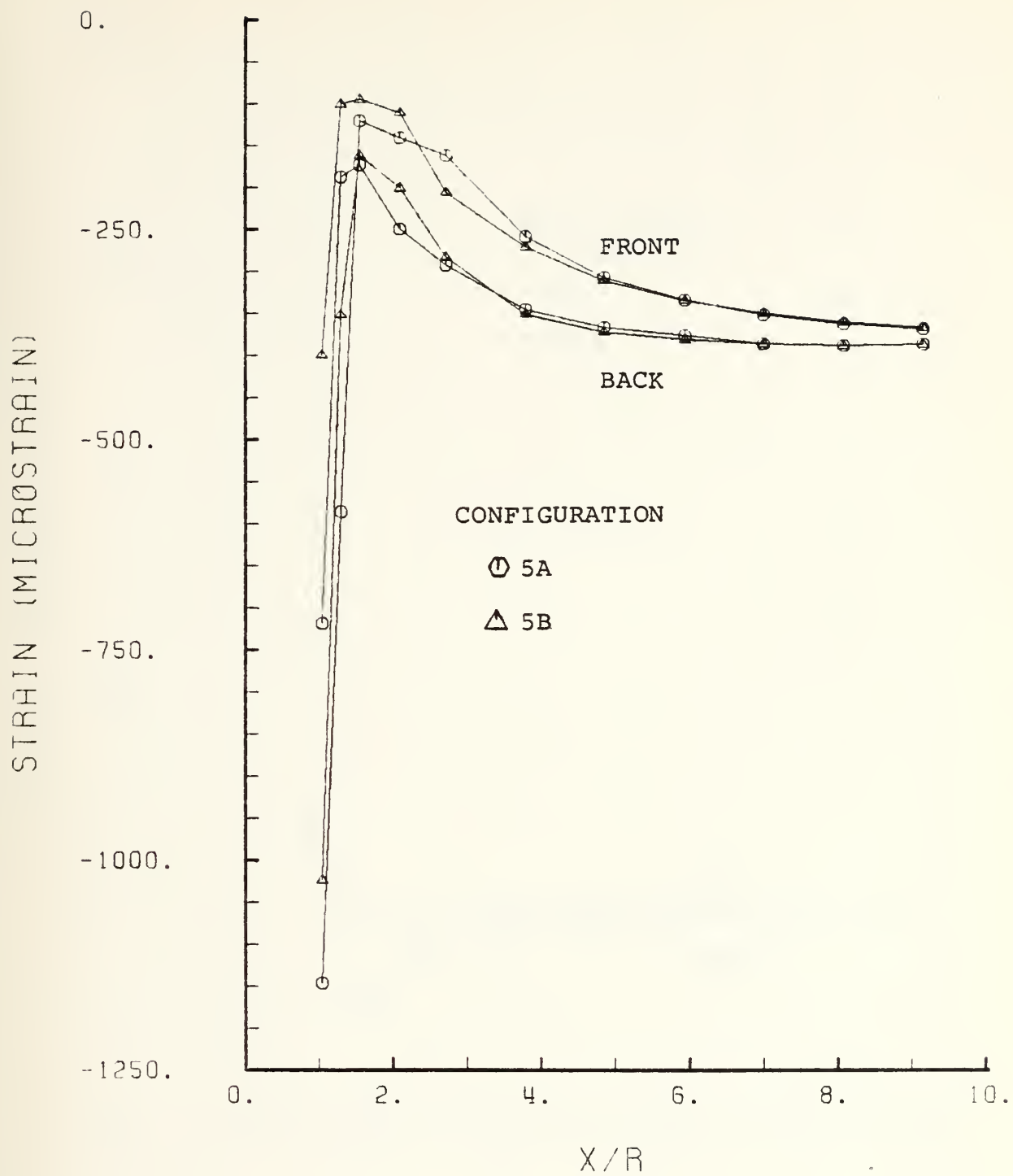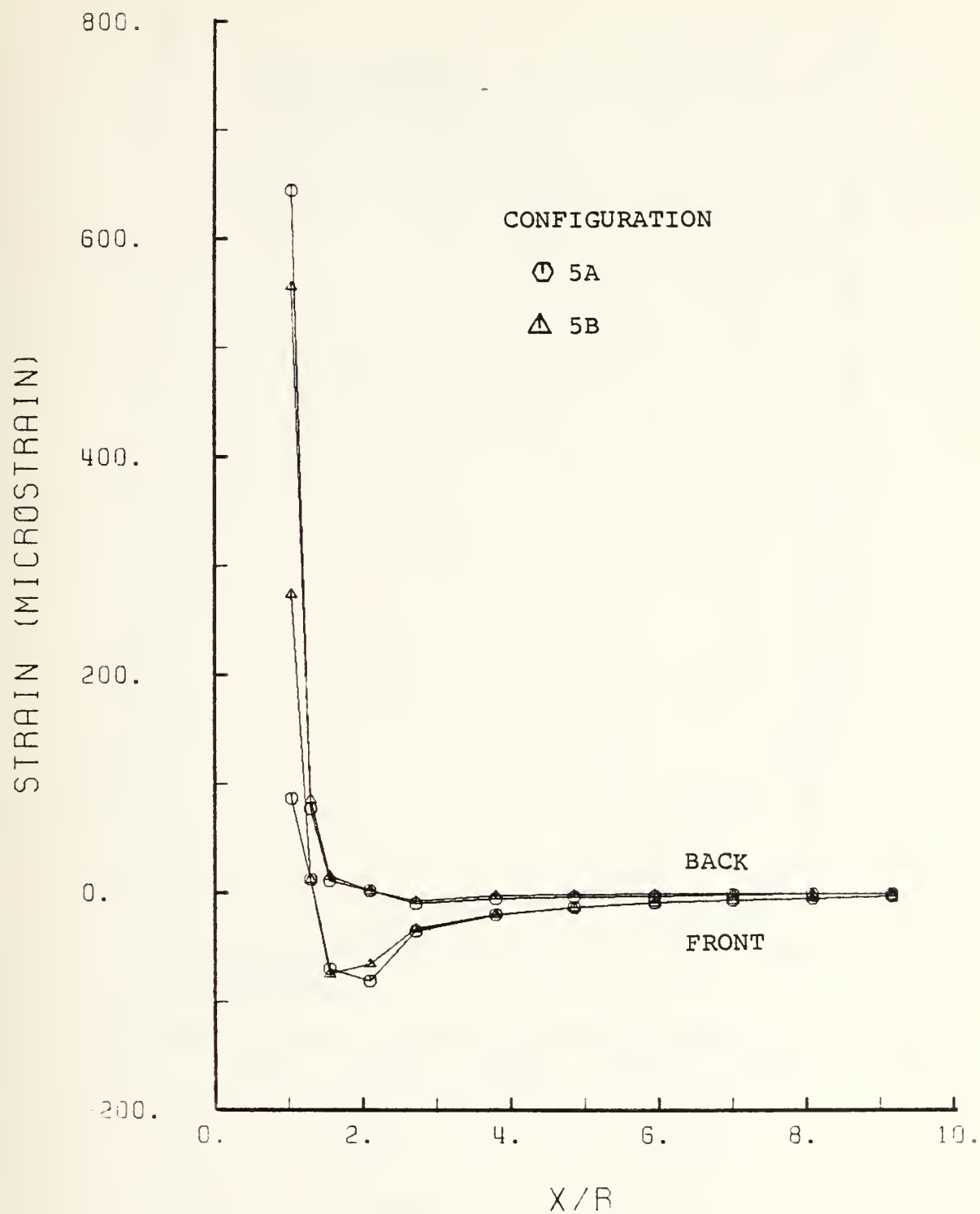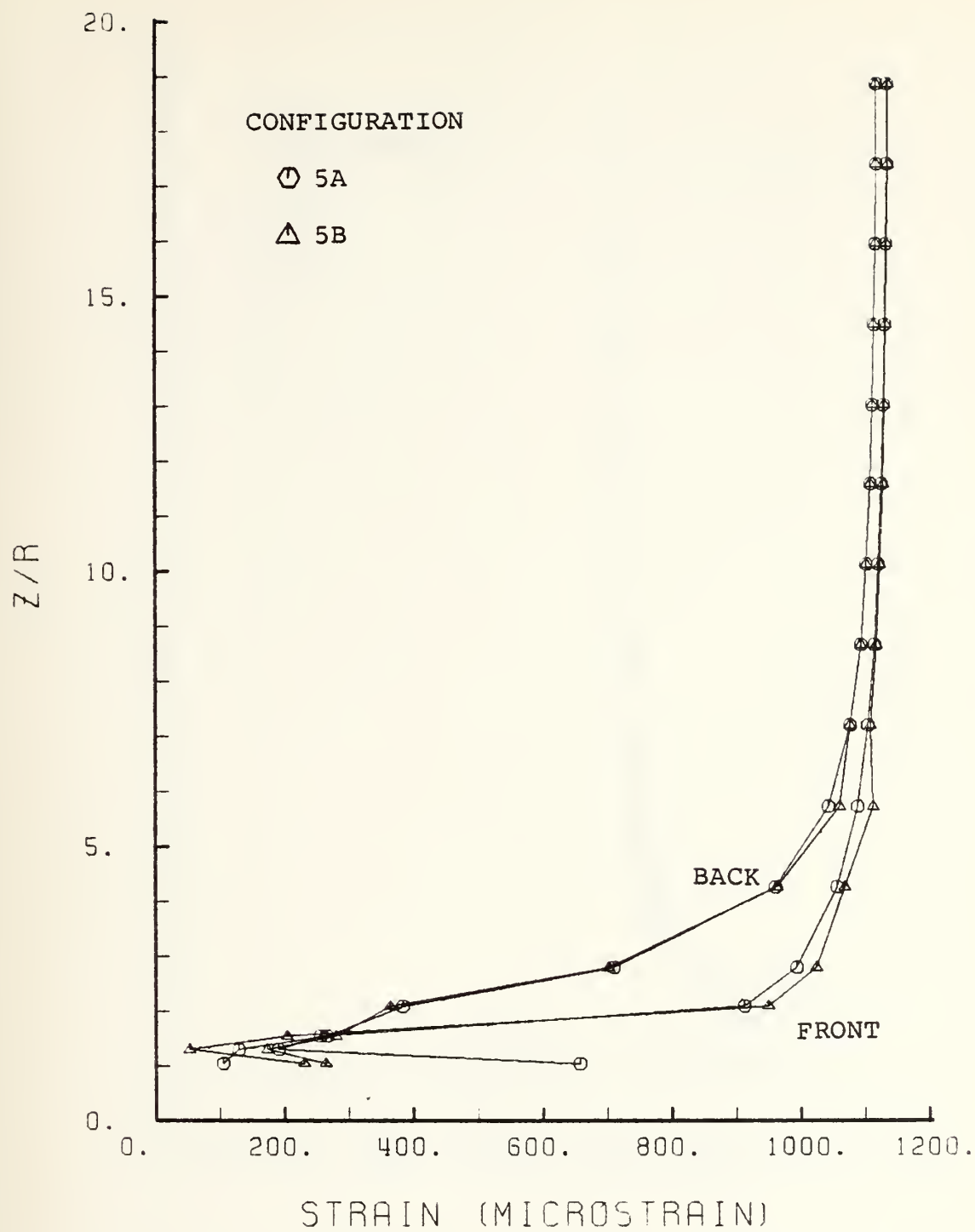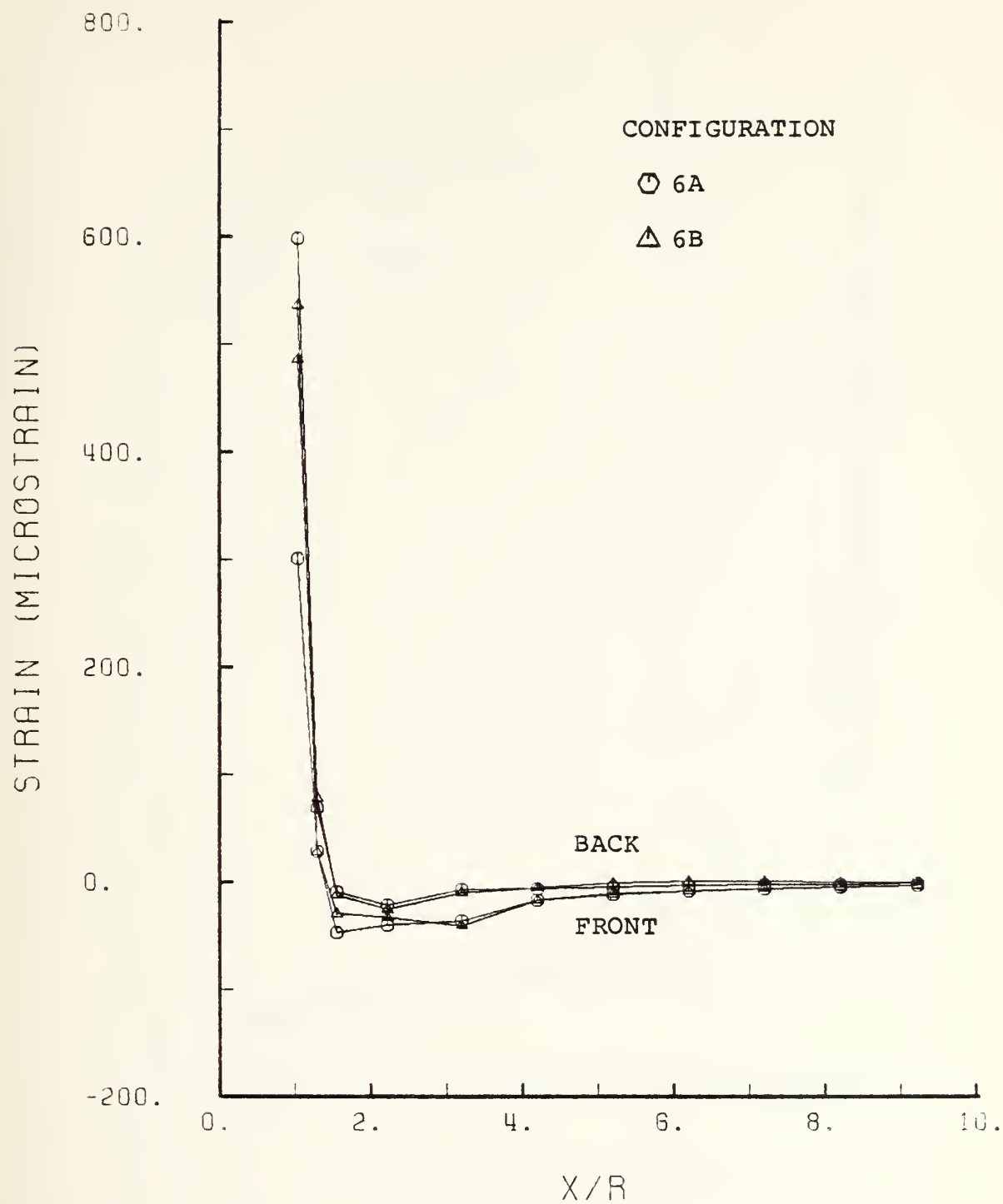
Figure 95. ε_z Vs X/R.

Figure 96. ε_x Vs X/R.

171

Figure 97. ε_{xz} Vs X/R.

172

Figure 98. ε_z Vs Z/R.

173

Figure 99. ε_x Vs Z/R.

174

Figure 100. ε_{xz} Vs Z/R.

175
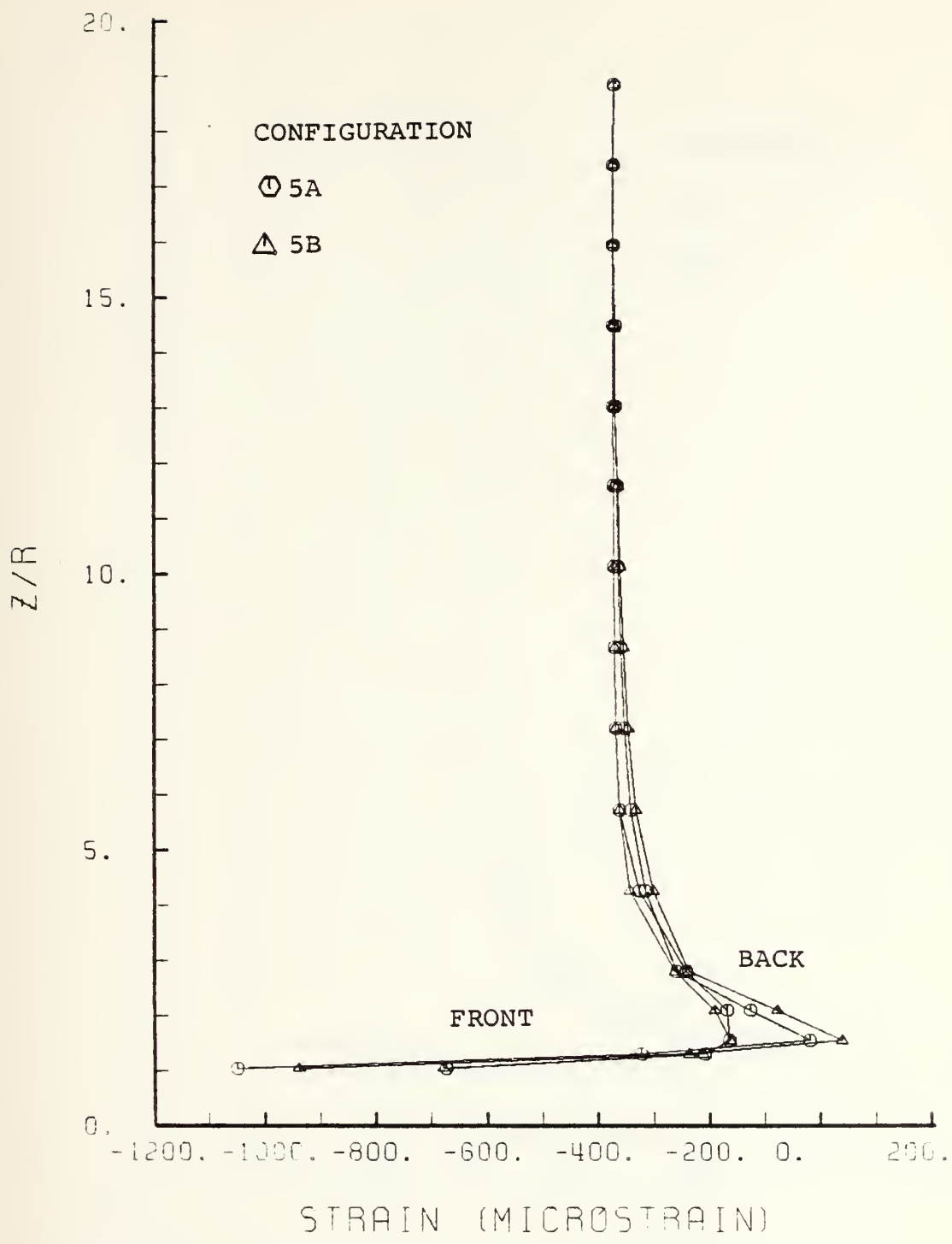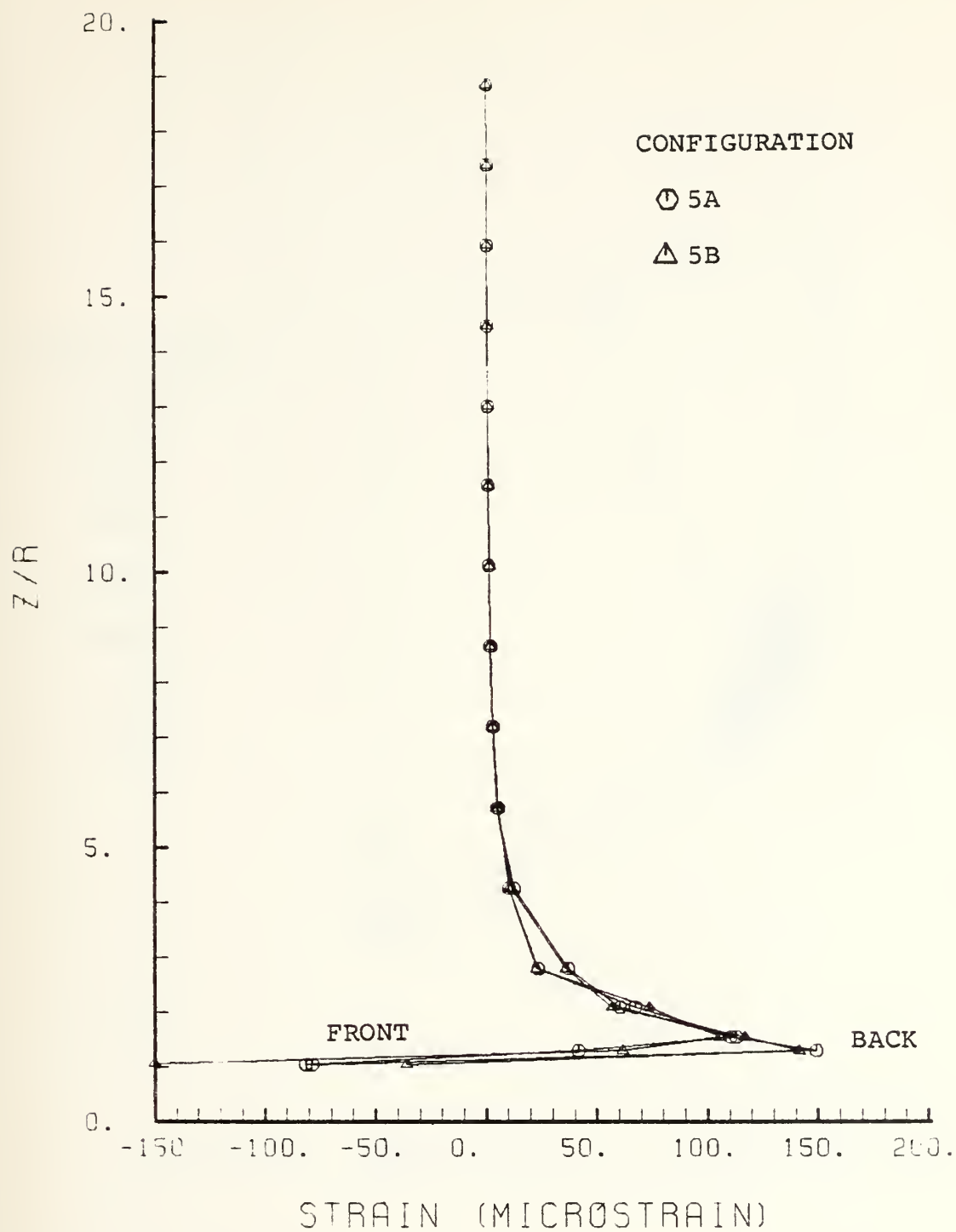
CONTOUR INDEX

1	-1.5×10^{-5}
2	2×10^{2}
3	4×10^{2}
4	6×10^{2}
5	8×10^{2}
6	1.0×10^{3}
7	1.2×10^{3}
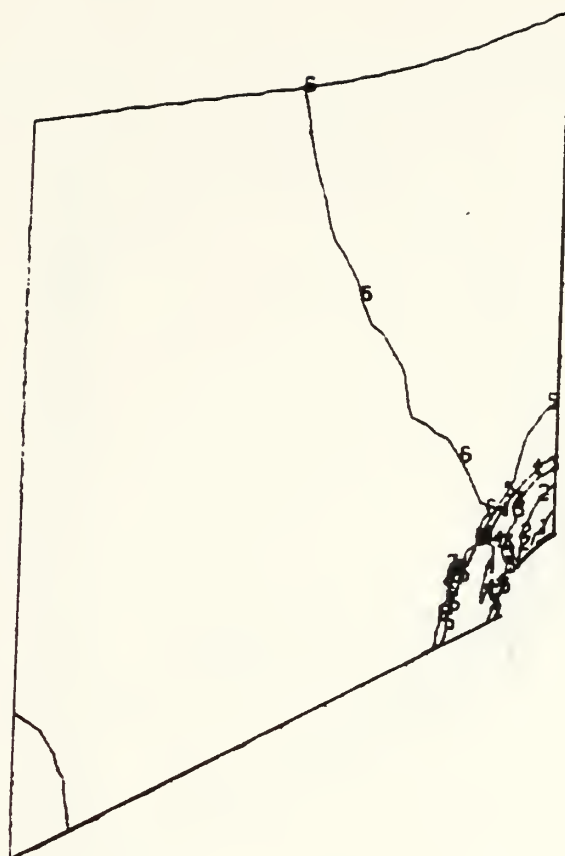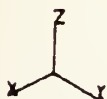
Figure 101. Contour Plot of N_z – Configuration 5A.

176

CONTOUR INDEX

1   -4×10^2

2   -3×10^2

3   -2×10^2

4   -1×10^2

5   0

6   $1. \times 10^2$

7   1.2×10^2
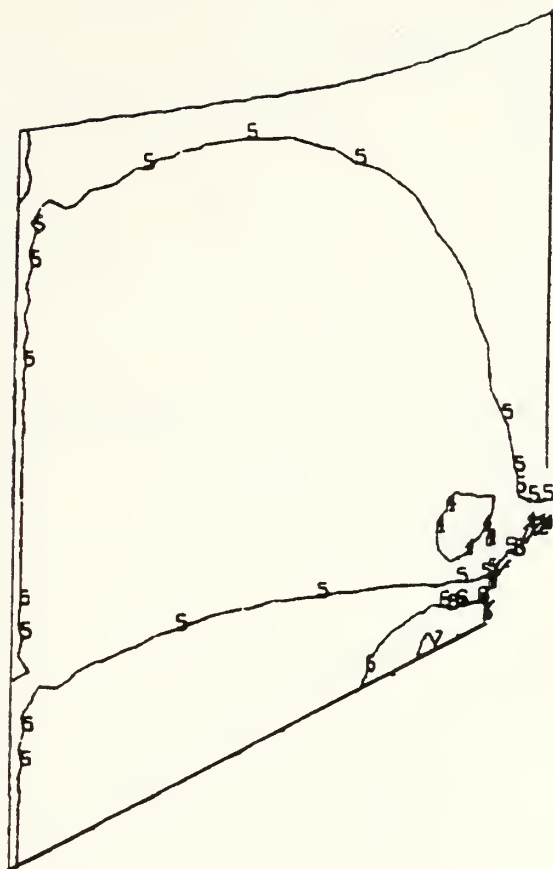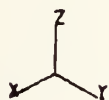
Figure 102.   Contour Plot of N_x - Configuration 5A.

CONTOUR INDEX

1   -1×10^2

2   0

3   1×10^2

4   2×10^2

5   3×10^2
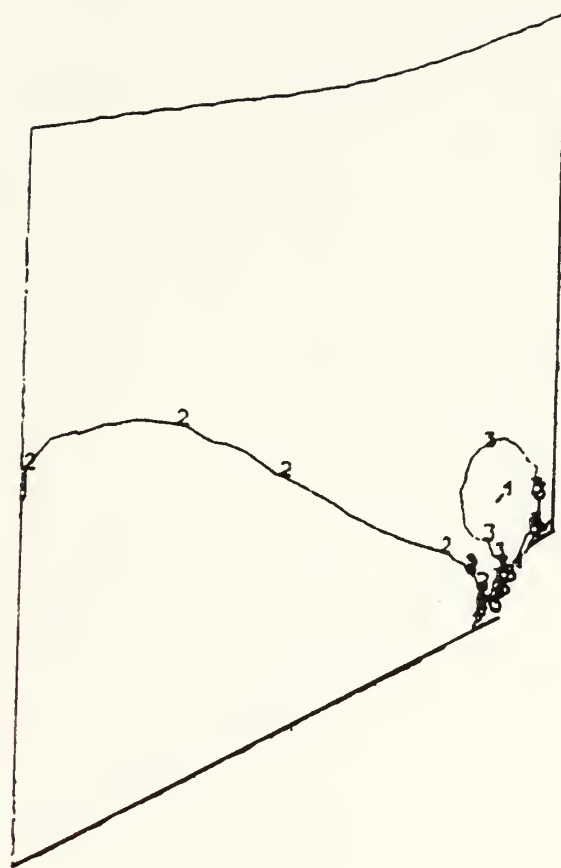
Figure 103.   Contour Plot of N_{xz} - Configuration 5A.

CONTOUR INDEX

1	0
2	2×10^{-3}
3	4×10^{-3}
4	6×10^{-3}
5	8×10^{-3}
6	1.0×10^{-2}
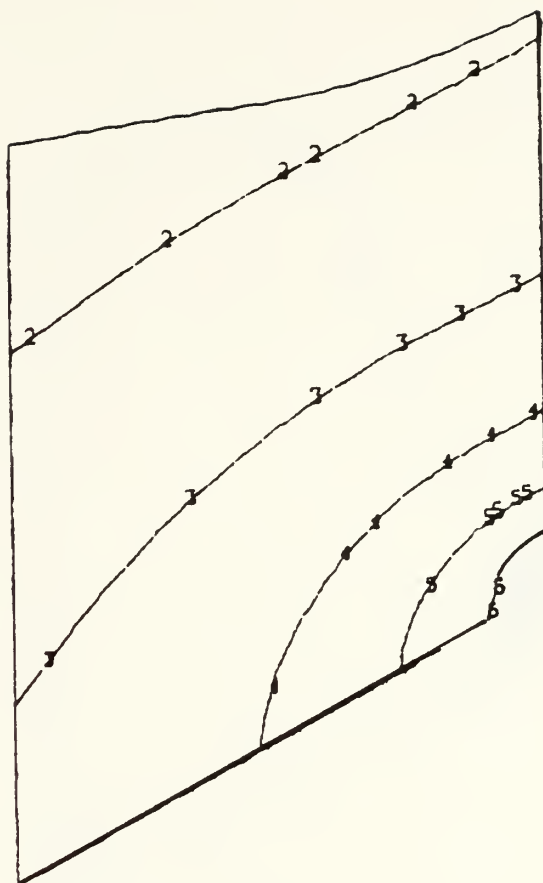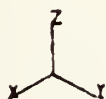
Figure 104. Contour Plot of Out of Plane Deflections Configuration 5A.

CONTOUR INDEX

1	-1.5×10^{-5}
2	2×10^{2}
3	4×10^{2}
4	6×10^{2}
5	8×10^{2}
6	1.0×10^{3}
7	1.2×10^{3}
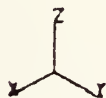
Figure 105.   Contour Plot of N_z - Configuration 5B.

Figure 106. Contour Plot of N_x - Configuration 5B.

181

CONTOUR INDEX

1   -1×10^2

2   0

3   1×10^2

4   2×10^2

5   3×10^2

Figure 107.   Contour Plot of N_{xz} - Configuration 5B.

CONTOUR INDEX

1   2×10^{-3}

2   4×10^{-3}

3   6×10^{-3}

4   8×10^{-3}

5   1×10^{-2}

6   1.2×10^{-2}

Figure 108.   Contour Plot of Out of Plane
             Deflections - Configuration 5B.

183

APPENDIX G

SIXTH REINFORCEMENT CONFIGURATION
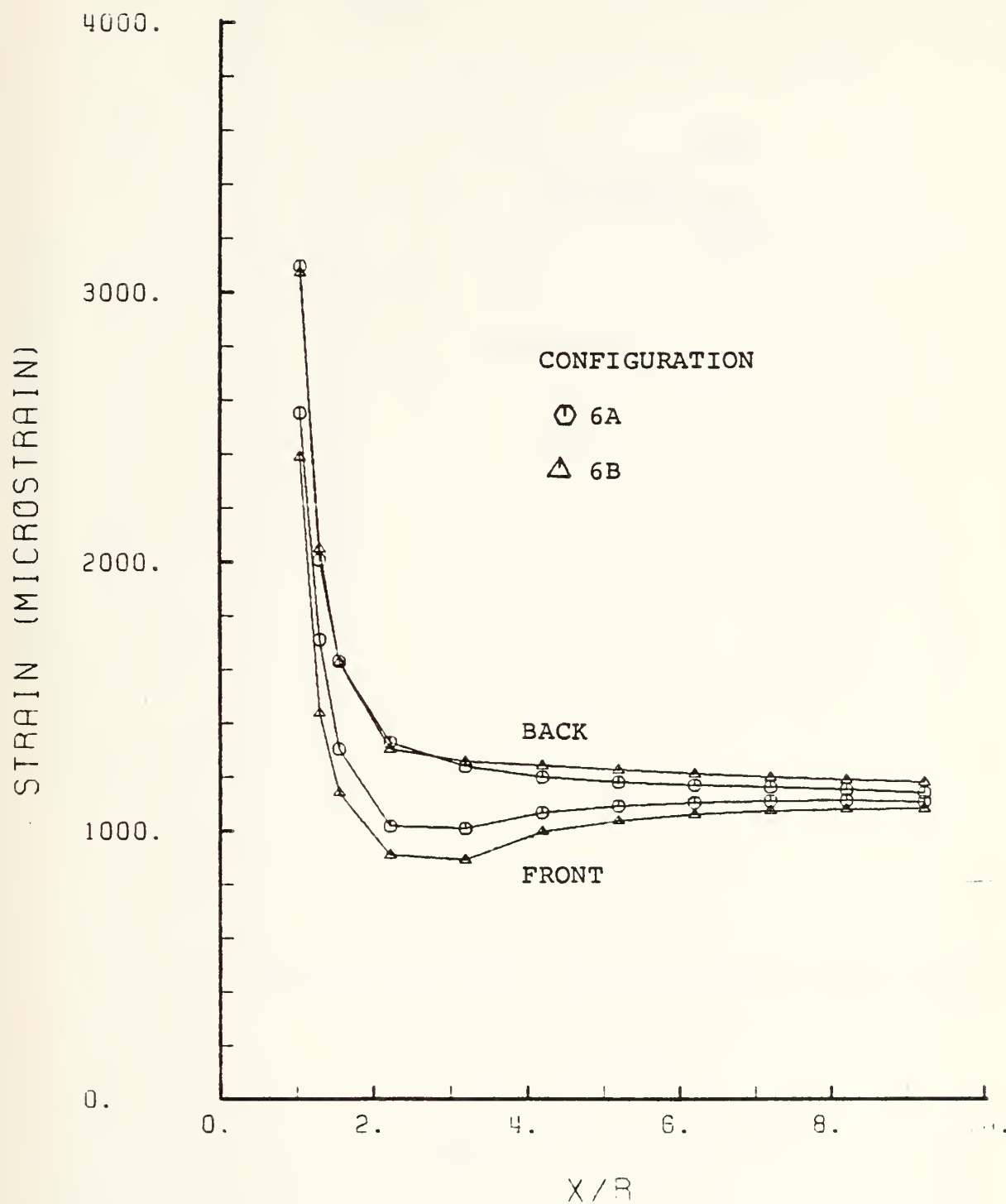
Figure 109. ε_z Vs X/R.
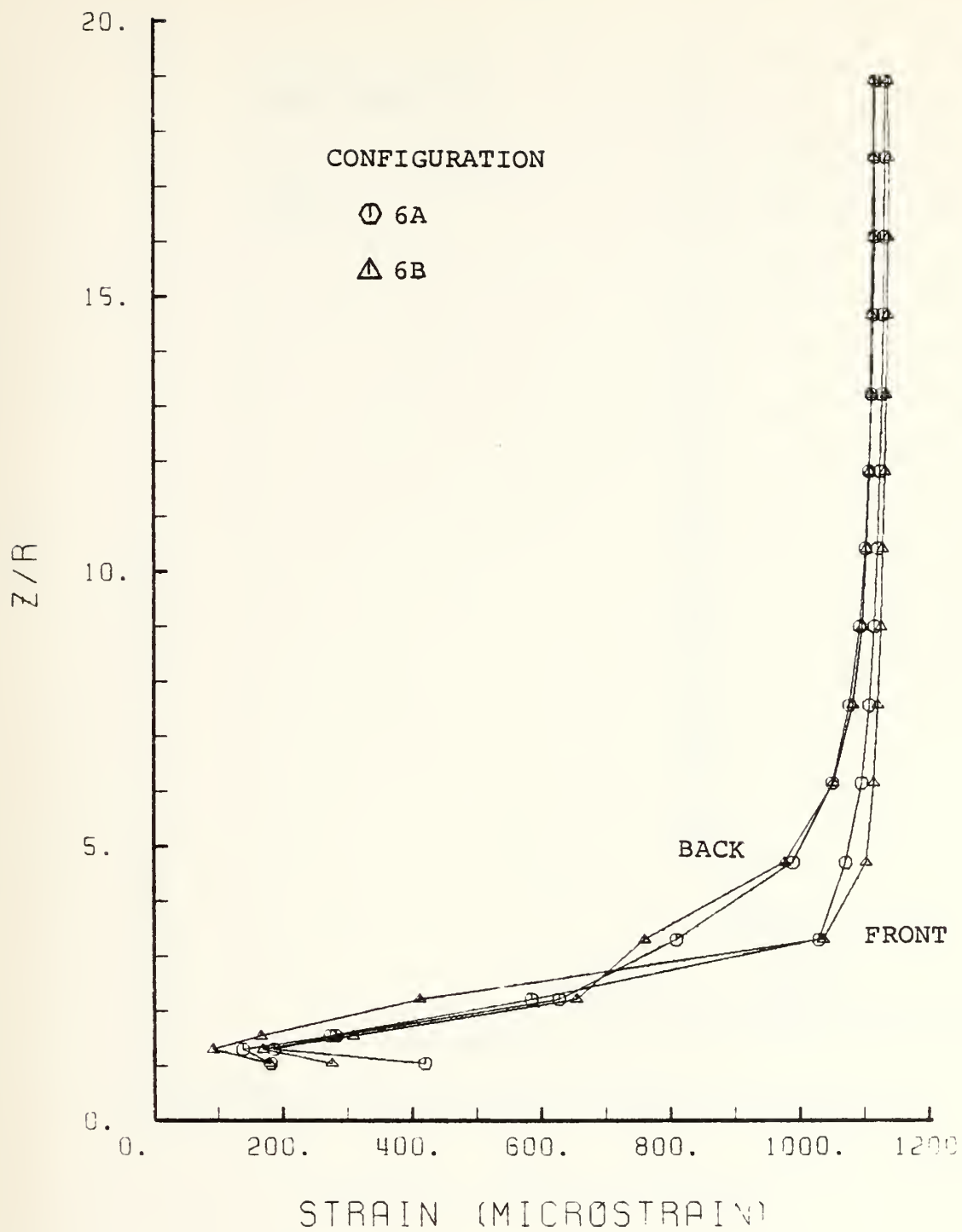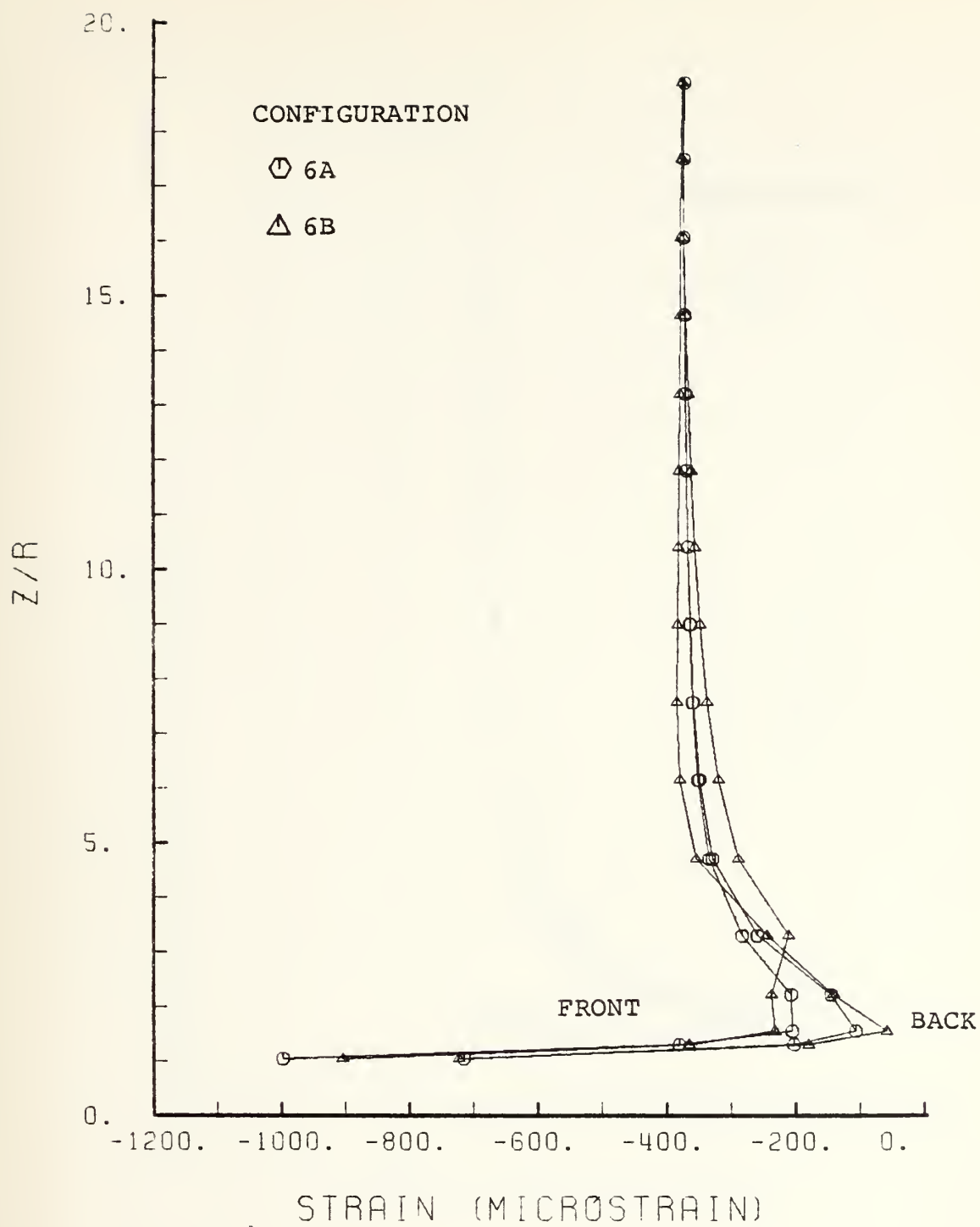
Figure 110. ε_x Vs X/R.

185

Figure. 111. ε_{xz} Vs X/R.

186

Figure 112. ε_z Vs Z/R.

187

Figure 113. ε_x Vs Z/R.

188

Figure 114. ε_{xz} Vs Z/R.

189
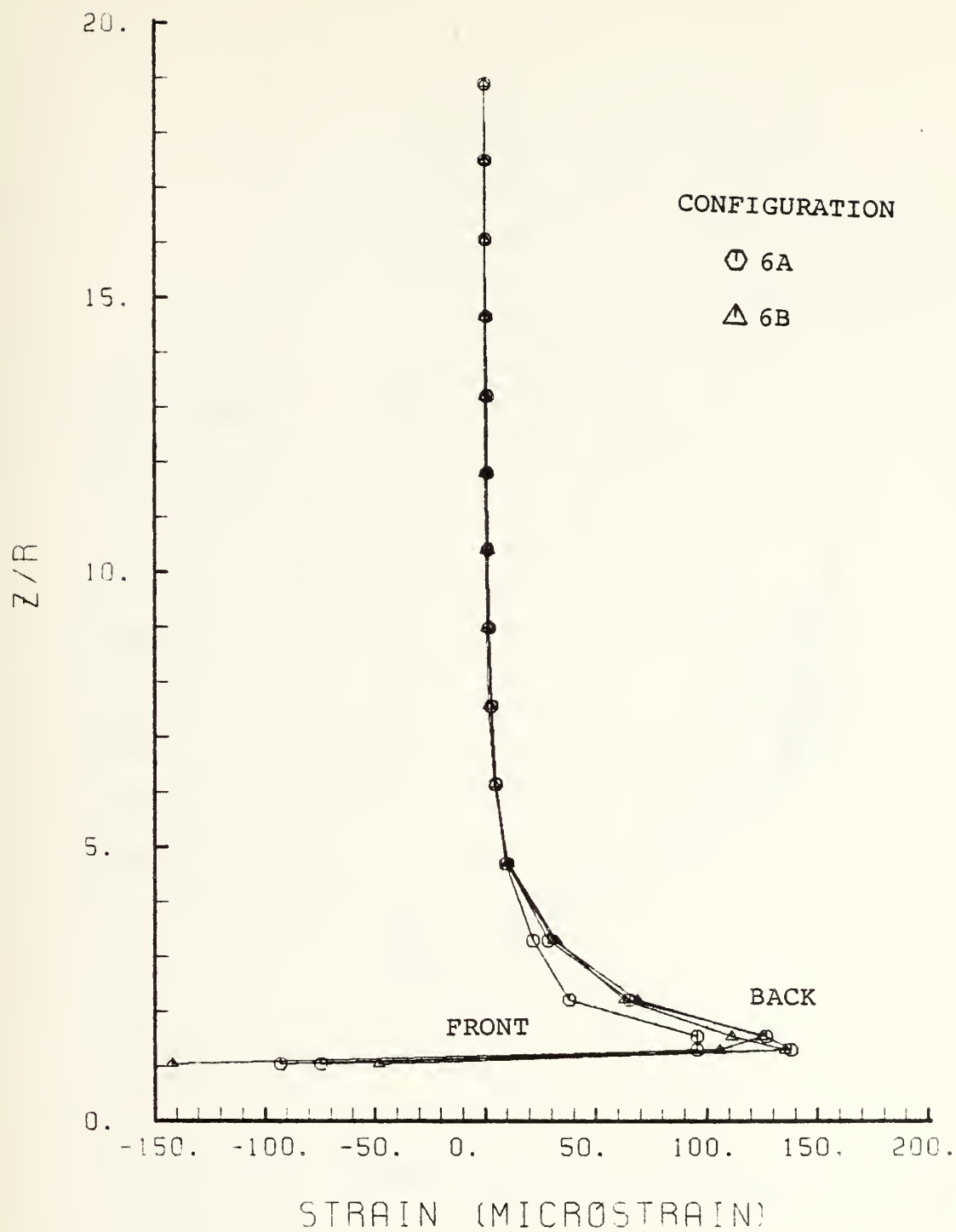
CONTOUR INDEX

1	-2×10^2
2	0
3	2×10^2
4	4×10^2
5	6×10^2
6	8×10^2
7	1.0×10^3
8	1.2×10^3
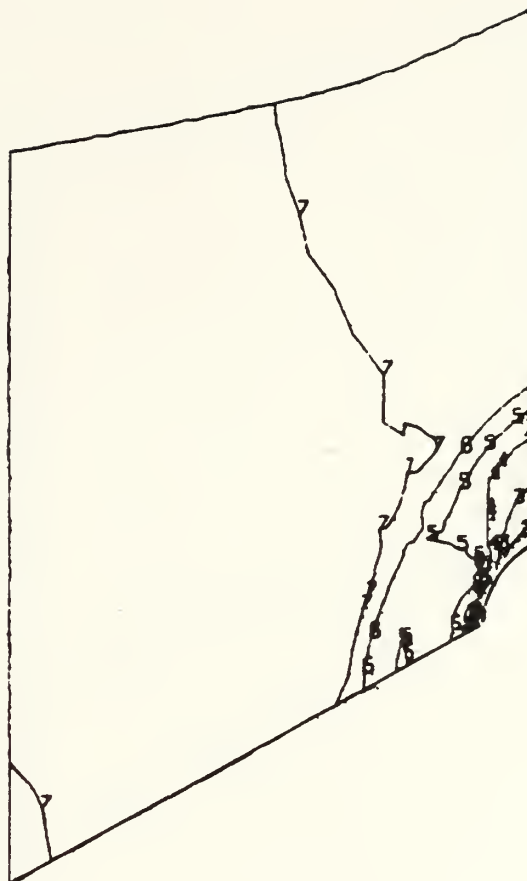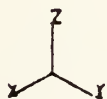
Figure 115. Contour Plot of N_z - Configuration 6A.

CONTOUR INDEX

1   -6×10^2

2   -4×10^2

3   -2×10^2

4   0

5   2×10^2
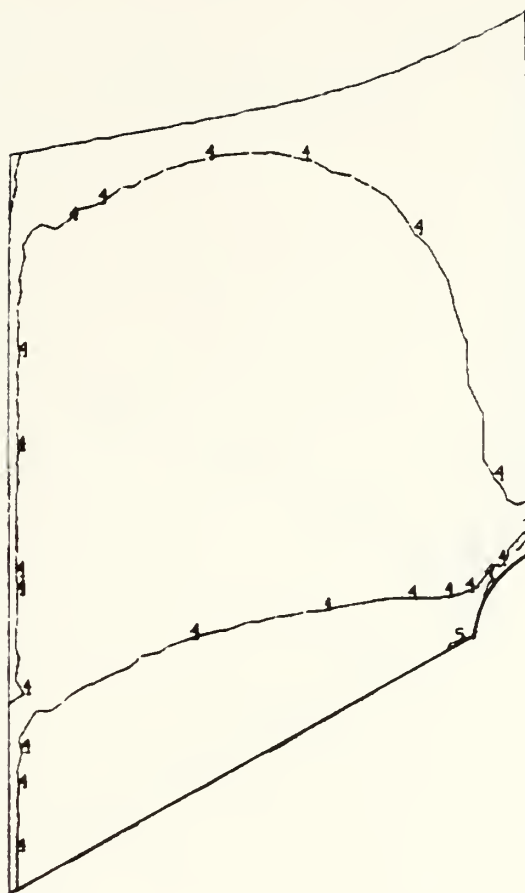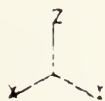
Figure 116.   Contour Plot of N_x - Configuration 6A.

CONTOUR INDEX

1	-1×10^2
2	0
3	1×10^2
4	2×10^2
5	3×10^2
6	4×10^2
7	5×10^2
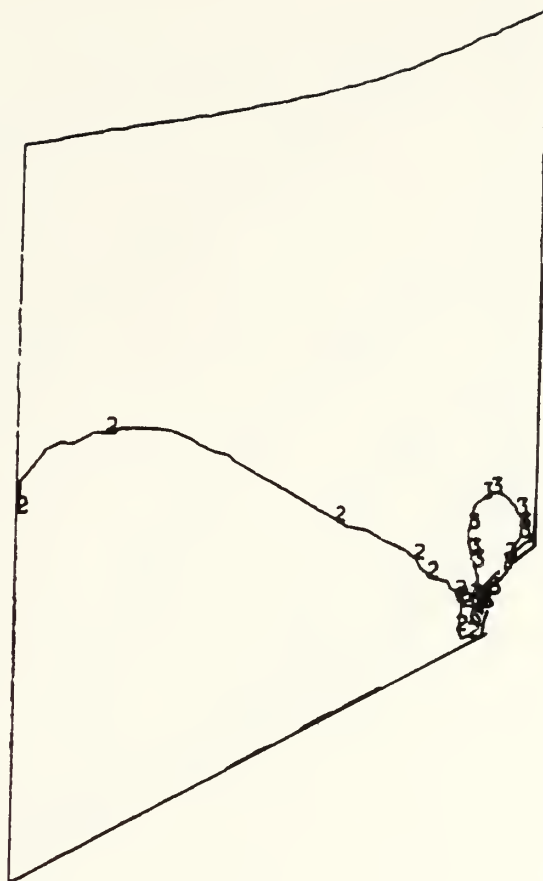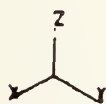
Figure 117.   Contour Plot of N_{xz} - Configuration 6A.

CONTOUR INDEX

1	0
2	2×10^{-3}
3	4×10^{-3}
4	6×10^{-3}
5	6×10^{-3}
6	8×10^{-3}
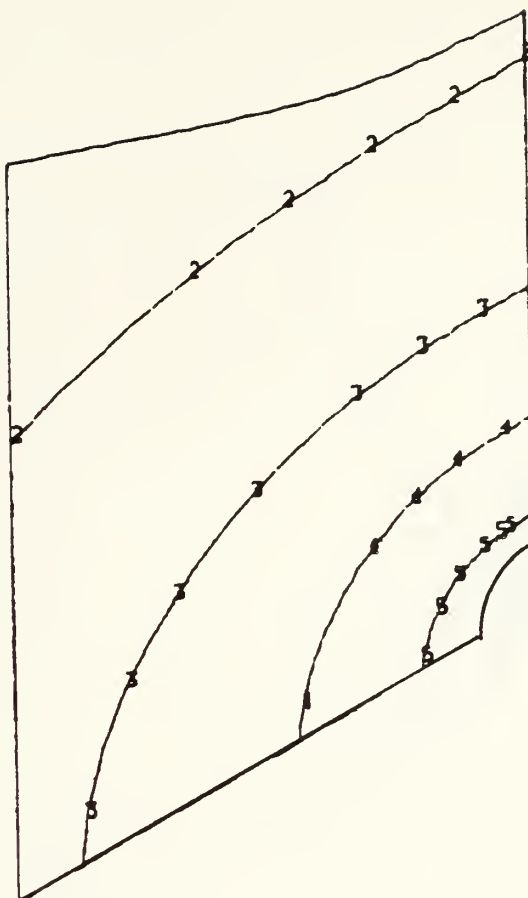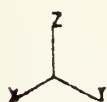
Figure 118.   Contour Plot of Out of Plane Deflections Configuration 6A.

CONTOUR INDEX

1	-2×10^2
2	0
3	2×10^2
4	4×10^2
5	6×10^2
6	8×10^2
7	1.0×10^3
8	1.2×10^3
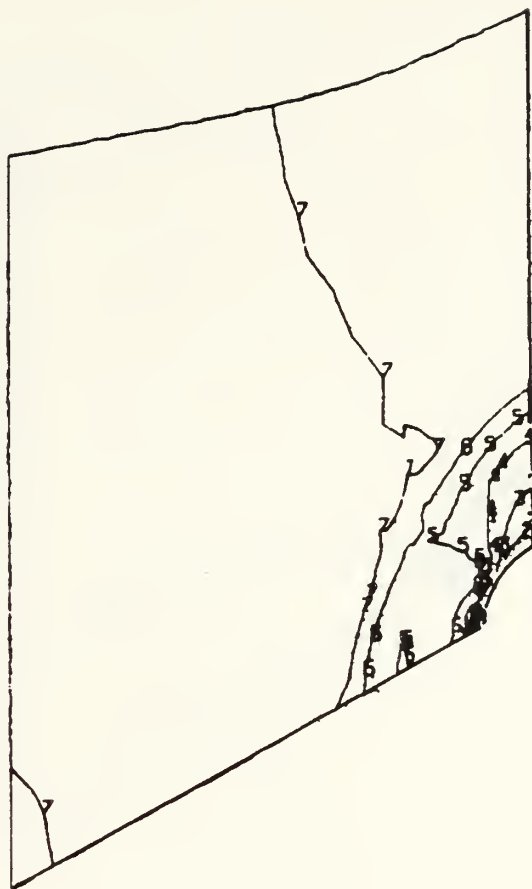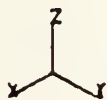
Figure 119.   Contour Plot of N_z - Configuration 6B.

CONTOUR INDEX

1	-6×10^2
2	-5×10^2
3	-4×10^2
4	-3×10^2
5	-2×10^2
6	-1.0×10^2
7	0
8	$1. \times 10^2$
9	2×10^2
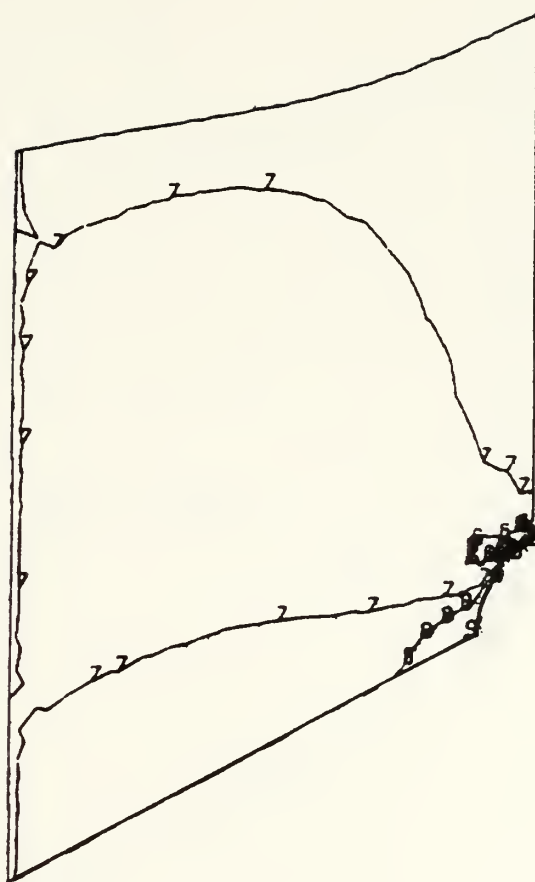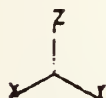
Figure 120. Contour Plot of N_x - Configuration 6B.

CONTOUR INDEX

1   -1×10^2

2   0

3   1×10^2

4   2×10^2

5   3×10^2

6   4×10^2

7   5×10^2
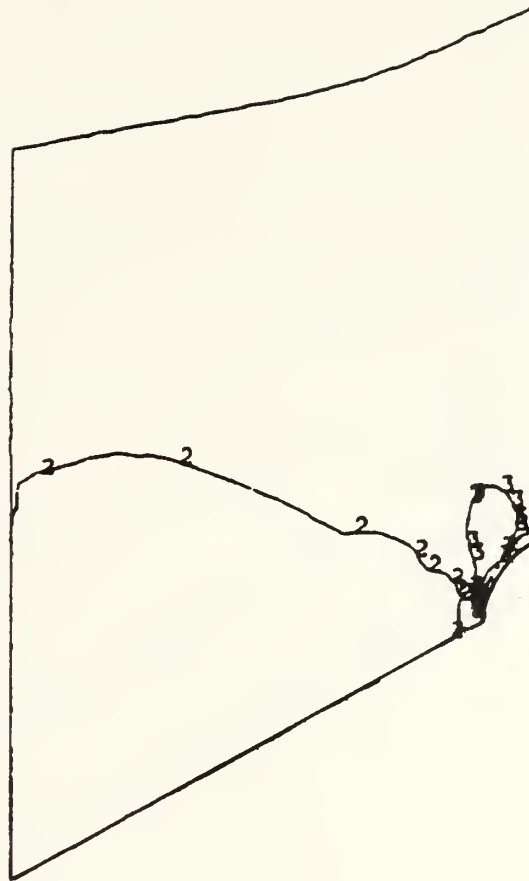
Figure 121.   Contour Plot of N_{xz} - Configuration 6B.

CONTOUR INDEX

1	2×10^{-3}
2	4×10^{-3}
3	6×10^{-3}
4	8×10^{-3}
5	1.0×10^{-2}
6	1.2×10^{-2}
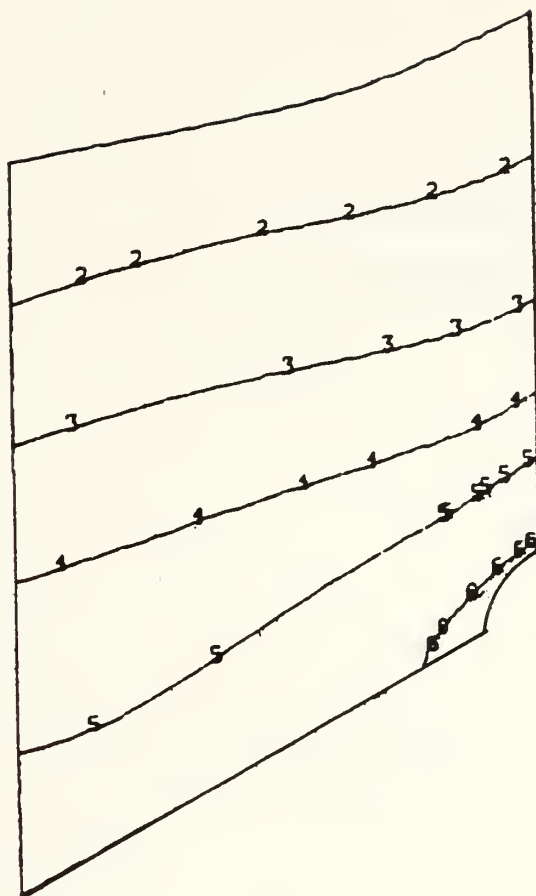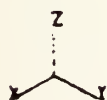
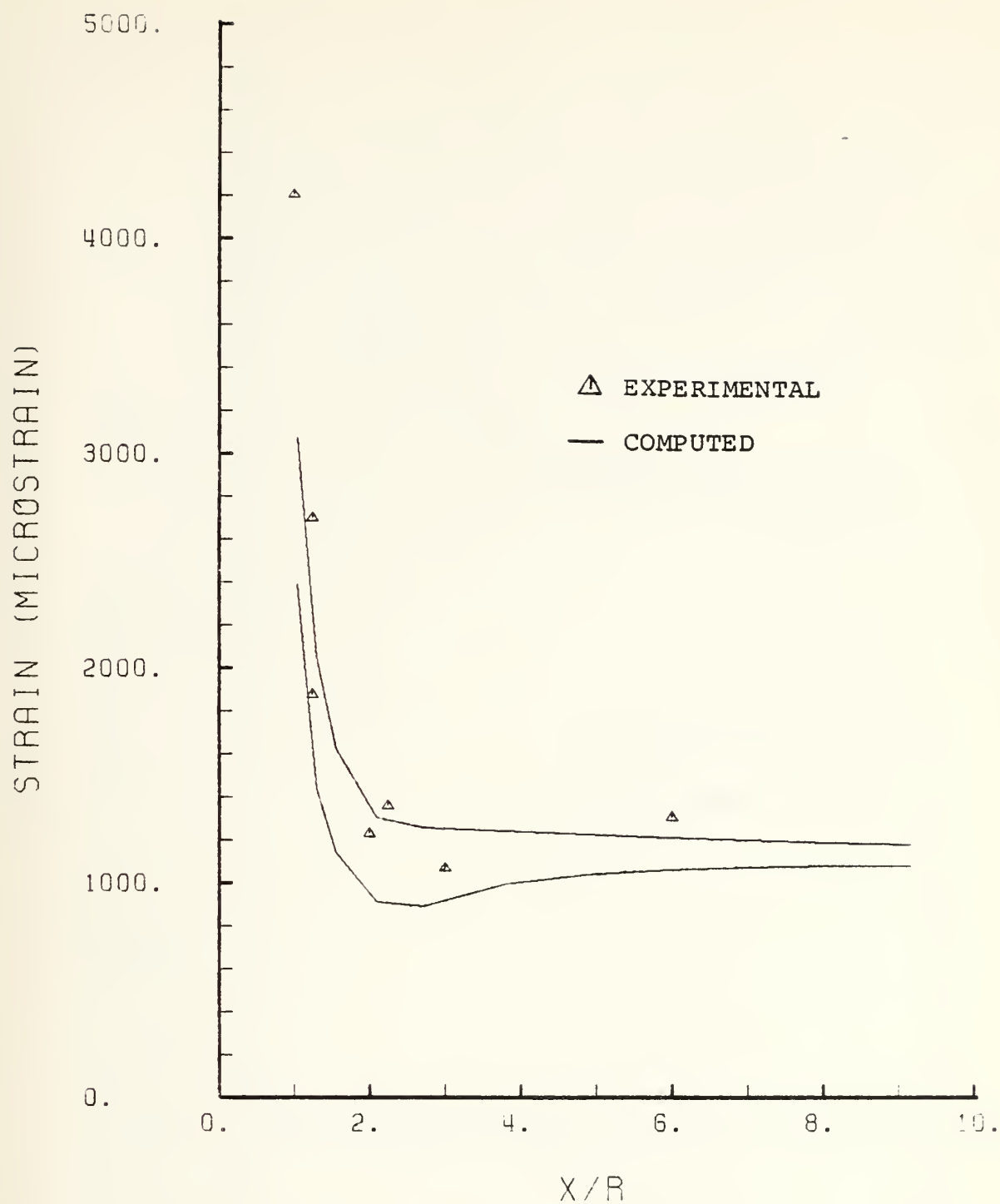Figure 122. Contour Plot of Out of Plane Deflections - Configuration 6B.

Figure 123. Comparison of Measured and Computed Strain - ε_z Vs X/R Configuration 6B.
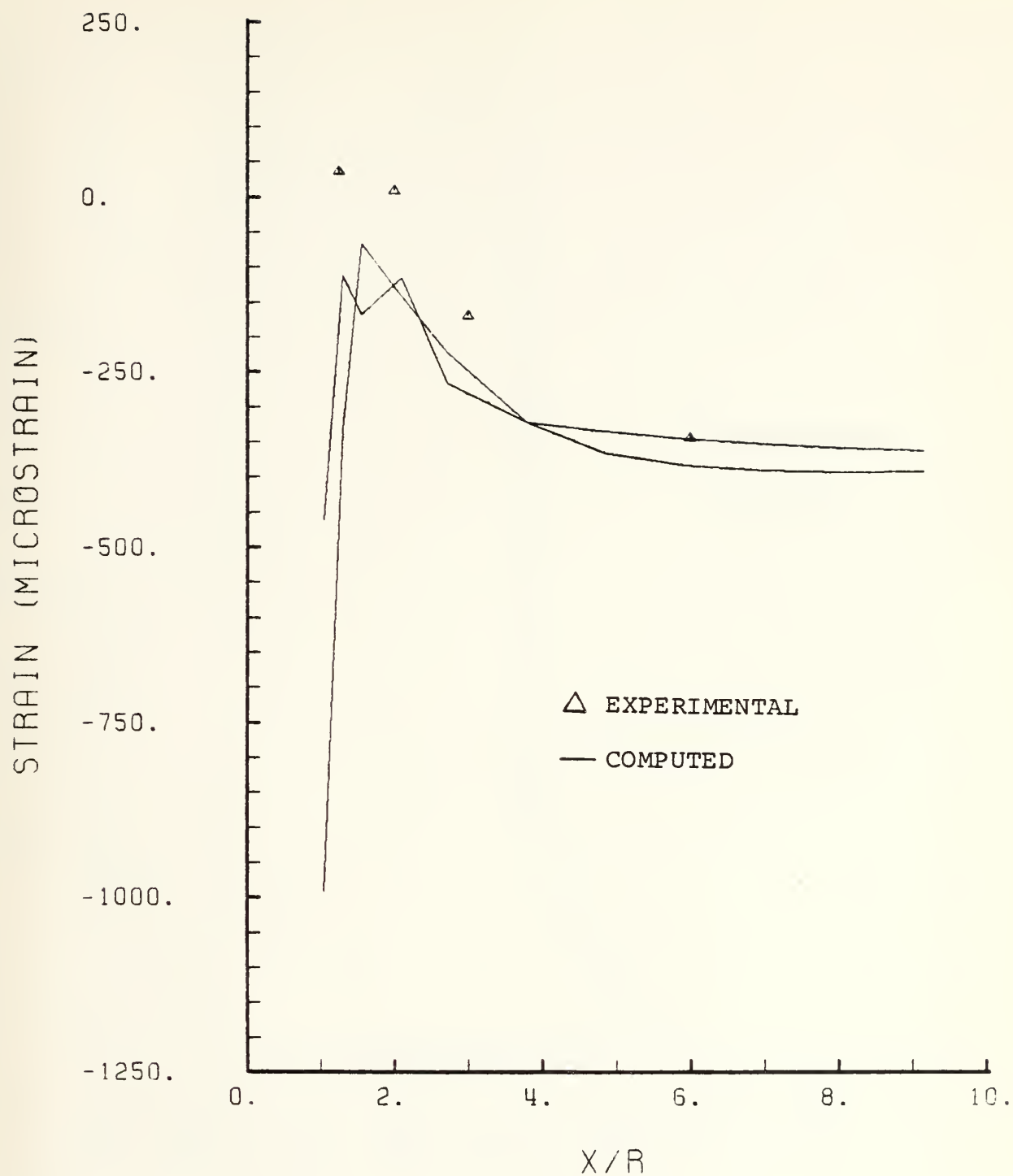
198

Figure 124. Comparison of Measured and Computed
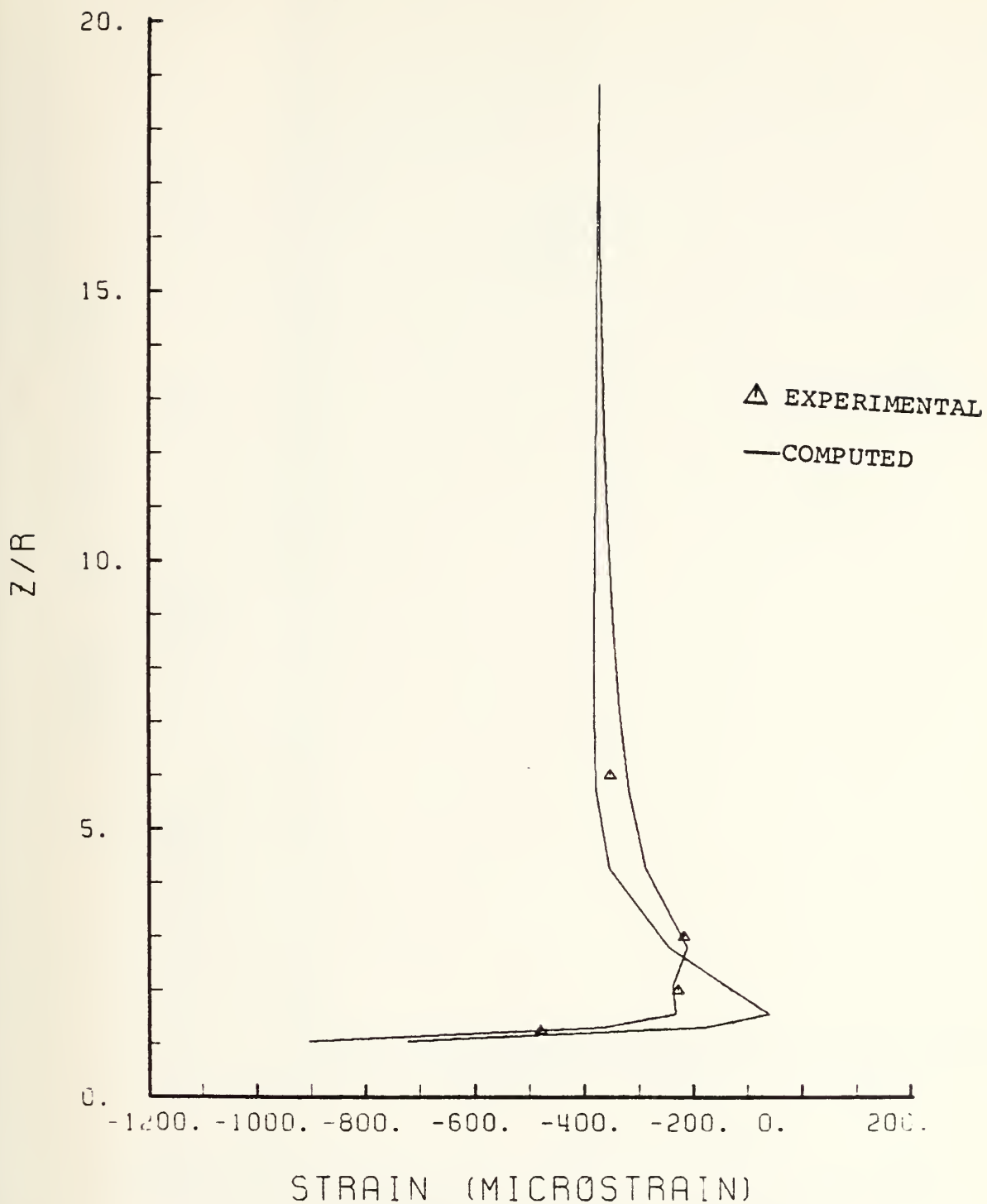   Strain - ε_x Vs X/R - Configuration 6B.

Figure 125. Comparison of Measured and Computed Strain ε_x Vs Z/R Configuration 6B.
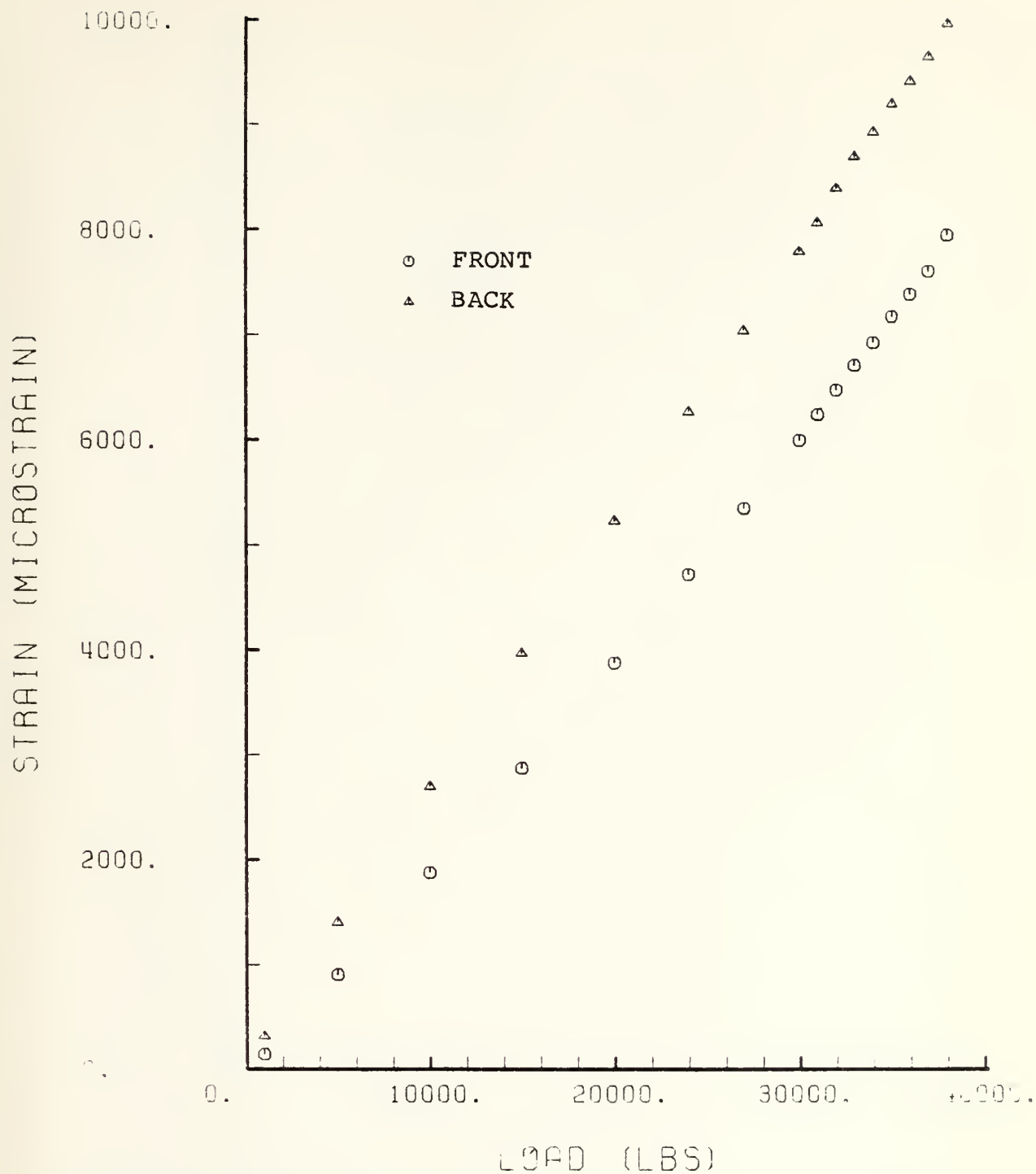
Figure 126. Comparison of Measured Front and Back
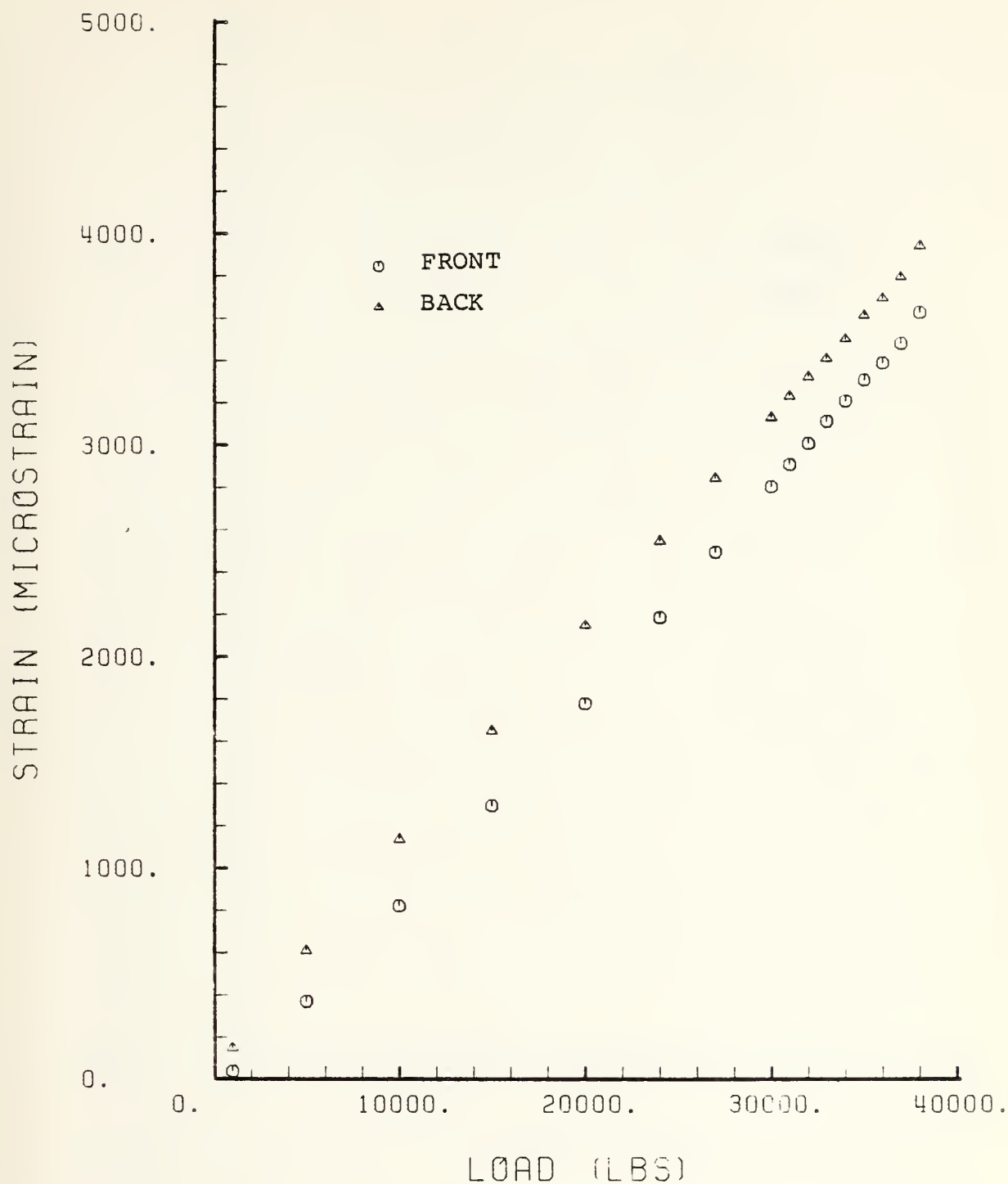Strains at Gauges 5 and 19 –
Configuration 6B.

201

Figure 127.   Comparison of Measured Front and Back
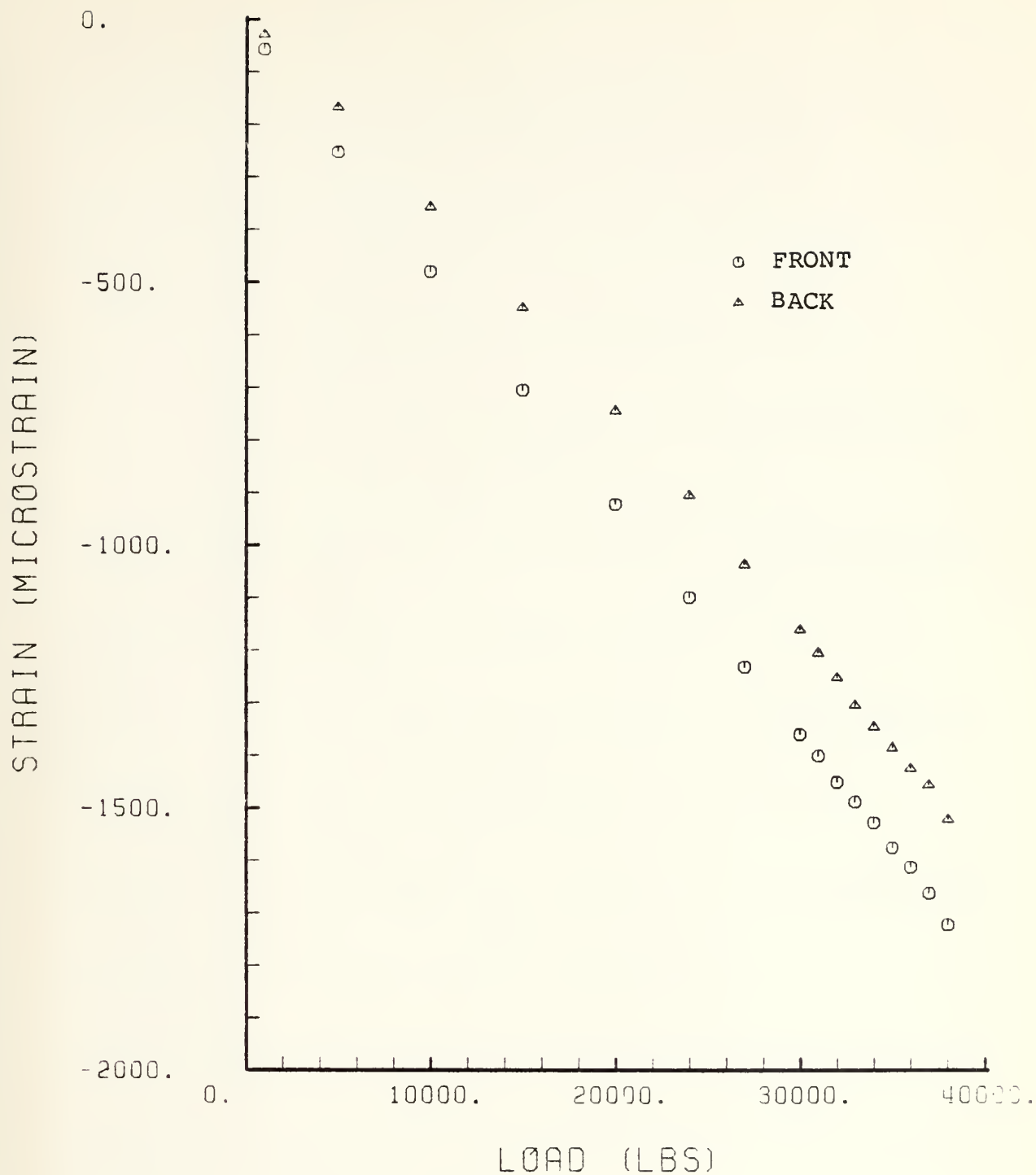Strains at Gauges 15 and 20 -
Configuration 6B.

Figure 128. Comparison of Measured and Computed Strains
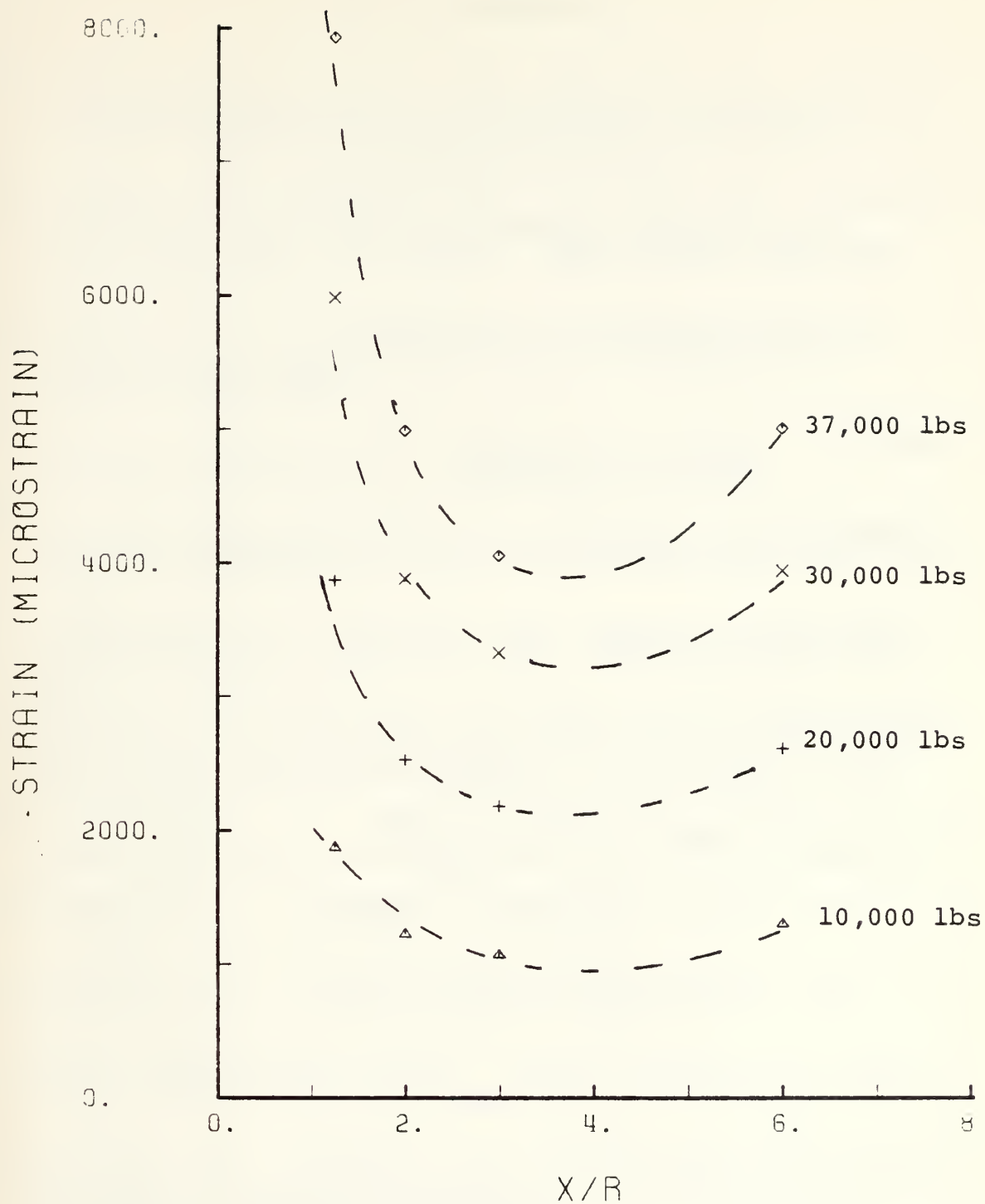at Gauges 9 and 21 - Configuration 6B.

Figure 129. Nonlinear Behavior of Panel 6B
ε_z Vs X/R at Hole Edge - Configuration 6B.

LIST OF REFERENCES

1. Rowlands, R.E., Daniel, I.M., Whiteside, J.B., "Stress and Failure Analysis of a Glass-Epoxy Plate with a Circular Hole", _Experimental Mechanics_, Jan 1973, p. 31.

2. Daniel, I.M., Rowlands, R.E., Whiteside, J.B., "Effects of Material and Stacking Sequence on Bheavior of Composite Plates with Holes", _Experimental Mechanics_, Jan. 1974, p. 1.

3. McKenzie, D.O., _The Analysis of Reinforced Holes in Carbon Fibre Plates_, Ph.D. Thesis, University of Bristol, Feb. 1976.

4. Freguson, G.H., Cyr, N., _"DIAL User's Manual"_, Lockheed Missiles and Space Co., Sunnyvale, CA, 1980.

5. Agarwal, B.D., Broutman, L.J., _Analysis and Performance of Fiber Composites_, John Wiley and Sons, New York, N.Y., 1980.

6. Timoshenko, S.P., Goodier, A.A., _Theory of Elasticity, Second Edition_, McGraw-Hill Book Co., New York, 1951.

7. Durelli, A.J., Phillips, L.A., Tsao, G.H., _Introduction to the Theoretical and Experimental Analysis of Stress and Strain_, McGraw-Hill Book Co., N.Y., 1951, p. 206.

8. Przemienicki, J.S., _Theory of Matrix Structural Analysis_, McGraw-Hill Book Co., New York, N.Y., 1968. Chapter 4.

9. Timoshenko, S., _Strenght of Materials, 3rd Ed_, Van Nostrant Co., Princeton, H.J., 1956.

10. Peterson, R.E., _Stress Concentration Factors_, John Wiley and Sons, New York, N.Y., 1974.

11. Royal Aeronautical Society, Stress Concentration Data, Report G5004, issued September 1956.

12. Whitney, J.M., Nuismer, R.J., "Stress Fracture Criteria for Laminated Composites Containing Stress Concentrations", _Journal of Composite Materials_, Vol. 8 (July 1974), p. 253.

13. Air Force Materials Laboratory, _Advanced Composites Design Guide_, Air Force Systems Command, Wright-Patterson AFB, Ohio, Vol II, Section 2.5.1, 1973.

14. Nuismer, R.J., Labor, J.D., "Application of the Average Stress Failure Criterion, Part I - Tension," _Journal of Composite Materials_, Vol. 12 (July 1978), p. 238.

INITIAL DISTRIBUTION LIST

No. Copies

1. Defense Technical Information Center   2
   Cameron Station
   Alexandria, Virginia   22314

2. Library, Code 0142   2
   Naval Postgraduate School
   Monterey, California   93940

3. Department Chairman, Code 67   1
   Department of Aeronautics
   Naval Postgraduate School
   Monterey, California   93940

4. Professor Milton H. Bank, Code 67Bt   7
   Department of Aviation Safety
   Naval Postgraduate School
   Monterey, California   93940

5. Dr. J. A. Bailie   5
   Org. 8112 Bldg 154
   Lockheed Missiles and Space Co.
   PO Box 504
   Sunnyvale, California   90486

6. LT Gary S. O'Neill   2
   1401 Collier Drive
   Smyrna, Georgia   30080